

FOSSIL ENERGY PROGRAM ANNUAL PROGRESS REPORT

APRIL 1, 1998-MARCH 31, 1999



O A K R I D G E N A T I O N A L L A B O R A T O R Y

**Fossil Energy Program Annual Progress Report
for
April 1998 Through March 1999**

**R. R. Judkins
Program Manager**

**P. T. Carlson
Technical Assistant**

July 1999

**Prepared for the
DOE Office of Fossil Energy
(AA, AB, AC, AW, AZ, SA)**

**Prepared by the
OAK RIDGE NATIONAL LABORATORY
Oak Ridge, Tennessee 37831-6285
Managed by
LOCKHEED MARTIN ENERGY RESEARCH CORP.
for the
U.S. DEPARTMENT OF ENERGY
under Contract DE-AC05-96OR22464**

CONTENTS

INTRODUCTION

MATERIALS RESEARCH AND DEVELOPMENT

Development of a Scaled-Up CVI System for Tubular Geometries

Development of Slurry-Based Oxide Coatings for Fossil Applications

Corrosion-Resistant Interface Coatings for Nicalon[®]/SiC Composites

Carbon Fiber Composite Molecular Sieve and Electrical Swing Adsorption Technology Development for the Separation and Capture of Carbon Dioxide

Intermetallic Reinforced Cr Alloys for High-Temperature Use

ODS Alloys for High-Temperature Applications

Bismuth Oxide Solid Electrolyte Oxygen Separation Membranes

Processing and Properties of Molybdenum Silicide Intermetallics Containing Boron

Fabrication of Test Tubes for Coal Ash Corrosion Testing

High-Temperature Corrosion Behavior of Iron Aluminide Alloys and Coatings

The Mechanical Reliability of Protective Alumina Scales

Evaluation of Iron Aluminide Hot-Gas Filters

ENVIRONMENTAL ANALYSIS SUPPORT

Environmental Support to the Low Emission Boiler System Program

Environmental Support to The Clean Coal Technology Program

BIOPROCESSING RESEARCH

Biological Upgrading of Petroleum Feedstocks and Heavy Oils via Microbial and Enzyme Biocatalysis

Fundamental Bioprocessing Research for Coal Applications

Integration of Combustion Power Systems With CO₂ Sequestration

CONTENTS

Biological Quality of Soils Containing Hydrocarbons and Efficacy of Ecological Risk Reduction by Bioremediation Alternatives

FOSSIL FUELS MODELING AND RESEARCH

Strategic Petroleum Reserve Planning and Modeling

OIL AND GAS PRODUCTION

Natural Gas and Oil Technology Partnership

Advanced Computational Tools for 3-D Seismic Data Fusion

Environmental Compliance Assistance System

Geologic Controls of Hydrocarbon Occurrence in Part of the Appalachian Basin in Tennessee, SW Virginia, Southern West Virginia, and Easternmost Kentucky

Ozone Treatment of Soluble Organics in Produced Water

Determination of Essential Thermophysical Properties for Sustainable Energy

Fundamental Chemistry of Heavy Oil

Development of a Centrifugal Downhole Separator

FOSSIL ENERGY PROGRAM ANNUAL PROGRESS REPORT FOR APRIL 1998 THROUGH MARCH 1999

R. R. Judkins, Program Manager

INTRODUCTION

This report covers progress made at Oak Ridge National Laboratory (ORNL) on research and development projects that contribute to the advancement of fossil energy technologies. Projects on the ORNL Fossil Energy Program are supported by the DOE Office of Fossil Energy, the DOE Federal Energy Technology Center, the DOE Fossil Energy Clean Coal Technology Program, the DOE National Petroleum Technology Office, and the DOE Fossil Energy Office of Strategic Petroleum Reserve.

The Oak Ridge National Laboratory (ORNL) Fossil Energy Program research and development activities cover the areas of coal, clean coal technology, gas, petroleum, and support to the Strategic Petroleum Reserve. An important part of the Fossil Energy Program is technical management of all activities on the DOE Fossil Energy Advanced Research and Technology Development (AR&TD) Materials Program. The AR&TD Materials Program involves research at other DOE and government laboratories, at universities, and at industrial organizations.

MATERIALS RESEARCH AND DEVELOPMENT

Materials research and development activities at Oak Ridge National Laboratory include development of ceramic composites for high temperature applications; new alloys with unique mechanical properties for advanced fossil energy systems; development of functional materials, such as ceramic filters, ceramic membranes, activated carbon materials, and solid oxide fuel cell materials; and corrosion research to understand the behavior of materials in coal-processing environments. Transfer of technology developed on this program is enhanced through interactions with industry and by joint research programs with interested end-users.

¹Research sponsored by the U.S. Department of Energy, Office of Fossil Energy, under contract DE-AC05-96OR22464 with Lockheed Martin Energy Research Corp.

ENVIRONMENTAL ANALYSIS SUPPORT

Activities in environmental analysis support included assistance to the Federal Energy Technology Center at Morgantown, West Virginia, and Pittsburgh, Pennsylvania, in reviewing and preparing documents required by the National Environmental Policy Act (NEPA) for projects selected for the Clean Coal Technology (CCT) Program and for the Low Emission Boiler System (LEBS) Program. An important activity for the CCT Program was the preparation of an Environmental Impact Statement (EIS) for a new circulating fluidized bed combustor fueled by coal and petroleum coke to repower an existing steam turbine at Jacksonville Electric Authority's Northside Generating Station in Jacksonville, Florida. An important activity for the LEBS Program was the preparation of an EIS for integrated coal-fired technologies for electric power generation at the proof-of-concept scale adjacent to the Turrill Coal Company's existing underground coal mine near Elkhart, Illinois.

BIOPROCESSING RESEARCH

Work on the Fossil Energy Bioprocessing Research Program includes fundamental research for coal applications, with emphasis on advanced reactor design for conversion of coal synthesis gas to liquid fuels, biological upgrading of petroleum feedstocks and heavy oils via microbial and enzyme biocatalysis, and integration of combustion power systems with CO₂ sequestration. In addition, the program includes studies of the biological quality of soils containing hydrocarbons and bioremediation alternatives to reduce ecological risk.

FOSSIL FUEL SUPPLIES MODELING AND RESEARCH

The fossil fuel supplies modeling and research effort focuses on U.S. Strategic Petroleum Reserve (SPR) planning and management. Topics covered include planning for an Asian Pacific emergency oil stockpile, reassessing the benefits of expanding the size of the U.S. SPR, updating models for SPR risk analysis, and fill-draw planning.

OIL AND GAS PRODUCTION

Research in oil and gas production at Oak Ridge National Laboratory is represented by activities in three research divisions: Chemical Technology, Computer Science and Mathematics, and Environmental Sciences. The areas of study involve measurements of wax points in crude oils and petroleum fluids, evaluation of the hydrocarbon potential of part of the Appalachian basin, the application of nuclear fuel reprocessing technology to the separation of petroleum and water downhole in an oil well, characterization and treatment of soluble organics in produced water, the application of global optimization methods to residual statics in seismic imaging, the use of neural networks in oilfield parameter estimation, and providing environmental compliance information for the National Petroleum Technology Office's Web site.

MATERIALS RESEARCH AND DEVELOPMENT

R. R. Judkins

Materials research and development activities at Oak Ridge National Laboratory include development of ceramic composites for high temperature applications; new alloys with unique mechanical properties for advanced fossil energy systems; development of functional materials, such as ceramic filters, ceramic membranes, activated carbon materials, and solid oxide fuel cell materials; and corrosion research to understand the behavior of materials in coal-processing environments. Transfer of technology developed on this program is enhanced through interactions with industry and by joint research programs with interested end-users.

DEVELOPMENT OF A SCALED-UP CVI SYSTEM FOR TUBULAR GEOMETRIES

T. M. Besmann and J. C. McLaughlin
Metals and Ceramics Division
Oak Ridge National Laboratory
P.O. Box 2008, Oak Ridge, TN 37831-6063
e-mail: tmb@ornl.gov

K. J. Probst and T. J. Anderson
Department of Chemical Engineering
University of Florida
Gainesville, FL 32611

T. L. Starr
Department of Chemical Engineering
University of Louisville
Louisville, KY 40292

Silicon carbide-based heat exchanger tubes are of interest to energy production and conversion systems due to their excellent high temperature properties. Fiber-reinforced SiC is of particular importance for these applications since it is substantially tougher than monolithic SiC, and therefore more damage and thermal shock tolerant. This paper reviews a program to develop a scaled-up system for the chemical vapor infiltration of tubular shapes of fiber-reinforced SiC. The efforts include producing a unique furnace design, extensive process and system modeling, and experimental efforts to demonstrate tube fabrication.

INTRODUCTION

Fiber-reinforced SiC-matrix composites are candidates for numerous high temperature applications. These composites possess high-temperature strength, high thermal conductivity, thermal shock and creep resistance, and damage tolerance. However, in the current commercial isothermal, isobaric chemical vapor infiltration process, thick-walled parts are difficult to densify. A leading alternative process is forced chemical vapor infiltration (FCVI) (1, 2). In FCVI, a thermal gradient is developed along the preform thickness by heating the preform exterior and cooling the interior. The reactant gases are constrained to flow from the cooled interior to the heated exterior. These gases react at the fiber surfaces throughout the preform volume and deposit the ceramic matrix. In the case of SiC deposited from chlorosilanes, the resulting effluent by-product HCl gas has a poisoning effect on the deposition rate. This poisoning combined with the reactant depletion through the preform thickness inhibits the matrix deposition rate. However, since the gases are forced toward the heated preform exterior, the higher temperatures support faster deposition rates due to the Arrhenius behavior of the deposition reaction. Therefore, the

SiC deposition is controlled by the counterbalance of thermal gradient and reactant depletion.

In the current work, emphasis is on the development of composites with tubular geometries. In order to demonstrate the fabrication of a prototypical tube, the efforts have centered on component diameters of 64 mm with a 6.4 mm wall thickness. Therefore, a unique furnace system was designed and constructed to facilitate the FCVI of such tubes with lengths of 350 mm. Supporting the developmental effort has been extensive process modeling that has successfully described and aided the optimization of the FCVI of composite plates (3,4).

EXPERIMENTAL

Tubular fiber preforms are fabricated prior to infiltration. The desired dimensions are provided in Table 1. Eleven concentric sleeves of Nextel™ 312 fiber are stretched over a cylindrical mandrel. These fibrous sleeve porosity are impregnated with a phenolic resin, compressed, and cured prior to furnace fixturing to rigidize the preform. Tubular preforms with fiber volumes between 35% and 50% are realized.

Table 1: Preform Dimensions.

Inside Diameter	50.8 mm
Thickness	6.4 mm
Length	305 mm

At temperatures greater than 200°C, the phenolic resin is pyrolyzed leaving carbon on the fiber surface. Excess application of phenolic resin to the fibrous sleeves results in excess carbon which coats the fibers and consumes a considerable fraction of intratow porosity. Porosity filled with carbon limits the ultimate achievable density. Figure 1 demonstrates this phenomenon. In Figure 2, no residual carbon at the fiber interface can be seen. A lower concentration of phenolic resin was thus used in preform fabrication to control carbon content while retaining the necessary rigidity.

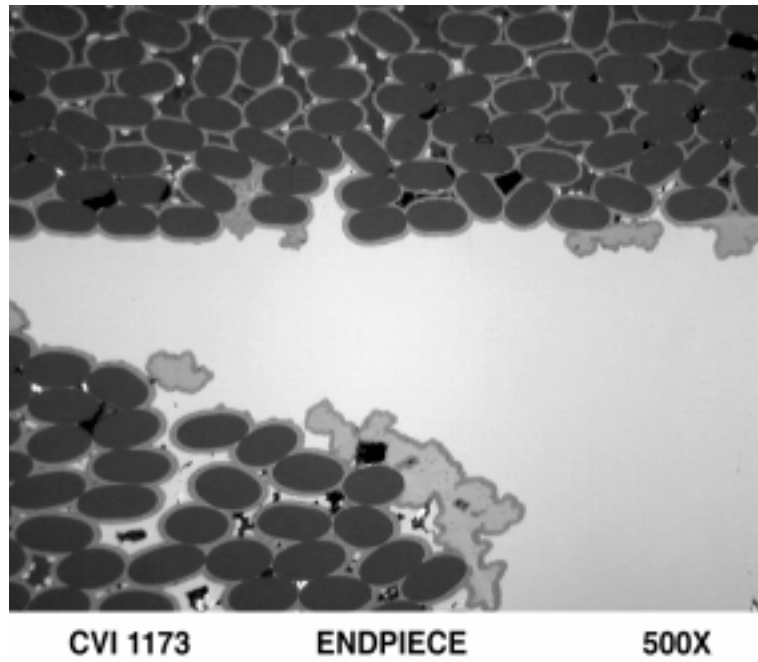


Figure 1. Excess fiber interfacial carbon is realized from application of excess phenolic resin.

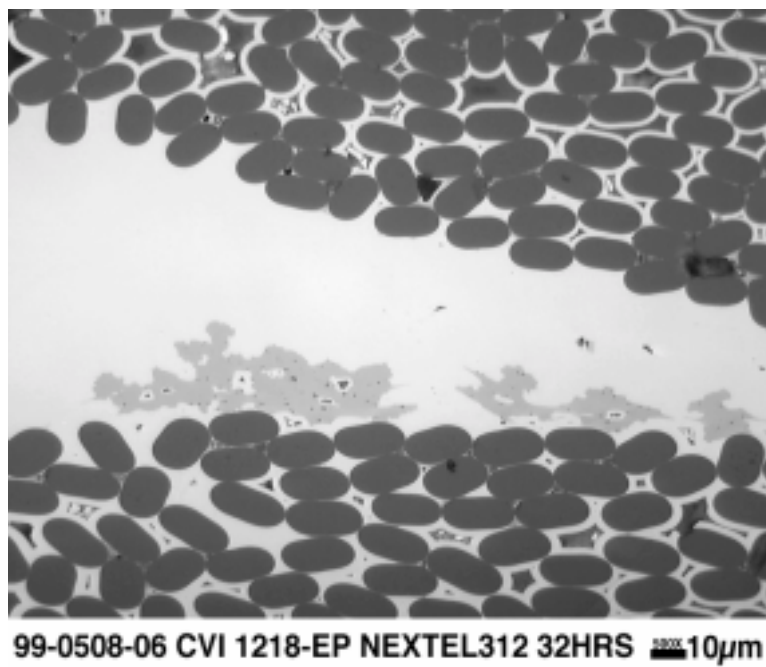


Figure 2: Residual carbon is eliminated using less phenolic resin. Preform rigidity is maintained with less resin.

Four tubular preforms of Nextel™ 312 were infiltrated for various times using the same experimental conditions. The FCVI conditions used included five l/min of hydrogen, a hydrogen/MTS feed ratio of five, and a coating chamber mid-line temperature of 1200°C. The average density of each composite tube was estimated using the initial fiber volume percents and final tares. The radial dimension increases after infiltration due to silicon carbide deposit on the tube exterior. The volume change lowers the initial fiber volume percent from 40% to approximately 35%. Infiltration and density data of these preforms are provided in Table 2.

Table 2: Density data of intermediate infiltrations.

<u>Identification</u>	<u>Infiltration Time</u>	<u>Fiber Volume</u>	<u>Theoretical Density</u>
CVI 1211	6 Hours	35.3%	39.7%
CVI 1223	12 Hours	34.7%	54.0%
CVI 1217	24 Hours	32.7%	69.6%
CVI 1218	32 Hours	32.4%	79.5%

The expected density increase with infiltration time is seen with these four infiltrated tubes. A lower fiber volume is associated with increasing infiltration time. This is due to a thicker exterior silicon carbide deposit resulting from longer infiltrations. Excess silicon carbide deposit on the preform interior was seen in previous work (5). No excess interior silicon carbide deposit was observed in any of the current tubes.

Two tubular preforms using Nextel™ 610 fiber were fabricated and infiltrated. Nextel™ 610 has higher strength retention at elevated temperatures than does the 312, yet the sleeve braid architecture of the Nextel™ 610 is similar to that of the Nextel™ 312. The two Nextel™ 610 preforms had different fiber volumes. Both tubes (Fig. 3) achieved theoretical densities greater than 80%. These Nextel™ 610 tubes were sent to Virginia Polytechnic Institute for mechanical testing (Dr. Scott Case).

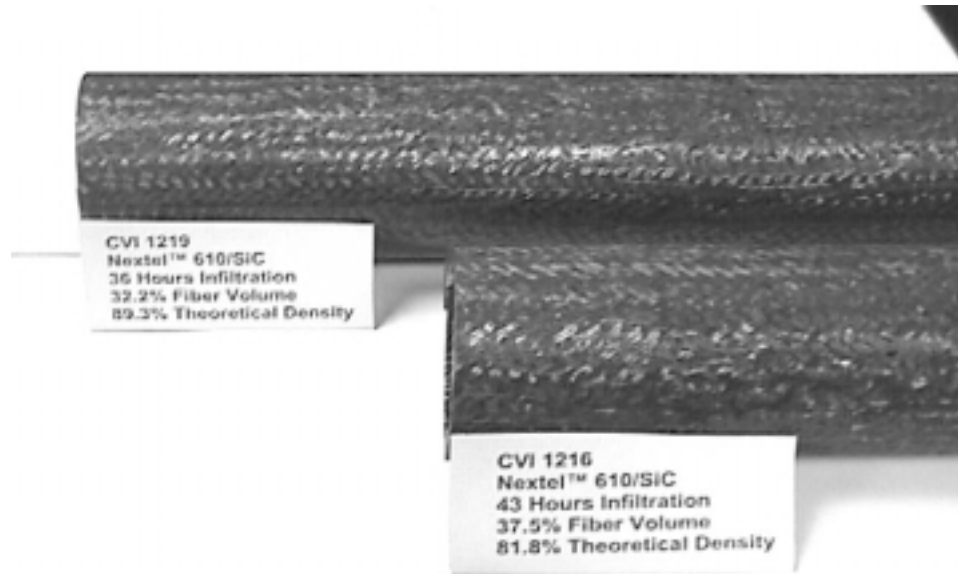


Figure 3: Infiltrated tubes using Nextel™ 610 fiber achieved post-infiltration theoretical densities of greater than 80%.

MODELING

A description of the FCVI model, GTCVI, discretization of the reaction configuration, and initial model results has been reported previously (5). Earlier FCVI model results indicate that higher temperatures, higher total flows, and lower hydrogen/MTS feed ratios resulted in higher densities at a specific time. The relative agreement between experimental tube densities and model prediction was good at infiltration completion. However, the model agreement with experimental tube densities at intermediate times was unknown.

GTCVI was run using two different functions describing the preform specific surface area (Module 1 and 2) (Fig. 4). The initial specific surface area in Module 1 assumes no adjacent fiber contact while the initial surface area used in Module 2 assumes some initial fiber contact and therefore a significant reduction in available surface area.

An average density plot comparing model results with experiment is shown in Figure 5. Both average density model results predict the experimental trend. However, the density results using Module 1 overshoot experimental results significantly. The results using Module 2 have an

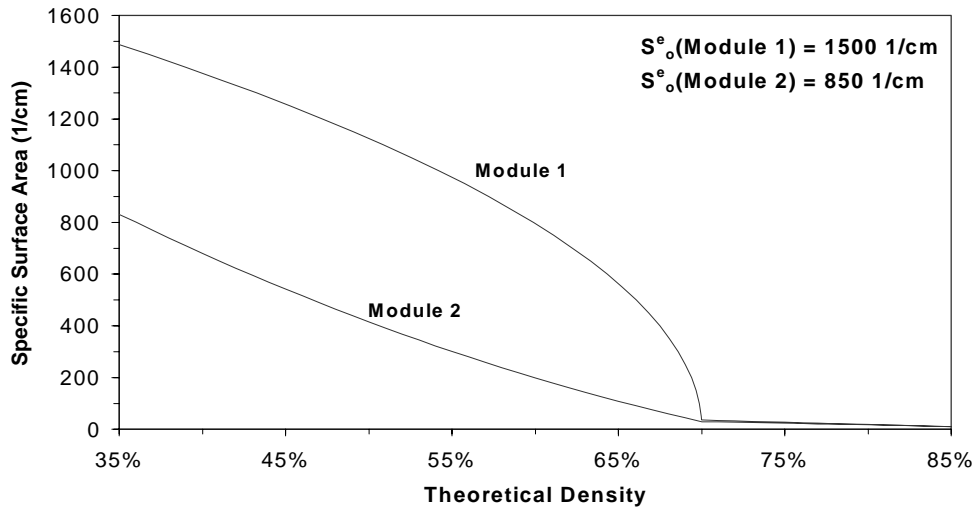


Figure 4: The two model functions used describing the preform specific surface area. A lower initial specific surface used in Module 2 represents probable initial fiber contact.

improved agreement with experiment. The assumption of initial fiber contact with Module 2 thus appears more realistic.

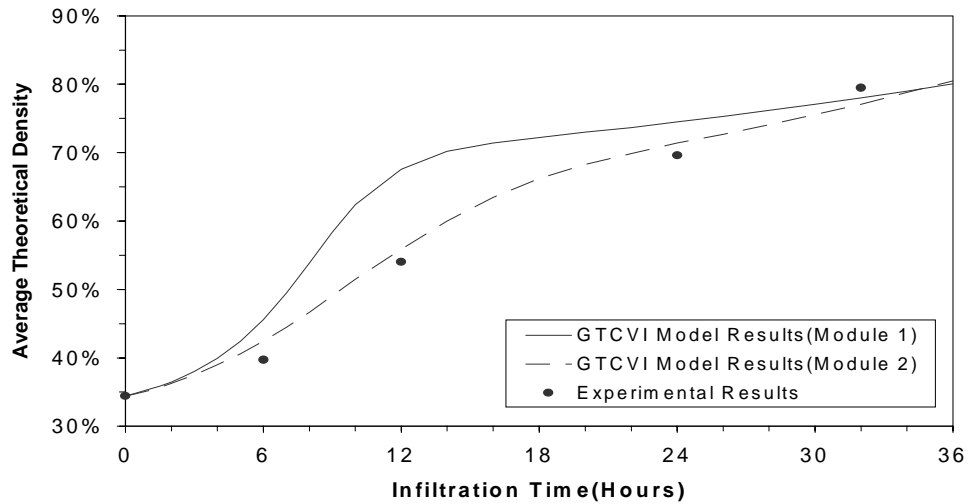


Figure 5: Model results from both specific surface area functions predict the general experimental trend. Results using Module 2 have improved agreement with experiment.

Figure 6 shows the model result of the initial tube temperature profile. The radial temperature gradient is relatively uniform with a slightly higher gradient located near the gas inlet. The exterior temperature profile reflects the parabolic temperature profile seen in experiment. The lower temperatures seen at the tube ends is due to heat loss through the ends of the furnace.

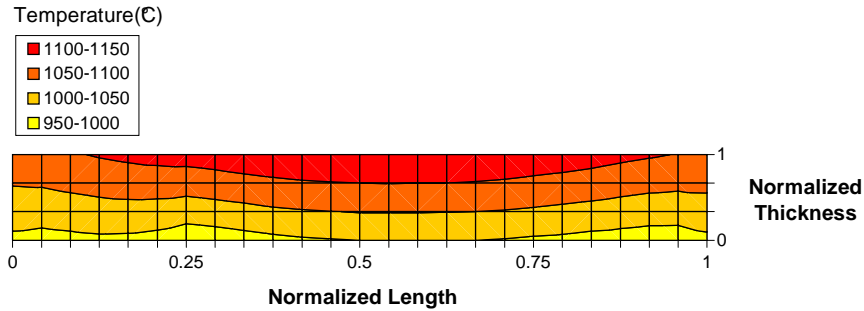


Figure 6: Initial temperature profile of the tube preform. A slightly higher temperature gradient is observed near the gas inlet.

Two model results of tube densities at intermediate infiltration times are shown in Figures 7 and 8. Figure 7 is at six hours of infiltration while Figure 8 is at 32 hours of infiltration. In both figures, the density values reflect the tube temperature profile seen in Figure 6. In Figure 8, the majority of the tube is at greater than 80% theoretical density with the ends lagging.

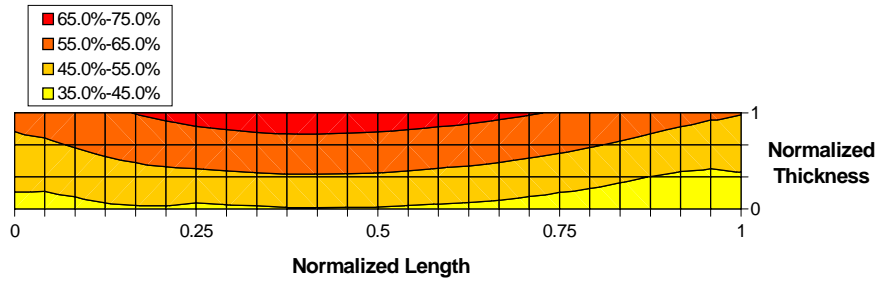


Figure 7: Tube density profile at six hours of infiltration.

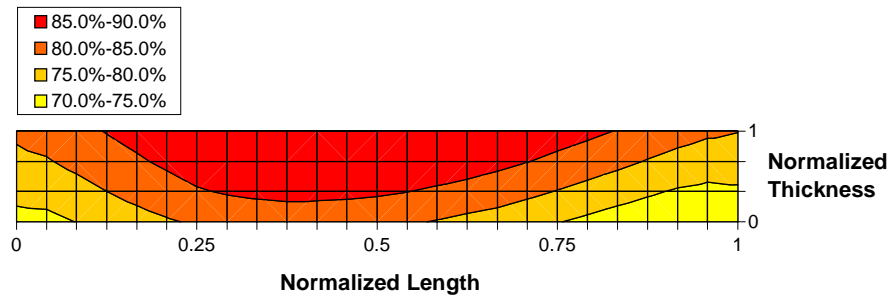


Figure 8: Tube density profile at 32 hours of infiltration.

With the successful development of composite tube fabrication by FCVI, there is a recognition that the fiber types used in the effort will not have sufficient high temperature (>1000°C) stability for the intended applications. Thus efforts to replace the Nextel™ series of

fibers with higher temperature materials have been initiated. The crystalline stoichiometric silicon carbide fibrils are being developed by Industrial Ceramic Solutions, Inc.

To assess the silicon carbide fibrils as reinforcement for silicon carbide matrix composites several preforms have been fabricated using Saffil fibers, as a stand-in for the fibrils under development, and infiltrated. A preform prepared from laminae of fibers was infiltrated. The laminae, however, were apparently too stiff to compress into a preform, and thus large voids were present between the layers (Fig. 9)

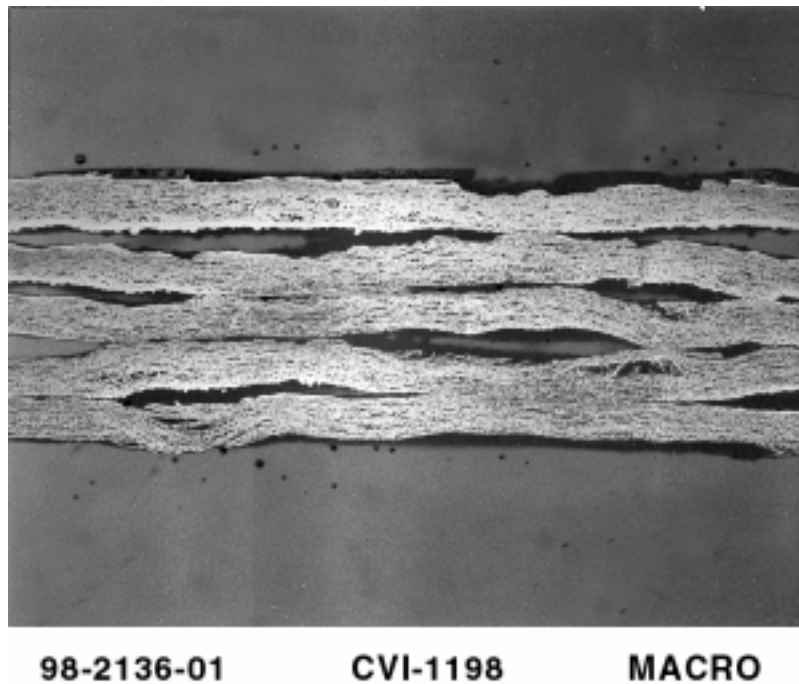


Fig. 9. Cross-section of a layered fibril reinforced composite (1.25 cm in thickness) showing large voids between layers.

Randomly oriented fiber preforms were also prepared and infiltrated. These were significantly more uniform in density, however, they had a lower fiber content. Infiltration of these preforms was also problematic in that the thermal and transport properties were sufficiently different from other fibers used in the past so that the FCVI conditions were not optimal. As a result the preforms were insufficiently densified on the cooled side, as seen in Fig. 10.

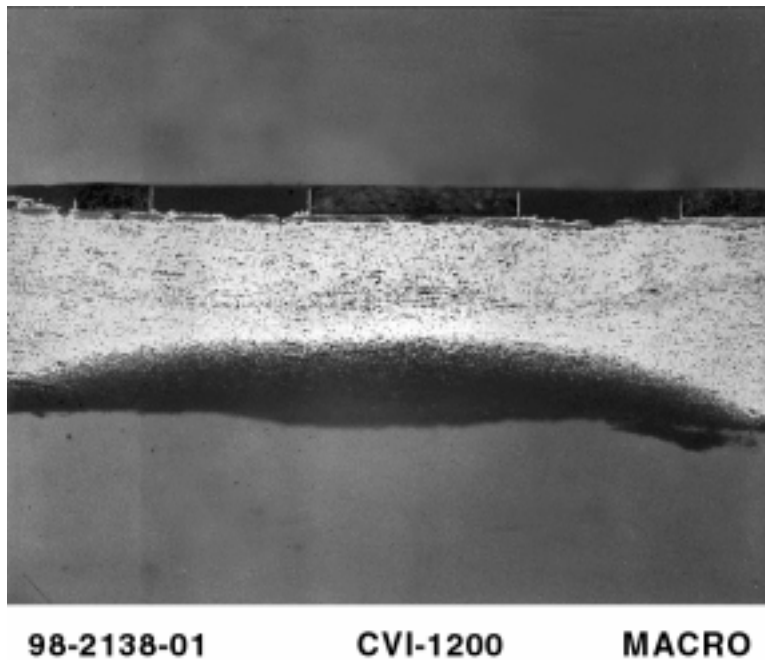


Fig. 10. Cross-section of a randomly oriented fibril preform (1.25 cm thick) that has been infiltrated. The cooled (lower) side is poorly infiltrated.

The microstructure of the densified region of the randomly oriented preforms can be seen in Fig. 11. While much of the void space has been well-filled with silicon carbide, the fracture surface reveals little fiber pull-out. This indicates that the fibers require an interace coatings, as likely will the fibrils, that will adjust the fiber-matrix bond in order to obtain more pull-out, and therefore the desired mechanical properties.

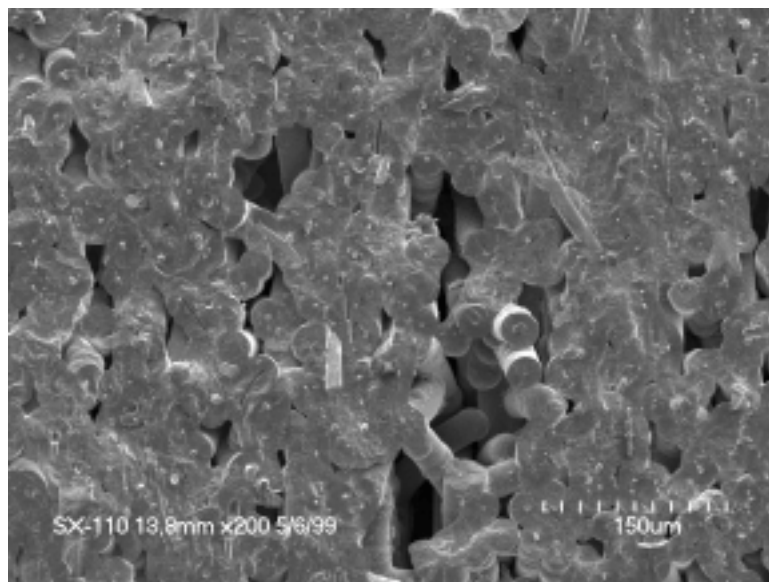


Fig. 11. Fracture surface of infiltrated, randomly oriented fibril preform.

CONCLUSIONS

Excess phenolic resin used in the preform fabrication results in excess residual carbon at the fiber interface. The excess carbon limits the ultimate achievable tube density. A lesser quantity of phenolic resin applied to the preform eliminates residual carbon while maintaining preform rigidity.

Tubular preforms of Nextel 312 were infiltrated at intermediate times. The tube average densities increased with increasing infiltration time. Tube preforms at longer infiltration times had slightly lower fiber volume fractions due to silicon carbide deposit on the preform exterior which increased the tube volume.

Two model results using two different functions describing the preform specific surface area were compared to the experimental densities. Model results using a lower initial specific surface area agreed very well with experiment. The lower initial specific area represents the effect initial fiber contact that results from preform compression.

Two tubular preforms of Nextel™ 610 were well-infiltrated using the FCVI process and these were provided to Virginia Polytechnic Institute for mechanical testing.

Efforts have begun to utilize crystalline, stoichiometric silicon carbide fibrils as preforms for the composite tubes in order to replace the current, relatively low temperature fibers. Initial work with Saffil fibers as a stand-in for silicon carbide is encouraging in that at least randomly oriented fibril preforms can be fabricated and partially infiltrated. Significant efforts remain in developing the necessary FCVI conditions for these materials and interface coatings that yield the desired mechanical properties.

REFERENCES

1. W. J. Lackey and A. J. Caputo, *U. S. Patent No. 4,580,524* (April 8, 1986).
2. T.M. Besmann, B.W. Sheldon, R.A. Lowden, and D.P. Stinton, *Science* **253**, 1104 (1991).
3. T.M. Besmann, in *Proc. High Temperature Matrix Composites II, Ceramic Transactions*, A. G. Evans and R. Naslain, Editors, **58**, p. 1, American Ceramic Society, Westerville, OH (1995).

4. W.M. Matlin, D.P. Stinton, T.M. Besmann, and P.K. Liaw, in *Ceramic Matrix Composites - Advanced High-Temperature Structural Materials*, R.A. Lowden, M.K. Ferber, J.R. Hellman, K.K. Chawla, and S.G. DiPietro, Editors, **365**, p. 309, Materials Research Society, Pittsburgh, PA (1995).

5. T.M. Besmann, J.C. McLaughlin, K.J. Probst, T.J. Anderson, and T.L. Starr, *Development of a Scaled-Up CVI System for Tubular Geometries*, Twelfth Annual Conference on Fossil Energy Materials, May 12-14, 1998.

DEVELOPMENT OF SLURRY-BASED OXIDE COATINGS FOR FOSSIL APPLICATIONS

Virginie M. Vaubert and David P. Stinton

Oak Ridge National Laboratory

P.O. Box 2008, Bldg. 4515, MS-6063

Oak Ridge, TN 37831-6063

Corrosion resistant $\text{Ca}_{0.5}\text{Sr}_{0.5}\text{Zr}_4(\text{PO}_4)_6$ (CS-50) coatings have been developed for fiber-reinforced, SiC-matrix composite heat exchanger tubes and clay-bonded SiC filters. Aqueous slurries were prepared and deposited on the SiC substrates. One coating process, for dense substrates, consisted of mechanically dipping the samples in a slip. A spin-coating process has also been created that produced thin, non-obstructing coatings for porous substrates. The thermal shock and corrosion resistance of coated parts were evaluated, and the results indicated that CS-50 is a very effective environmental barrier coating.

INTRODUCTION

The necessity of operating in a high temperature and highly corrosive environment requires the use of ceramic materials in many fossil energy applications. SiC-based materials are excellent candidates for these applications because they combine high strength and high thermal shock resistance at these temperatures. However, corrosion of silicon-based materials in the presence of alkali species^{1,2} is a major problem. By-products from the combustion of fossil fuels, mainly sodium compounds, can cause dissolution of the protective SiO_2 layer and recession of the bulk SiC. Therefore, corrosion/oxidation resistant coatings for SiC components are needed to ensure durability and reliability in such environments.

Thirty years ago, a new family of ceramic materials was developed based on the crystal structure of sodium zirconium phosphate [$\text{NaZr}_2(\text{PO}_4)_3$, (NZP)].^{3,4} $\text{Ca}_{0.5}\text{Sr}_{0.5}\text{Zr}_4(\text{PO}_4)_6$ (CS-50)⁵ has been derived from this family and possesses a near-zero thermal expansion coefficient, low thermal conductivity and good thermal stability up to 1500°C which makes it an excellent candidate for high-temperature applications. Additionally, this oxide has shown great promise for operating in an alkali environment. The interaction between plasma-sprayed CS-50 coatings and sodium sulfite at high temperature has been studied, and CS-50 remained unaffected after alkali exposure.^{6,7} The goal of this study is to develop a protective coating of CS-50 for dense and porous SiC substrates. Processing techniques focused on cost-effective, water-based slurry-coating methods.

EXPERIMENTAL PROCEDURE

Substrate Preparation

Ceramic-grade Nicalon™ fiber-reinforced SiC matrix composites prepared by chemical vapor infiltration by the Ceramic Surface Systems Group at the Oak Ridge National Laboratory (ORNL) were used in this study. Flat samples, as well as ring samples, cut from prototypical heat exchanger tubes were machined to the appropriate size. Rings of clay-bonded silicon carbide were cut from commercial candle filters (Schumacher, Germany).

Powder and Slip Preparation

Powder Preparation

Particle size distribution was optimized to obtain high quality coatings. Sub-micron size particles are desirable to obtain low temperature sintering and prevent substrate degradation. The optimized particle size was reached after 48 hr of wet milling with partially stabilized zirconia media ($ZrO_2 - 5 \text{ mol\% } Y_2O_3$). Particle size analysis was completed using a Horiba LA-700 particle size analyzer. A mean particle size of $0.9 \mu\text{m}$ was obtained for CS-50. The particle size distribution was very narrow with a standard deviation of $0.25 \mu\text{m}$.

Slip Composition

An aqueous CS-50 slurry was prepared at 60 vol% solids. A high solids loading was desired to reduce shrinkage during drying and firing. Zinc oxide [ZnO (ME Science)] was added to the slurry as a sintering aid. The effect of ZnO on the sintering behavior of NZP materials is to create a liquid phase which promotes the sintering reaction.^{8, 9} Since the coating densification was constrained by the rigid substrate, sintering was often accompanied by cracking. The liquid phase provided mobility to the particles and reduced the number of cracks.

Coating Deposition

Dip-Coating

Coatings used to be applied to composite rings by hand-dipping the samples in the CS-50 slurry. The samples are now mechanically dipped in the oxide slurry which yields uniform coatings and enables close control of the withdrawal speed and acceleration. The coating quality was greatly improved by mechanical dipping. The controlled withdrawal rate also reduced the number of processing variables. Three rates of withdrawal, $0.57 \text{ cm}\cdot\text{s}^{-1}$, $0.98 \text{ cm}\cdot\text{s}^{-1}$ and $1.5 \text{ cm}\cdot\text{s}^{-1}$, were investigated to determine the effect of dipping speed on coating quality. The coatings obtained did not display any significant variation in

terms of thickness or likeliness to crack. The coating quality appears more directly linked to the viscosity and solids loading of the ceramic slip. High solids loading and low viscosity slips yield high-density, thin, green coatings, therefore, minimizing shrinkage and cracking during sintering.

Spin-Coating

Ring sections cut from Schumacher SiC candle filters were immersed in the CS-50 slurry and then placed in a dessicator under vacuum. As air was evacuated, the slurry fully penetrated the pores of the filter material. Subsequently, the filter ring was placed in a centrifuge and spun at 2000 rpm for 1 min. Most of the slurry was removed from the pores leaving only a thin layer on the internal and external surfaces. Fig 1 shows a SiC ring clamped in the centrifuge before and after spinning.

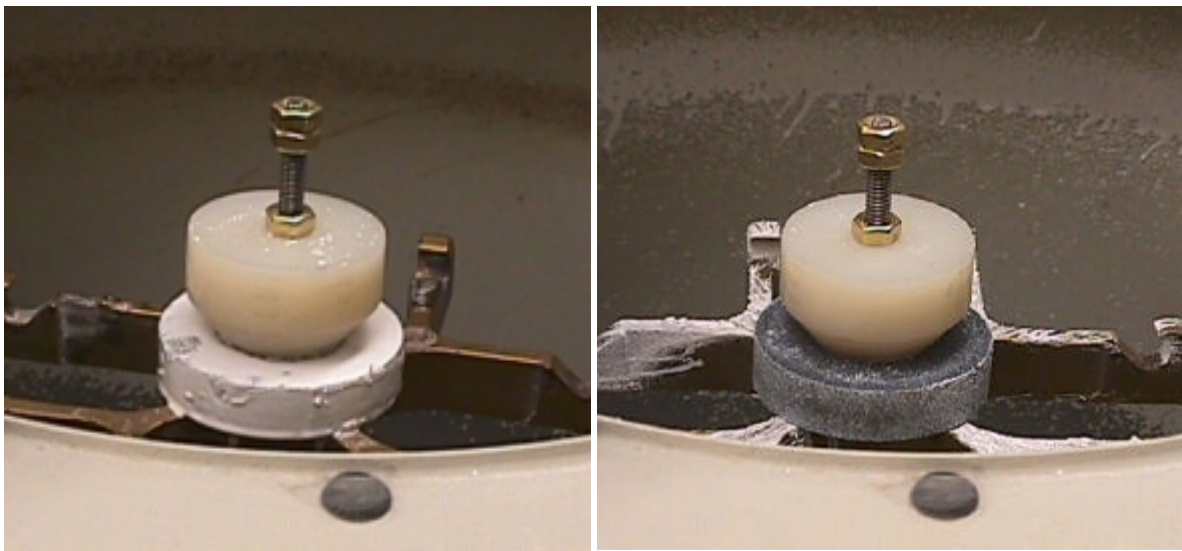


Figure 1 : Spin-coating removed excess slurry from the filter rings.

Drying and Sintering

After coating, the samples were dried at ambient temperature and 80 % relative humidity (RH) for 48 h, followed by ambient temperature and 50% RH for another 48 h. The samples were then heated at 0.5°C/min up to 600°C and held for 4 h to enable burnout of the binder. The samples were crack-free after this treatment. The specimens were then ramped at 1°C/min up to 1100°C, soaked for 60 min, and cooled at the same rate to room temperature. A summary of the coating process is presented in Fig 2.



Figure 2 : Coating deposition, drying and sintering process

Microscopy

Samples were embedded in epoxy resin, cut with a diamond saw, and polished. Characterization of the coating/composite interface was first performed with an optical microscope, Nikon 4X, and then with a scanning electron microscope (SEM) Hitachi S800. The porous samples were broken, and the fracture surfaces were observed under a SEM to determine if the coating was obstructing the pores.

Evaluation of the CS-50 as an Oxidation Barrier Coating

CS-50 coatings had been shown to provide a good protection against alkali degradation, but little was known regarding their efficiency as oxidation barriers. Since oxidation degradation of clay-bonded SiC is a relatively slow process, CS-50 was first evaluated as an oxidation barrier for carbon-carbon composites. Samples of carbon/carbon composites were first coated with CS-50 slurry according to the dip-coating method. These samples were then oxidized at various temperatures with non-coated, carbon/carbon samples as reference, and the weight variations were monitored.

Evaluation of the Thermal Shock Resistance of the Coated Samples

The thermal shock and thermal cycling resistance of CS-50 coatings on SiC fiber-reinforced SiC-matrix composite was evaluated. The samples were heated at 10°C per min to 1000°C, soaked for 30 min, and quenched in ice water. The effect of thermal cycling was studied by heating the samples to 1000°C, soaking for 30 min, and bringing them to room temperature almost instantaneously. After 10 min of cooling, the samples were weighed and then put back in the furnace at 1000°C. This operation was repeated 25 times in order to thermally fatigue the coatings.

Corrosion Resistance of the Coatings

The surface of SiC oxidizes at high temperature to form a silica layer which is responsible for the oxidation resistance of the material. There have been excellent reviews of the oxidation of SiC and Si₃N₄ which have shown that the protective silica layer, when in contact with molten sodium salts, reacts to form

or sodium carbonate and heating the coated specimen to the desired temperature,¹¹ and (c) partial or complete immersion of the specimen in a crucible containing the alkali melt. A thin film procedure was performed for this evaluation. A total of four specimens were used, two coated with CS-50, and two reference composites. The dimensions of the samples were carefully measured and the specimens were weighed. Then, the specimens were washed in an ultrasonic cleaner in acetone followed by distilled water. The samples were dried overnight in an oven at 60°C. The sodium sulfate loading was performed by heating the specimen on a hot plate to 90°C and dispensing drops of saturated Na₂SO₄ solution onto the surface. The samples were left to dry for an hour, weighed, and more sodium sulfate was added until the loading reached 8 mg/cm². The samples were then heated in a furnace at 1000°C for 100 h in flowing O₂ (200 cm³/min). The specimens were weighed, washed in hot distilled water for two hours to dissolve any residual sodium sulfate, and then weighed again. Phases present on the sample surface were determined before and after corrosion by standard XRD. Some samples were then broken and viewed with the SEM to determine any microstructural changes.

RESULTS

Visual Evaluation

Good quality coatings exhibiting few cracks and a smooth surface were obtained with the dip-coating process, cf Fig. 3. A photograph illustrating the effect of ZnO on the coating sintering behavior is presented in Fig. 4. Because of the liquid phase present, the coating flowed around the substrate and was less likely to crack during densification. Thin, crack-free coatings were also obtained for filter samples by the spin-coating process. One example is shown in Fig. 5.

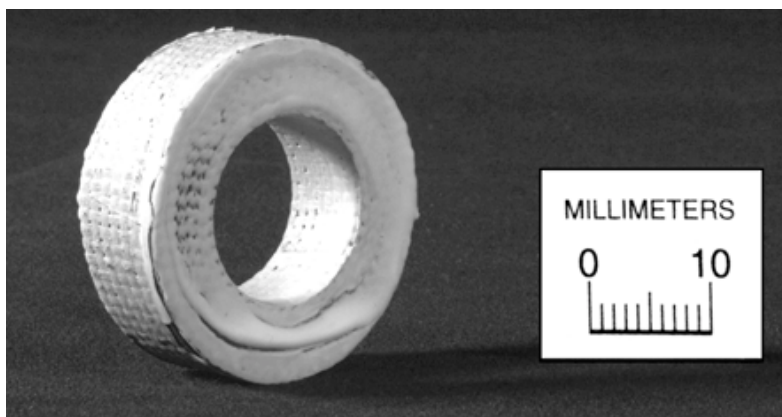


Figure 3 : Examples of CS50 coating (dip-coating process)

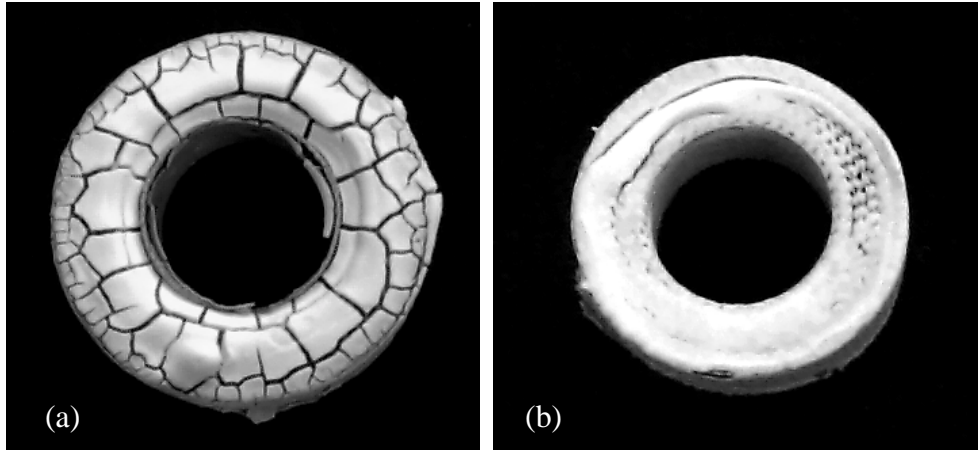


Figure 4 : Influence of ZnO on coating quality, (a) without ZnO, (b) with ZnO

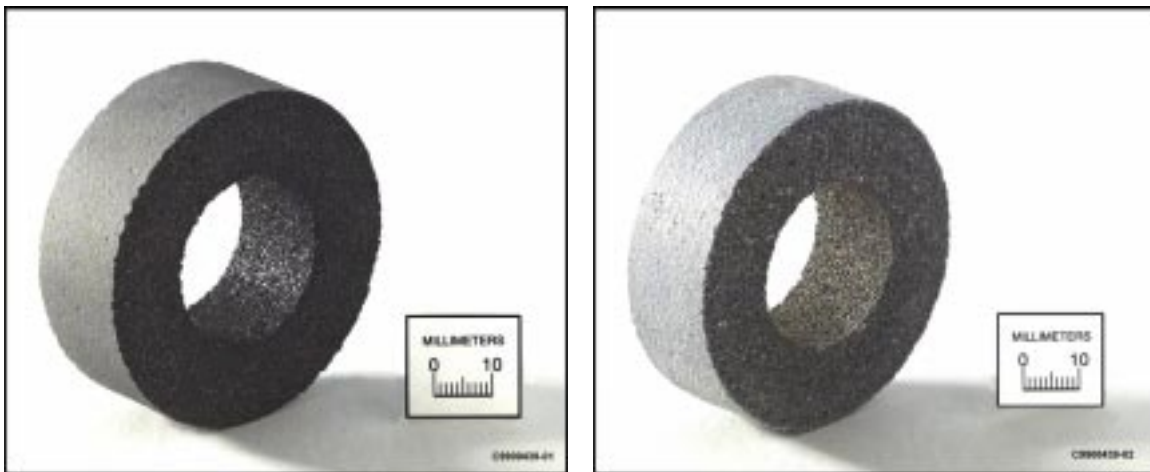


Figure 5 : SiC filter ring before and after coating

Analysis

Microscopy

Optical micrographs of CS50 coatings obtained by dip-coating are shown in Fig. 6. The coatings are very uniform, and no gap or debonding can be seen at the coating matrix interface. SEM micrographs of fractured SiC grains coated with CS-50 obtained by spin-coating are presented in fig 7.

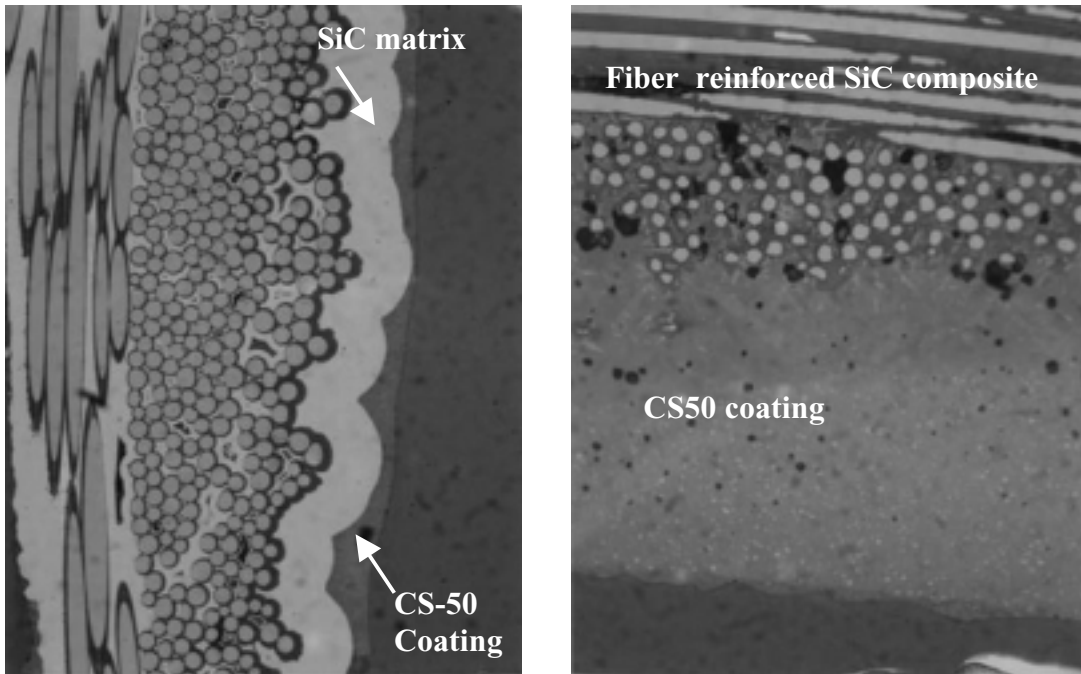


Figure 6 : Optical micrographs of CS-50 coatings

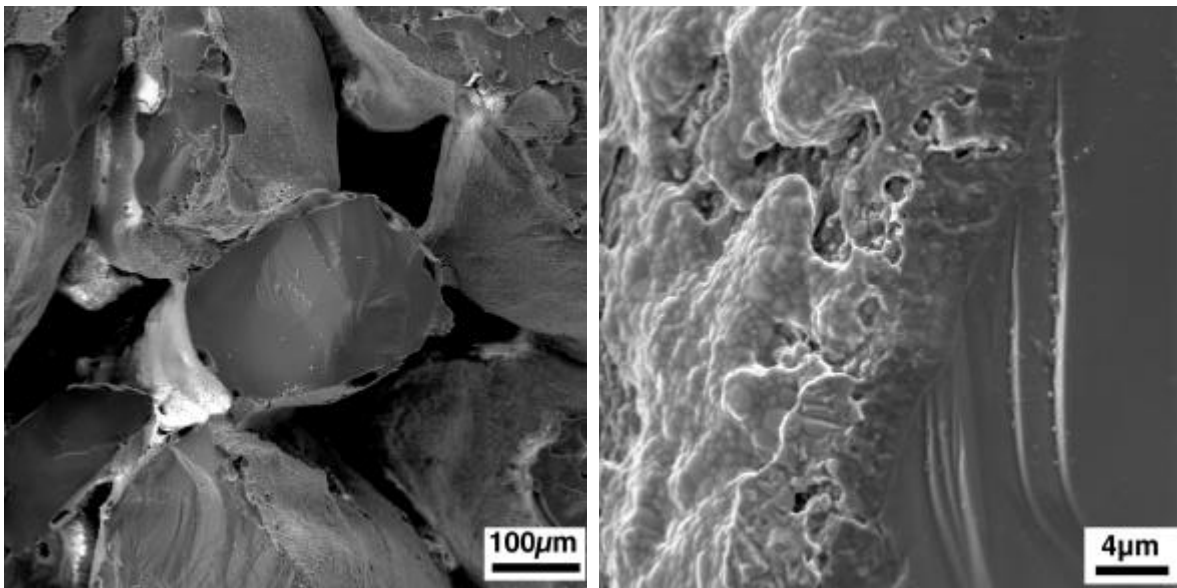


Figure 7 : SEM micrographs of CS-50 coatings on CS-50 (spin-coating process)

Evaluation of the CS-50 as an Oxidation Barrier Coating

The oxidation of resistance of coated vs. non-coated carbon-carbon composites was evaluated. Up to 700°C, the weight loss measured for the coated samples was approximately ten times less than that for the uncoated samples. At 800°C, the coated samples presented a weight loss of 18 wt%, while the non-coated samples were vaporized. The corners of the carbon/carbon composites were not rounded before applying the coating which resulted in cracking of the coating in these areas. Better oxidation protection should be expected for more continuous coatings.

Thermal Shock Resistance of the Coatings

The coated, fiber-reinforced, SiC matrix composites remained intact after quenching in ice water, and after 25 thermal cycles. No significant weight loss was measured.

Corrosion Resistance of the Coatings

No significant weight loss was observed for both coated and reference samples after exposure. The samples used in the study were very porous, consequently, the sodium sulfate flowed into the pores and lowered the surface loading to less than 8 mg/cm². No sign of degradation was found on the coated samples, but a white deposit was visible on both non-coated composites. No microstructural degradation was observed during microscopic evaluation of the polished samples. Samples were then broken and observed with a SEM. SEM micrographs of as-received, corroded, and corroded with coating Nextel fiber-reinforced SiC matrix composites are shown in Fig. 8. The corroded, non-coated samples contain a glassy phase indicating degradation of the SiC matrix. In contrast, coated (CS50) samples show very little degradation. EDX results indicate that sodium was present in the CS50 coating but not in the composite. Thus, most of the sodium was trapped in the coating which prevented the degradation of the substrate.

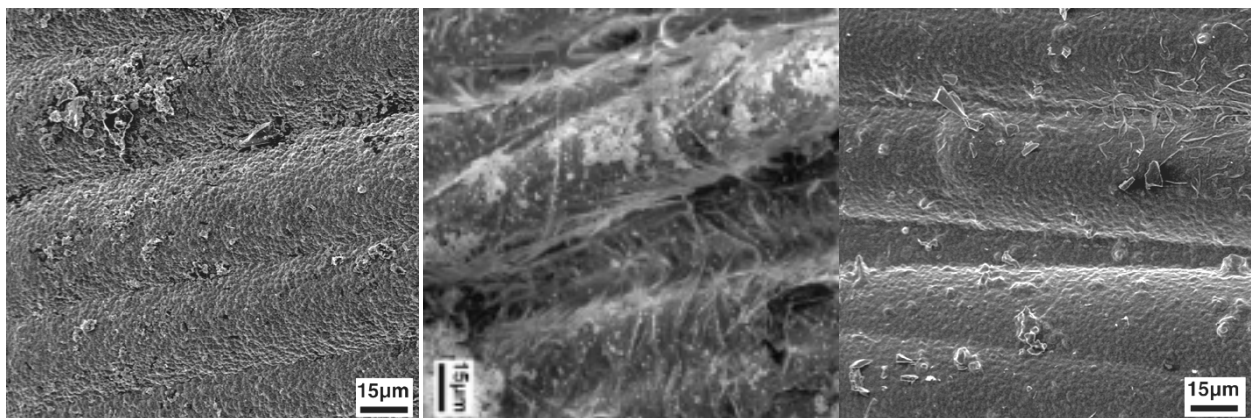


Fig 8 : As-received, corroded, and corroded with coating Nicalon fiber-reinforced SiC matrix composite

CONCLUSIONS

A good quality, relatively inexpensive coating process for applying protective oxide coatings on SiC-matrix materials has been developed, and an understanding of the most critical factors controlling the process has been obtained. The glaze-like behavior of CS-50 obtained with ZnO additions was beneficial to the quality of the coating. A coating deposition technique was developed which yielded very thin, non-obstructing coatings for the corrosion protection of hot-gas filters. The corrosion and thermal shock resistance of the coatings are very encouraging, and further improvements in coating quality should make NZP coatings even more efficient in terms of corrosion protection. Effort is now focused on developing mullite slurry compositions for similar coating applications.

ACKNOWLEDGMENTS

This work was supported by the Advanced Research and Technology Development Materials Program of the Office of Fossil Energy, U.S. Department of Energy under contract DE-AC05-84OR21400 with Lockheed Martin Energy Corporation. We would like to thank Carolyn Angel for the photography work, Tom Geer for the metallography, and LoTEC, Inc. for providing us with CS-50 powder. We would also like to thank Claudia Walls for her help and advice on coating processing.

REFERENCES

-
- ¹ N. S. Jacobson, "Corrosion of Silicon-Based Ceramics in Combustion Environments", *Journal of the American Ceramic Society*, **76**, [1], 3-28, 1993
 - ² G. R. Pickrell, T. Sun, J. J. Brown, "High temperature Corrosion of SiC and Si₃N₄", *Fuel processing technology*, **44**, 213-236, 1995
 - ³ L. O. Hagman and P. Kierkegaard, "The Crystal Structure of NaMe₂^{IV}(PO₄)₃; Me^{IV}=Ge, Ti, Zr", *Acta Chemica Scandinavica*, **22**, 1822-1832, 1968
 - ⁴ R. Roy, D. K. Agrawal, J. Alamo and R.A. Roy, "[CTP]: A New Structural Family of Near Zero Expansion Ceramics," *Materials Research Bulletin*, **19**, 471-77, 1984
 - ⁵ S. Y. Limaye, D. K. Agrawal, and H. A. McKinstry, "Synthesis and Thermal Expansion of MZr₄(PO₄)₆, (M=Mg, Ca, Sr, Ba)", *Journal of the American Ceramic Society*, **70**, C232-36, 1987
 - ⁶ W. Y. Lee, K. M. Cooley, C. C. Berndt, D. L. Joslin and D. P. Stinton, "High-Temperature Chemical Stability of Plasma-sprayed Ca_{0.5}Sr_{0.5}Zr₄P₆O₂₄ Coatings on Nicalon/SiC Ceramic Matrix Composite and Ni-based Superalloy Substrates", *Journal of the American Ceramic Society*, **79**, [10], 2759-62, 1996
 - ⁷ W. Y. Lee, D. P. Stinton, and Debra L. Joslin, "Interaction of low-expansion NZP Ceramics with Na₂SO₄ at 1000°C," *Journal of the American Ceramic Society*, **79**, [2], 484-486, 1996
 - ⁸ D. K. Agrawal and V.S. Stubican, "Synthesis and sintering of Ca_{0.5}Zr₂P₃O₁₂- A Low Thermal Expansion Material", *Materials Research Bulletin*, **20**, 99-106, 1985

⁹ J. R. Clarke, “The Sintering Effects of Time, Temperature and ZnO Additions on $\text{Ca}_{0.6}\text{Mg}_{0.4}\text{Zr}_4(\text{PO}_4)_6$ [CMZP] Ceramics”, M.S. Thesis, Materials Science and Engineering, Virginia Polytechnic Institute and State University, Blacksburg, VA, 1996

¹⁰ D. S. Fox and J. L. Smialek, “Burner Rig Hot Corrosion of Silicon Carbide and Silicon Nitride.” *Journal of the American Ceramic Society*, **73**, [2], 303-311, 1990

¹¹ N. S. Jacobson, J. L. Smialek, “Hot Corrosion of Sintered α -SiC at 1000°C.”, *Journal of the American Ceramic Society*, **68**, [8], 432-39, 1985

CORROSION-RESISTANT INTERFACE COATINGS FOR NICALON[®]/SiC COMPOSITES

R. A. Lowden, J. J. Henry, J. C. McLaughlin, N. L. Vaughn, and K. L. More

Oak Ridge National Laboratory

P.O. Box 2008

Oak Ridge, Tennessee

The environmental stability of the fiber-matrix interface continues to be of significant importance to the successful utilization of ceramic composite components in advanced energy-related applications. Numerous materials including carbon, boron-doped carbon, boron nitride, and oxide ceramics have been examined for use as fiber coatings for silicon carbide-based composites with mixed results. Boron nitride has become the primary composition of interest for controlling fiber-matrix interactions in the aforementioned composites, however, many factors can influence the performance of BN in this application. Oxygen contamination of the layer produces unwanted reactions with the matrix and reinforcement causing embrittlement. Boron nitride is also susceptible to attack by water vapor at moderate temperatures. Volatile species are formed and the BN is removed in the same manner as carbon is in air. Modifications to the composition and microstructure of BN are being explored to improve its performance as an interlayer for SiC composites.

Boron nitride coatings are typically deposited on fibrous preforms from gas mixtures containing boron trichloride (BCl_3), ammonia (NH_3), and hydrogen (H_2). Deposition at high temperatures can produce coatings with increased order and thus corrosion resistance; however, infiltration of fiber bundles and fabrics is hindered, resulting in poor uniformity. Doping of BN with other elements has produced promising results without sacrificing uniformity. Silicon and titanium additions to the BN fiber coating are being examined to enhance the environmental stability and corrosion resistance of Nicalon[®]/SiC composites. Once oxygen contamination was minimized, composites with excellent mechanical properties were fabricated from fibers coated with Si-doped BN interlayers. The addition of titanium, however, did not produce favorable results. Composites were embrittled even at the lowest Ti concentrations. Additional work is planned to examine other dopants such as aluminum and zirconium.

INTRODUCTION

Typically, fiber coatings or "interlayers" are used to protect the reinforcements in ceramic composites from chemical attack during processing and to control interfacial forces. An interlayer must be thermochemically compatible with the fibers and matrix, control stresses and frictional forces within the composite, and be environmentally stable. Carbon, whether intentionally deposited on the fibers prior to consolidation¹⁻³ or formed serendipitously during processing⁴ was once the most commonly used interlayer in ceramic composites. Carbon fiber coatings protect the reinforcements during processing, and control bonding and friction at the fiber-matrix interface.

Exceptional room- and elevated-temperature mechanical properties were realized, and thus ceramic composites have become prime candidates for use in many advanced elevated-temperature applications.

The poor oxidation resistance of carbon, however, is well known, as is the fact that any disturbance at the fiber-matrix interface can have a profound effect on the properties of a composite. Carbon begins to oxidize at temperatures around 400°C and oxidation is rapid in air at temperatures above 900°C.⁵ It has been shown that the oxidation of Nicalon[®]/SiC composites at temperatures around 1000°C begins by attack of the carbon interface coating through cracks in the matrix or at exposed fiber ends.⁶ Once the carbon is removed along the entire fiber length, the matrix and fiber oxidize to form a silica layer that eventually bonds the components together, resulting in brittle behavior.

In order to improve the elevated temperature stability of fiber-reinforced ceramic matrix composites, boron-containing replacements for carbon fiber coatings have been examined. Hexagonal boron nitride is the leading candidate for it possesses a structure and mechanical properties similar to those of graphitic carbon, but exhibits improved oxidation resistance.^{7,8} Hexagonal BN has been used successfully as an interlayer in a variety of ceramic/ceramic composites.^{9,10} Nicalon[®]/SiC composites with polycrystalline BN interlayers, deposited using boron trichloride (BCl₃), ammonia (NH₃), and hydrogen (H₂) gas mixtures exhibited flexure strengths comparable to analogous specimens with a graphitic carbon interlayer.⁹ The composites with the BN interlayers showed improved short-term oxidation resistance, however, toughness was diminished after a 24 h exposure in air at 1000°C. It was found that oxygen contamination in the as-deposited BN layers caused the fibers to decompose, which lead to a decrease in reinforcement strength and a loss of toughness.

Recent efforts have been devoted to the examination of the effects of dopants on the properties, microstructure and environmental stability of boron nitride interface coatings for composites with silicon carbide matrices and reinforcements. Silicon doping is one method being explored to improve the moisture resistance and high-temperature stability of the BN fiber coatings. In the past, Si:B:N coatings have been examined not only for enhanced corrosion resistance¹¹ but also for wear and friction applications.¹² The goal of the tribological coatings project was to co-deposit silicon nitride and boron nitride, preferably Si₃N₄ with BN as a dispersed second phase, to produce a self-lubricating hard ceramic coating.¹² Coatings were

deposited on flat substrates using gas mixtures similar to those used for the fiber coatings described in this paper. The system was studied in detail, however, only amorphous mixtures of boron, nitrogen, and silicon were produced.

As noted, silicon is also being added to BN to improve moisture resistance and high temperature stability.¹¹ It was desired that upon oxidation, the Si-doped BN will form a borosilicate glass surface layer, which will be more stable in water-containing environments than boria. In this effort, the microstructure and composition of the layers did not appear to be of concern. Results were promising, however, the Si-doped BN fiber coatings were deposited at relatively high temperatures that are not favorable for uniform infiltration of preforms, and might damage many of the available reinforcements.

Therefore, Si-doping of BN layers deposited employing conditions more typical for chemical vapor infiltration is being examined. There are numerous silicon-containing reactants; however, silicon tetrachloride was selected for this study. In early experiments, the addition of SiCl₄ to the BCl₃:NH₃:H₂ gas mixture produced composites that were weak, brittle and exhibited poor corrosion resistance. Characterization of the samples found the Si-doped BN fiber coatings to be composed of BN crystallites in a silica matrix. Extensive reaction between the Si-doped BN and the fiber and matrix produced embrittlement and chemical instability (Fig. 1).

The deposition furnace and gas delivery systems were inspected and thoroughly cleaned, and BN layers with very low oxygen levels were deposited. Composites fabricated from fibers coated with “clean” un-doped BN exhibited good strength, toughness, and environmental stability. Due to this achievement, and observations made regarding low oxygen BN interlayers, the Si-doping of BN interlayers for Nicalon[®]/SiC composites was revisited.

The addition of titanium to BN fiber coatings has also been explored. It was hypothesized that titanium would getter any oxygen in the coatings during deposition and in service. A review of the free energy of formation of the oxides showed that titanium should oxidize before silicon and boron thus gettering any oxygen in the system (Table 1). Titanium was thus added to the BN fiber coatings to potentially enhance the stability of the coating and prevent reaction of oxygen with the SiC fibers and matrix.

Table 1. Heat and Free Energy of Formation for Various Oxides from the Metals at 1000°C

Reaction	ΔH_f (kJ/mole)	ΔG_f (kJ/mole)
$2 \text{ Al} + 3/2 \text{ O}_2 \rightarrow \text{Al}_2\text{O}_3 (\text{s})$	-1127	-841
$2 \text{ B} + 3/2 \text{ O}_2 \rightarrow \text{B}_2\text{O}_3 (\text{l})$	-819	-636
$\text{Si} + \text{O}_2 \rightarrow \text{SiO}_2 (\text{s})$	-900	-679
$2 \text{ Ta} + 5/2 \text{ O}_2 \rightarrow \text{Ta}_2\text{O}_5 (\text{s})$	-805	-592
$\text{Ti} + \text{O}_2 \rightarrow \text{TiO}_2 (\text{s})$	-941	-709
$\text{Zr} + \text{O}_2 \rightarrow \text{ZrO}_2 (\text{s})$	-1091	-853

Values normalized to 1 mole of oxygen.

EXPERIMENTAL PROCEDURE

(1) Composite Fabrication

Fibrous preforms were fabricated by stacking multiple layers of ceramic-grade Nicalon[®] plain-weave fabric rotated in a $0 \pm 30^\circ$ sequence within the cavity of a graphite holder. The layers were hand compressed to produce a preform with a nominal fiber loading of 40 vol. % and were held in place by a perforated graphite lid pinned to the holder. The polyvinylacetate cloth sizing was removed through multiple washings with acetone. The fibrous preforms were a nominal 45-mm in diameter and 12.5 mm thick.

Preforms were next coated with the boron nitride interface layers. The coatings were deposited using a forced-flow, isothermal chemical vapor infiltration approach from gas mixtures containing boron trichloride (BCl_3), ammonia (NH_3), and hydrogen (H_2), a preform temperature of 1100°C, and a reactor pressure of ≈ 5 kPa. The ratio of boron to nitrogen in the reactant gas mixture was held constant at unity, and reactant flows and concentrations were modified to produce deposition rates similar to those for the standard graphitic carbon layer and a uniform layer thickness throughout the preform. Typical gas flows for the deposition of BN for the given furnace and preform configuration are: 25 sccm BCl_3 , 25 sccm NH_3 , and 500 sccm H_2 . The thicknesses of the interface layers were calculated from preform weight gains.

Silicon tetrachloride, SiCl_4 , was added to the BCl_3 , NH_3 , and H_2 gas mixture to produce silicon-doped BN layers. The SiCl_4 flow was varied to produce different levels of doping and while all other gas flows remained constant. Deposition time was 2h. A summary of the effects of the silicon additions to the deposition of the BN fiber coatings is given in Table 2.

Table 2. Gas Mixtures and Flexure Strengths for Nicalon[®]/SiC Composites with Si-Doped BN Interlayers

Dopant	Gas Flows BCl₃:NH₃:SiCl₄ (sccm)	As-Fabricated Flexure Strength (MPa)	Oxidized Flexure Strength (MPa)
<i>None</i>	25:25:0	365	341
<i>Silicon</i>	25:25:10	191	178
	25:25:10	189	190
	25:25:25	285	261
	25:25:25	363	450

Titanium tetrachloride, TiCl₄, was added to the BCl₃, NH₃, and H₂ gas mixture to dope the BN fiber coatings with titanium. The TiCl₄ flow was varied to alter dopant concentration while the other gas flows remained constant. Deposition time was 2h. A summary of the effects of the TiCl₄ additions to the deposition of the BN fiber coatings is given in Table 3.

Table 3. Gas Mixtures and Flexure Strengths for Nicalon[®]/SiC Composites with Ti-Doped BN Interlayers

Dopant	Gas Flows BCl₃:NH₃:TiCl₄ (sccm)	As-Fabricated Flexure Strength (MPa)	Oxidized Flexure Strength (MPa)
<i>None</i>	25:25:0	365	341
<i>Titanium</i>	25:25:1.5	263	210
	25:25:2.5	248	219
	25:25:10	not tested	not tested
	25:25:25*	not tested	not tested

* Run was interrupted due to the rapid deposition of what appeared to be TiN.

The preforms were densified with silicon carbide using the forced-flow, thermal-gradient chemical vapor infiltration (FCVI) process.¹³ The SiC matrix was produced by the decomposition of methyltrichlorosilane (CH₃SiCl₃ or MTS) in hydrogen at a hot-surface temperature of 1200°C and atmospheric pressure. The preforms were infiltrated with SiC to 85 to 90 % of theoretical density in ~ 20 h.

(2) Testing and Characterization

Test bars were cut from the composite samples parallel to the 0° orientation of the top layer of cloth using a diamond saw, and tensile and compression surfaces were ground parallel to the long axis of the specimen. The average dimensions of the specimens were 2.5 x 3 x 40 mm and all specimens were measured and weighed to determine densities. Half of the specimens were oxidized in static air at 950°C for 24 hours.

Room-temperature flexure strengths for as-fabricated and heat-treated composites were measured in four-point bending. A support span of 25 mm and a loading span of 6 mm were used with a crosshead speed of 0.50 mm/min. The load was applied perpendicular to the layers of cloth. Load-displacement curves were recorded to examine the fracture process and determine the loads for ultimate strength calculations

The composition and microstructure of a portion of the BN interlayers were examined using transmission electron microscopy. Specimens were prepared such that the area for analysis contained a quantity of fibers oriented perpendicular to the surface. The specimens were mechanically ground, polished, dimpled, and ion-milled to perforation using standard techniques. Microstructural characterization was conducted on a high-resolution transmission electron microscope (HRTEM).

RESULTS AND DISCUSSION

Results for silicon doping of BN are summarized in Table 2 and graphically depicted in Figure 2. As in previous efforts, the majority of the composites exhibited less than expected strength and toughness.¹⁴ There was, however, no loss in strength after 24 h in air at 950°C. Preliminary examination of the samples revealed features similar to those observed for earlier oxygen contaminated samples. The furnace and other systems were inspected once again, and additional composites fabricated. As shown in Table 2, a composite with excellent strength, composite behavior, and exceptional short-term oxidation resistance was produced. Specimens from the composite will be characterized in detail employing electron microscopy, and additional composites fabricated for long term oxidation and exposure to moisture-containing and combustion environments.

A summary of the results for the TiCl_4 additions is given in Table 3 and graphically depicted in Figure 3. The addition of TiCl_4 diminished room temperature flexure strength, and produced brittle behavior. Strength was decreased further with increased TiCl_4 concentration. Difficulties were noted at the higher TiCl_4 concentrations. The composite fabricated from fibers coated with 10 sccm TiCl_4 added to the gas mixture was extremely weak and brittle and could not be tested. The deposition of BN fiber coatings with the highest levels of TiCl_4 (25 sccm) was terminated prematurely due to a rapid pressure rise in the gas injection system. Upon removal of the part from the furnace, a heavy build up of a golden coating, likely pure TiN, was found. The composite was not densified.

CONCLUSIONS

Many factors influence the properties and performance of BN fiber coatings. Contaminants such as oxygen and carbon have proven to be detrimental to the environmental stability of BN. At elevated temperatures, oxygen present in the BN layer reacts with the fibers and matrix, degrading composite properties.¹⁵ Oxygen contamination of the BN appears to accelerate the corrosion process when composites are exposed to corrosive environments. Methane additions to the deposition process not only contaminated the BN with carbon but also disrupted the deposition process. These significant changes in interface coating microstructure likely result in differences in interlayer and interfacial properties, and thus diminished composite properties and stability. It can be concluded that contamination of the BN interlayer must be minimized or eliminated to produce stable composites with the given fiber coating and SiC-containing constituents.

The doping of BN has the potential of alleviating a portion of the problems associated with oxygen contamination. A dopant that getters oxygen during processing and in service should help protect the reinforcement from attack and degradation. Doping with titanium degraded composite properties and it seemed that titanium did not appear to function as an oxygen getter. If oxygen contamination of the deposition system was minimized, silicon appeared to produce improvements in composite stability. Additional work must be done to examine the long-term behavior of SiC/SiC composites with Si-doped BN fiber coatings. It is important to note that Si-doped BN is being evaluated in numerous other programs and thus the benefits of this composition should be determined rather quickly.

ACKNOWLEDGEMENTS

This project is being conducted in collaboration with the Supporting Technologies Task of the CFCC Program. Special thanks to K. L. More, H.T. Lin, Pete Tortorelli, Edgar Lara-Curzio, and the others involved in the testing and characterization of fiber-reinforced ceramic composites.

REFERENCES

1. R. A. Lowden, "Fiber Coatings and the Mechanical Properties of a Fiber-Reinforced Ceramic Composite," pp. 619-630 in *Ceramic Transactions*, Vol. 19, Advanced Composite Materials, ed. by Michael D. Sacks, The American Ceramic Society, Westerville, Ohio (1991).
2. Fretty, N. and M. Boussuge, "Relationship Between High-Temperature Development of Fiber-Matrix Interfaces and the Mechanical Behavior of SiC-SiC Composites," *Composites Science and Technology* **37**, 177-189 (1990).
3. Kmetz, M. A., Laliberte, J. M., and Suib, S. L., "Synthesis, Characterization, and Tensile Strength of CVI C/SiC, SiC/B₄C, and C/B₄C Composites," *Ceram. Eng. Sci. Proc.* **13**[9-10], 743-751 (1992).
4. J. J. Brennan, "Interfacial Characterization of Glass and Glass-Ceramic Matrix/Nicalon SiC Fiber Composites," pp. 549-560 in *MRS Proceedings*, Vol. 20, *Tailoring Multiphase and Composite Ceramics*, ed. R. E. Tressler et al., Plenum Publishing Corporation (1986).
5. Hove, J. E., and W. C. Riley, "Graphite," pp. 14-76 in *Ceramics for Advanced Technologies*, John Wiley and Sons, New York, New York (1965).
6. James, R. D., R. A. Lowden, and K. L. More, "The Effects of Oxidation and Corrosion on the Properties of Nicalon[®]/SiC Composites," pp. 925-935 in *Ceramic Transactions*, Vol. 19, Advanced Composite Materials, ed. by Michael D. Sacks, The American Ceramic Society, Westerville, Ohio (1991).
7. Archer, N. J., "The Preparation and Properties of Pyrolytic Boron Nitride," pp. 167-181 in *High Temperature Chemistry of Inorganic and Ceramic Materials*, Special Publication No. 30, Edited by F. P. Glasser and P. E. Potter, The Chemical Society, London (1976).
8. Matsuda, T., "Stability to Moisture for Chemically Vapour-Deposited Boron Nitride," *J. Mater. Sci.* **24**, 2353-2358 (1989).
9. R. A. Lowden, K. L. More, O. J. Schwarz, and N. L. Vaughn, "Improved Fiber Coatings for Nicalon/SiC Composites," pp. 345-352 in the Proceedings of HT-CMC1, High Temperature Ceramic Matrix Composites, edited by R. Naslain, J. Lamon, and D. Doumeings, Woodhead Publishing Limited: Cambridge (1993).

10. O. Dugne, et.al., "AES, XPS, and TEM Characterization of Boron Nitride Deposited Under Chemical Vapor Infiltration (CVI) Conditions," *Journal de Physique*, Colloque C5, Supplement au n-5, Tome 50, 333-341, (1989).
11. A. Moore and H. Sayir, "Improved Interface Coatings for SiC Fibers in Ceramic Composites," *Ceram. Eng. Sci. Proc.* **16**[4], 409-416 (1995).
12. T. M. Besmann, "Thermodynamic Analysis of the Chemical Vapor Deposition of Composite $\langle\text{Si}_3\text{N}_4\rangle\text{-}\langle\text{BN}\rangle$ Coatings," *J. Amer. Ceram. Soc.* **69**[1], 69-74 (1986).
13. D. P. Stinton, A. J. Caputo, and R. A. Lowden, "Synthesis of Fiber-Reinforced SiC Composites by Chemical Vapor Infiltration," *Ceram. Bull* **65** [2] 347-50 (1986).
14. R. A. Lowden, J. J. Henry, K. L. More, H. T. Lin, and P. F. Tortorelli, "Corrosion-Resistant Interface Coatings for Nicalon[®]/SiC Composites," in the Proceedings of the 12th Annual Conference on Fossil Energy Materials, Knoxville, TN (1998)
15. B. W. Sheldon, E. Y. Sun, S. R. Nutt, and J. J. Brennan, "Oxidation of BN-Coated SiC Fibers in Ceramic Matrix Composites," *J. Amer. Ceram. Soc.* **79**[2], 539-543 (1996).

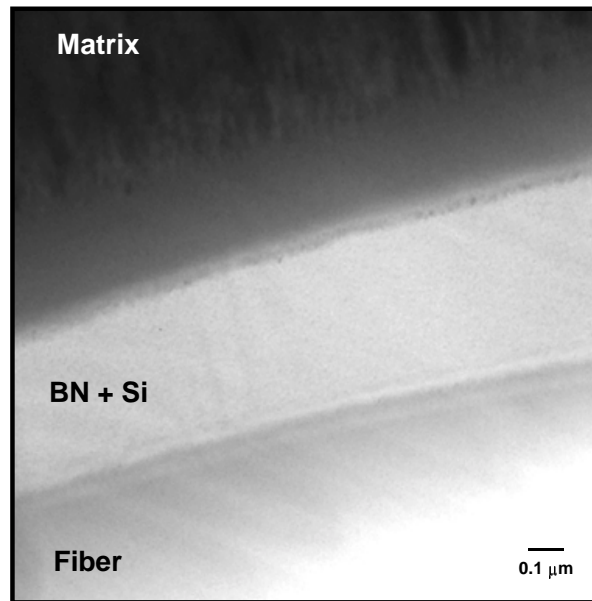


Figure 1. Transmission electron micrograph of Nicalon[®]/SiC composites with a Si-doped BN fiber coating after oxidation in air at 950°C for 24 h. Note the reaction layers at the fiber-BN and BN-matrix interfaces. (K. L. More, ORNL)

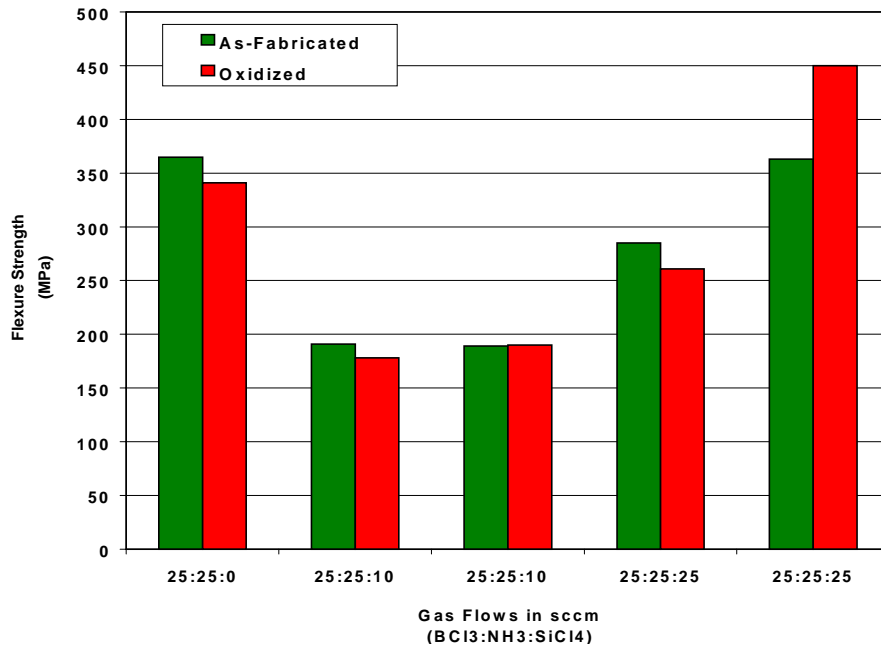


Figure 2. Room temperature, four-point flexure test results for Nicalon[®]/SiC composites with Si-doped BN fiber coatings. Note the improvement in properties for the most recent composite (bars on far right).

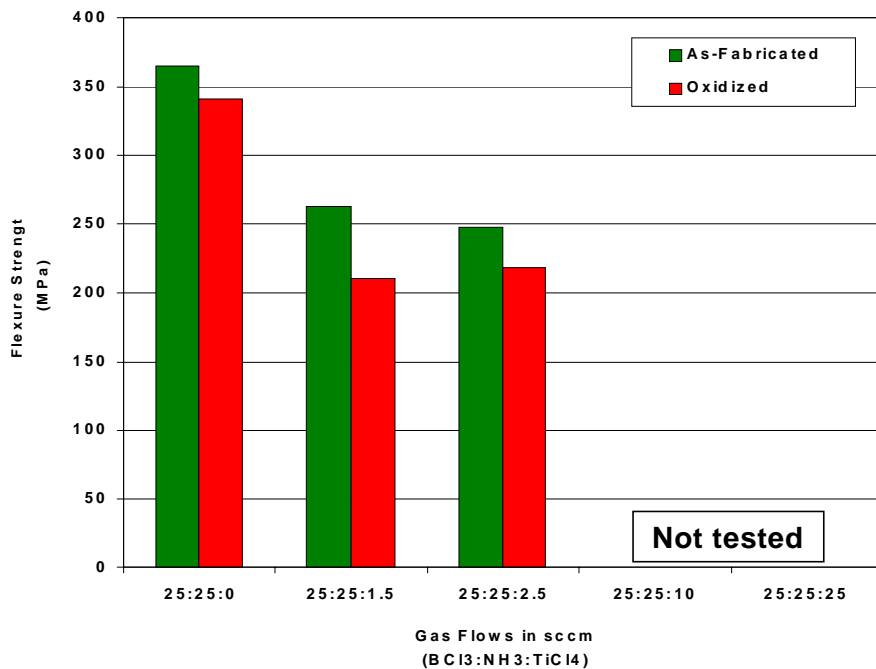


Figure 3. Room temperature, four-point flexure test results for Nicalon[®]/SiC composites with Ti-doped BN fiber coatings. Note the composites with highest levels of TiCl₄ were not tested.

**CARBON FIBER COMPOSITE MOLECULAR SIEVE AND ELECTRICAL SWING
ADSORPTION TECHNOLOGY DEVELOPMENT FOR THE
SEPARATION AND CAPTURE OF CARBON DIOXIDE**

J. P. Strizak, T. D. Burchell and M. R. Rogers

INTRODUCTION

This research activity is directed toward the development of porous activated carbon fiber composite materials, and a novel electrical swing adsorption (ESA) separation process recently developed at Oak Ridge [1, 2]. The material, known as a carbon fiber composite molecular sieves (CFCMS) will find wide application in the field of gas separations and storage, or as a catalyst support [2]. In previous years we have explored different methods of activation (development of the microporous texture) and demonstrated the ability of the material to preferentially adsorb certain gasses from a gas mixture [2-4]. Increased awareness of the detrimental environmental effect of CO₂ gas release to the atmosphere (global warming) has prompted research into novel methods to separate and capture CO₂. The largest sources of CO₂ are fossil fuel burning power plants. However, numerous smaller sources of greenhouse gasses (CO₂, CH₄, etc.) can be identified, and it is these smaller sources that our research is initially directed.

DISCUSSION OF CURRENT ACTIVITIES

In the current reporting period we have directed our efforts toward the construction, modification and preliminary use of a gas flow loop that will allow gas separation experiments to be conducted under field relevant conditions of temperature and pressure.

The Gas Flow Loop

A schematic drawing of the gas flow loop is shown in Figure 1. A premixed gas is circulated at pressures up to 1000 psi around the flow loop and passes through a water bath, allowing the gas temperature to be raised to temperature of 100°C or less. A side stream is led from the loop and passes through the adsorption cell, which is housed in a pressure vessel (Figure 2). The vessel internal space is filled with an inert gas at the same pressure as the flow loop. The adsorption cell (Figures 3 and 4) contains a large piece of activated CFCMS which is electrically insulated from the stainless steel cell wall. Copper head ring connectors are attached at each end of the CFCMS and electrical connections are led out of the cell and pressure vessel to a low voltage (0-8 V DC) power supply. The loop and cell are instrumented to allow the gas pressure, temperature and flow rates in the loop and adsorption cell to be monitored and recorded. A sample of the cell outlet gas is led to a mass spectrometer so that breakthrough of the adsorbed gas may be detected. A general view of the Gas Flow Loop is shown in Figure 5.

Initial trials of the gas flow loop were successful [5]. The loop was pressure tested and trouble shooting was completed. The Electrical Swing Adsorption (ESA) sub-system of the loop was tested and the ability to heat the large CFCMS sample (9.5 cm diameter x 25 cm length) to temperatures exceeding 100°C was demonstrated. Figure 6 shows the voltage-current relationship for the CFCMS sample in our ESA cell. The CFCMS attained a temperature in the ESA cell of 130°C when the applied voltage was 8V DC and the current was 20A.

The problems previously encountered [5] when running at high pressure ($P > 200$ psi) have been overcome by providing the large capacity holding tanks for the exhaust gas stream. The exhaust gasses are then fed to a combustor at an acceptably low pressure/velocity from the holding tanks. Gas separation experiments (CH_4/CO_2) are ongoing at this time.

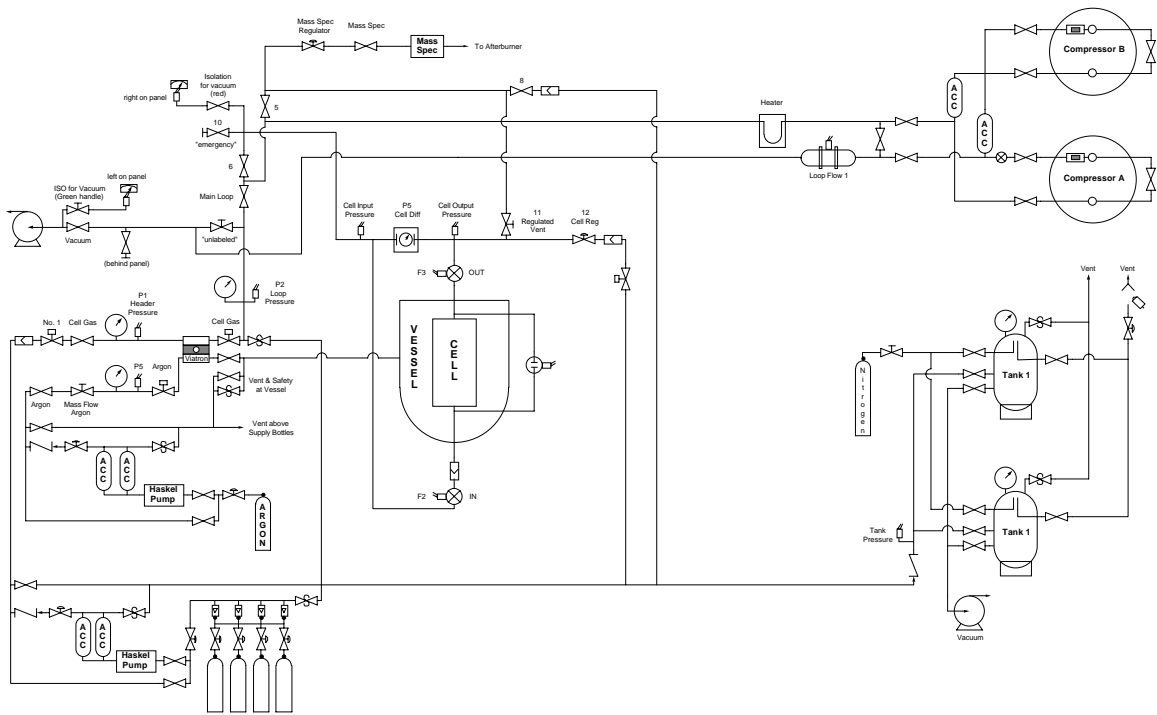


Figure 1. Schematic Diagram of the Modified Gas Flow Loop



Figure 2. Gas Flow Loop Pressure Vessel

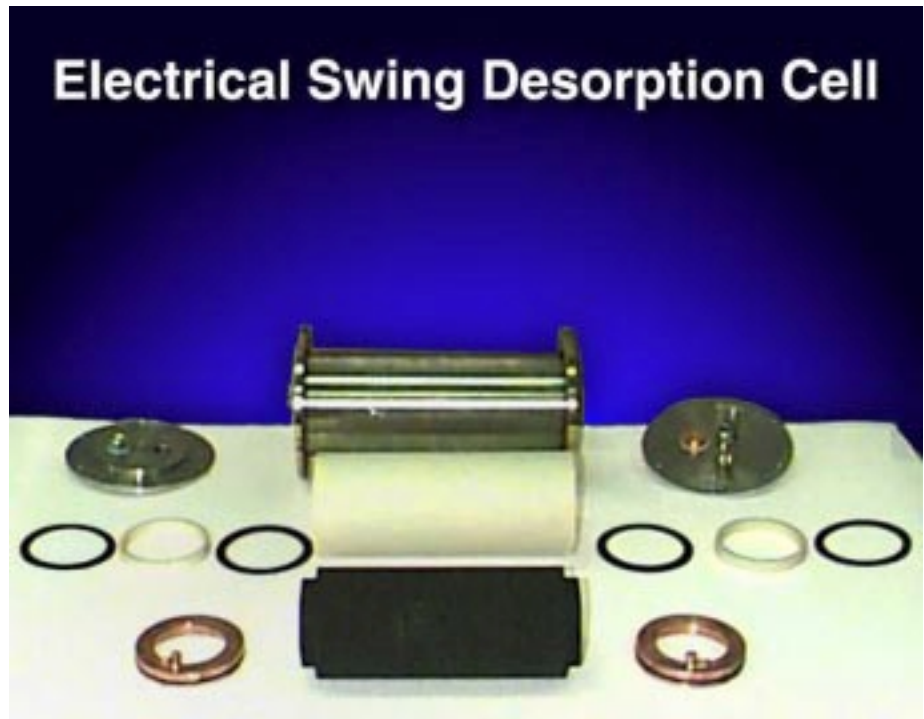


Figure 3. Gas Flow Adsorption Cell

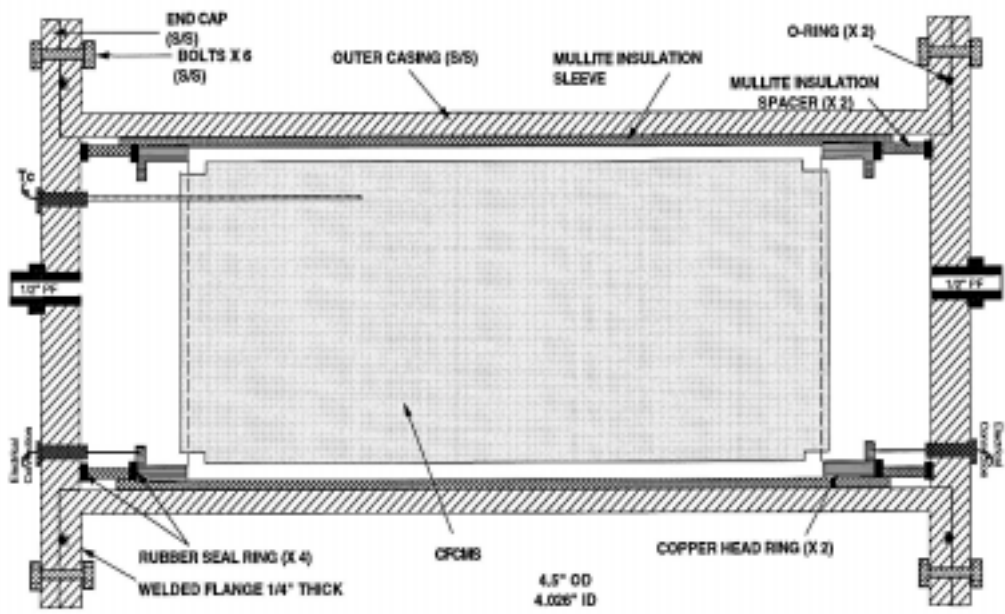


Figure 4. Schematic illustration of the Gas Flow Loop Adsorption Cell



Figure 5. General View of the Gas Flow Loop

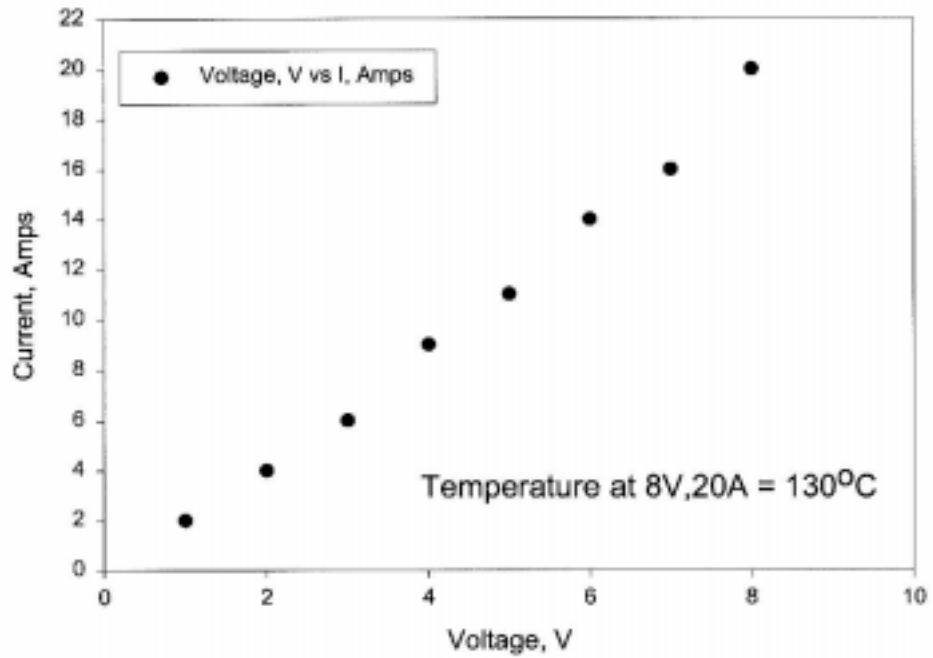


Figure 6. The Current-Voltage Characteristics for a Large CFCMS Sample (95 mm dia. X 250 mm len.) Measured in a Gas Flow Loop Separation Cell

REFERENCES

1. Wei, G.C. and Robbins, JM. *Ceramic Bulletin*, **64** No. 5 (1985), pp. 691-699.
2. Burchell, T.D., Judkins, R.R., Rogers, M.R. and Williams, A.M. *CARBON*, **35** No. 9 (1997), pp. 1279-1294.
3. Burchell, T.D. and Judkins, R.R. *Energy Convers. Mgmt.* **37** Nos. 6-8 (1996), pp.947-954.
4. Burchell, T.D. and Judkins, R.R. *Energy Convers. Mgmt.* 38 Suppl., (1997), pp. S99-S104.
5. Burchell T.D., In *Fossil Energy Program Annual Progress Report for April 1997 Through March 1998*. **ORNL-6943**, (1998), pp. 45-50.

INTERMETALLIC REINFORCED Cr ALLOYS FOR HIGH-TEMPERATURE USE

**M.P. Brady, J.H. Zhu, C.T. Liu, P.F. Tortorelli, L.R. Walker, C.G. McKamey, J.L. Wright,
C.A. Carmichael, D.J. Larson, M.K. Miller, W.D. Porter**

Metals and Ceramics Division
Oak Ridge National Laboratory
Oak Ridge, TN 37831-6115 USA

INTRODUCTION

The objective of this work is to develop high-strength, oxidation- and corrosion-resistant intermetallic reinforced alloys for use as hot components in advanced fossil energy conversion and combustion systems to help meet the efficiency goals of the Vision 21 Concept. Successful development of these alloys is expected to allow improvement in thermal efficiency through decreased cooling requirements in advanced gas turbines. Initially targeted applications include components such as vanes, seals, and nozzles. However, these materials may also find other uses such as combustion gas cleaning system components (e.g. hot-gas filters), wear-resistant parts in coal handling systems, drill bits for oil/gas wells, valve guides in diesel engines, and thermowells.

Recently, we identified a promising new class of alloys based on the Cr(Ta)-Cr₂Ta eutectic with melting points in the 1600-1750°C range¹⁻³ (Fig. 1). Toughness and oxidation resistance are provided by a relatively soft Cr(Ta) (solid solution) matrix with the Cr₂Ta Laves phase acting as reinforcement in order to provide high-temperature strength. Preliminary evaluation suggested that these Cr(Ta)-Cr₂Ta based alloys possess a promising combination of high-temperature oxidation/nitrogen embrittlement resistance and high-temperature strength, but only a modest degree of room-temperature toughness^{2,3}. This report presents an overview of the results of long-term (1000 h range), high-temperature oxidation and creep testing of these alloys and discusses approaches for further improvement in properties, in particular room-temperature fracture toughness.

DEVELOPMENT OBJECTIVES AND CURRENT COMPOSITIONS

Three properties are key to the initial development of the two phase Cr(Ta)-Cr₂Ta based alloys: high-temperature oxidation resistance, high-temperature strength and creep resistance, and room-temperature fracture toughness. The target oxidation behavior is kinetic behavior comparable to the range exhibited by commercial chromia-forming alloys in the 900-1000°C temperature range and, at higher temperatures

where chromia scale volatility is significant ⁶, noncatastrophic oxidation behavior of the bare substrate alloy such that use of a protective coating is a reasonable protection approach (i.e. local coating failure would not result in rapid component loss). The target mechanical properties are 350 MPa tensile fracture strength at 1200°C and room temperature fracture toughness $\geq 15\text{-}20 \text{ MPa}\sqrt{\text{m}}$.

The most promising alloys to date fall in the general composition range of Cr-(6-10)Ta-5Mo-0.5Ti-(0-3)Si-(0.1-0.2)La/Ce (all compositions reported in atomic percent, at.%, unless otherwise noted) ⁷. The Mo is added for solid solution strengthening, the Ti for interstitial gettering, the Si for oxidation resistance, and the La/Ce for oxidation resistance and interstitial gettering. Both Laves phase dispersed (cast, hot-extrusion) and lamellar (cast, heat treated and/or hot isostatically pressed) microstructures have been produced.

HIGH-TEMPERATURE OXIDATION

Evaluation and characterization of the long-term oxidation behavior of Si-containing and/or reactive element doped alloys, which had previously shown good resistance to oxidation during short term screening tests at 1100°C, were performed. Disk shaped oxidation specimens of 12-13 mm in diameter and 1-1.5 mm thickness were sectioned from as-cast and/or heat treated material and polished to a 600 grit finish using SiC paper. Long-term cyclic oxidation exposures were conducted in covered alumina crucibles (1 sample per crucible) for ten 100 h cycles (1000 h total) at 1100°C in a tube furnace open to humid air. Chromia volatility was evident during the 1100°C exposures by green stains on the underside of the alumina lids.

At 1100°C in air after ten 100 h cycles, Cr-8Ta-5Mo-3Si-0.25Ge-0.2La showed cyclic oxidation resistance comparable to Haynes 230 and MA754, two of the better commercial chromia-forming alloys available (Fig. 2). The Cr-8Ta-5Mo-0.2La alloy exhibited a relatively high weight gain during this test and was only marginally more oxidation resistant than cast Ni-27Cr wt.%. The high degree of oxidation resistance exhibited by the Si-bearing alloy meets the oxidation-related goals of this development effort.

The superior behavior of the Si bearing alloy is likely the result of the formation of an inner, partly or completely continuous, layer of silica at the alloy/scale interface. Such silica scale formation has been reported for other chromia scale forming alloys ^{8,9}. Additions of Si were initially found to reduce the isothermal rate of oxidation but also resulted in extensive scale spallation during thermal cycling. The

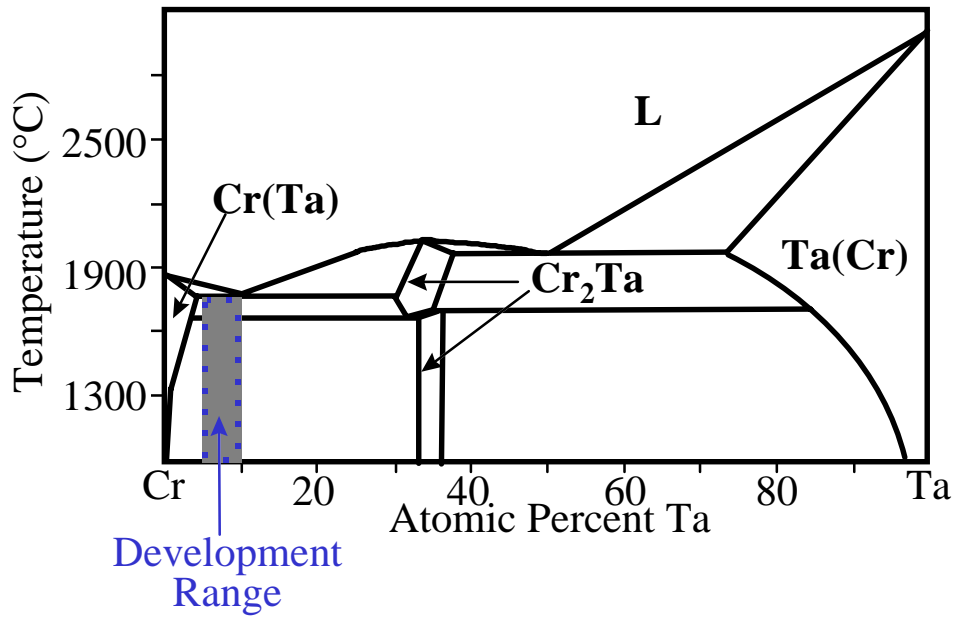


Fig. 1- Schematic binary Cr-Ta phase diagram^{4,5}.

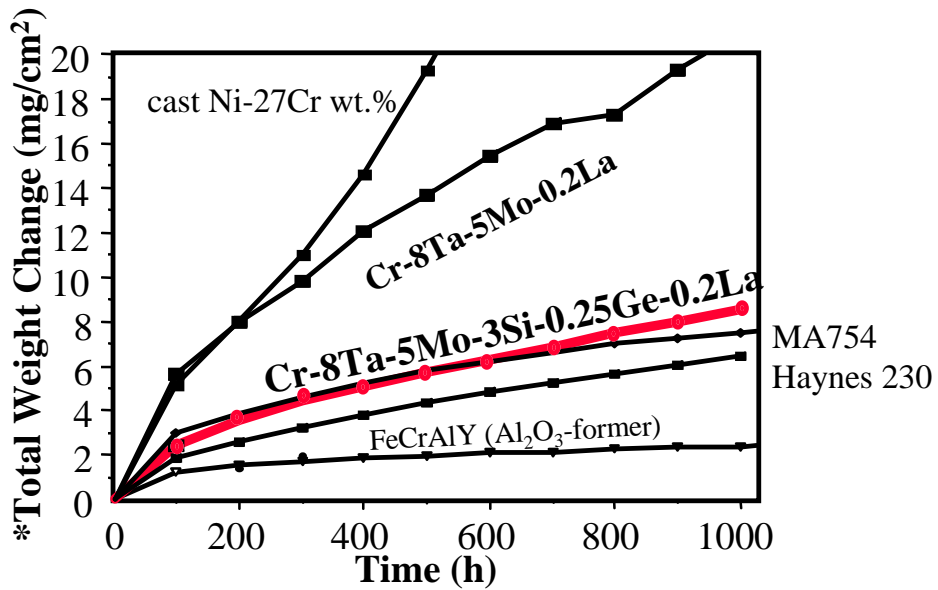


Fig. 2- Cyclic oxidation behavior at 1100°C in humid air (comparison data of B.A. Pint and I.G. Wright, unpublished, 1999). (* includes scale volatility and spallation).

addition of Ge was found to reduce the spallation, presumably by increasing the thermal expansion of the silica, making it more compatible with metallic substrates¹⁰. In combination with reactive elements, excellent oxidation resistance was achieved. Unfortunately, the Ge addition also embrittled the alloy.

Preliminary evaluation of the cyclic oxidation resistance of Cr-8Ta-5Mo-0.5Ti-0.1La-3Si at 1100°C suggests that scale adherence can be achieved with the La addition alone and that the embrittling Ge addition is not necessary to achieve scale adherence (Fig. 3). Neither the Si nor La additions are embrittling and the room-temperature toughness of Cr-8Ta-5Mo-0.5Ti-0.1La-3Si is among the highest of any Cr-Ta alloy tested to date in this program (12 MPa√m- see section on room-temperature fracture toughness for further details). Long-term cyclic oxidation testing of this alloy is planned.

Ingress of nitrogen during elevated temperature exposure in air is well known to harden and embrittle Cr. Cross-section analysis of oxidized Cr-Ta alloys by wavelength dispersive (WDS) electron probe microanalysis (EMPA) indicates that nitrogen also penetrates through the chromia-based scales formed by these alloys during elevated temperature exposure in air. However, the extent of nitrogen penetration in Cr-Ta is much less than in pure Cr, especially in the Si and/or reactive element containing alloys, due presumably to the more protective chromia scale that is formed. Further, in all Cr(Ta)-Cr₂Ta alloys examined, as well as a similar family of Cr(Nb)-Cr₂Nb alloys, the Laves phase was found to be selectively nitrated ahead of the alloy/scale interface (Fig. 4)³. From a practical standpoint this is a beneficial effect in that preferential gettering of nitrogen by the Laves phase limits nitrogen penetration and embrittlement of the Cr solid solution phase. Because it is already quite brittle, nitridation of the Laves phase is unlikely to significantly degrade the toughness of the alloy.

HIGH-TEMPERATURE CREEP BEHAVIOR

High-temperature creep testing was conducted for Cr-8Ta-5Mo-0.5Ti-0.01Ce in two microstructural conditions: dispersed Laves phase particles in a Cr matrix (produced by extrusion) and lamellar Cr(Ta)/Cr₂Ta (produced by casting/heat treating). The evaluation was conducted at 1000°C in humid air with a loading stress of 138 MPa (20 ksi). Both the Laves phase dispersed and lamellar microstructures exhibited outstanding resistance to creep under these conditions, so much so that the MAR 246 grip rods and Ni₃Al plate suffered from extensive deformation during the test, and in the case of the lamellar microstructure, the test was stopped due to failure of this test equipment. It was necessary to correct the

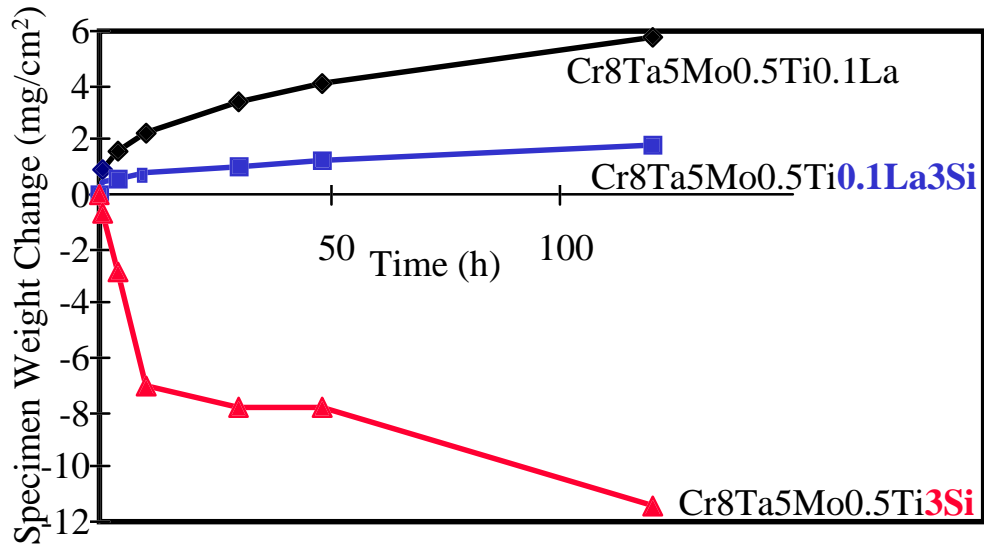


Fig. 3- Cyclic oxidation data at 1100°C in humid air.

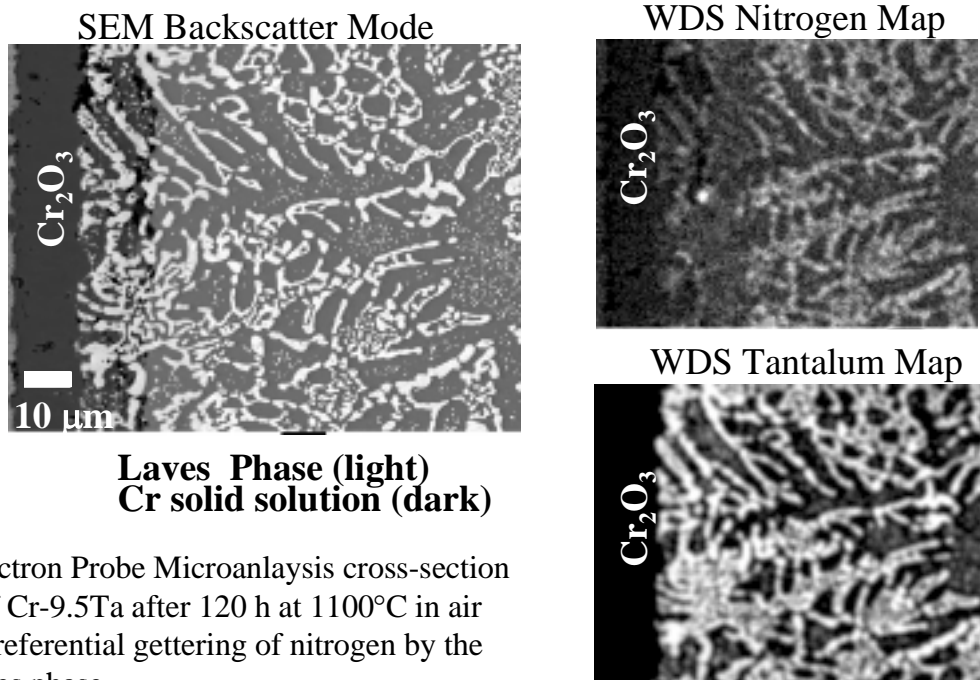


Fig. 4- Electron Probe Microanalysis cross-section analysis of Cr-9.5Ta after 120 h at 1100°C in air showing preferential gettering of nitrogen by the Cr₂Ta Laves phase.

creep data for the deformation of the grip rods and plate-as such the data should be considered semi-quantitative due to possible errors introduced by this correction.

The elongation vs. time curves for the two microstructures are shown in Fig. 5. The dispersed Laves phase microstructure failed in a ductile manner by creep cavitation after 695 h of exposure. Little elongation of the lamellar microstructure creep test sample was observed when the test was stopped after 1438 h of exposure due to failure of the grip rods and plates. The superior creep resistance of the lamellar microstructure is consistent with tensile property measurements which also showed that the lamellar microstructure is stronger (but also less ductile) than dispersed Laves phase microstructures at high-temperatures.

For comparative purposes, the creep data for dispersed Laves phase Cr-8Ta-5Mo-0.5Ti-0.01Ce is displayed on the Larson-Miller plot shown in Fig. 6. These preliminary data indicate that this Cr-Ta based alloy, which is polycrystalline, possesses creep resistance comparable to that of some single-crystal superalloys and meets the high-temperature strength goals of this development effort.

Nitrogen penetration on the order of 0.5 mm was observed in the dispersed Laves phase microstructure test sample after 695 h at 1000°C and nearly 1 mm in the lamellar microstructure test sample after 1438 h at 1000°C. (These differences in nitrogen penetration likely reflect the different hold times at temperature). It is interesting to note that nitrogen penetration did not result in the failure of either test sample; in fact, the Laves phase dispersed microstructure test sample failed in a ductile manner by creep cavitation. Although most of the nitrogen was preferentially gettered by the Laves phase, a nitrogen embrittled surface region was observed. The tolerance of a thin nitrogen-embrittled surface region may be due to the excellent ductility of these alloys at high temperatures (tensile elongation from 15-40% has been achieved at 1200°C) (ref. 2). Longer term, lower load creep testing is planned to investigate whether such nitrogen penetration will act as a life-limiting factor. It should be noted that the Cr-8Ta-5Mo-0.5Ti-0.01Ce alloy contained insufficient reactive element addition (Ce) to improve oxidation resistance. Higher levels of Ce (or La) in conjunction with Si additions slow the rate of oxidation by greater than an order of magnitude as well as significantly reduce scale permeability to nitrogen.

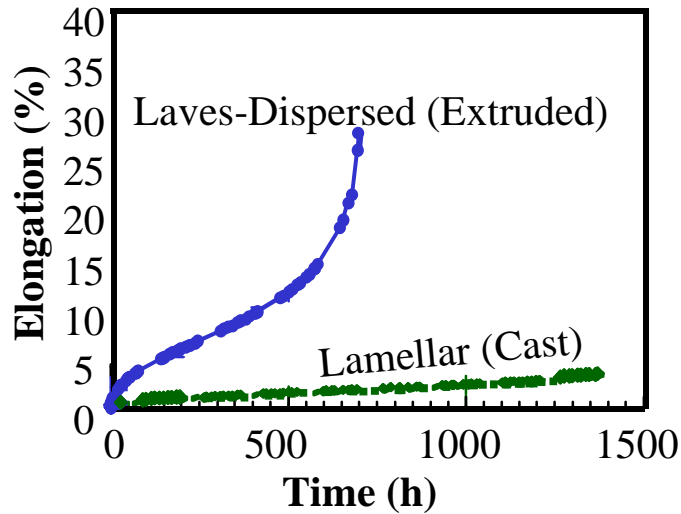


Fig. 5- Creep data obtained at 1000°C and 138 MPa in humid air for Cr-8Ta-5Mo-0.5Ti-0.01Ce with Laves phase dispersed or lamellar microstructures. Note that the lamellar microstructure test was stopped due to failure of the grip rods and plate.

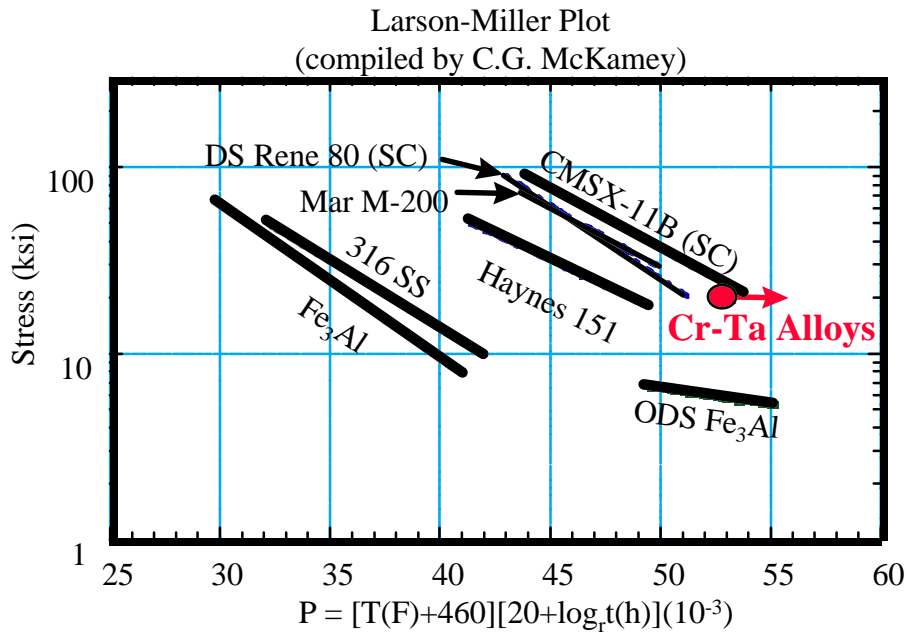


Fig. 6- Larson-Miller plot for Laves phase dispersed Cr-8Ta-5Mo-0.5Ti-0.01Ce (data from Fig. 5) compared with several other high-temperature alloys. The arrow for the Cr-Ta alloys is for the lamellar microstructure test sample from Fig. 5 which was stopped prior to failure. SC=single-crystal.

ROOM-TEMPERATURE FRACTURE TOUGHNESS

Chevron notched three-point bend samples approximately 3 mm x 4 mm x (20-25) mm were used to evaluate fracture toughness at room temperature. A modulus of 250 GPa was estimated for the Cr(Ta)-Cr₂Ta based alloys. Details of this technique are provided in ref. 11.

Current Cr(Ta)-Cr₂Ta based alloys have a room temperature fracture toughness in the 11-12 MPa√m range. Although this represents significant progress, it is still short of the goal of at least 15-20 MPa√m.

Two strategies have been adopted to increase room-temperature toughness: 1) weakening the Cr(Ta)/Cr₂Ta lamellar interface and 2) ductilizing of the Cr(Ta) phase. Efforts to weaken the Cr(Ta)/Cr₂Ta lamellar interface have not proven successful to date. However, some progress has been made in ductilization of the Cr(Ta) phase.

A major contributor to the ambient brittleness of Cr is the presence of nitrogen interstitials. Work by Scruggs and co-workers in the 1960's demonstrated that plastic tensile elongation in the range of 20 % could be achieved at room-temperature in Cr via the addition of MgO particles ¹². During powder processing, the MgO particles convert to a CrMg₂O₄ spinel, which was hypothesized to getter nitrogen from the Cr, rendering it ductile ¹².

An extruded ingot of Cr-6MgO-0.5Ti wt.% was provided by Scruggs and plasticity at room-temperature was confirmed, with an average plastic tensile elongation of 8.2% (3 samples) obtained at a strain rate of $3.33 \times 10^{-3}/s$ and a 600 grit surface finish. Further, preliminary atom probe analysis of this material is consistent with the proposed mechanism of nitrogen gettering by the spinel phase. Efforts to fabricate this alloy have been modestly successful, with plastic tensile elongation averaging 4.75 % (4 samples) obtained from hot-pressed material tested at room-temperature ($3.33 \times 10^{-3}/s$ and a 600 grit surface finish). The greater plasticity of the original Scruggs alloy ingot is speculated to result primarily from the extruded microstructure, which resulted in a fine distribution of oxide particles aligned in the tensile test direction. The hot-pressed material had a more equiaxed structure and the oxide particles had a tendency to agglomerate. Efforts to duplicate this effect within the Cr solid solution phase in the two-phase Cr(Ta)-Cr₂Ta alloys in order to increase ambient toughness are underway.

REFERENCES

1. M.P. Brady, J.H. Zhu, C.T. Liu, P.F. Tortorelli, J.L. Wright, C.A. Carmichael, and L. R. Walker, in *Proc. of the Eleventh Annual Conference on Fossil Energy Materials*, R.R. Judkins (comp.), U. S. Department of Energy, p. 195 (December 1997).
2. M.P. Brady, J.H. Zhu, C.T. Liu, P.F. Tortorelli, J.L. Wright, and C.A. Carmichael, in *Proc. of the Twelfth Annual Conference on Fossil Energy Materials*, Knoxville, R.R. Judkins (comp.), U. S. Department of Energy, paper 4.9 (1998).
3. M.P. Brady, J.H. Zhu, C.T. Liu, P.F. Tortorelli, L.R. Walker, "Oxidation Resistance and Mechanical Properties of Laves Phase Reinforced Cr In-Situ Composites", submitted to "Intermetallics for the Third Millennium" Special Issue of *Intermetallics*.
4. M. Venkatraman and J.P. Neumann, in Binary Alloy Phase Diagrams, Vol. 1, T.B. Massalaski, J.L. Murray, L.H. Bennett, and H. Baker eds., ASM, p. 867 (1986).
5. J.H. Zhu and C.T. Liu, unpublished research (1997).
6. E.J. Opila, N.S. Jacobson, in: *Fundamental Aspects of High Temperature Corrosion*, Shores, D.A., Rapp, R.A., and Hou, P.Y. (Eds.), The Electrochemical Society, Pennington, NJ, pp. 269-280 (1997).
7. C.T. Liu, M.P. Brady, J.H. Zhu, and P.F. Tortorelli, "Dual Phase Cr-Ta Alloys for Structural Applications", submitted to U.S. Patent Office.
8. G.C. Wood, J.A. Richardson, M.G. Hobby, J. Boustead, *Corr. Sci.*, 9, pp. 659-671 (1969).
9. R.C. Lobb, H.E. Evans, in: *Microscopy of Oxidation*, M.J. Bennett, G.W. Lorimer, eds., The Institute of Metals, pp. 119-124 (1991).
10. B.V. Cockeram, R.A. Rapp, *Mat. Sci. Eng. A*, 192/193, pp. 980-986 (1995).
11. J.H. Schneibel, C.A. Carmichael, E.D. Specht, and R. Subramanian, *Intermetallics*, 5, p. 61 (1997).
12. D.M. Scruggs, L.H. Van Vlack, W.M. Spurgeon, *J. Amer. Ceram. Soc.*, 51, 9, pp. 473-481 (1968).

ACKNOWLEDGEMENTS

The authors thank D.M. Scruggs for donation of a Cr-MgO alloy ingot and helpful discussions regarding his efforts in the 1960's to ductilize Cr. The authors also thank R.J. Lauf for valuable input regarding spinel defect structures and insight into the mechanism of Cr ductilization via MgO additions, and C. Leyens and J.H. Schneibel for their reviews of this manuscript. This research was sponsored by the Fossil Energy Advanced Research and Technology Development (AR&TD) Materials Program, U.S. Department of Energy, under contract DE-AC05-96OR22464 with Lockheed Martin Energy Research Corporation.

ODS ALLOYS FOR HIGH-TEMPERATURE APPLICATIONS

I. G. Wright, C. G. McKamey, B. A. Pint, and P. J. Maziasz

INTRODUCTION

Although oxide dispersion-strengthened alloys have been available for some 30 years, their potential for use in very high-temperature fossil energy applications was demonstrated only in the last five years, by British Gas in the U.K.⁽¹⁾ and recently in the DOE's High-Performance Power Systems (HIPPS) program⁽²⁾. In addition to their use for very high-temperature heat exchanger tubes, typical applications include furnace hardware, catalytic converter substrates, combustor components, abradable seal structures, and resistance heater elements. In heat exchanger tubing applications, these alloys can provide an increase in temperature capability of 138 to 167°C (250 to 300°F) compared with conventional wrought alloys⁽³⁾. For applications where resistance to high-temperature oxidation is required in addition to high-temperature creep strength, alloys that form alumina scales are preferred, and ODS-FeCrAl-based alloys are now commercially available from two manufacturers. The unique resistance of the Fe₃Al-based alloys to sulfidizing gases, together with their potentially longer oxidation lifetimes due to their higher Al contents compared to existing ODS-FeCrAl or ODS-NiCrAl alloys, has led to the development of a new ODS-Fe₃Al⁽⁴⁾. For the temperature range of interest in, for example, advanced steam cycles, ODS-FeCr-based alloys are under consideration for use as bolting materials because of their increased creep strength. This represents an important but different application since, although these alloys must exhibit high creep strength and good environmental resistance, the environments in which they will be applied are typically less demanding than the fireside conditions encountered by the ODS-FeCrAl and Fe₃Al alloys, and so an alumina scale is not critically needed.

Despite the excellent potential of ODS alloys, their wider use is contingent on an improved awareness by plant designers and operators that different approaches are required in designing and using these alloys compared to wrought alloys. When properly applied, it is expected that ODS-FeCrAl and Fe₃Al alloys, for instance, will be usable to metal temperatures up to 1150°C (2100°F) in components at the lower end of the temperature range where ceramics typically are thought to be required.

Optimization of the microstructure of ODS-FeCr alloys also is of interest. Developments in alloy processing to maximize strength for specific component forms (tube versus plate, for instance) or environmental resistance for particular service conditions are expected to be generally applicable to the whole class of ODS alloys. The data generated are intended to form a resource for designers wishing to incorporate ODS alloys into components. The alloys of interest are indicated in Table I, which also gives their typical chemical compositions.

Table I. Nominal Compositions of Available Ferritic ODS Alloys (weight percent)

Alloy	Fe	Cr	Al	Mo	W	Ti	Si	RE*
Kanthal APM	Bal	20.0	5.5	—	—	0.03	0.23	ZrO ₂ -Al ₂ O ₃
INCO MA 956	Bal	20.0	4.5	—	—	0.5	—	Y ₂ O ₃ -Al ₂ O ₃
INCO MA956HT	Bal	21.6	5.9	—	—	0.4	0.07	Y ₂ O ₃ -Al ₂ O ₃
PM 2000	Bal	20.0	5.5	—	—	0.5	—	Y ₂ O ₃ -Al ₂ O ₃
Dour Alloy ODM 751	Bal	16.5	4.5	1.5	—	0.6	—	Y ₂ O ₃ -Al ₂ O ₃
ODS-Fe ₃ Al	Bal	2.2	15.9	—	—	0.07	0.1	Y ₂ O ₃ -Al ₂ O ₃
Kobe FeCr	Bal	12	—	—	3.0	0.4	—	Y ₂ O ₃

*reactive element addition, in the form of an oxide dispersion.

DISCUSSION OF CURRENT ACTIVITIES

Mechanical Properties

The tensile strengths of the ODS-FeCrAl and ODS-Fe₃Al alloys as a function of temperature are shown in Fig. 1a. For the commercially-available ODS-FeCrAl alloys data from the manufacturers or from the literature are used; experimentally-obtained data are presented for the ODS-Fe₃Al and ODS-FeCr alloys. None of the experimental ODS-Fe₃Al alloys incorporated the processing modifications that are being developed to minimize microstructural defects that probably degrade the high-temperature properties.

As shown in Fig. 1b, the ductility of the commercial ODS-FeCrAl alloys is of the order of 9-13 percent below approximately 400°C, whereas for the ODS-Fe₃Al alloy the elongation falls from 8-9 percent at 400°C to 3-4 percent at room temperature. These alloys exhibit maximum ductility in the range 400 to 1000°C (400 to approximately 850°C for MA956), so that it would appear advantageous to perform hot deformation in this temperature range during processing.

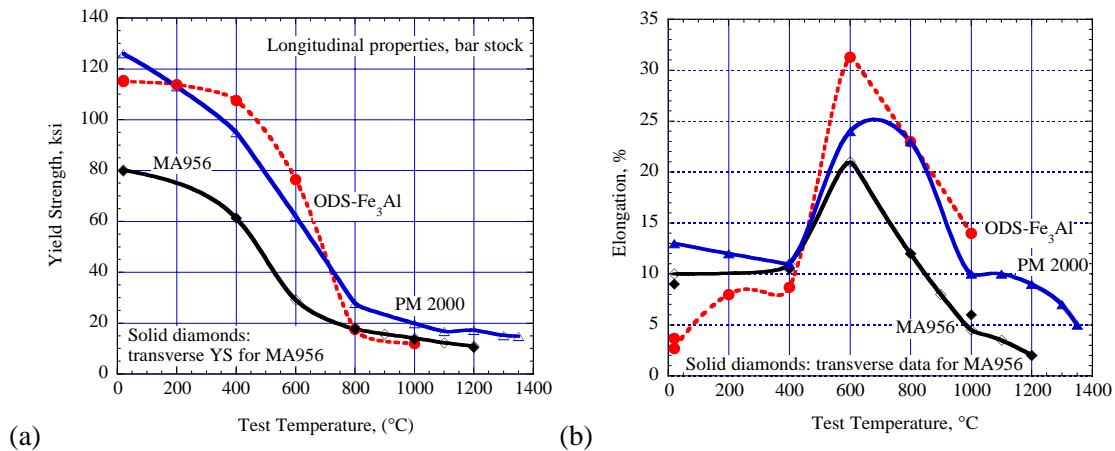


Fig. 1. Tensile strengths (a) and tensile ductilities (b) of ODS-FeCrAl and ODS-Fe₃Al alloys.

The behavior of the alloys in tensile creep is shown in the Larson-Miller plots in Figs. 2 and 3. The data are for specimens in the form of rods, tested with the long axis of the elongated grain structure aligned along the axis of the test rod. Note that the alumina-forming and chromia-forming classes of ODS alloys exhibit creep strength at temperatures beyond the capabilities of the strongest non-ODS versions of the same alloys or of currently used alloys (for instance, Fe₃Al and the FeAl-based alloy FA-180 compared to ODS-Fe₃Al in Fig 2). Recent results for ODS-Fe₃Al are tending to move the Larson-Miller parameter to the right in the diagram (as indicated by the arrow), which indicates that the creep strength of this developmental alloy is of the same order as that of commercial MA-956 ODS-FeCrAl alloy (Fig. 2), suggesting the good potential of this new, alternative alloy.

The data in Fig. 3 illustrate the creep behavior of a new ODS-FeCr alloy developed in a joint program between Kobe Specialty Tube Co. Ltd., and Nagoya University in Japan as part an alloy development program for nuclear power applications. This new alloy also has good potential for use in fossil-fueled plants in, for instance, high-temperature bolting or blading for steam turbines, or possibly for high-temperature steam tubing. Note that the Larson-Miller parameters used in Fig. 3 are different than those in Fig. 2. Although the creep testing of this alloy has just started, preliminary data from the tests still in progress show similar creep strength to the ODS-FeCrAl alloy MA956 at the higher temperatures at which tests are being run. The creep strength of this alloy results from a modification in the processing

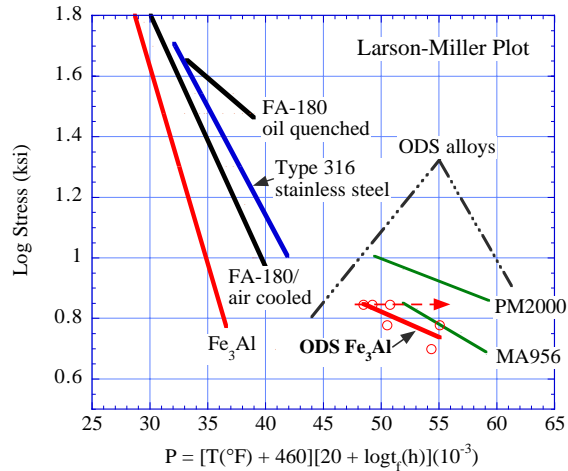


Fig. 2. Larson-Miller plot for ODS-FeCrAl and ODS-Fe₃Al alloys

route which has apparently enabled the development of an extremely fine distribution of ‘inert’ particles. High-resolution analytical microscopy to better understand these changes is in progress.

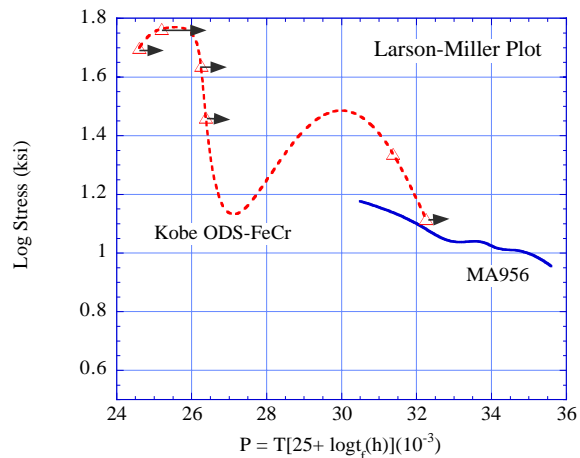


Fig. 3. Larson-Miller plot comparing ODS-Fe-Cr and ODS-FeCrAl alloys

While Larson-Miller diagrams are a conventional and convenient means of comparing alloy behavior, they do not adequately represent nor differentiate the behavior of the ODS alloys. Figure 4 illustrates that ODS alloys exhibit unusual creep behavior, in which the progressive stages of creep exhibited by conventional alloys are typically not observed. Instead, the response to creep is long periods of no measurable activity, with occasional small step increases in elongation presumably as dislocations are able to climb over pinning dispersed oxide particles. At sufficiently high levels of applied stress, such activity is terminated by an abrupt failure with essentially no warning, as shown in Fig. 4. However, at lower stress levels, essentially no creep is observed for extremely long times. This behavior is an example of the strain rate sensitivity of ODS alloys which must be fully appreciated when considering their application.

As a tool to help assess the capabilities of ODS alloys, a diagram of the type shown in Fig. 5 is suggested which would provide an initial indication of the temperature-stress regimes in which advantage could be taken of the superior creep behavior of these alloys. Such diagrams would only be useful when used in conjunction with consideration of the strain rates involved and conventional strain rate-sensitivity data,

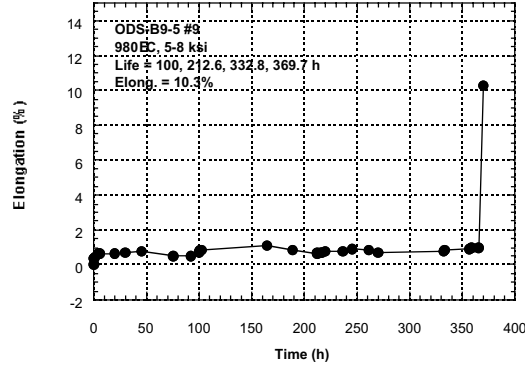


Fig. 4. Typical creep curve for ODS-Fe₃Al. Load was increased from 34 to 55 MPa (5 to 8 ksi) in 7 MPa (1 ksi) increments at 100-hr intervals until failure.

but could have some practical usefulness. Note that Fig. 5 has only one data point (from results shown in Fig. 4) and the shape of the curve currently is entirely arbitrary; further data points are being generated as part of a process to determine the threshold stress levels to be used for creep testing of ODS-Fe₃Al.

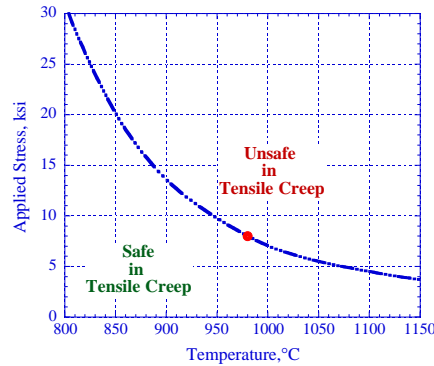


Fig. 5. Suggested representation of regimes of safe/unsafe application of ODS alloys.

Physical Properties

Table II is a compilation of available data on physical properties of the ODS-FeCrAl and ODS-Fe₃Al alloys. This will be expanded with input from the alloy manufacturers and from data published in the literature as these become available. Where specific properties needed by designers and potential users are not available, consideration will be given to measuring them. For instance, the coefficient of thermal expansion of ODS-Fe₃Al was measured experimentally as part of the current program.

Table II. Physical properties of ODS-FeCrAl and ODS-Fe₃Al alloys.

Property	MA956 ⁽⁵⁾	PM2000 ⁽⁶⁾	ODS-Fe ₃ Al
MPt (°C)	≈1482	1480	1430-1477
Density (gcm ⁻³)	7.2	7.18	6.53
Coeff. of thermal expansion (x 10 ⁻⁶ /K)	14.9 (1000°C)	10.7 (50°C)	21.3 (1000°C)
Thermal conductivity (W/mK)	27.0 (1100°C)	10.9 (20°C)	[23.8 (1100°C)] ^a
Specific heat (J/kg°C)	769 (1100°C)	480 (20°C)	—
Electrical resistivity (x 10 ⁻⁶ Ωm)	1.44 (1100°C)	1.31 x 10 ⁻⁶ (20°C)	[1.62 x 10 ⁻⁶ (1000°C)] ^b
Modulus of elasticity (GPa)	191 (1000°C)	218 (20°C)	—

a: for cast Fe-28Al-5Cr-0.5Nb-0.2C (at%); W. D. Porter and P. J. Maziasz, unpublished results, Oak Ridge National Laboratory.

b: for cast Fe-28Al-5Cr-0.05B (at%); C. G. McKamey, unpublished results, Oak Ridge National Laboratory.

Joining

While ODS alloys can be joined by conventional fusion welding, in these processes the disruption of the alloy microstructure in the weld fusion zone is sufficient to drastically reduce the creep strength. INCO reported⁽⁷⁾ that the level of retained high-temperature strength of MA956 after welding using the following processes decreases in the order: pulsed-laser welding; electron-beam welding; and resistance spot welding. With these processes, the fusion-weld beads of this alloy must be oriented so that the weld centerlines are parallel with any tensile loads. Laser fusion welding has been used to join thin foils (90 to 150 μm -thick) of ODS-FeCrAl (PM2000) in the fabrication of honeycomb structures for abradable seals in gas turbine engines⁽⁸⁾. For brazing, resistance spot welding is recommended for prebrazing assembly. Brazed joints (using a Pd-40Ni filler material) have been used to join PM2000 tubes⁽⁹⁾; tests of these joints in creep (both shear tests and internally-pressurized tests) at 800°C (1472°F) indicated sufficient strength to allow practical application. For diffusion bonding, a surface finish of 0.08 μm using a water-cooled polishing wheel or belt is recommended⁽⁷⁾. Transient liquid phase (TLP) bonding of an ODS-NiCr alloy has been used successfully to fabricate a serpentine tube heat exchanger used in the United Technology Research Center's radiant heat exchanger for the HIPPS pilot-scale unit⁽¹⁰⁾. This process requires the parts to be joined to be mounted on jigs and heat treated in a furnace, but results in a metallurgical bond with very little interference with the alloy microstructure. Bond strengths some 80% of the parent alloy have been reported. In the British Gas Advanced Heat Exchanger program⁽¹⁾ safe ends were explosively bonded to ODM-751 tubes, thus allowing conventional handling and joining of the tubes to the headers. However, INCO indicates that for MA956 adiabatic shearing and microcracking are likely to result from explosively bonding⁽⁷⁾, so that this process is not recommended for this alloy.

In this program, joining of rod stock by rotary friction welding has been explored with TWI, U.K..⁽¹¹⁾ Sound welds have been made of ODS-Fe₃Al to itself in the as-extruded and as-recrystallized conditions, and of ODS-Fe₃Al to Haynes 230 (one of the strongest conventional wrought alloys used for tubing). Initial tensile tests of these joints indicated, surprisingly, that the strength of the ODS-Fe₃Al self joints in the unrecrystallized state was similar to that of the parent alloy, whereas those in the recrystallized alloy retained only 54 to 69 percent of the strength of the parent alloy. The ODS-Fe₃Al-to-Haynes 230 joints retained 54 to 62 percent of the strength of ODS-Fe₃Al. The microstructures of the joined areas indicated massive flow of the ODS-Fe₃Al with associated agglomeration of the oxide dispersion, and recrystallization to produce fine, equiaxed grains. In an attempt to improve the grain structure in the joint area, samples of ODS-Fe₃Al which had been joined in the unrecrystallized state were subjected to a range of conditions intended to promote recrystallization through the joint. A resulting microstructure is shown in Fig. 6, which indicates that relatively large grains can be developed across the joined interface, although in this case their orientation is perpendicular to the major stress axis. Further details of these structures are reported by Kad, et al.⁽¹²⁾ Mechanical testing of such a joint is planned.

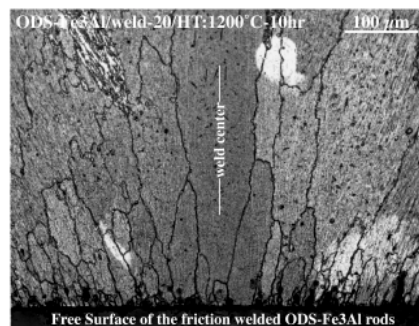


Fig. 6. Recrystallized microstructure across the joint line in a friction-welded ODS-Fe₃Al self joint.

Oxidation-Limited Life Determination

The available ODS-FeCrAl and ODS-Fe₃Al alloys exhibit very low oxidation rates up to 1300°C (2372°F) due to the formation of a protective Al₂O₃ film. Under conditions where the mechanical load is below the stress at which significant creep occurs, the effective lifetime of these alumina scale-forming ODS alloys depends on their reservoir of available Al (which is a function of the Al activity) and on the section thickness. The minimum Al level (C_b) at which protective oxidation can no longer be sustained is of practical significance, and is also an important input for modeling the oxidation lifetimes. Further, as the rate of oxidation increases with increasing temperature, the selective depletion of Al limits the minimum cross section which can be safely employed. The oxidation lifing model currently used is based on that suggested by Quadakkers, et al.⁽¹³⁾ in which the oxidation lifetime (t_b) is simply expressed as:

$$t_b = [4.44 \times 10^{-3} \cdot (C_o - C_b) \cdot \rho \cdot d/k]^{1/n}$$

The input required includes a description of the alloy in terms of initial (C_o) and minimum (C_b) Al contents, density (ρ), and section thickness (d) and, for a given temperature, the oxidation rate (k) and time-dependence exponent (n , which is 0.5 for parabolic oxidation behavior). This version of the model describes only the protective oxidation behavior, and takes as the end-of-life criterion the onset of rapid oxidation associated with the growth of a less-protective scale over a significant area of the surface. Figure 7a shows the oxidation kinetic data for a 0.13 mm-thick sample of Kanthal APM exposed in air at 1300°C. The exposure was run at an elevated temperature to allow relatively short test times; earlier studies had indicated that the oxidation mechanism was the same at 1300°C as at the expected use temperatures of 1100-1200°C. In this test, specimens are exposed in lidded alumina crucibles to allow all oxide growth (and spallation) to be accounted. This alloy exhibited excellent resistance to scale spallation and, although the rate of oxidation was faster than expected from a parabolic rate law, the kinetic curve could be represented by a single rate law, the exponent for which was 0.72. The oxidation lifetime predicted using the model, based on this exponent [and a rate constant calculated from a weight gain-(time)^{0.72} plot] was 1,450 hours, which corresponded very well with the actual lifetime of approximately 1,400 hr. If the calculation were made with an exponent of 0.5 and a rate constant derived from a parabolic plot, the predicted lifetime would be 1,210 hr.

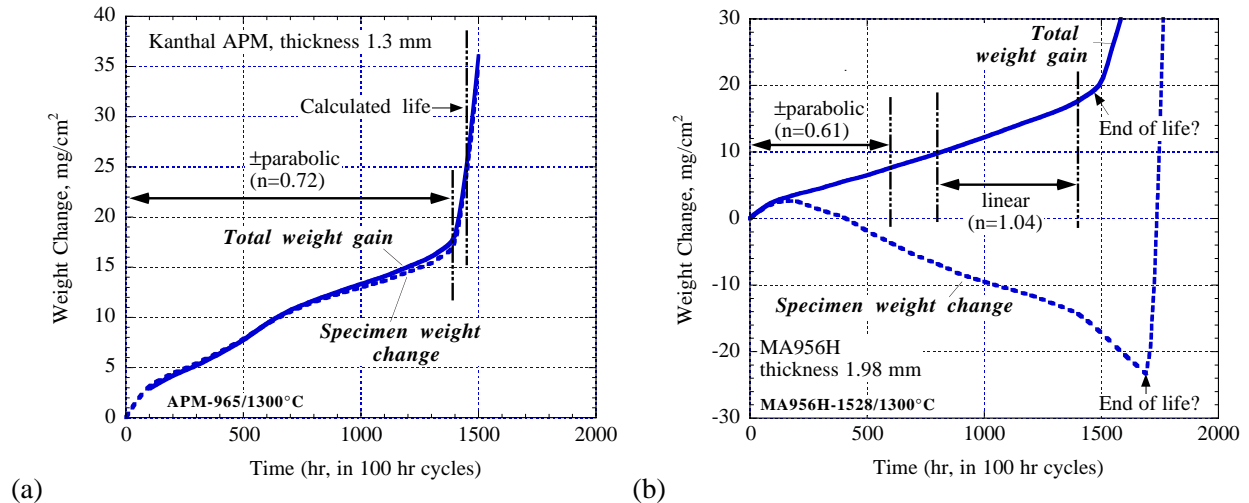


Fig. 7. Oxidation kinetics for (a) Kanthal APM and (b) Inco 956H at 1300°C (100-hr cycles)

Figure 7b shows the oxidation kinetics for a 1.98 mm-thick specimen of alloy MA956HT exposed at 1300°C in 100-hr cycles to laboratory air. Specimens of different thickness were used to provide information on oxidation lifetime for use in testing and developing the model. The weight gain shown in Fig. 7b indicates the total oxygen consumption (total weight gain) and the scale spallation (specimen weight gain) by the specimen. Although the oxidation for the first few hundred hours could be described as approximately parabolic ($n = 0.61$), the considerable scale spallation experienced by this alloy resulted in a transition to faster kinetics, with n approximating 1.0. The transition to linear kinetics occurred at a weight gain of approximately 7.5 mg/cm². Degradation of the protective behavior of a thermally-grown alumina scale in the temperature range 1050 to 1300°C has been found to occur at weight gains over 1.5 to 3 mg/cm² (equivalent to 8 to 16 μm)⁽¹⁴⁾, and results from the development of porosity in the scale. Hence, the observed change in oxidation rate in this severe test of MA956 should not be considered unusual. The fact that the rate of growth of the scale on Kanthal APM occurred at a rate faster than parabolic (Fig. 7a) also may be explained by this observation, but the reasons why this alloy attained a total weight gain of approximately 17 mg/cm² with very little scale loss by spallation before failure await further evaluation.

Using the rapid upturn in the total weight gain and specimen weight change curves as the end-of-life criterion, Fig. 8 was plotted to show the trend of lifetime with wall thickness (half the specimen thickness). Note that the total weight gain curve in Fig. 7b indicates the initiation of an increased rate of oxidation some 200 hr earlier than does the specimen weight change curve. Also shown in Fig. 8 is the prediction of the current model. Based on values of k and n derived from the initial oxidation period ($n = 0.61$) the lifetime was grossly overpredicted (but the potential improvement if scale spallation could be reduced is clearly indicated). The k and n values from the period when approximately linear kinetics were followed also resulted in overprediction of the oxidation lifetime, but resulted in a trend much closer to the measured dependence than that from the early stage kinetic data.

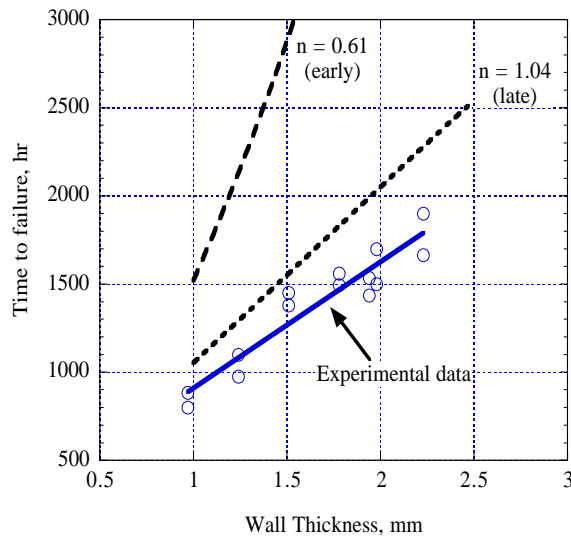


Fig. 8. Comparison of actual dependence of oxidation lifetime on wall thickness with predicted values.

These results highlight a problem of some importance in that the model is very sensitive to the value of n , and the values of n calculated from experimental data are sometimes greater or less than 0.5, and may not be constant with time. Where significant scale spallation (or cracking and rehealing) occurs or, for thicker scales, defects such as porosity can develop, n can increase with time. Conversely, for alloys that form very protective scales, at lower temperatures the value of n is often found to be less than 0.5. It is

currently unclear to what extent the values of n are influenced by the method of calculation, or if the low/decreasing values represent a change in the mechanism of scale growth.

A further area of uncertainty is the AI level (C_b) corresponding to the end of life criterion, and the extent to which it varies with temperature. Attempts to measure this value from specimens such as those represented in Fig. 7 have produced unsatisfactory results because the specimens are examined only at 100-hr intervals, at which time those suffering accelerated oxidation are typically not easily characterized. The next phase of this work will make use of wedge-shaped specimens, suggested by Tatlock, et al.⁽¹⁵⁾ as a way of controlling the location on the specimen at which accelerated oxidation occurs, and of reaching the oxidation life limits at lower temperatures in manageable times.

If the model is to be truly useful, and not simply rely on input from curve fitting, it must be based on reasonable descriptions of the actual mechanisms of scale growth and degradation, and their dependence on time and temperature. Efforts are continuing to examine the methodology for calculating n , and to better model the observed oxidation behavior.

SUMMARY AND CONCLUSIONS

There exists a family of ODS alloys that have significantly higher-temperature capabilities, in terms of their combined creep strength and environmental resistance, than conventionally-strengthened alloys. This family includes ODS-FeCrAl alloys available from two commercial suppliers, as well as new ODS-Fe₃Al and ODS-FeCr-based alloys under active development. The combination of mechanical properties and resistance to aggressive, high-temperature environments found in these alloys require that they be given serious consideration for application in power generation processes of interest in the DOE's Vision 21 strategy. Properly applied, they could be used in components at the lower end of the temperature range where ceramics typically are thought to be required. Efforts have been initiated in this program to address the lack of detailed understanding of the behavior of ODS alloys in all phases of their use, including fabrication, service performance, life prediction, mode of failure, repair, and refurbishment, with the goal of developing a resource for designers wishing to incorporate ODS alloys into components.

REFERENCES

1. F. Starr, A. R. White, and B. Kazimierzak, in Materials for Advanced Power Engineering 1994, D. Coutsouradis, et al., Eds., (Kluwer Academic Publishers, 1994) pp. 1393-1412
2. D. J. Seery and J. Sangiovanni, "Engineering Development of a Coal-Fired High-Performance Power Generating System," Paper No. 1.7 in Proc. of the Advanced Coal-Based Power and Environmental Systems'98 Conference, Morgantown, West Virginia, July 21-23 1998, DOE/FETC-98/1072
3. I. G. Wright and J. Stringer, "Materials Issues for High-Temperature Components in Indirectly-Fired Cycles," ASME paper No. 97-GT-300, June 1997.
4. I. G. Wright, C. G. McKamey, E. K. Ohriner, and B. A. Pint, "Development of ODS-Fe₃Al Alloys," Paper No. 4.1 in Proc. 12th Annual Conference on Fossil Energy Materials, Knoxville, Tennessee, May 12-14 1998, CONF-980561, ORNL/FMP-98/1 (1998).
5. INCO Data Sheet PP-1: Physical Properties of INCOLOY alloy MA956.
6. Material Data Sheet ODS-Superalloy PM 2000, Metallwerk Plansee GmbH/Lechbruck, Feb. 1993.
7. IncoMAP Data Sheets: J-2 to J-4, Joining of Alloys MA 754, MA 956, MA 6000.
8. C. Brown, E. Verghese, *Neomet Limited, Stockport, England*, and D. Sporer, and R. Sellors, *Plansee*, "PM2000 Honeycomb Structures," Paper 98-GT-565, presented at the 43rd AMSE Gas Turbine and Aeroengine Technical Congress, Exposition, and Users Symposium, Stockholm, Sweden, June 2-5, 1998.
9. S. Holmstrom, M. Siren, L. Heikinheimo, P. Auerkari, J. Varmavuo, and R. Saarinen, "Performance of an Iron-Based ODS Alloy in a Boiler Environment," pp. 769-777 in Materials for Advanced Power Engineering 1998, J. LeCompte-Beckers, F. Schubert, and P. J. Ennis, Eds., Forschungszentrum Juelich Zentralbibliothek, Germany (1998).
10. N. S. Bornstein and D. J. Seery, "Progress in Using an ODS Alloy in the HITAF Air Heater, Pp. 10-11 in Materials and Components—a DOE-EPRI Newsletter, No. 136, Oct. 1998.
11. P. L. Threadgill, Friction Welding of an Fe₃Al-based ODS Alloy, Report No. ORNL/Sub/97-SX373/01, July 1998. See, also, B. J. Inkson and P. L. Threadgill, "Friction welding of Fe-40Al Grade 3 ODS alloy," *Mat. Sci. and Eng.*, **A258**, 313-318 (1998).
12. B. K. Kad, "Oxide-Dispersion-Strengthened Fe₃Al-Base Alloy Tubes," these proceedings.
13. W. J. Quadackers, K. Bongartz, F. Schubert, H. Schuster, in Materials for Advanced Power Engineering 1994, D. Coutsouradis, et al., Eds., (Kluwer Academic Publishers, 1994) pp. 1533-1542.
14. J. P. Wilbur, J. R. Nicholls, and M. J. Bennett, "Assessment of defects in alumina scales formed on ferritic ODS alloys," pp. 207-220 in Microscopy of Oxidation-3, S. B. Newcomb and J. A. Little, The Institute of Materials (1997).
15. G. J. Tatlock, University of Liverpool, private communication, 1998.

BISMUTH OXIDE SOLID ELECTROLYTE OXYGEN SEPARATION MEMBRANES

S. D. Nunn and E. A. Payzant
Oak Ridge National Laboratory
Oak Ridge, Tennessee

Test samples of baseline compositions of CaO-, SrO-, and BaO-doped Bi₂O₃ were prepared and analyzed using x-ray diffraction (XRD), differential thermal analysis (DTA), and neutron diffraction. In addition, the sample conductivity was measured as a function of temperature, which extended across the β_1 - β_2 phase transformation range. Mixed dopant compositions were also prepared in order to evaluate the structure, conductivity, and stability of the β -Bi₂O₃ phase. High temperature x-ray diffraction analysis and neutron diffraction analysis were performed to help characterize the β_1 - β_2 phase transformation in these compositions. Crystallographic structural changes, which occur during the transformation, were analyzed to help identify the mechanism that enhances the oxygen ion conductivity in the high-temperature phase. The samples that were tested for conductivity showed a range of peak conductivity levels. The enhanced conductivity that is associated with the β_2 - β_1 phase change was clearly observed in the tests. The measured transformation temperature for the individual compositions was consistent in XRD, DTA, and the conductivity data. Evidence of crystallographic texture was observed in both XRD and neutron diffraction.

INTRODUCTION

Doped β -Bi₂O₃ exhibits oxygen ion conductivity that is much higher than yttria-stabilized ZrO₂ at lower operating temperatures.¹ The conductivity increases by nearly ten-fold due to a subtle phase change in the temperature range of 565°C to 745°C, depending upon the dopant used to form the β -phase and the amount of dopant present.¹⁻³ At the transformation temperature, the low-temperature β_2 phase transforms to the high-temperature β_1 phase. The β -phase of Bi₂O₃ is formed by partial substitution for the bismuth atoms by divalent alkaline earth ions such as calcium, strontium, or barium. Divalent cation substitutions change the structure and properties of Bi₂O₃ through the creation of oxygen-site defects and lattice distortions due to ionic size effects. For such substitutions, it has been shown that the resulting single phase, randomly oriented ceramic is a very good ionic conductor with conductivities that are higher than well-known electrolytes such as zirconia at temperatures below 565°C. There is a subtle phase

transformation in the doped bismuth oxide at moderate temperatures above which the ionic conductivity is increased by an order of magnitude. In the binary oxide systems, the transformation temperature depends both on the amount and type of solute ion. In the present study, the lowest transformation temperatures (~565°C) were found with barium substitution and the highest (~745°C) with calcium substitution. The ionic conductivity of polycrystalline β -Bi₂O₃ can be further enhanced by the development of crystallographic orientation in the ceramic.⁴

EXPERIMENTAL PROCEDURE

Baseline compositions containing a single alkaline earth oxide dopant were prepared. The phase diagrams for the binary systems Bi₂O₃ – CaO, Bi₂O₃ – SrO, and Bi₂O₃ – BaO were examined to identify a single dopant level which would form β -Bi₂O₃ in all three systems.^{3, 5} A dopant level of 28 mol % was chosen for this study. Mixed dopant compositions were also prepared. The alkaline earth oxides were combined in pairs and added in equal molar amounts, again with a total of 28 mol % dopant. The compositions that were prepared and the starting raw materials are shown in Table 1. The starting powders were milled in a small attritor using 3-mm yttria-stabilized zirconia milling media and isopropyl alcohol as the solvent. After milling, the slurry was poured through a sieve into a glass tray and dried under low heat to evaporate the alcohol. The dried cake was crushed into loose powder using a mortar and pestle. The powder was then placed in a crucible and heated to 625°C for 12 hr. to decompose the carbonate raw materials and to react the constituents to form the desired compounds. The calcined material was again crushed to form a loose powder. Samples were fabricated by uniaxially pressing the calcined powder into disks and bars. The pressed shapes were then sintered at 700°C for 48 hr. to fully react the constituents and to densify the samples.

Table 1. Doped bismuth oxide sample compositions.

Composition	Raw Materials, wt. %			
	Bi ₂ O ₃	CaCO ₃	SrCO ₃	BaCO ₃
Bi ₂ O ₃ -28CaO	92.29	7.71		
Bi ₂ O ₃ -28SrO	89.03		10.97	
Bi ₂ O ₃ -28BaO	85.86			14.14
Bi ₂ O ₃ -14CaO-14SrO	90.66	3.86	5.49	
Bi ₂ O ₃ -14CaO-14BaO	89.08	3.86		7.07
Bi ₂ O ₃ -14SrO-14BaO	87.45		5.49	7.07

Powder and sintered samples were examined by x-ray diffraction analysis (XRD) to determine the phases present. Both room temperature and elevated temperature measurements were made using Cu $K\alpha$ radiation. Selected samples were cycled through the phase transformation temperature to examine the reversibility of the phase change. Selected samples were cycled through the phase transformation temperature to examine the reversibility of the phase change in air. Preferred orientation was examined by X-ray pole figure analysis.

Neutron diffraction measurements were made at Oak Ridge National Laboratory's High Flux Isotope Reactor (HFIR). Diffraction patterns were recorded at room temperature and at temperatures below and above the $\beta_2 - \beta_1$ phase transformation temperature of the individual compounds in air. Since no facility existed at HFIR to conduct these high temperature experiments in air, such an apparatus was assembled, tested, and successfully utilized on the HB-4 high-resolution neutron powder diffractometer.

Differential thermal analysis (DTA) measurements were made on a small fragment of sintered ceramic. Data were recorded while the samples were heated from room temperature to 800°C at a rate of 5°C/min. Data were also recorded on cooling from the peak temperature, again at a rate of 5°C/min.

Conductivity measurements were done by Pacific Northwest National Laboratory which has established facilities for accomplishing these tests. Small bars, which measured approximately 25mm long and 3mm square, were prepared for conductivity measurements. The DC 4-point conductivity of the sample bars was measured over a temperature range from ambient to 700-900°C, depending on the composition.

RESULTS AND DISCUSSION

X-ray diffraction was used to evaluate the processed. All of the compositions formed a single-phase compound (β -Bi₂O₃) after calcining and sintering. A typical x-ray diffraction pattern for the β -Bi₂O phase is shown in Fig. 1. The lattice parameters of the compounds varied with dopant addition due to the differences in the ionic radii. XRD data taken at high temperatures showed the large change in the c-axis dimension that is associated with the β_2 - β_1 phase transformation. Selected samples were examined at high temperature over a period of days to evaluate the stability of the phase and of the phase transformation. An example of the high temperature XRD data that was used to characterize the phase change is shown in Figs. 2 and 3. This transformation was also observed in the DTA measurements, which showed hysteresis in the transformation temperature. A sample of the DTA characterization is shown in Fig. 4. The β_1 -to- β_2 phase transformation (cooling) occurred at a lower temperature than the β_2 -to- β_1 transformation (heating). The phase transformation temperatures varied with sample composition and are tabulated in Table 2.

Table 2. Phase transformation temperatures determined by DTA.

Composition	Transformation Temperature, °C		Temperature Difference, °C
	Heating	Cooling	
Bi ₂ O ₃ -28CaO	750.8	725.3	25.5
Bi ₂ O ₃ -28SrO	708.0	674.2	33.8
Bi ₂ O ₃ -28BaO	565.0	518.8	46.2
Bi ₂ O ₃ -14CaO-14SrO	730.8	707.8	23.0
Bi ₂ O ₃ -14CaO-14BaO	655.2	624.4	30.8
Bi ₂ O ₃ -14SrO-14BaO	637.8	600.0	37.8

Neutron diffraction data taken at high temperatures is being used to develop crystallographic models to understand the structural mechanism behind the high anion conductivity seen in the high temperature β -Bi₂O₃ phase. Neutron diffraction permits much greater resolution of the oxygen sub-lattice structure, which is felt to be critical to the understanding of the dramatic increase in oxygen ion conductivity. The Bi₂O₃-14CaO-14SrO sample was examined in the greatest detail. The General Structure Analysis Software (GSAS) program was used to locate the anion and cation sites, to determine the bond lengths, and to determine the changes in site occupancy with temperature. The preliminary crystallographic structure analysis results are shown in Fig. 5. The analysis is ongoing, but the preliminary finding is that above the phase transformation temperature a previously empty oxygen site becomes partially occupied. This increases the number of mobile anion vacancies elsewhere in the structure and improves the overall ionic conductivity. The vacancies appear to cluster around the divalent cation dopant sites. The bond lengths to these sites are somewhat fixed so that the cation size plays a role in the degree of bonding.

Both neutron diffraction and x-ray diffraction measurements on the sintered samples showed very different relative peak intensities compared to powder samples. This is attributed to a high degree of preferred orientation of crystallites in the ceramics. Although in the case of x-rays this effect might only be due to surface texture, the neutron diffraction method demonstrated that the texture was a bulk phenomenon rather than simply a surface effect. An example of the strong texture that was observed is shown in the x-ray pole figure diagrams in Fig. 6 for the Bi₂O₃-14CaO-14SrO composition. These results indicate that the material may be readily oriented with appropriate processing in order to align the more conductive crystallographic directions (normal to the c-axis) in the direction of intended oxygen flow.

The results of the preliminary conductivity measurements are shown in Fig. 7. The plots clearly show the step increase in conductivity above the $\beta_2 - \beta_1$ phase transformation temperature. The data also indicate that the conductivity of the samples with mixed alkaline earth oxide dopants is higher than that of the samples containing a single dopant oxide.

CONCLUSIONS

Test samples of baseline compositions of CaO-, SrO-, and BaO-doped Bi₂O₃ were prepared and analyzed using x-ray diffraction (XRD), differential thermal analysis (DTA), and neutron diffraction. The sample conductivity was measured as a function of temperature, which extended across the $\beta_1 - \beta_2$ phase transformation range. Mixed dopant compositions were prepared in order to evaluate the effect on the structure, conductivity, and stability of the β -Bi₂O₃ phase in these compounds. High temperature x-ray diffraction analysis and neutron diffraction analysis were performed to help characterize the $\beta_1 - \beta_2$ phase transformation in these compositions. Crystallographic structural changes, which occur during the transformation, were analyzed to help identify the mechanism that enhances the oxygen ion conductivity in the high-temperature phase. The samples that were tested for conductivity showed a range of peak conductivity levels depending upon the composition. The enhanced conductivity that is associated with the $\beta_2 - \beta_1$ phase change was clearly observed in the tests. The measured transformation temperature for the individual compositions was consistent in XRD, DTA, and the conductivity data. Evidence of crystallographic texture was observed in both XRD and neutron diffraction.

ACKNOWLEDGEMENTS

We would like to thank R. A. Peascoe for her assistance in the x-ray and neutron diffraction analyses and B. C. Chakoumakos for assistance in arranging neutron beam time and help with data collection.

REFERENCES

1. T. Takahashi, H. Iwahara, and Y. Nagai, "High Oxide Ion conduction in Sintered Bi₂O₃ Containing SrO, CaO or La₂O₃," *J. Appl. Electrochem.* **2** 97-104 (1972).
2. J. C. Boivin and D. J. Thomas, "Structural Investigations On Bismuth-Based Mixed Oxides," *Solid State Ionics* **3/4** 457-462 (1981).
3. P. Conflant, J. C. Boivin, G. Nowogrocki, and D. Thomas, "High Temperature X-ray Structural Study of the Anionic Conductor Bi_{0.844}Ba_{0.156}O_{1.422}," *Solid State Ionics* **9&10** 925-928 (1983).
4. J. C. Boivin and D. J. Thomas, "Crystal Chemistry and Electrical Properties of Bismuth-Based Mixed Oxides," *Solid State Ionics* **5** 523-526 (1981).
5. R. S. Roth, N. M. Hwang, C. J. Rawn, B. P. Burton, and J. J. Ritter, "Phase Equilibria in the Systems CaO-CuO and CaO- Bi₂O₃," *J. Am. Ceram. Soc.*, **74** [9] 2148-51 (1991).

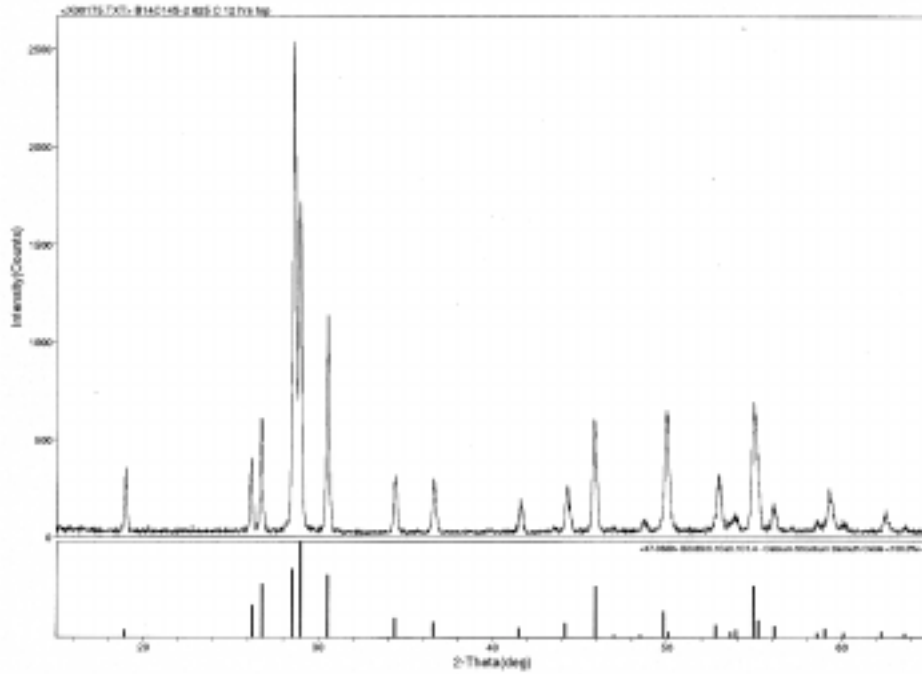


Fig. 1. X-ray diffraction pattern of sintered Bi_2O_3 -14CaO-14SrO showing single phase β - Bi_2O_3 .

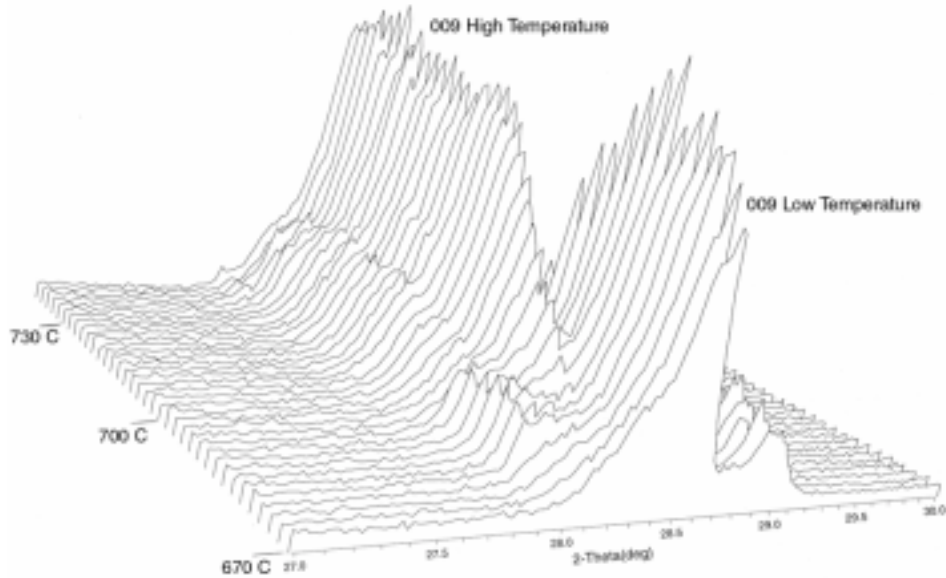


Fig. 2. High temperature x-ray diffraction patterns of the 009 diffraction peak for the composition Bi_2O_3 -14CaO-14SrO showing the shift in the peak position that occurs with the transformation from the low temperature β -phase to the high temperature β -phase.

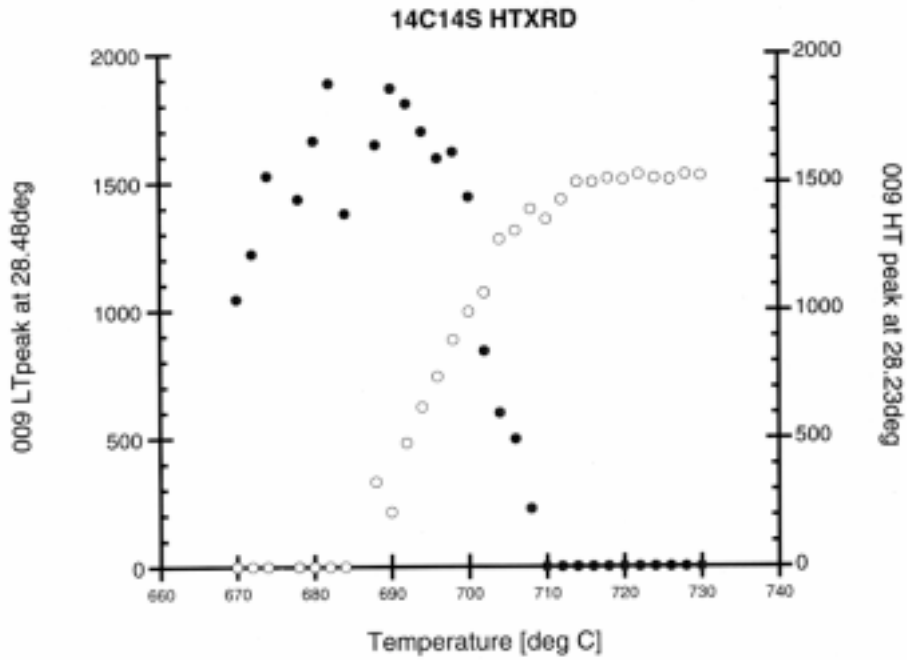


Fig. 3. Plot of the 009 diffraction peak intensity of composition $\text{Bi}_2\text{O}_3\text{-14CaO-14SrO}$ as a function of temperature. The phase transition starts at about 685C and is complete at 710C.

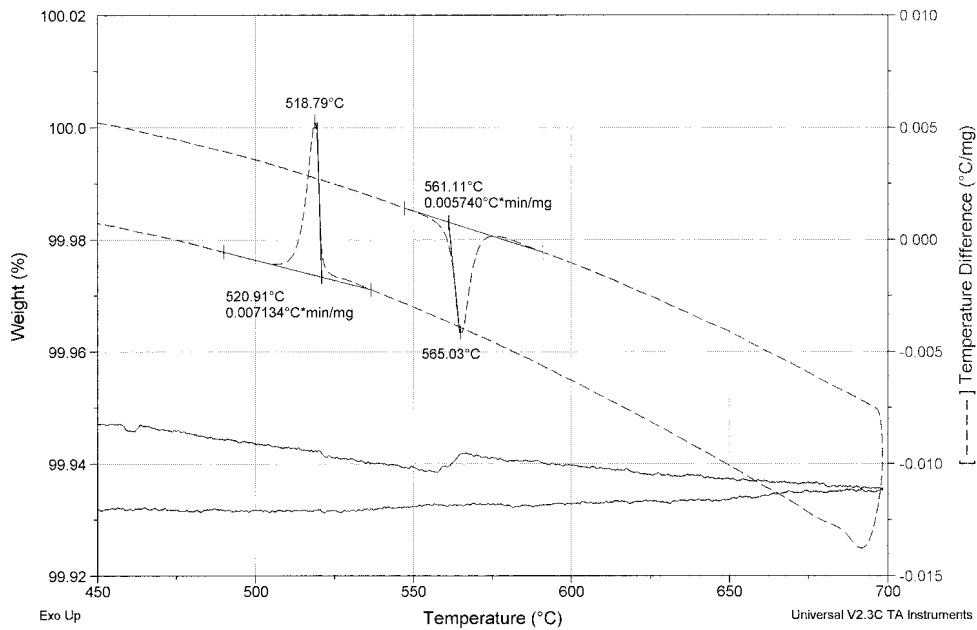


Fig. 4. Differential thermal analysis plot for $\text{Bi}_2\text{O}_3\text{-28BaO}$ showing the reversible $\beta_2 - \beta_1$ phase transformation. The endothermic transformation on heating occurs at a higher temperature than the exothermic transformation on cooling.

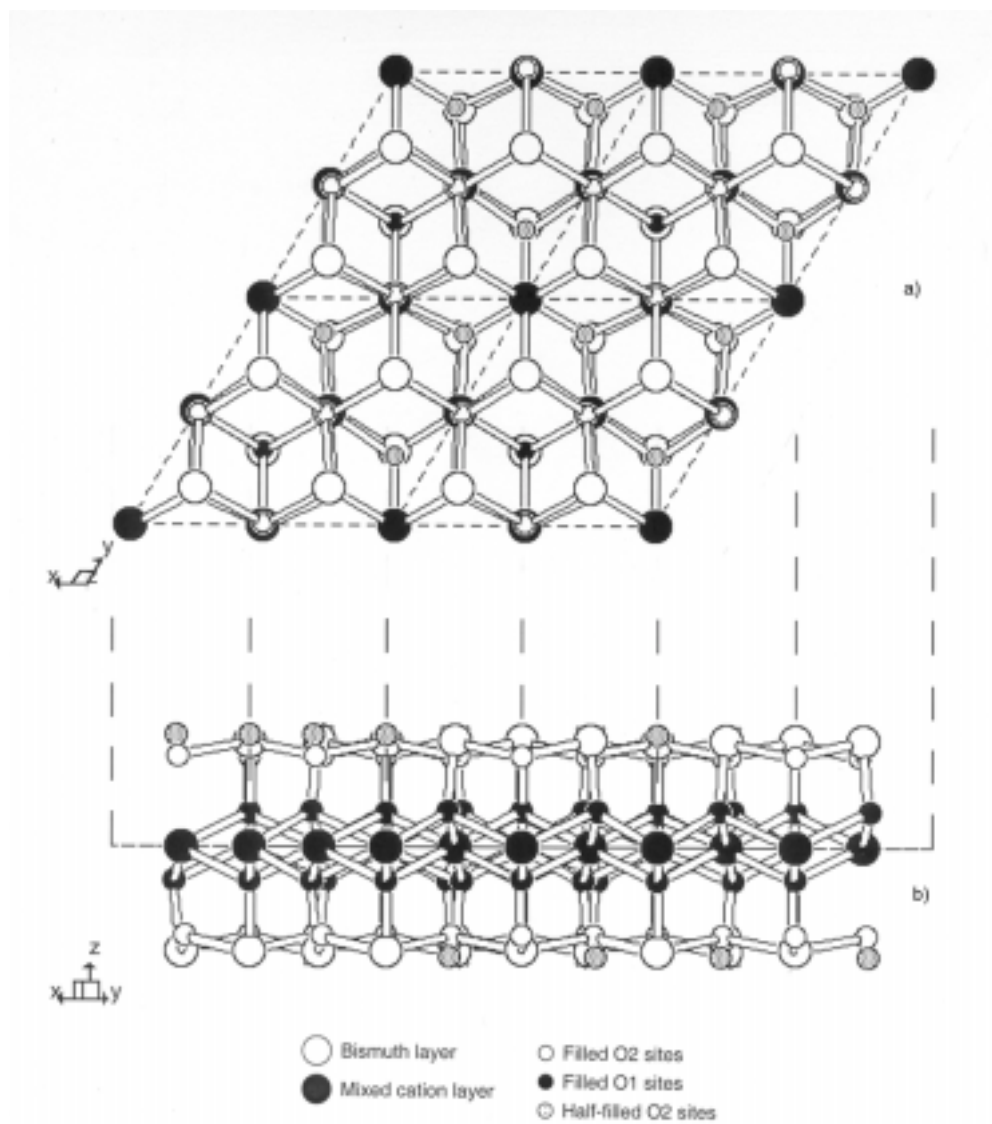


Fig. 5. Preliminary representation of the substituted beta bismuth oxide structure that is composed of offset layers stacked along the z-axis. a) Viewed in the x-y plane, a doped bismuth oxide/alkaline earth oxide sheet (represented by the black spheres) forms the central framework of each layer. b) Z-axis view.

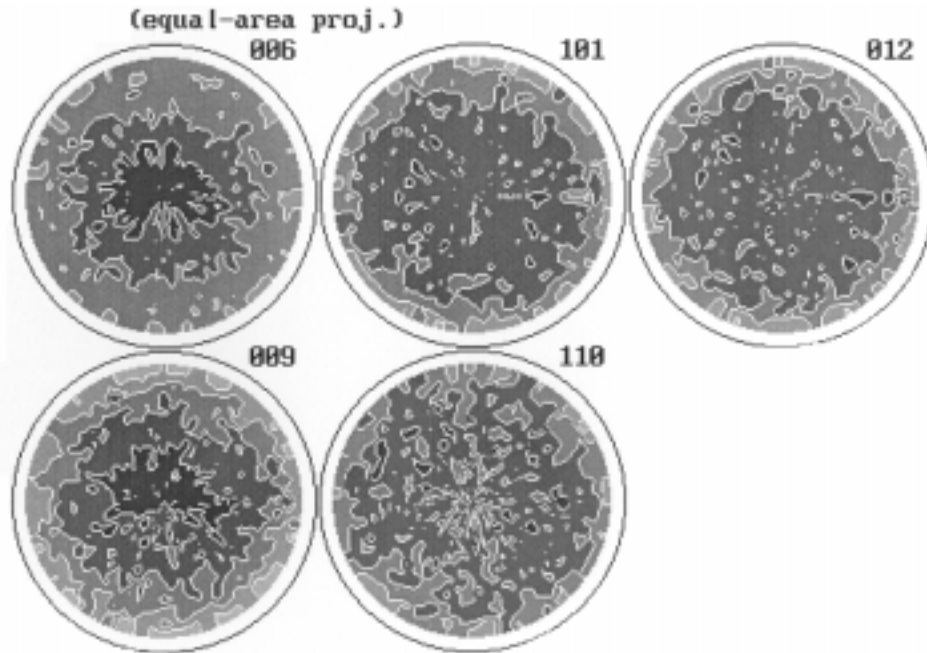


Fig. 6. X-ray pole figure analysis of composition Bi_2O_3 -14CaO-14SrO showing equal-area projections for several diffraction peaks. Note the strong 'fiber texture' indicated for the $00l$ peaks.

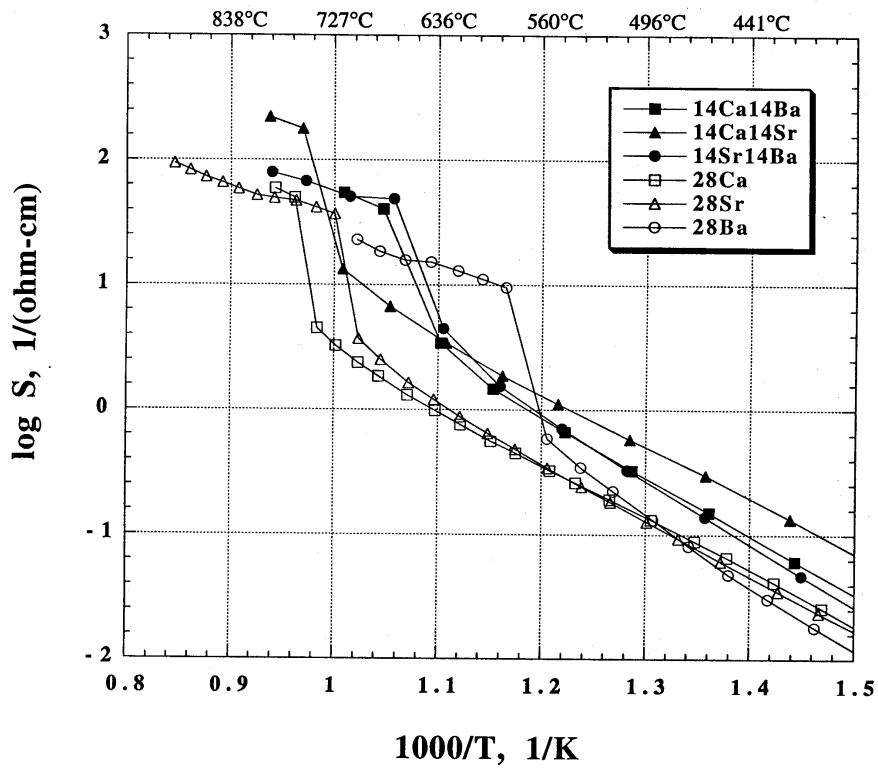


Fig. 7. Plots of the measured conductivity versus temperature for the different doped β - Bi_2O_3 compositions.

PROCESSING AND PROPERTIES OF MOLYBDENUM SILICIDE INTERMETALLICS CONTAINING BORON

J. H. Schneibel and C. A. Carmichael

Oak Ridge National Laboratory

P. O. Box 2008

Oak Ridge, TN 37831

INTRODUCTION

The objective of this task is to develop new-generation corrosion-resistant Mo-Si alloys for use as hot components in advanced fossil energy combustion and conversion systems. The successful development of Mo-Si alloys is expected to improve the thermal efficiency and performance of fossil energy conversion systems through an increased operating temperature, and to increase the service life of hot components exposed to corrosive environments at temperatures as high as 1600°C. While MoSi₂ is highly oxidation resistant at elevated temperatures, it is extremely brittle at ambient temperatures and has poor creep resistance at elevated temperatures. Molybdenum compounds with lower Si contents, such as Mo₅Si₃ or Mo₃Si, are potentially less brittle and exhibit higher strengths at elevated temperatures, but do not have the required oxidation resistance. Boron additions appear to alleviate the oxidation problem. As early as 1957, Nowotny et al.¹ pointed out that boron-containing silicides possess high oxidation resistance due to the formation of borosilicate glass on their surface. Based on Nowotny et al.'s work, boron-containing molybdenum silicides based on Mo₅Si₃ were recently developed at Ames Laboratory.²⁻⁴ These silicides consist of approximately 25 vol.% Mo₃Si, 50 vol.% Mo₅Si₃ (T1), and 25 vol.% Mo₅SiB₂ (T2). A typical composition, which is indicated in Fig. 1, is Mo-26.7Si-7.3B, at. % (unless indicated otherwise, compositions will be given in at. %). This alloy has an oxidation resistance comparable to that of MoSi₂, and it does not appear to show catastrophic oxidation ("pest reaction") at intermediate temperatures such as 800°C.⁴ Also, its creep strength is superior to that of MoSi₂. Since these types of alloys consist exclusively of brittle phases, they tend to be brittle. Another class of Mo-Si-B alloys of interest are those developed by Berczik,^{5,6} which consist of α-Mo, Mo₃Si, and Mo₅SiB₂ (T2). These types of alloys have also been studied recently by Perepezko and co-workers.⁷⁻⁹ While their

oxidation resistance is inferior to that of the Mo_3Si -T1-T2 alloys, it is likely that it can be improved by minimizing the α -Mo volume fraction, by suitable alloying additions, and/or by silicide coatings. The main advantage of the Mo- Mo_3Si -T2 alloys is that they do not consist exclusively of brittle phases. As shown in our previous annual report,¹⁰ these alloys have reasonably high fracture toughnesses on the order of $10 \text{ MPa m}^{1/2}$. The present report focuses on the processing of these alloys to achieve different microstructures, and on their mechanical properties.

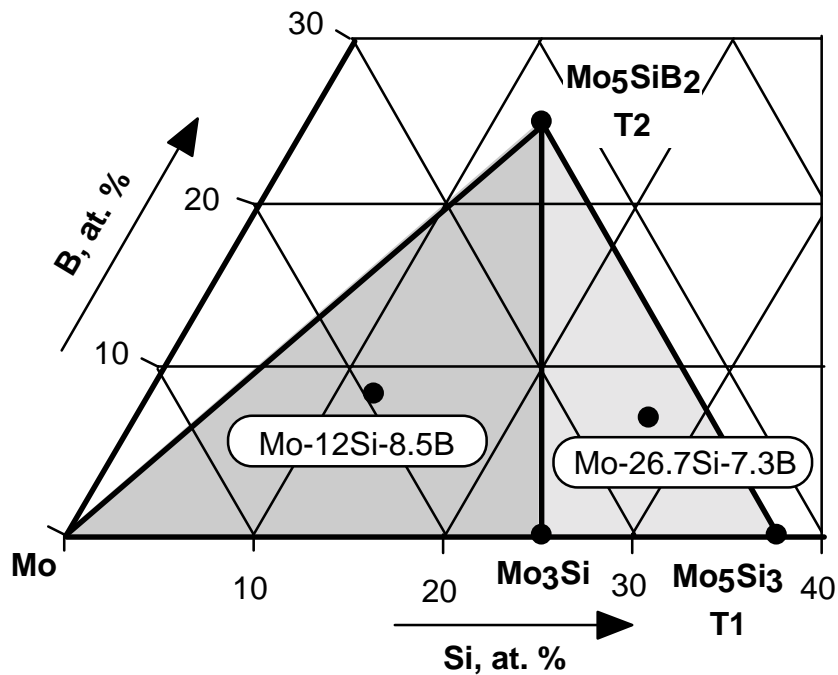


Figure 1: Schematic section of the ternary Mo-Si-B phase diagram showing phases and alloy compositions of interest.

RESULTS AND DISCUSSION

Extrusion of Mo-Si-B Alloys

Mo-Si-B alloys were arc-melted and drop-cast into 25 mm diameter molds (Table 1). One alloy (#522, Mo-14Si-10B) was cooled very slowly by dropping it into a MgO mold inserted into a highly insulating fire brick. Four cast pieces with random lengths and a total length of 130 mm were inserted into a Mo can with an outer diameter of 50 mm. The can was then sealed in vacuum by electron beam welding.

Extrusion with a carbonaceous lubricant at 1600°C through a zirconia-coated H13 steel die with an inner diameter of 25 mm proceeded without difficulties. The extruded material was however severely cracked and unusable. Another alloy (#531, Mo-12Si-8.5B) was prepared by drop-casting into a 25 mm diam. Cu chill mold. Extrusion at 1450°C was aborted because the load capacity of the press was reached after some Mo near the nose of the can was extruded. A second extrusion attempt with a glass lubricant at 1550°C was successful in the sense that the material exited the die. However, the Mo-Si-B alloy was again severely cracked. Research carried out at Universal Energy Systems (UES) in Dayton, Ohio, is in qualitative agreement with our results¹¹. In this work, a silicide with the composition Mo-12Si-12B was extruded at 1800°C. The resulting material was also heavily cracked. Clearly, the extrusion of cast Mo-Si-B alloys containing substantial volume fractions of Mo₃Si and Mo₅SiB₂ is difficult. For the time being, extrusion is therefore not being pursued.

Table 1. Summary of extrusion experiments (area reduction 4:1) with Mo-Si-B alloys

Specimen Number	Composition, at. %	Casting conditions	Extrusion conditions and resulting structures
#522	Mo-14Si-10B	Ingot very slowly cooled (MgO mold in firebrick)	Extrusion at 1600°C: severe cracking of alloy
#531	Mo-12Si-8.5B	Ingot drop cast into 25 mm diam. Cu chill mold	Extrusion at 1450°C incomplete (load capacity of press reached)
#531	Mo-12Si-8.5B	Ingot drop cast into 25 mm diam. Cu chill mold	Extrusion at 1550°C: severe cracking of alloy

Cast and annealed Mo-12Si-8.5B (at. %)

Mo-12Si-8.5B was cast and annealed for 1 day at 1600°C in vacuum. The α -Mo formed isolated particles in a brittle matrix of Mo₃Si and T2. Based on the molar volumes of Mo, Mo₃Si, and T2, and assuming pure Mo (i.e., Mo without Si in solid solution), as well as stoichiometric compositions for the compounds, the volume fractions of these phases were estimated to be 38, 32, and 30%, respectively (see Table 2). Three-point flexure strengths (specimen cross section 3x4 mm, span 20 mm) were determined at 1200°C in air. The cross head speed was 10 μ m/s. In Table 3 these results are compared to data obtained earlier at different temperatures¹⁰. The significantly higher strength at 500°C, as compared to room temperature, may be due to the improved ductility, and the associated reduction in notch sensitivity, of the α -Mo phase at 500°C. The alloy retains a reasonably high strength at 1200°C showing its potential as a high temperature structural material.

Table 2. Estimated volume fractions in Mo-12Si-8.5B (at. %)

Composition	Molar Volume, cm ³	Molar Mass, g	Density, Mg/m ³	Volume Fraction, %
Mo	9.3868	95.94	10.22	38.4
Mo _{0.75} Si _{0.25}	8.8027	78.976	8.97	31.9
Mo _{0.625} Si _{0.125} B _{0.25} (T2)	7.5084	66.176	8.81	29.8

Table 3. Three-point flexure strengths of cast and annealed (1 day/1600°C/vacuum) Mo-12Si-8.5B (at. %)

Specimen Number	Temp, °C	Flexure Strength, MPa
531-A1#1	20	484
531-A1#2	20	539
531-A2#1	500	722
531-A2#2	500	697
531-A3#4	1200	428
531-A3#7	1200	553

Room temperature fracture toughnesses were measured by determining the energy dissipated during the controlled 3-point fracture of chevron-notched specimens. Similar to the flexure specimens, a cross section of 3x4 mm, a span of 20 mm, and a crosshead speed of 10 $\mu\text{m/s}$ were employed. During the testing, crack nucleation started at the apex of a triangle with a height of about 2 mm and a base of about 3 mm. The fracture toughness was determined as $K_q=(G \times E')^{1/2}$, where $G=W/A$, W is the energy absorbed during the test, A is the area of the triangle through which the crack propagated, $E'=E/(1-\nu^2)$ is the plane strain Young's modulus and ν is Poisson's ratio. The ultrasonically determined elastic constants were $E=327$ GPa and $\nu=0.29$ (see previous annual report¹⁰). The 1200°C fracture toughness evaluated in this manner is shown in Table 4 and compared to previous results for lower temperatures. It is

considerably higher than that at room temperature or 500°C. This increase may be due to the high ductility of α -Mo at 1200°C.

Table 4. Fracture toughness of Mo-12Si-8.5B (at. %) alloys annealed for 1 day at 1600°C in vacuum

Specimen Number	Temp., °C	A, mm ²	W, mJ	G, J/m ²	K _q , MPa m ^{1/2}
531-A1#3	20	2.94	0.6800	231.0	9.1
531-A1#4	20	2.88	0.7750	269.5	9.8
531-A2#3	500	2.62	0.7087	271.0	9.8
531-A2#4	500	2.93	1.0599	361.7	11.4
531-A3#5	1200	2.73	3.582	1312	21.6
531-A3#8	1200	2.73	2.63	965	18.5

Powdermetallurgical Mo-Si-B alloys

A powdermetallurgical (PM) specimen with the nominal composition Mo-12Si-8.5B (#544) was prepared in the following manner: arc-cast ingots of Mo₃Si and T2 were pulverized into –100 mesh (< 150 μ m) powders. These powders were mixed with 2-8 μ m Mo powder and sealed in an evacuated Nb can, which was subsequently hot isostatically pressed (HIPed) for 1h at 1650°C and 200 MPa. A metallographic specimen was prepared and etched with Murakami's etch. The back-scattered scanning electron micrograph (SEM) of this specimen is shown in Fig. 2 and illustrates that the microstructure consisted indeed of intermetallic particles embedded in an α -Mo matrix. The dark spots in the α -Mo are SiO₂ inclusions. No compositional analysis was performed for this particular micrograph, but the brightest phase with the highest mass contrast is clearly α -Mo, and T2 can be distinguished from Mo₃Si by the etching contrast at the periphery of T2. The large and brittle intermetallic particles were often cracked.

Table 5 shows the room temperature flexure strength and fracture toughness of PM Mo-12Si-8.5B (#544). Due to the high density of cracks it is not surprising that its strength is lower than that of cast and annealed material with the same nominal composition (see Table 3). Its fracture toughness, on the other hand, is much higher than that of the cast and annealed material. There are two reasons for this. First, the microstructure consists of a continuous α -Mo matrix instead of individual α -Mo particles. Second, the microstructure in the PM material is much coarser than that in the cast and annealed alloys,

and it is well known that coarse microstructures result in higher ductile-phase toughening than fine microstructures.¹² The arrowed ridge in Fig. 3 shows that the α -Mo on a room temperature fracture surface shows some evidence for plastic deformation (although not as clearly as

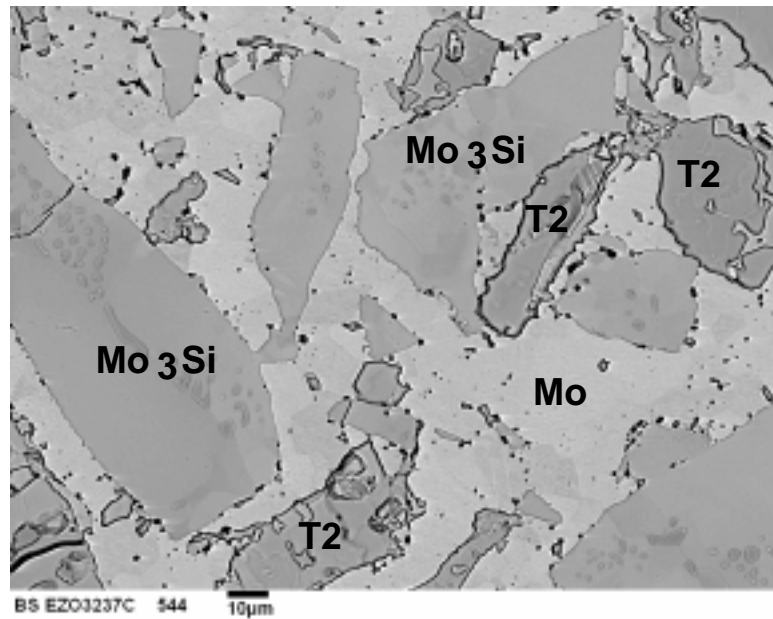


Figure 2: Back scattered SEM of polished and etched section of PM specimen #544 (Mo-12Si-8.5B) illustrating Mo_3Si and T2 particles in a matrix of α -Mo.

Table 5. Mechanical properties of PM specimen #544 with the nominal composition Mo-12Si-8.5B (at. %)

Specimen Number	Room Temperature Flexure Strength, MPa	Room Temperature Fracture Toughness, $\text{MPa}^{\text{ml}/2}$
544#1	384	
544#1	376	
544#2	412	
544#2	408	
544#3		14.0
544#4		15.6

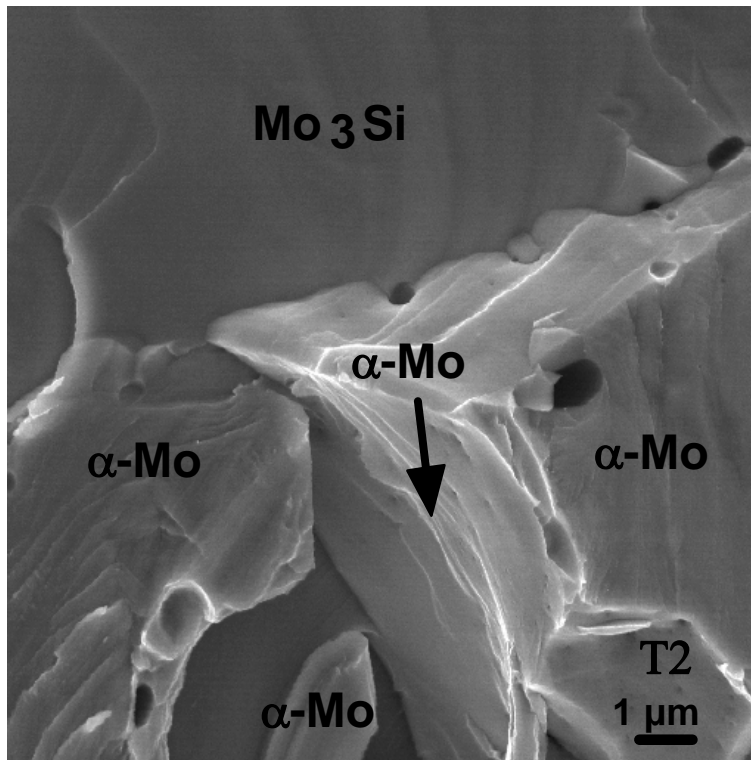


Figure 3: Room temperature fracture surface of PM Mo-12Si-8.5B (#544).

the corresponding cast and annealed alloys – see previous quarterly report¹⁰). The PM processing did therefore not unduely embrittle the Mo.

The microstructure of PM specimen #544 needs improvement in two ways. First, the cracking of the intermetallic particles needs to be avoided. Second, the α -Mo volume fraction needs to be further reduced in order to improve the oxidation resistance. The first point was addressed by using finer Mo_3Si and T2 particles. In specimen #571, arc-cast and annealed Mo_3Si and T2 ingots were pulverized and screened to $-635/+325$ mesh ($20\ \mu\text{m} < \text{diameter} < 45\ \mu\text{m}$). The second point was addressed by using a relatively small volume fraction of Mo powder (size range 2-8 μm). The corresponding powder mixture was hot pressed in vacuum for 2 hours at 1600°C. Figure 4 shows an SEM micrograph of a polished and etched section of the resulting coupon. The dark spots in the micrograph are again SiO_2 inclusions. In addition to the large intermetallic particles, there are also large Mo particles. It appears, however, that the Mo is often mixed with very fine intermetallic particles. Fracture toughness measurements have not yet been made. Therefore, the contribution of this mixture to ductile phase toughening is not known as

yet. The fine intermetallic particles may very well reduce the ductility of the α -Mo, thus reducing its contribution to ductile phase toughening. Future processing experiments will focus on removing the fine intermetallic particles in order to obtain improved microstructures.

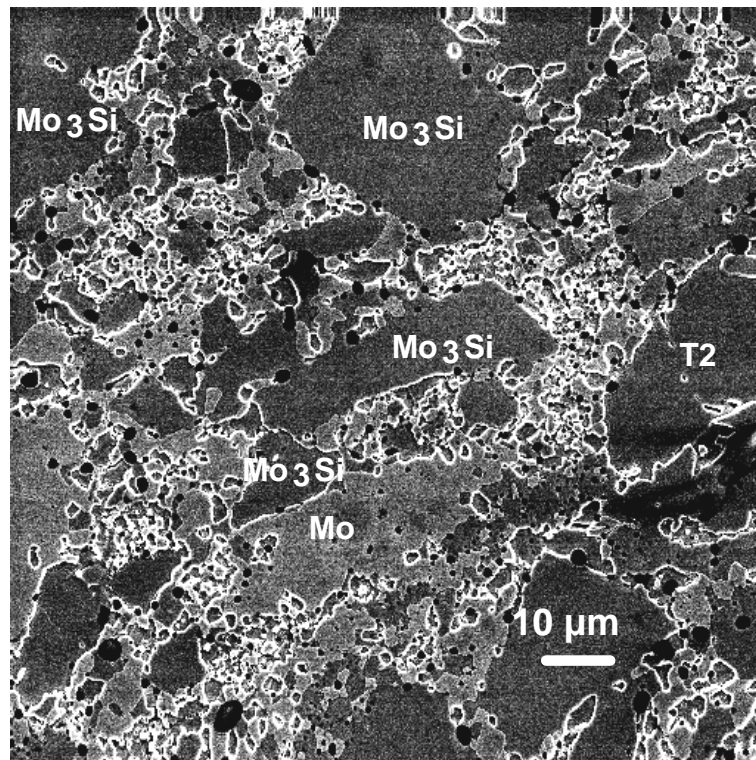


Figure 4: SEM micrograph of polished and etched alloy #571. The volume ratios were Mo:Mo₃Si:T2=18:41:41 (wt ratio 20:40:40).

ACKNOWLEDGMENTS

This research was sponsored by the Office of Fossil Energy, Advanced Research and Technology Development (AR&TD) Materials Program, U.S. Department of Energy, under contract DE-AC05-96OR22464 with Lockheed Martin Energy Research Corporation. Larry R. Walker's help in providing backscattered SEM's is appreciated.

REFERENCES

1. H. Nowotny, E. Kimakopoulou, and H. Kudielka, "Untersuchungen in den Dreistoffsystemen: Molybdän-Silizium-Bor, Wolfram-Silizium-Bor und in dem System: $\text{VSi}_2\text{-TaSi}_2$," Mh. Chem. 88 (1957) 180.
2. A. J. Thom, M. K. Meyer, Y. Kim, and M. Akinc, "Evaluation of $\text{A}_5\text{Si}_3\text{Z}_x$ Intermetallics for Use as High Temperature Structural Materials," in "Processing and Fabrication of Advanced Materials III, V. A. Ravi et al., eds., TMS, 1994, p. 413.
3. M. K. Meyer, M. J. Kramer, and M. Akinca [sic], "Compressive Creep Behavior of Mo_5Si_3 with the Addition of Boron," Intermetallics 4 (1996) 273.
4. M. Meyer, M. Kramer, and M. Akinc, "Boron-Doped Molybdenum Silicides," Adv. Mater. 8 (1996) 85.
5. D. M. Berczik, United States Patent 5,595,616 (1997), "Method for enhancing the oxidation resistance of a molybdenum alloy, and a method of making a molybdenum alloy."
6. D. M. Berczik, United States Patent 5,693,156 (1997) "Oxidation Resistant Molybdenum Alloy."
7. J. H. Perepezko, C. A. Nunes, S.-H. Yi, and D. J. Thoma, "Phase Stability in Processing of High Temperature Intermetallic Alloys," MRS Symposium Proceedings Vol. 460, C. C. Koch et al., eds., 1996, pp. 3-14
8. C. A. Nunes, R. Sakidja, and J. H. Perepezko, "Phase Stability in High Temperature Mo-rich Mo-B-Si Alloys, in *Structural Intermetallics 1997*, eds. M. V. Nathal et al., TMS, 1997, pp. 831-839.
9. R. Sakidja, H. Sieber, and J. H. Perepezko, "Microstructural Development of Mo-rich Mo-B-Si Alloys, to be published in proceedings of "Molybdenum & Molybdenum Alloys," San Antonio, TX, TMS, 1998.
10. J. H. Schneibel, C. T. Liu, L. Heatherly, Jr., and C. A. Carmichael, "Processing and Properties of Molybdenum Silicide Intermetallics containing Boron," Proc. 12th Annual Conference on Fossil Energy Materials, R. R. Judkins, ed., Knoxville, TN, 1998.
11. M. G. Mendiratta, personal communication, April 28, 1999.
12. M. F. Ashby, F. J. Blunt, and M. Bannister. "Flow Characteristics of Highly Constrained Metal Wires," Acta Metall. 37 (1989) 1847-1857.

FABRICATION OF TEST TUBES FOR COAL ASH CORROSION TESTING

V. K. Sikka, R. W. Swindeman, I. G. Wright, R. R. Judkins, and R. Johnson*
Metals and Ceramics Division
Oak Ridge National Laboratory
P.O. Box 2008
Oak Ridge, Tennessee 37831

*Pacific Northwest National Laboratory
Richland, Washington 99352

INTRODUCTION

Babcock & Wilcox (B&W) prepared a plan⁽¹⁾ to corrosion test perspective superheater alloys for advanced supercritical boilers through the installation of test sections at Ohio Edison Power, Niles Plant. Figure 1 shows the configuration of three superheater test sections. One test section is to be removed and examined after one year of exposure, a second one after three years, and a third after five years. For the steam inlet to outlet, the tubing of each test section makes four horizontal passes across the furnace. The flue gas temperature in this area is about 2100°F (1150°C). Steam enters the bottom of each section at approximately 615°F (325°C) and leaves the top at approximately 1000°F (538°C). On its first traverse across the furnace, the tubing's external temperature is relatively low [970 to 1070°F (520 to 575°C)], so no coal ash corrosion is expected. By the middle of the third pass where the alloy test segments begin, the surface metal temperature is about 1200°F (650°C), and the corrosion rates are expected to be substantial.

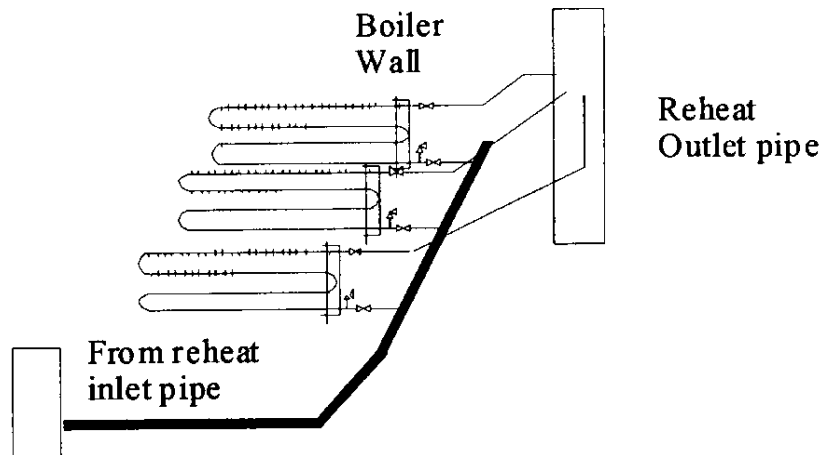


Fig. 1. Configuration of three proposed superheater test sections by Babcock & Wilcox for installation into Ohio Edison Power, Niles Plant for corrosion testing of perspective superheater alloys.

The drawing in Fig. 2 shows the numbered test sections to identify the alloys to be tested: 1 – Incoclad, 2 – Thermie, 3 – 310HCbN, 4 – 310 Ta, 5 – 800 mod., 6 – Save 25, 7 – HR120, 8 – NF709, 9 – Fe₃Al/304H, and 10 – 347HFG. ERNiCrMo-3 weld filler metal (similar to Inconel 625 chemistry) was chosen to be the filler metal for welding all of the test segments. All of the test sections have to be 2.5-in. OD by 0.4-in. wall and approximately 6 in. in length. The exception to the above sizes was Incoclad, which was 0.266-in. wall thickness. The balance of the loop to which the test sections are connected is type 310H stainless steel with a wall thickness of 0.220 in.

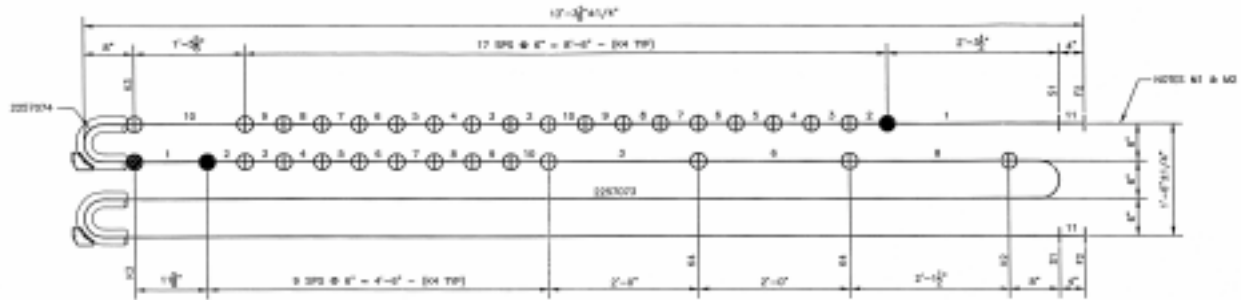


Fig. 2. Drawing showing the test sections of ten different alloys proposed for corrosion testing.

Ohio Edison Power, Niles Plant is burning an Ohio coal containing approximately 3.4% S (dry basis) and approximately 0.4% alkali. The coal causes chronic coal ash corrosion of the unit's superheater tubing.

Four of the ten materials chosen for the coal ash corrosion were to be supplied by the Oak Ridge National Laboratory (ORNL) and one of the four required coating processes by Pacific Northwest National Laboratory (PNNL). The purpose of this paper is to describe the details of the tube samples fabricated at ORNL and PNNL. The paper also includes chemical analysis and microstructure of the fabricated tube sections.

MATERIALS TO BE SUPPLIED BY ORNL AND PNNL

The four materials to be supplied by ORNL and PNNL include:

1. Type 304H coated with ORNL-developed Fe_3Al alloy FAS. The coating was to be applied at PNNL by the electrospark discharge process.
2. 310 stainless steel + Ta, which is an ORNL-developed high-strength type 310 stainless steel.
3. Modified 800H, which is an ORNL modified version of alloy 800H developed by Inco Alloys International, Inc. (Inco) [Huntington, West Virginia].
4. Thermie, a nickel-based alloy developed by Inco.

In each case, the materials were to be supplied in the form of 2.5-in.-OD \times 0.4-in.-wall \times 6-in.-long tube sections. At least eight to ten pieces of each material were required. The fabrication details of these tube sections are given below.

ITEM 1: TYPE 304H COATED WITH ORNL-DEVELOPED Fe_3Al ALLOY FAS AT PNNL

For this item, type 304H tubes of 2.5-in. OD by 0.4-in. wall was procured from a commercial vendor, Consolidated Pipe & Supply. Although supplied by an American vendor, the tube was produced in Japan by Kobe Special Tube Company, Chofu-Kita Plant. The tube was manufactured to ASTM A51-96 specifications. The tube was hot-finished and annealed at 2012°F (1100°C) for 5 min followed by quenching in water. The incoming tube was checked for its chemical analysis, which is compared with the vendor and specifications in Table 1. The vendor's analysis showed that it met the ASTM specification, and the check analysis confirmed the vendor's analysis.

Table 1. Comparison of specification with vendor and actual analyses of type 304H stainless steel

Element	Weight percent		
	Specification	Vendor	Actual
C	0.08 (max)	0.05	0.054
Mn	2.00 (max)	1.81	1.76
P	0.40 (max)	0.03	0.026
S	0.03 (max)	0.004	0.004
Si	1.00	0.41	0.41
Ni	8.00-11.00	8.66	8.46
Cr	18.00-20.00	18.44	18.47
Mo	--	--	0.26
V	--	--	0.05
Cb	--	--	<0.01
Ti	--	--	0.005
Co	--	--	0.21
Cu	--	--	0.18
Al	--	--	0.01
Fe	--	--	<i>a</i>
N ₂	--	--	0.062
O ₂	--	--	0.005

^aBalance.

The as-received tube was cut into 6-in.-long sections, and its grain size showed a need for a grain coarsening treatment. This treatment consisted of heating the tubes in an argon-purged furnace to 1093°C, holding for 0.5 h, and cooling in air. The grain structure of such heat-treated tube at various locations from outside and inside diameters is shown in Fig. 3. The average grain size of this tube at various locations is shown in Table 2. The observed grain size of 201 μm or ASTM 1.7 suggests that the tubing was subjected to the proper heat treatment.

In order for the tubes to be coated with Fe₃Al alloy FAS, a 1/8-in. wire of the composition was produced. For this task, the wire was produced by air-induction melting (AIM) a 10-lb heat of the FAS composition (see Table 3 for specifications) and using Pyrex™ tubes of 1/8 in. ID for vacuum suctioning of the wires. After suction, the Pyrex™ tubes broke from the thermal shock resulting in clean wires of the alloy. In this particular case, all of the wires had a good surface finish, and the length of each was 18 in. A photograph of the wires is shown in Fig. 4. After casting wires by the suction process, a small chemistry sample was poured, and its results are compared with the specifications in Table 3, which shows that the aluminum content matched extremely well with the specified value. However, chromium was a bit low. The lower chromium could have resulted from its oxidation because the wire suction process was carried out in air. It is the aluminum content that provides the sulfidation resistance, and its value is in good agreement with the specified value.

The weld wires of FAS were later shipped to PNNL for the electrospark discharge coating process.

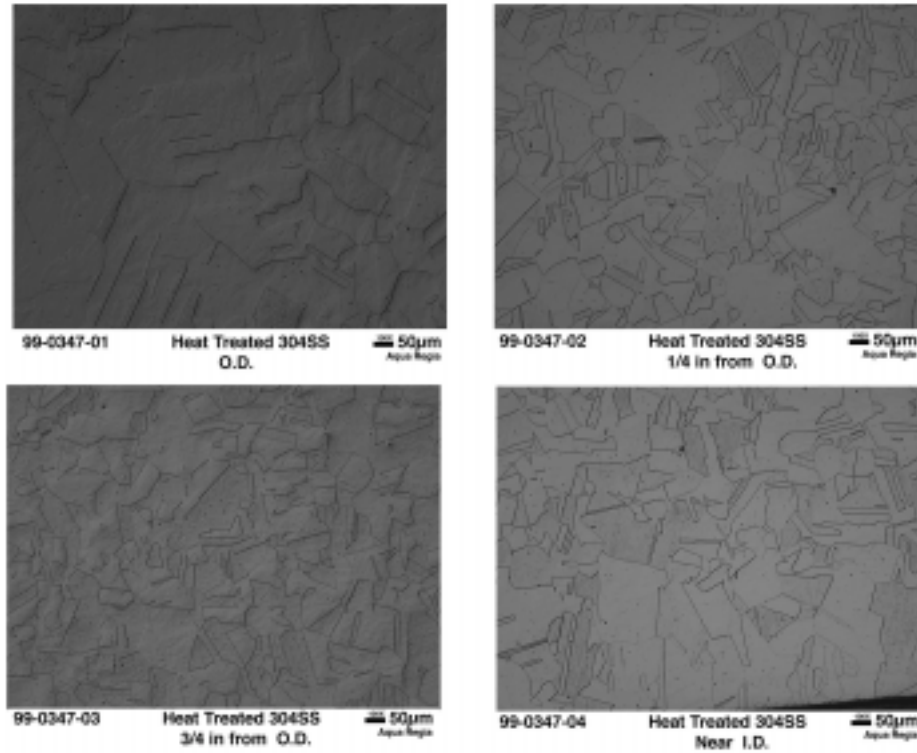


Fig. 3. Optical microstructure of commercially procured type 304H stainless steel after annealing treatment of 1093°C for 0.5 h; transverse orientation.

Table 2. Grain size of fabricated tubes of various alloys after heat treatment

Alloy	Heat no.	Heat treatment		Grain size	
		(°C)	(h)	(µm)	(ASTM)
304 H	V80210	1093	0.5	201	1.7 ^a
310-Ta	17425	1200	2.0	123	3 ^b
310-Ta	17426	1200	2.0	133	3 ^b
310-Ta	17431	1200	2.0	70 ^b	4.7
Mod. 800	17423	1200	2.0	73	4.5 ^c
Mod. 800	17424	1200	2.0	63 ^c	5.0
Mod. 800	17433	1200	2.0	167 ^c	2.2
Thermie	17421	1200	2.0	79 ^d	4.3
Thermie	17422	1200	2.0	88 ^d	4.0
Thermie	17454	1200	2.0	94 ^d	3.9

^aVery high annealing twin density.

^bLow annealing twin density.

^cNo annealing twins.

^dAnnealing twinning near outside and inside diameters but very low density in the mid thickness.

Table 3. Chemical analyses of FAS cast into 1/8-in.-diam wires for coating process. The weld rods were cast by vacuum-induction melting process using Pyrex™ tubes.

Element	Weight percent	
	Target	Actual (Heat No. 17433)
C	--	0.008
Mn	--	<0.01
S		0.002
Si		<0.01
Ni		<0.01
Cr	2.19	1.59
Mo		0.01
V		<0.01
Cb		<0.01
Co		<0.01
Al	15.93	15.79
B	0.011	0.010
Zr		<0.01
N ₂		0.001
O ₂		0.005
Fe	B alance	Balance



Fig. 4. Photograph showing 1/8-in.-diam wires of Fe₃Al-based alloy FAS prepared by the vacuum suction process.

GENERAL APPROACH FOR FABRICATION OF ITEMS 2, 3, AND 4

For the fabrication of 310 + Ta, modified 800H and Thermie alloys, 50-lb heats were melted by the AIM process. In each case, the heat was poured into a 5.5-in.-diam by 8-in.-long graphite mold (see Fig. 5 for its schematic) with a hot top. After cutting the hot tops, the ingots were machined to 5.40-in. OD (consistent with the extrusion press liner size at ORNL) and a 1.5-in.-diam hole was drilled for incorporating a mandrel during hot extrusion. For type 310 + Ta and modified 800H, 1.5-in. holes could be drilled by conventional tooling. However, the Thermie alloy required drilling by the electrodischarge machining process. A photograph of a cast and machined billet is shown in Fig. 6. For each alloy, the billets were heated to the appropriate temperature and hot extruded using a 1.5-in.-diam mandrel and a 2.75-in.-diam opening die. Heated billets were glass-lubricated in each case prior to extrusion. All of the extrusions were carried out on a 1250-ton horizontal extrusion press available in the Materials Processing Group at ORNL. The specific details of each item are given below.

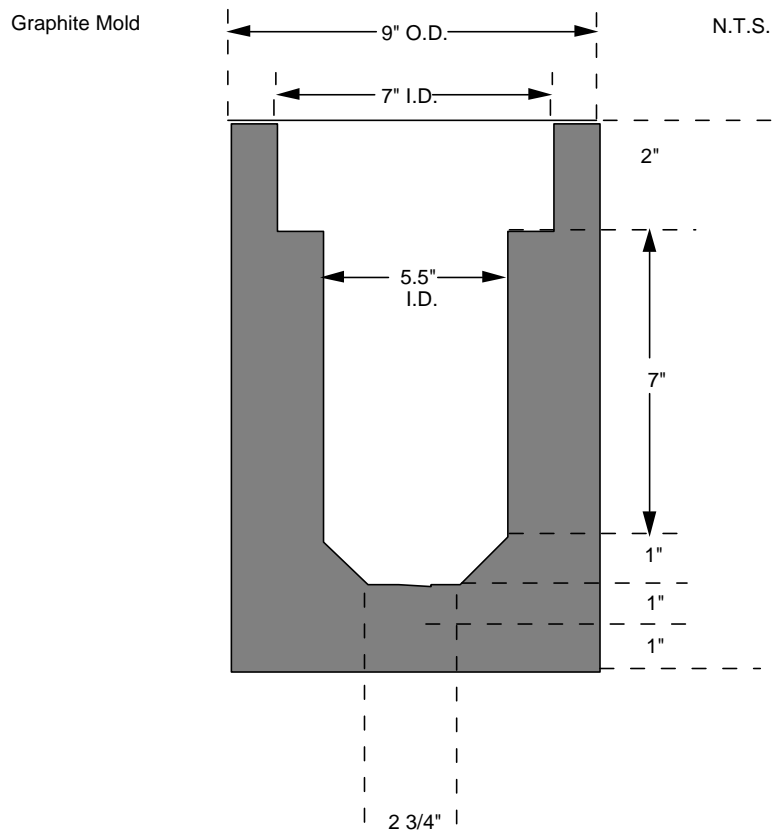


Fig. 5. Drawing of graphite mold used in casting billets for tube fabrication.

ITEM 2: 310 + Ta STAINLESS STEEL

For this steel, the billets were from ORNL heat numbers 17425, 17426, and 17431. In each case, the billets were heated to 1150°C for 3 h in air followed by glass lubrication and hot extrusion. The hot-extruded tubes were typically 36 in. long. After cutting the nose and tail, they were given a solution annealing treatment at 1200°C for 2 h in an air furnace followed by forced air-cooling. The heat-treated tubes were cut into 6-1/8-in.-long pieces and a ring for chemical analysis and metallography. Each cut section was machined to a final dimension of 2.5-in. OD × 0.4-in. wall × 6-in. long. Several of the machined tube sections of type 310 + Ta are shown in Fig. 7.



Fig. 6. Photograph of as-cast ingot and machined and drilled billet prior to hot extrusion.



Fig. 7. Photograph of eight pieces of type 310 + Ta stainless steel and three pieces of modified 800 alloy ready for shipment.

The chemical analyses of rings from heats 17425, 17426, and 17431 of type 310 + Ta are compared with the target chemistry in Table 4. All elements of type 310 + Ta heats except tantalum met the target chemistry extremely well. Somewhat lower values of tantalum are caused by its oxidation during the AIM process. However, based on the previous data⁽²⁾ on heats of different tantalum levels, the observed tantalum levels are not expected to have a significant effect for the current test. The microstructure of rings from each heat of type 310 + Ta are shown in Figs. 8 through 10, and the grain size of each heat is included in Table 2.

Table 4. Comparison of actual chemistry of type 310 stainless steel plus tantalum with target chemistry

Element	Weight percent			
	Target	Heat 17425	Heat 17426	Heat 17431
C	0.05	0.063	0.063	0.060
Mn	2.00	1.74	1.66	1.89
P	--	0.008	0.009	0.013
S	--	0.006	0.006	0.006
Si	0.25	0.25	0.24	0.27
Ni	21.0	21.63	21.08	21.12
Cr	24.5	23.74	23.78	24.01
Mo	--	<0.01	<0.01	<0.01
V	--	<0.01	<0.01	0.01
Cb	--	<0.01	<0.01	<0.01
Ti	--	<0.01	<0.01	0.01
Co	--	0.02	0.02	0.01
Cu	--	<0.01	<0.01	<0.01
Al	--	<0.01	<0.01	--
Fe	--	<i>a a</i>	<i>a</i>	
N ₂	0.22	0.22	0.22	0.24
O ₂	--	0.013	0.014	0.018
Ta	1.75	1.18	1.03	1.24
B	0.005	<i>b</i>	<i>b</i>	<i>b</i>

^aBalance.

^bNot analyzed.

ITEM 3: MODIFIED 800H

For this item, the billets were from ORNL heats 17423, 17424, and 17433. For heats 17423 and 17424, billets were heated at 1175°C for 3 h and hot extruded through a 2-3/4-in. die over a 1.5-in.-diam mandrel. The test billet of heat 17433 was held at 1200°C in air for 16 h for better homogenization. However, such an exposure resulted in nearly 1/8-in.-thick oxide scale, which made the billet too large to extrude. The oxide was machined off, and the billet was heated at 1175°C for 3 h and extruded in the same manner as the first two billets. After cutting the nose and tail, the extruded tubes were given a solution annealing treatment at 1200°C for 2 h in an air furnace followed by forced air cooling. The heat-treated tubes were cut into 6-1/8-in.-long pieces and a ring for chemical analysis and metallography. Each cut section was machined to final dimensions of 2.5-in. OD × 0.4-in.-wall × 6-in.-long. Some of the machined tubes are shown in Fig. 7 along with type 310 + Ta.

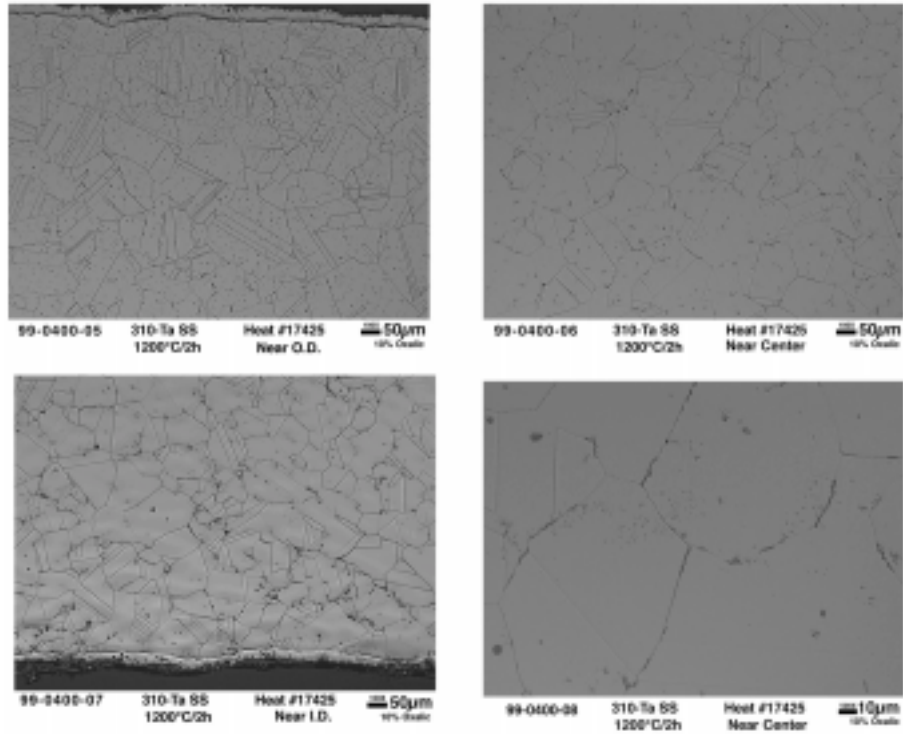


Fig. 8. Optical microstructure of type 310 plus tantalum stainless steel tube (Heat No. 17425). Final anneal 1200°C/2 h/forced air cool. Transverse orientation.

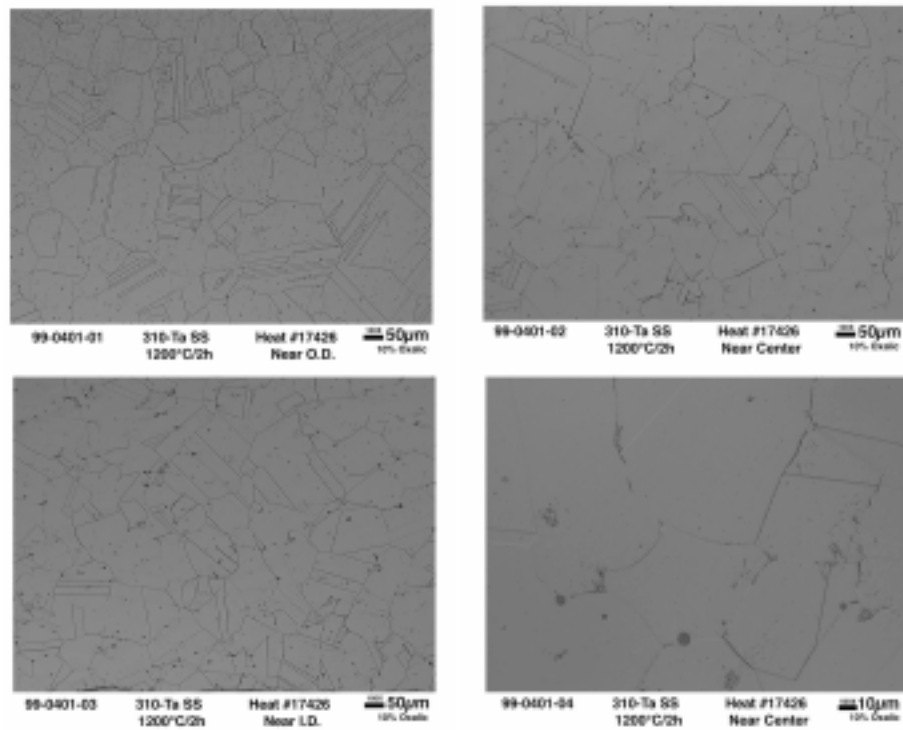


Fig. 9. Optical microstructure of type 310 plus tantalum stainless steel tube (Heat No. 17426). Final anneal 1200°C/2 h/forced air cool. Transverse orientation.

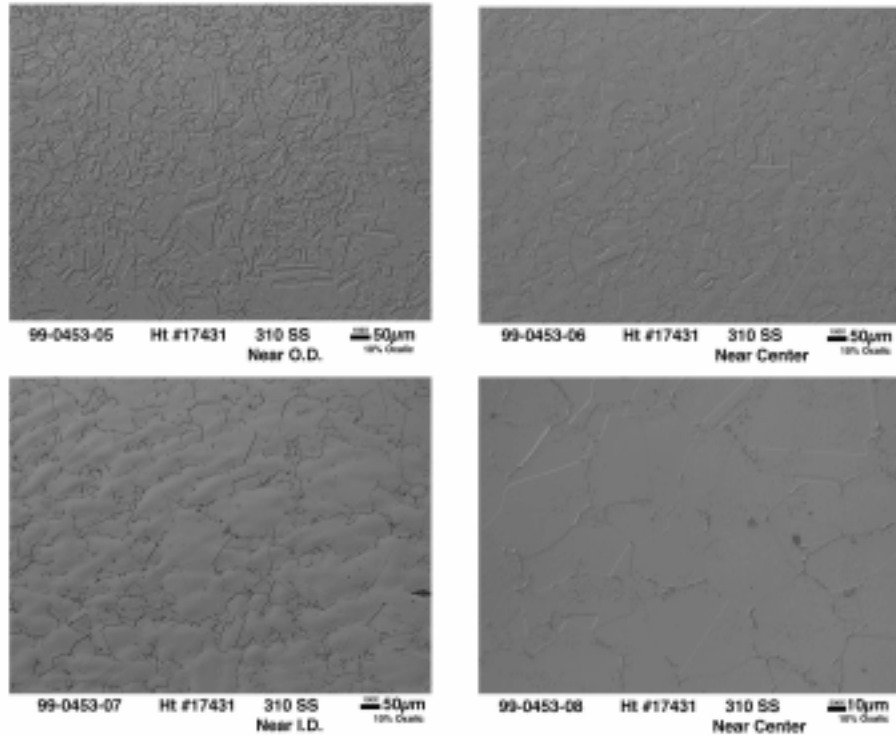


Fig. 10. Optical microstructure of type 310 plus tantalum stainless steel tube (Heat No. 17431). Final anneal 1200°C/2 h/forced air cool. Transverse orientation.

The chemical analysis of rings from heats 17423, 17424, and 17433 of modified 800H are compared with the target chemistry in Table 5. All elements except titanium showed a good match with the target chemistry. Poor titanium recovery is caused by its oxidation during the AIM process. The optical microstructure of rings from each of the modified 800H alloy are shown in Figs. 11 through 13, and the grain size of each heat is included in Table 2. The grain size of the tubing for the billet heated at 1200°C for 16 h for homogenization was nearly three times that of the grain size for tubes from the other two billets.

ITEM 4: THERMIE ALLOY

For this alloy, the billets were from ORNL heats 17421, 17422, and 17454. After two unsuccessful extrusions at 1210 and 1250°C, 1250°C was used for successful extrusion of this alloy. All three billets were heated at 1275°C for 3 h in air and hot extruded through 2-3/4-in.-diam die over a 1.5-in.-diam mandrel. Although the billets extruded to tube at 1275°C, the tubes showed significant regions of surface irregularities. The extruded tubes were given a solution anneal treatment at 1200°C for 2 h followed by forced air cooling. The annealed tubes were cut into 6-1/8-in.-long pieces and a ring for metallography and chemical analysis. The cut pieces were machined to the final dimensions of 2.5-in. OD × 0.4-in. wall × 6-in. long. The machined pieces of the Thermie alloy are shown in Fig. 14. Metallography of the rings from each heat of Thermie alloy is shown in Figs. 15 through 17, and the grain size measurements are presented in Table 2. The chemical analysis of the three heats of the Thermie alloy is compared with the target chemistry in Table 6. Except for slightly higher carbon, all other elements of the three Thermie alloy heats met all elements of the target chemistry.

Table 5. Comparison of actual chemistry of modified 800H

Element	Weight percent			
	Target	Heat 17423	Heat 17424	Heat17433
C	0.09	0.10	0.10	0.10
Mn	2.00	1.93	1.94	1.93
P	--	0.009	--	0.002
S	--	0.003	0.002	0.005
Si	0.25	0.24	0.24	0.26
Ni	31.0	30.74	31.04	31.10
Cr	20.0	19.89	19.98	19.91
Mo	1.5	1.50	1.52	1.51
V	0.4	0.38	0.23	0.37
Cb	0.25	0.26	0.26	0.25
Ti	0.25	0.11	0.15	0.03
Co	--	0.03	<0.01	<0.01
Cu	--	<0.01	<0.01	<0.01
Al	--	<0.01	<0.01	0.01
Fe	<i>a</i>	<i>a</i>	<i>a</i>	<i>a</i>
N ₂	--	0.026	0.029	0.018
O ₂	--	0.004	0.008	0.015
Ta	--	<0.01	--	--
B	0.005	<i>b</i>	<i>b</i>	<i>b</i>

^aBalance.

^bNot analyzed.

INSPECTION AND SHIPMENTS

All machined tubes of 310 + Ta, modified 800H, and Thermie alloys were visually inspected and shipped with an inspection report. The inspection data and the number of tubes of each alloy shipped are shown in Table 7.

SUMMARY AND CONCLUSIONS

This paper deals with the fabrication of tube sections of four alloys for incorporating into test sections to be assembled by Babcock & Wilcox (B&W) for installation at Ohio Edison Power, Niles Plant. The primary purpose of the installation was to determine the corrosion behavior of ten different alloys for flue gas corrosion. Ohio Edison Power, Niles Plant is burning an Ohio coal containing approximately 3.4% S (dry basis) and approximately 0.4% alkali which causes chronic coal ash corrosion of the unit's superheater tubing.

The 2.5-in.-OD × 0.4-in.-wall × 6-in.-long sections of four alloys {type 304H coated with Fe₃Al alloy FAS [developed at the Oak Ridge National Laboratory (ORNL), 310 + Ta, modified 800H, and Thermie alloy]} were fabricated at ORNL. Each alloy tubing was characterized for its chemical analysis and microstructure. The machined tubes of each of the alloys were inspected and shipped on time for incorporation into the test loop fabricated at B&W.

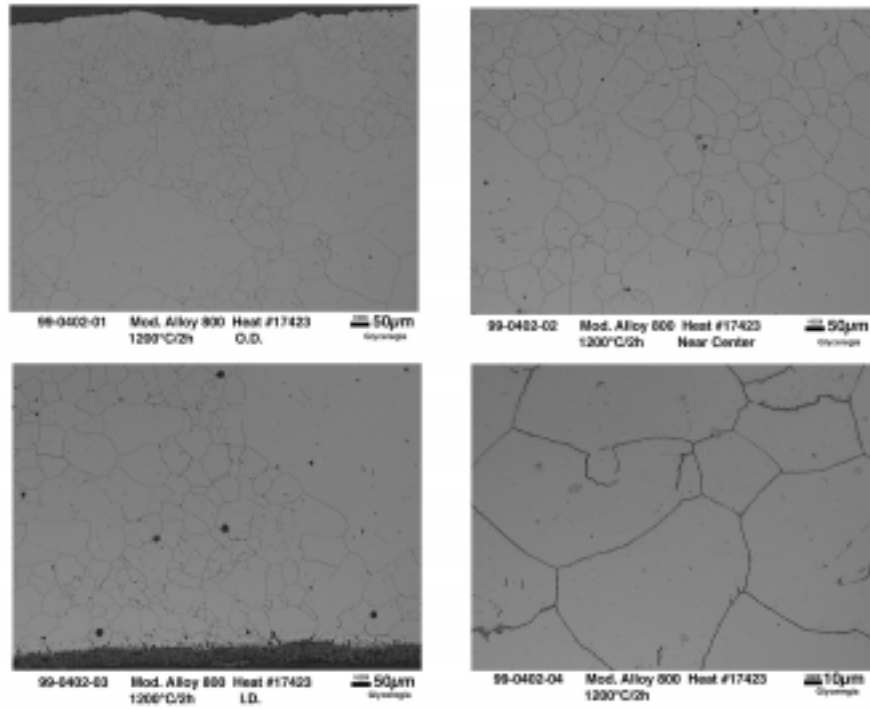


Fig. 11. Optical microstructure of modified 800 alloy tubes (Heat No. 17423) fabricated at the Oak Ridge National Laboratory, annealed 1200°C/2 h/forced cooled. Transverse orientation.

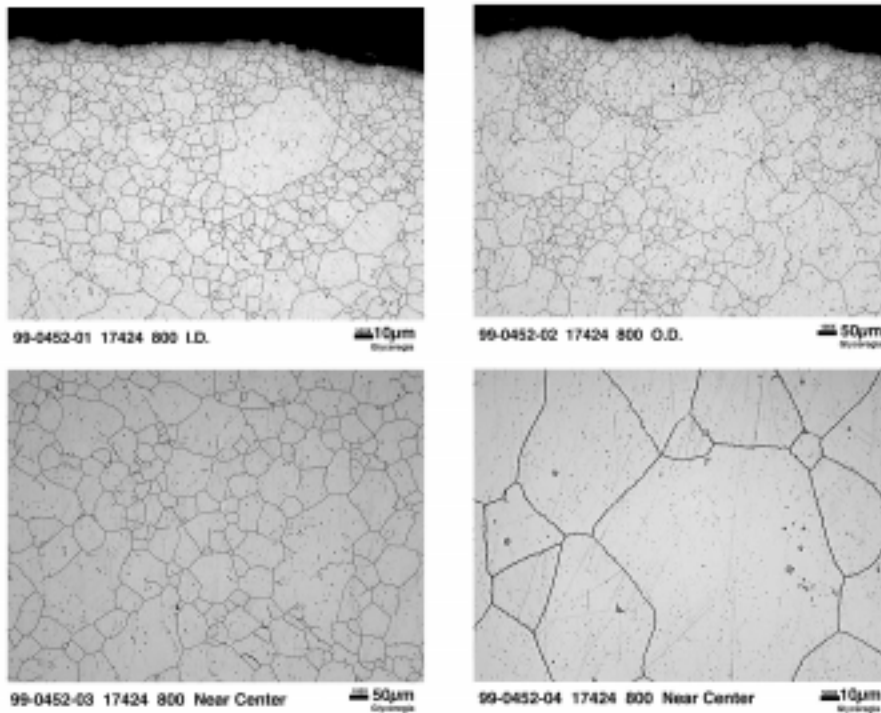


Fig. 12. Optical microstructure of modified 800 alloy tube (Heat No. 17424), final anneal 1200°C/2 h/forced air cool. Transverse orientation.

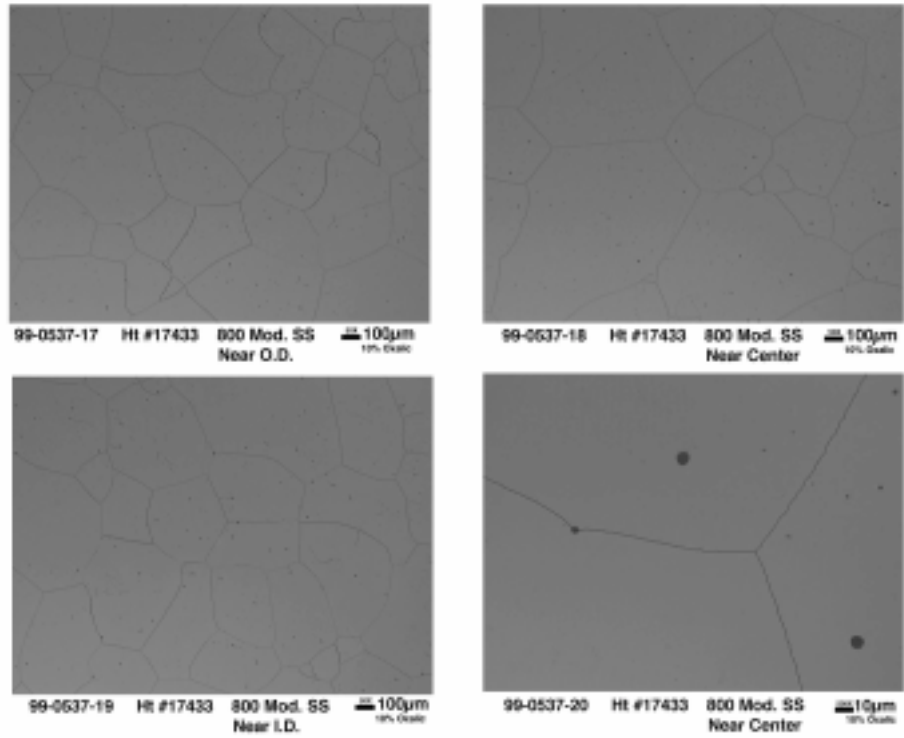


Fig. 13. Optical microstructure of modified 800 alloy tube (Heat No. 17433), final anneal 1200°C/2 h/forced air cool. Transverse orientation.



Fig. 14. Photograph of machined tubes of Thermie alloy.

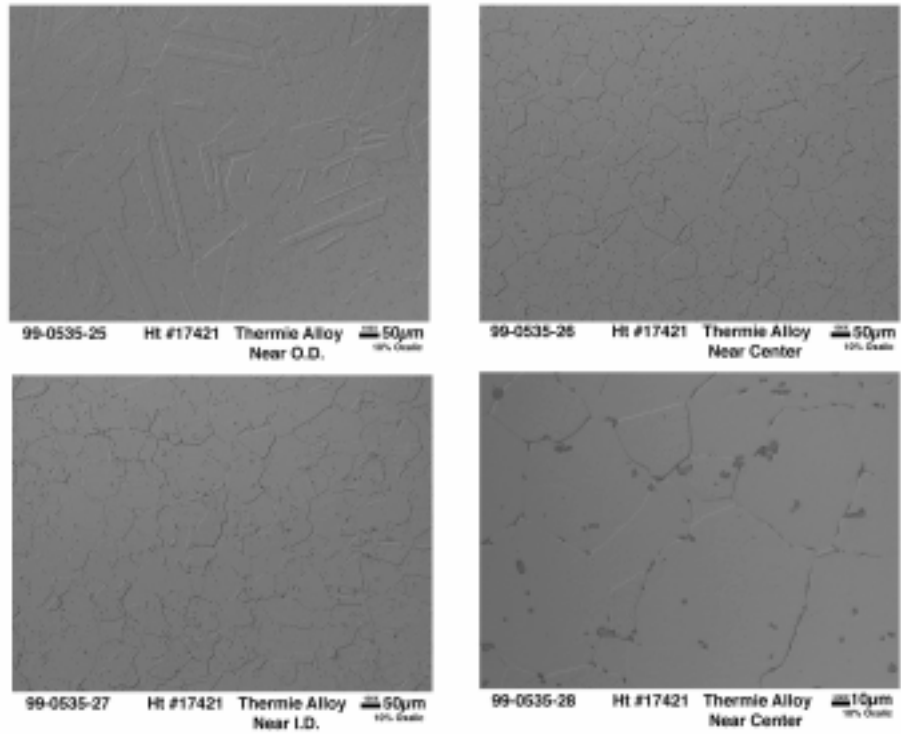


Fig. 15. Optical microstructure of machined piece of Thermie alloy tube (Heat No. 17421), final anneal 1200°C/2 h/forced air cool. Transverse orientation.

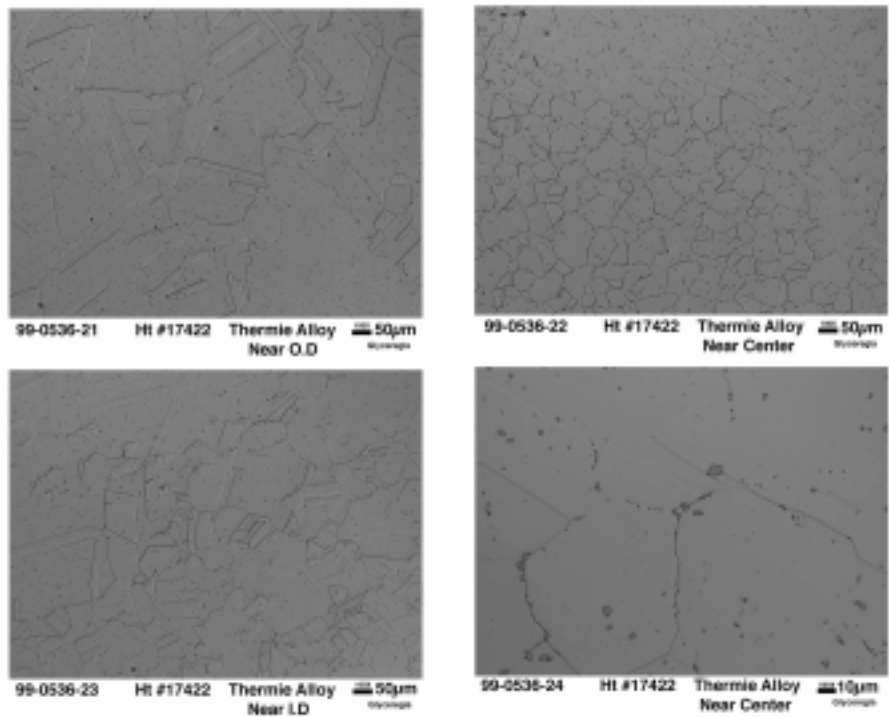


Fig. 16. Optical microstructure of machined piece of Thermie alloy tube (Heat No. 17422), final anneal 1200°C/2 h/forced air cool. Transverse orientation.

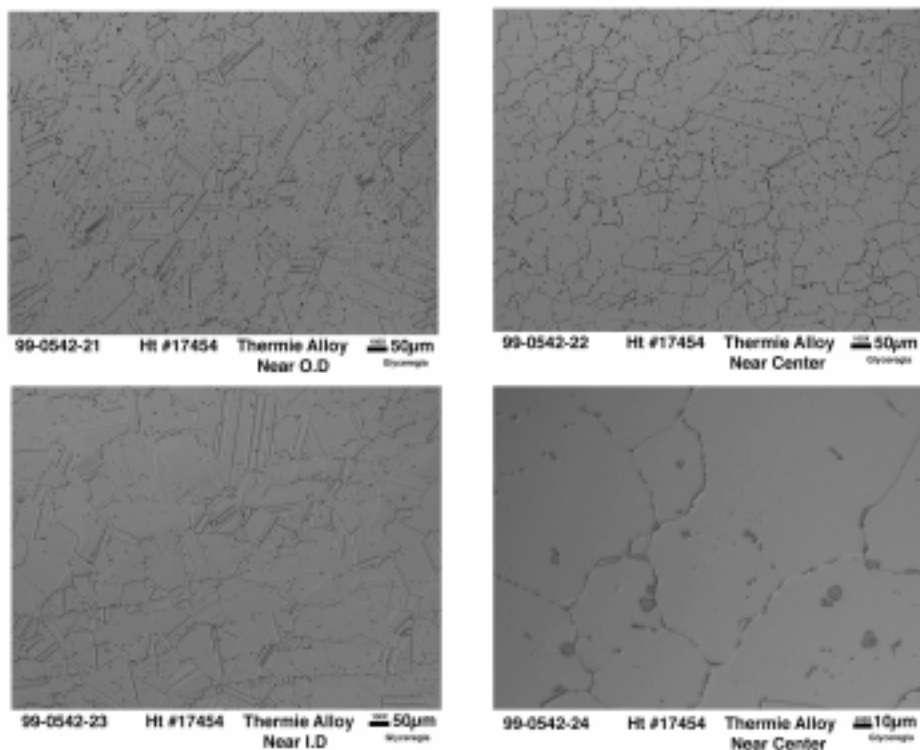


Fig. 17. Optical microstructure of machined piece of Thermie alloy tube (Heat No. 17454), final anneal 1200°C/2 h/forced air cool. Transverse orientation.

Table 6. Comparison of actual chemistry of Thermie alloy with target chemistry

Element	Weight percent			
	Target	Heat 17421	Heat 17422	Heat 17454
C	0.07	0.10	0.088	0.094
Mn	0.3	0.32	0.32	0.32
P	--	<0.002	<0.002	<0.002
S	--	0.005	0.003	0.009
Si	0.5	0.50	0.51	0.49
Ni	48.0	48.83	49.06	48.92
Cr	24.0	23.48	23.08	23.63
Mo	0.5	0.43	0.43	0.42
Cb	2.0	2.16	2.20	1.95
Ti	2.0	2.08	2.10	2.01
Co	19.8	19.22	19.39	19.42
Cu	--	<0.01	<0.01	<0.01
Al	0.8	0.75	0.74	0.60
Fe	2.0	2.11	2.06	2.11
N ₂	--	0.011	0.013	0.022
O ₂	--	0.002	0.003	0.004
B	0.002 ^a	<i>b</i>	<i>b</i>	<i>b</i>
Zr	0.015 ^a	<i>b</i>	<i>b</i>	<i>b</i>

^aMaximum.

^bNot analyzed.

Table 7. Summary of visual tube inspection and number of 310 + Ta, modified 800H, and Thermie tubes shipped to Babcock & Wilcox from the Oak Ridge National Laboratory

Alloy	Heat no.	Tube no.	Visual observations
310 + Ta	17425	1,2,3,4	All good. No defects.
310 + Ta	17426	1,2,3,4	All good. No defects.
310 + Ta	17433	<u>1,2,3,4</u>	All good. No defects.
	Total pieces:	12	
	Total shipped:	12	
Mod. 800H	17423	1,2	Both tubes' OD surfaces showed very small flaws.
Mod. 800H	17424	1,2,3 4	Tubes' OD surfaces showed slight flaws. Tube showed larger flaw on OD surface. Sent for weld practice.
Mod. 800H	17433	1 2,3 <u>4</u>	Tube showed one small surface flaw. All good. No defects. Tube 3 saved at ORNL as archive. Surface flaw.
	Total pieces:	10	
	Total shipped:	9	
Thermie	17421	1 3 4	Two places on OD and an end did not clean up during machining. Flaw on ID and one end. No defects.
Thermie	17422	2 3	Bad machining job, saved at ORNL. No defects.
Thermie	17454	1,2 <u>3</u>	No defects. Two places on OD and one end did not clean up during machining.
	Total pieces:	8	
	Total shipped:	7	

Conclusions from this study include:

1. Among the four alloys, Thermie was the hardest to machine and drill. The hole in the billet of this alloy had to be drilled by EDM.
2. The extrusion temperatures for 310 + Ta, modified 800H, and Thermie alloys were 1175, 1200, and 1275°C, respectively.
3. The yield of the final tube sections was the highest for 310 + Ta and lowest for the Thermie alloy.
4. A total of four 304H coated with FAS, twelve 310 + Ta nine modified 800, and seven Thermie alloy tubes were supplied for the test installation at Ohio Edison Power, Niles Plant.

ACKNOWLEDGMENTS

The authors thank Joseph D. Vought for melting and machining the billets, David C. Harper, Edward C. Hatfield, and Kenneth S. Blakely for extrusion, Hu F. Longmire for metallography, Michael L. Santella and Evan K. Ohriner for paper review, and Millie L. Atchley for preparing the manuscript.

Research was sponsored by the U.S. Department of Energy, Office of Fossil Energy, Advanced Research and Technology Development Materials Program, [DOE/FE AA 15 10 10 0, Work Breakdown Structure Element ORNL-2(H)] under contract DE-AC05-96OR22464 with Lockheed Martin Energy Research Corp.

REFERENCES

1. Letter, Larry Davison at McDermott Technology, Inc. to Materials Review Committee, February 26, 1999.
2. R. W. Swindeman, "Stainless Steels with Improved Strength for Service at 760°C and Above," *ASME International*, Book No. H01155 (1998) 291-298.

HIGH-TEMPERATURE CORROSION BEHAVIOR OF IRON ALUMINIDE ALLOYS AND COATINGS

B. A. Pint, C. Leyens[†], J. R. Regina^{*}, P. F. Tortorelli and I. G. Wright

Oak Ridge National Laboratory

Oak Ridge, TN USA

[†]on leave from DLR-German Aerospace Center

Cologne, Germany

^{*}Lehigh University

Bethlehem, PA USA

INTRODUCTION

The good high temperature oxidation and sulfidation resistance of iron aluminides has been widely recognized and carefully studied over the past decade, e.g. Refs.1-3. However, in recent years it has been found that, relative to other alumina-forming alloys, the external alumina scale spalls more readily on iron aluminides,⁴⁻⁵ even with additions of Zr, Y or Y₂O₃ which are known to improve scale adhesion.⁶⁻⁷ Several attempts have been made to understand the nature of this accelerated spallation and improve the performance of iron aluminides by micro-alloying additions. Recent results are presented below.

As described previously,^{2,3} the oxidation and sulfidation resistance of iron aluminides based on Fe₃Al extends to temperatures well above the point at which ingot-processed (IP) alloys have adequate mechanical strength. Consequently, oxide-dispersion-strengthened (ODS) iron aluminides are being developed to improve the strength of this alloy system while maintaining or improving corrosion resistance.^{4,8,9} Data for a commercially fabricated ODS Fe₃Al are presented below. Furthermore, iron aluminides could be used as coatings or claddings on higher-strength, less corrosion-resistant materials. Previous studies have focused on weld-overlay coatings.^{2,10-12} This paper reports initial results for coatings produced by thermal spraying.

RESULTS & DISCUSSION

Ingot-Processed Alloys

Previous work indicated that reactive element (RE) alloy additions (Zr, Y, Hf) to a base Fe-28Al-2Cr (FAS) alloy all had a similar beneficial effect on the oxidation behavior when added at the level of approximately 0.1at.% (Ref. 5). (All compositions are listed in atomic percent and were determined by inductively coupled plasma analysis of as-cast material.) However, based on the superior performance of a 0.05% Hf addition to NiAl (Ref. 13). and the significant internal oxidation observed for FAS+0.1%Hf (Fig. 1), a lower Hf content was investigated.

The oxidation performance of FAS+0.05Hf was found to be superior to any

previously studied ingot- or powder-processed iron aluminide. The lower Hf content eliminated the excessive internal oxidation observed for the higher (0.1%) Hf content (Fig. 1), which resulted in excessive weight gains at 1000°C (Fig. 2). Due to the relatively low oxidation temperature, the benefit of 0.05% Hf was not observed relative to the more-common IP iron aluminide composition, FAL (Fe-28Al-5Cr-0.1Zr). The difference is more distinct at 1100°C, where FAS+0.05Hf showed a lower total weight gain compared to both FAS+0.1Hf and FAL (Fig. 3). The specimen weight gain curves (dashed lines) also are plotted in Fig. 3 which indicate that the 0.05Hf addition did not eliminate scale spallation but rather reduced the scale growth rate. All of the alloys spall at 1100°C except for FeCrAlY where the specimen and total weight gains are equal. Thus the total weight gain of FAS+0.05Hf will eventually exceed that of FeCrAlY due to scale spallation.

Similar results were observed for cyclic testing at 1200°C, however, the optimized effect of Hf is more clearly illustrated in isothermal tests at 1200°C (Fig. 4). Compared to undoped FAS, 0.1% additions of Hf or Zr reduce the isothermal growth rate. Multiple tests were performed to check repeatability of this result. With the addition of 0.05% Hf, the growth rate is reduced by an order of magnitude to $1.3\text{-}1.5 \times 10^{-12} \text{ g}^2/\text{cm}^4\text{s}$. (Reducing the Zr content to 0.03% did not produce a similar effect.) Thus, the principal benefit of optimizing the Hf content is in minimizing the $\alpha\text{-Al}_2\text{O}_3$ scale growth rate and not in preventing scale spallation. The scale still spalls from this alloy; however, even with spallation, the scale appears to re-grow at the slower rate, thus retaining a long-term benefit for this alloy. This is also apparent in 100h cycles at 1200°C (Fig. 5) where FAS+0.05Hf has a lower weight gain initially but, due to its linear increase, it soon exceeds the weight gains of more adherent (but faster-growing) FeCrAlY and ODS FeCrAl substrates. At 1300°C, the detrimental effect of 0.1% Hf in FAS was not observed, thus lowering the Hf content did not result in any improvement. The scales on the 0.05 and 0.1Hf FAS alloys after 100h at 1300°C were very similar (Fig. 6). As in the case of Hf-doped NiAl, it is not clear why Hf in FAS is more effective than Zr in reducing the alumina scale growth rate. Higher rates with Y are attributed to the formation of Y-rich precipitates which internally oxidize, thereby increasing the total weight gain. However, Y additions are much more effective than Hf in improving scale adhesion in NiCrAl or FeCrAl.¹⁴ One possibility is that, when segregated to $\alpha\text{-Al}_2\text{O}_3$ grain boundaries,⁷ Hf has a higher effective ionic radii than other dopants and thus is able to inhibit the rate-limiting diffusion along these pathways.

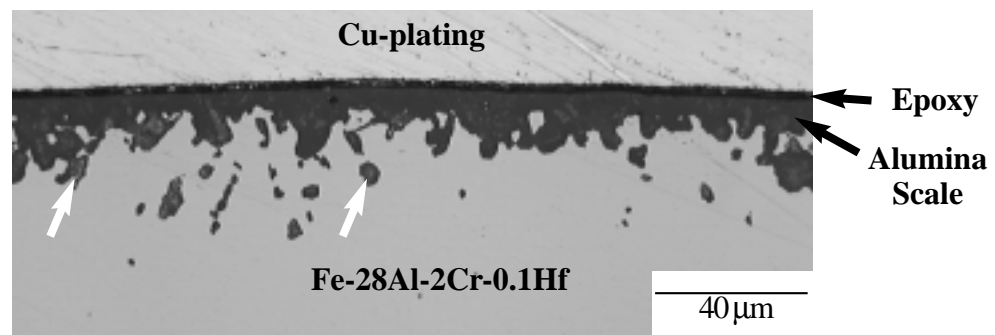


Figure 1. Copper-plated metallographic cross-section of the scale formed on FAS+0.1%Hf after 5000h at 1000°C in laboratory air. Little spallation was observed but deep oxide penetrations (pegs) consisting of alumina-encapsulated Hf-rich oxide (arrows) were observed.

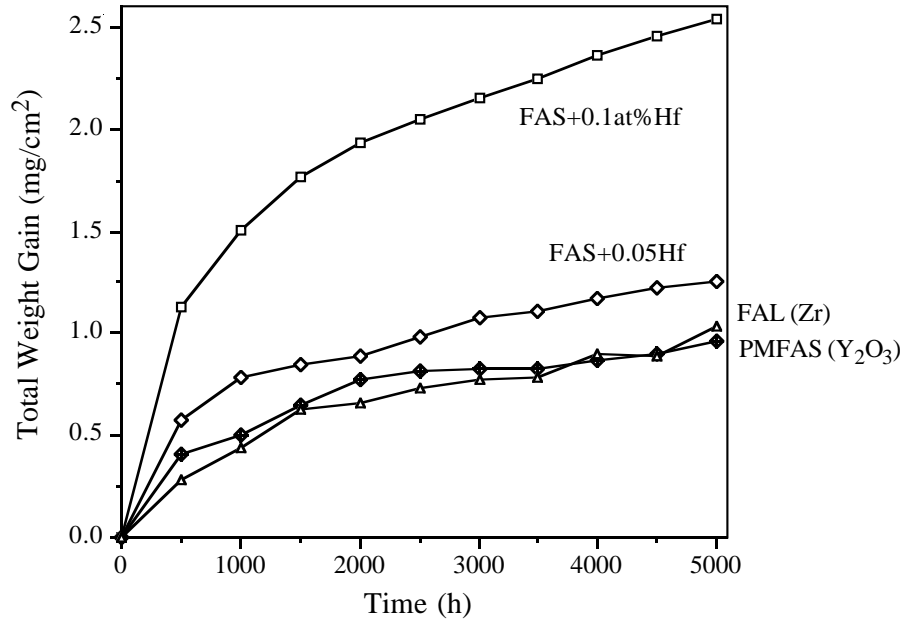


Figure 2. Total weight gain (specimen + spalled oxide) for several iron aluminides during 500h cycles at 1000°C in laboratory air. A 0.1%Hf addition resulted in high weight gains, not due to spallation, but due to excessive internal oxidation. This problem was eliminated by reducing the Hf content to 0.05%. Specimens were contained in pre-annealed alumina crucibles.

A sample of FAS+0.05Hf was included in a hot corrosion test using 1h cycles in flowing O₂ at 950°C. Specimens were coated with 1.0mg/cm² Na₂SO₄ prior to testing and recoated every 100h. While catastrophic oxidation was not observed (unlike NiAl+Hf), the

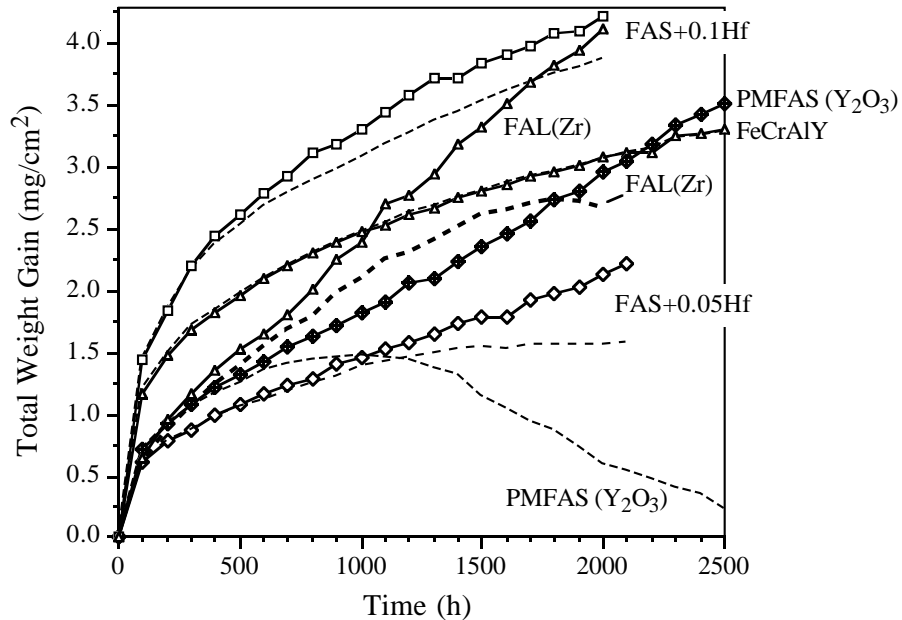


Figure 3. Total weight gain (specimen + spalled oxide) for several iron aluminides during 100h cycles in alumina crucibles at 1100°C in laboratory air. FAS+0.05Hf shows a lower total weight gain than other IP Fe₃Al compositions. The dashed lines indicate specimen weight change. All of the compositions spalled except for FeCrAlY.

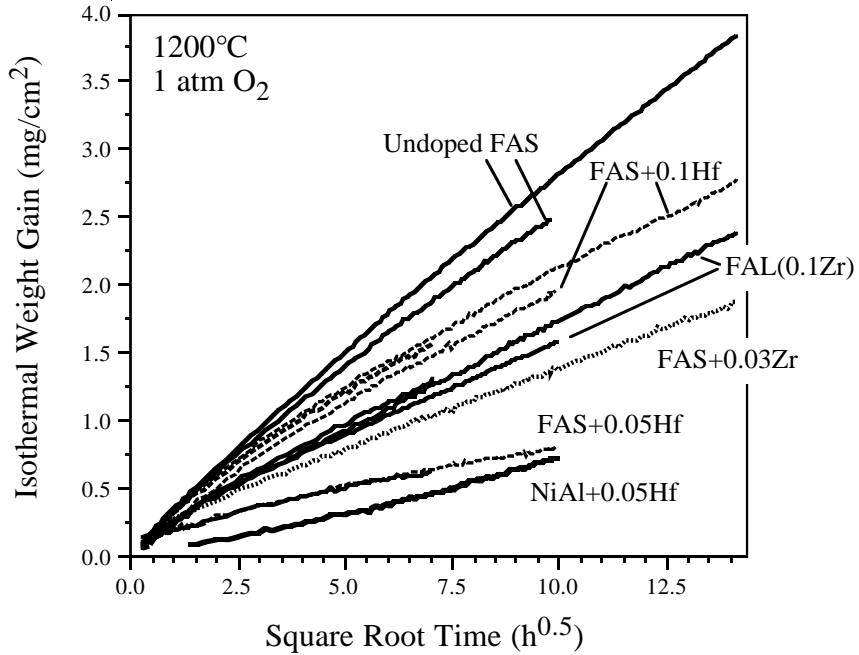


Figure 4. Isothermal weight gains at 1200°C plotted versus the square root of time to illustrate the near-parabolic relationship. The addition of 0.1Hf or Zr to iron aluminide reduces the growth rate relative to undoped FAS but further reducing the Hf content to 0.05% reduces the rate nearly an order of magnitude, similar to the rate observed for Hf-doped β -NiAl.

weight gains were substantially higher than observed for NiCoCrAlY (Fig. 7) and much higher than those observed in air at 1000°C (Fig. 2). However, similar weight changes to FeCrAlY with 20%Cr (rather than 2% in FAS) were observed. This is different than with

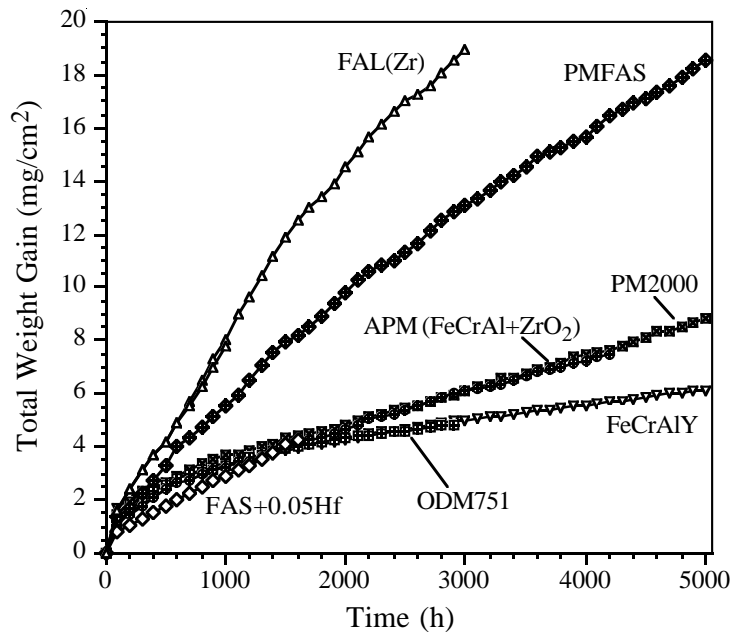


Figure 5. Total weight gain (specimen + spalled oxide) for several iron aluminides during 100h cycles in alumina crucibles at 1200°C in laboratory air. FAS+0.05Hf shows a lower initial total weight gain but, due to scale spallation, it is increasing at a linear rate. FeCrAlY and ODM751 show little spallation and have a nearly parabolic weight gain.

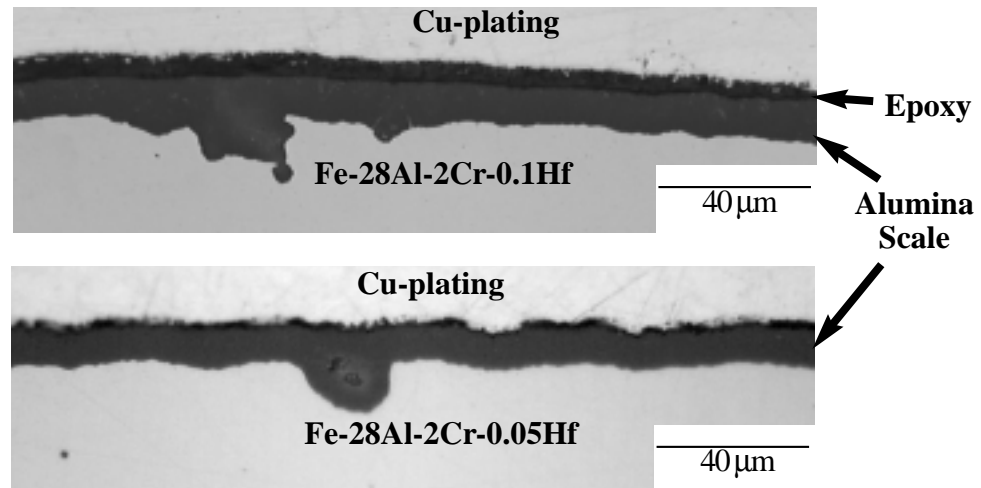


Figure 6. Copper-plated metallographic cross-sections of the scale formed after 100h at 1300°C on (a) FAS+0.1%Hf and (b) FAS+0.05%Hf. Under these conditions, changing the Hf content of the alloy had little effect.

Ni-base alloys, where increasing the Cr content improved resistance to hot corrosion.¹⁵

Oxide-Dispersed Fe₃Al Alloys

Long-term testing has been nearly completed on commercially-produced ODS Fe₃Al (PMFAS). At 1000°C, the scale growth rate is very similar to that observed for FAL and other alumina-forming alloys (Fig. 2). In a similar manner to lab-produced ODS FAS, spallation problems began at 1100°C and continued at higher temperatures. A comparison of PMFAS performance at 1100°C to several commercial ODS FeCrAl alloys [Y₂O₃-dispersed FeCrAl made by Inco (MA956), Dour Metal (ODM751) and Plansee (PM2000) and ZrO₂-dispersed FeCrAl, Kanthal APM] is shown in Fig. 8. The higher total weight gain for PMFAS is a direct result of the scale spallation noted by the specimen weight loss (dashed lines). ODS FeCrAl alloys also show some spallation (as illustrated for ODM751) but this loss is relatively minor and involves mostly spallation at specimen edges. These tests will continue to 10,000h. Testing with 100h cycles at 1200°C has been completed to 5000h for a number of different materials with very similar performance observations (Fig. 5). These higher temperature data give confidence to long-life predictions at lower temperatures. Very similar behavior is observed for very long times.

Tests at 1200°C also included 1h cycles (Fig. 9). PMFAS (1.5mm thick) has completed 2250, 1h cycles. At this point, its weight change is similar to that for ODS FeCrAl (PM2000) and FeCrAl. However, without total weight gain data, it is difficult to predict the relative lifetimes of these materials. A 1mm thick undoped FAS specimen had a lifetime of 1800, 1h cycles. The effect of cycle time has been investigated at 1200°C (Fig. 10). The time to first spallation decreases with increasing cycle frequency.¹⁶ More difficult to explain is the observation that the weight loss does not continue linearly, as for Ni-base alumina-formers,¹⁷ and can actually show weight increases for both 1h and 100h cycles. Weight gains are associated with macroscopic specimen deformation and thick, convoluted, non-protective oxides on the surface.¹⁶

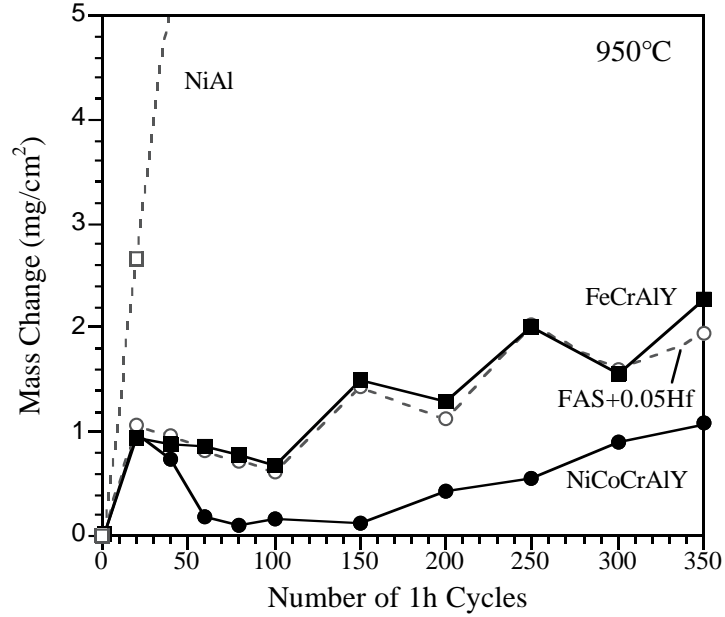


Figure 7. Specimen mass change for several alumina-forming alloys during hot corrosion testing in 1h cycles at 950°C. Specimens were coated with 1.0mg/cm² Na₂SO₄ prior to testing and recoated every 100h. After 350h, weight gains were higher than those observed after 5000h at 1000°C in air, indicating significant accelerated attack due to the salt.

Several attempts have been made to improve the oxidation performance of ODS FAS including varying the type and amount of oxide dispersion. PMFAS contains an optimized amount of Y₂O₃ (0.2%Y), as determined for lab-processed ODS FAS.⁴ One

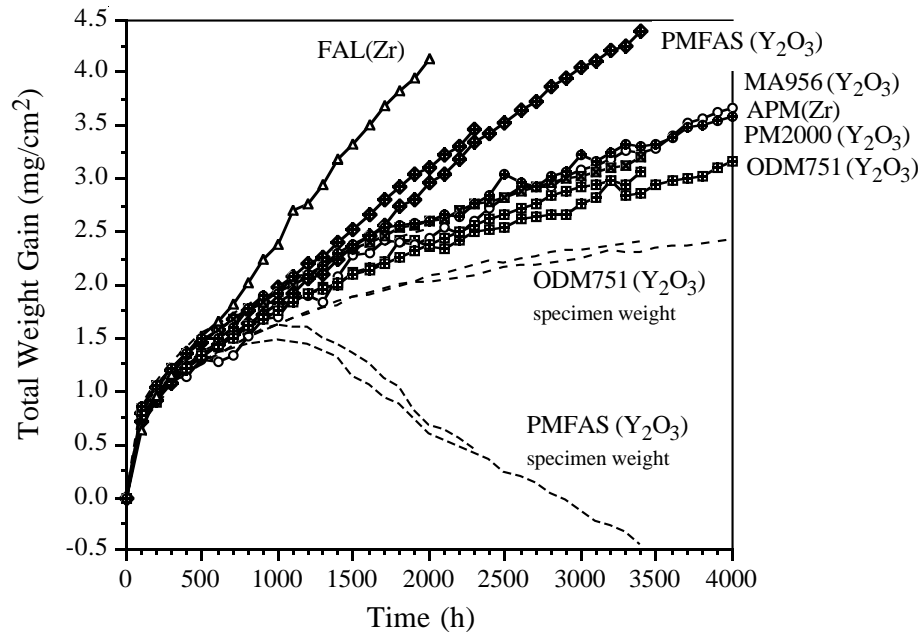


Figure 8. Total weight gain (specimen + spalled oxide) for several ODS alloys during 100h cycles in alumina crucibles at 1100°C in laboratory air. The dashed lines indicate specimen weight change. PMFAS shows higher total weight gains because of excessive scale spallation compared to the ODS FeCrAl alloys. ODM751 (FeCrAl+Y₂O₃) only has scale spallation at the specimen edges.

further approach was to de-sulfurize PMFAS, which has been shown to improve the oxidation performance of Ni-base superalloys¹⁸ and FeCrAl.¹⁹ The de-sulfurization was performed at NASA, Cleveland, OH and the specimens were tested in 100h cycles at 1100°C (Fig. 11) and 1h cycles at 1200°C (Fig. 12). In both cases, the de-sulfurized PMFAS performed slightly better than the nominal material, but no dramatic improvement in performance was observed, in contrast to what is found for Ni-base superalloys. It is likely that the Y_2O_3 addition is sufficient to inhibit any detrimental role of indigenous S in PMFAS. Further reducing the S content in the alloy provides no additional benefit.

Thermally-Sprayed Fe-Al Coatings

As a complement to research on weld overlays of iron aluminides,^{2,10-12,20-21} a first attempt was made to fabricate thermal-sprayed coatings and qualitatively evaluated their high-temperature corrosion behavior by simple gravimetric measurements. Using wire produced for gas metal arc deposition of weld-overlay coatings as the feedstock,¹⁰ coatings of Fe-Al-Cr were deposited by thermal spray onto carbon steel substrates made from round stock and machined to have hemispherical ends (see Fig. 13a). The coated specimens were then exposed in individual alumina crucibles to air at 900 and 1000°C and to air-1%SO₂ at 800°C.

Large mass gains were measured for all the exposed specimens. As shown in Fig. 14, these weight gains are much larger than for IP FAL exposed under similar conditions. Furthermore, at 1000°C, the weight gains over the second 24-h exposure period were substantially larger than those measured for the initial 24h of oxidation. Such behavior indicates that a second, less protective corrosion product was starting to form. Visual examination of the specimens indicated that a darker (gray-dark blue) product had formed

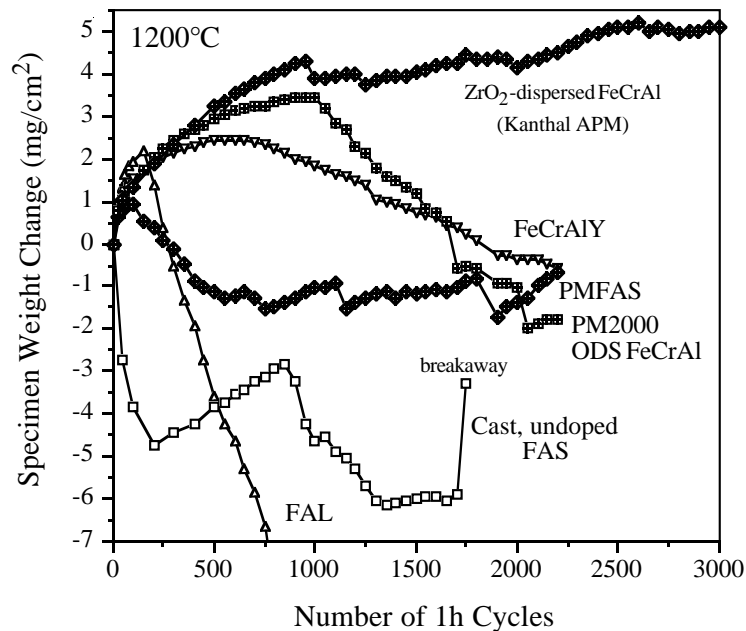


Figure 9. Specimen weight change for several alumina-forming alloys during 1h cycles at 1200°C in dry flowing O₂. PMFAS began spalling relatively quickly but did not continue to lose weight like FAL. With only specimen weight change, it is difficult to predict lifetime in this test.

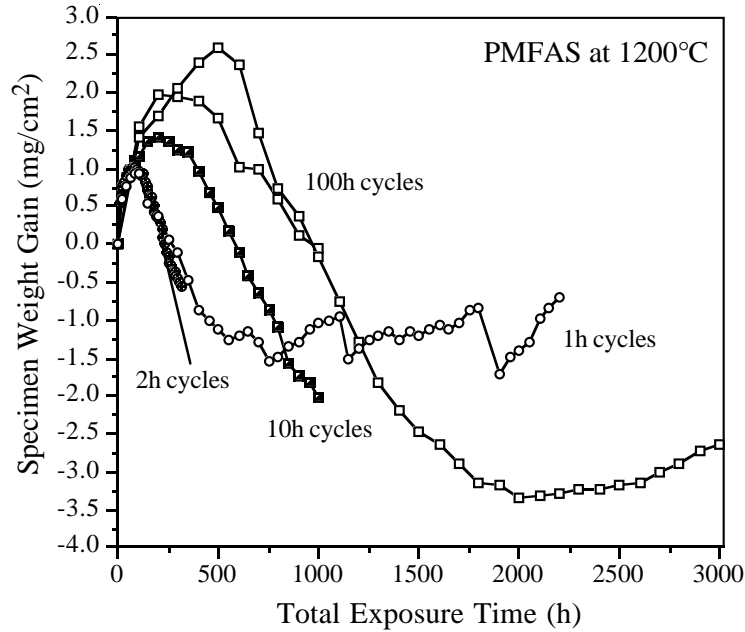


Figure 10. Specimen weight change for PMFAS with different cycle times at 1200°C plotted versus time at temperature. Shorter cycles decreased the time to initial spallation (downturn in the mass). At longer times, the rate of weight loss decreased and begins to increase slightly for both 1h and 100h cycles.

on the specimens exposed at 1000°C, in addition to a medium-gray scale, and that it was more prevalent on the specimen with the higher weight gain (Fig. 13). Only the medium-gray product was observed after 48 h at 900°C. It appeared that this gray scale (presumably

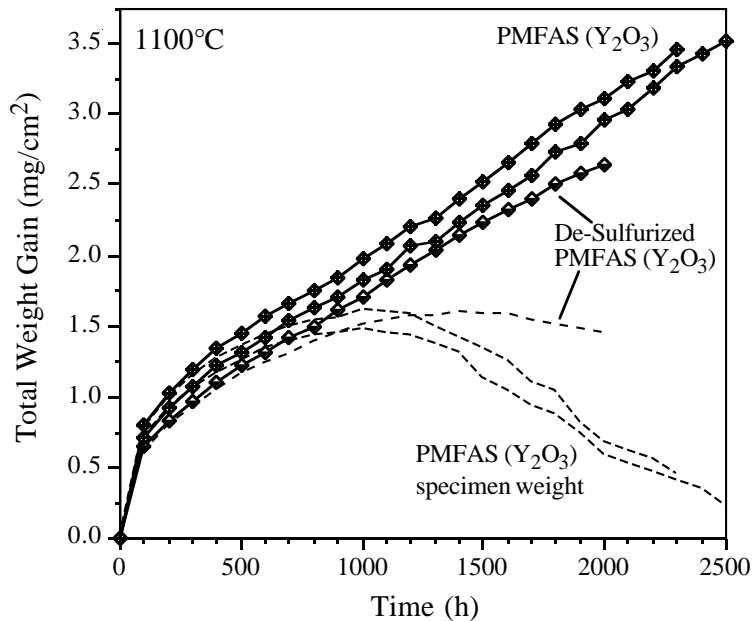


Figure 11. Total weight gain (specimen + spalled oxide) for PMFAS during 100h cycles in alumina crucibles at 1100°C in laboratory air. De-sulfurizing PMFAS produced only a minimal improvement in performance with a slightly reduced amount of spallation.

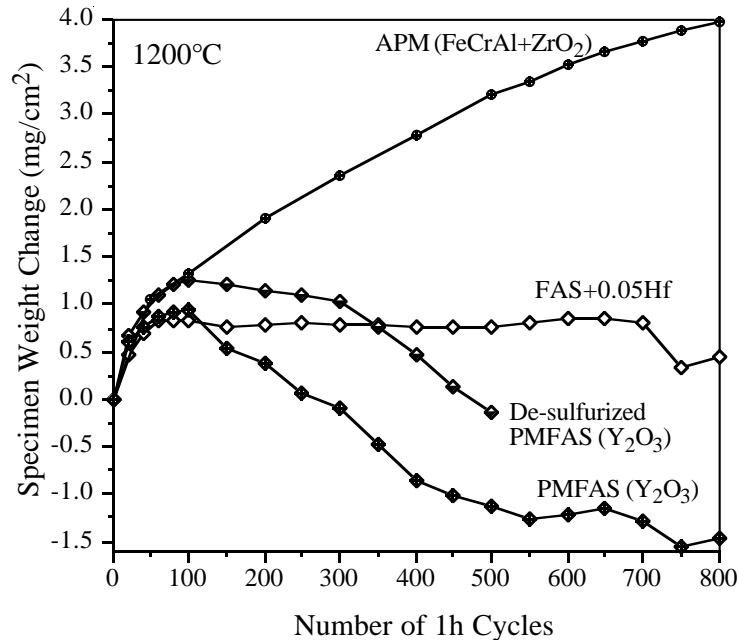


Figure 12. Specimen weight change for several alumina-forming alloys during 1h cycles at 1200°C in dry flowing O₂. De-sulfurizing PMFAS slightly reduced the amount of spallation but is unlikely to significantly extend the lifetime to breakaway in this test.

containing some Al) was the initial product to form (albeit at a rate faster than normally observed for alumina on Fe₃Al – see the FAL data in Fig. 14 as well as ref. 1), but that, within 48 h at 1000°C, it yields to an even faster growing product because most of the available aluminum must have already been consumed by reaction (as observed in breakaway oxidation²²). Accordingly, a similar transition to a higher rate of weight gain would be expected at 900°C when sufficient oxidation has occurred to deplete the aluminum in the coating (estimated from the data in Fig. 14 to occur when a mass increase of approximately 4–5 mg/cm² is reached). The coated specimen exposed at 800°C in air-1%SO₂ had a significant weight gain (~6 mg/cm²) and showed both gray and reddish-brown (iron oxide) corrosion products after 100 h.

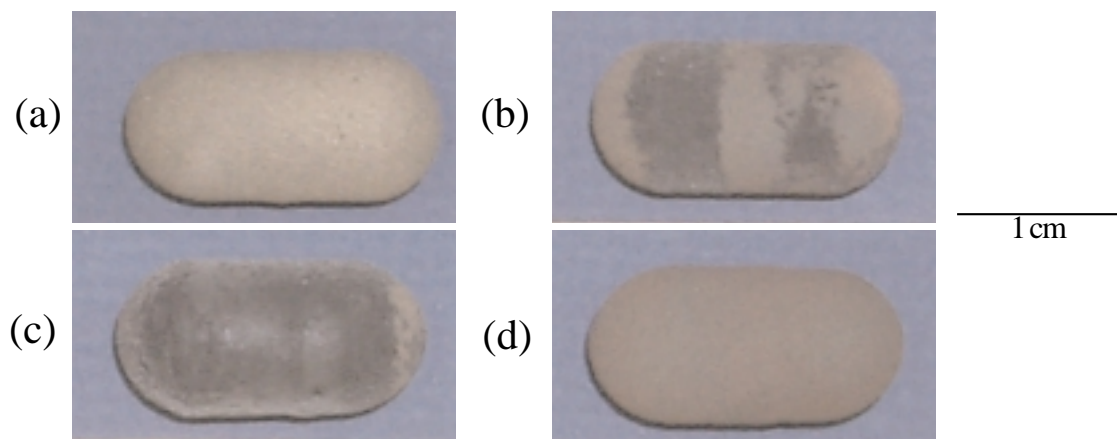


Fig. 13. Carbon steel coated with Fe-Al-Cr by a thermal spray process. (a) as-deposited. (b) 1000°C, two 24-h cycles in air, total weight gain of 13.1 mg/cm². (c) 1000°C, two 24-h cycles in air, total weight gain of 45.3 mg/cm². (d) 900°C, two 24-h cycles in air, total weight gain of 3.6 mg/cm².

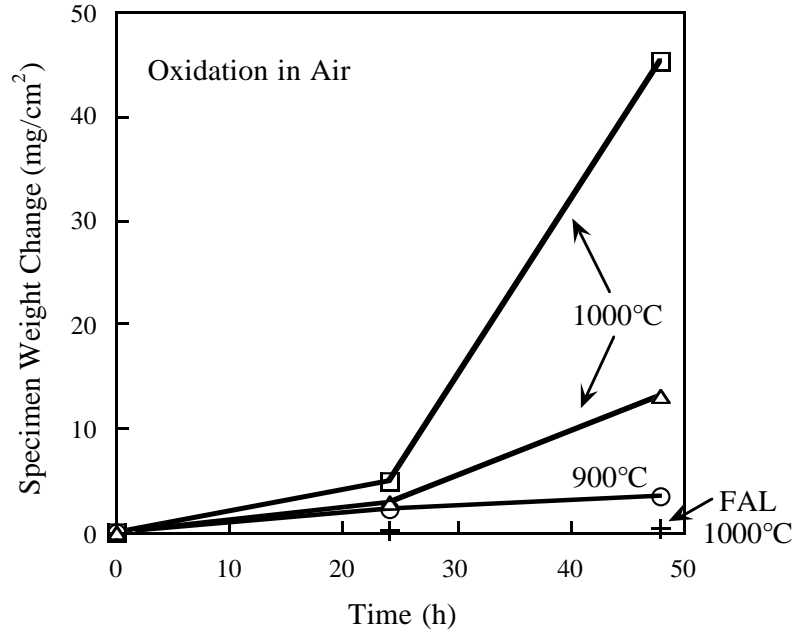


Fig. 14. Specimen weight changes versus time for thermally-sprayed coatings of Fe-Al-Cr on carbon steel substrates exposed to air at 900° and 1000°C (same specimens as shown in Fig.13). Similar data for IP FAL also are shown.

Given the very high weight gains observed in the initial experiments with the thermal spray coatings and the observation of corrosion products that are visibly different from protective alumina, it wasn't deemed necessary to conduct microstructural analyses of the specimens. Obviously, in the present case, this thermal-spray process produced coatings either not fully dense or with low Al levels such that a continuous protective alumina scale could not be maintained for even relatively short periods of time. This could be due to loss of Al by oxidation during the thermal spraying itself and may require even higher aluminum concentrations in the feedstock or the use of low-pressure thermal spraying to prevent the oxidation of Al during spraying. Previous limited results from spray coatings of iron aluminides (using powder) also showed high corrosion rates.²³ A more extensive effort will thus be required to produce uniform iron-aluminide coatings with sufficient aluminum concentration to proffer adequate oxidation and sulfidation protection.

SUMMARY

An Fe-28Al-2Cr alloy with an optimized Hf concentration (0.05%) has shown significantly better high-temperature oxidation resistance than other iron aluminide compositions. Its improved performance is mainly related to a slower isothermal α -Al₂O₃ scale growth rate and is observed mainly at 1100°-1200°C. Long-term oxidation resistance of a commercially fabricated ODS Fe₃Al (dispersed with Y₂O₃) has been studied. It spalled more readily than ODS FeCrAl for exposures at 1100° and 1200°C but overall showed relatively good oxidation resistance. De-sulfurization of ODS Fe₃Al had little additional benefit on oxidation performance. Preliminary results for thermal-sprayed Fe-Al coatings on carbon steel showed that corrosion resistance was poor, most likely due to insufficient Al

in the as-deposited coating. A continuous protective alumina layer was not maintained even after relatively short exposures at 900° and 1000°C.

ACKNOWLEDGMENTS

The authors wish to thank M. Howell, L.D. Chitwood, and G. Garner for assistance with the experimental work; J. R. Distefano, S. J. Pawel and C. G. McKamey for comments on the manuscript; J. L. Smialek at NASA, Cleveland, OH for performing the de-sulfurization and J. White at ORNL for thermal-spraying the Fe-Al coatings. The research was sponsored by the Fossil Energy Advanced Research and Technology Development (AR&TD) Materials Program, U. S. Department of Energy, under contract DE-AC05-96OR22464 with Lockheed Martin Energy Research Corp.

REFERENCES

1. P. F. Tortorelli and J. H. DeVan, *Mat. Sci. and Eng.* A153 (1992) 573-7.
2. P. F. Tortorelli, B. A. Pint, and I. G. Wright pp. 235-46 in *Proc. Eleventh Annual Conf. Fossil Energy Materials*, R. R. Judkins (comp.), U. S. Department of Energy, December, 1997.
3. P. F. Tortorelli and K. Natesan, *Mater. Sci. and Eng.* A258 (1998) 115-25.
4. B. A. Pint, P. F. Tortorelli and I. G. Wright, *Mater. and Corr.* 47 (1996) 663-74.
5. B. A. Pint, P. F. Tortorelli and I. G. Wright, *Mater. High Temp.* in press (1999).
6. A. Strawbridge and P. Y. Hou, *Mater. High Temp.* 12 (1994) 177-81.
7. B. A. Pint, *Oxid. Met.* 45 (1996) 1-37.
8. I. G. Wright, C. G. McKamey, E. K. Ohriner, and B. A. Pint, paper 4.1 in *Proc. Twelfth Annual Conf. Fossil Energy Materials*, U. S. Department of Energy, September, 1998.
9. I. G. Wright, C. G. McKamey, B. A. Pint, and P. J. Maziasz, these proceedings.
10. G. M. Goodwin, pp. 381-92 in *Proc. Tenth Annual Conf. Fossil Energy Materials*, N. C. Cole and R. R. Judkins (comp.), U. S. Department of Energy, August 1996.
11. P. F. Tortorelli, J. H. DeVan, G. M. Goodwin, and M. Howell, pp. 203-12 in *Elevated Temperature Coatings: Science and Technology I*, N. B. Dahotre, J. M. Hampikian, and J. J. Stiglich (eds.), TMS, Warrendale, PA, 1995.
12. K. Natesan and R. N. Johnson, pp. 591-99 in *Heat-Resistant Materials II*, K. Natesan, P. Ganesan, and G. Lai (eds.), ASM International, Materials Park, OH, August 1995.
13. B. A. Pint, I. G. Wright, W. Y. Lee, Y. Zhang, K. Prüßner and K. B. Alexander, *Mater. Sci. and Eng.* A245 (1998) 201-11.
14. B. A. Pint, P. F. Tortorelli and I. G. Wright, Oak Ridge National Laboratory, unpublished research 1999.
15. C. Leyens, I. G. Wright and B. A. Pint, pp.79-90 in *Elevated Temp. Coatings: Sci. and Tech. III*, J. M. Hampikian and N. B. Dahotre eds., TMS, Warrendale, PA, 1999, p.79-90.
16. B. A. Pint, P. F. Tortorelli and I. G. Wright, submitted to the European Federation of Corrosion International Workshop on Cyclic Oxidation, Feb. 1999, Frankfurt,

Germany.

17. J. A. Nesbitt, E. J. Vinarcik, C. A. Barrett, and J. Doychak, *Mater. Sci. Eng.*, A153 (1992) 561-6.

18. J. L. Smialek, D. T. Jayne, J. C. Schaeffer and W. H. Murphy, *Thin Solid Films* 253 (1994) 285-92.

19. G. H. Meier, F. S. Pettit and J. L. Smialek, *Werk. Korr.* 46 (1995) 232-40.

20. S. W. Banovic, J. N. DuPont, and A. R. Marder, paper 4.3 in *Proc. Twelfth Annual Conf. Fossil Energy Materials*, R. R. Judkins (comp.) U. S. Department of Energy, September 1998.

21. P. F. Tortorelli, B. A. Pint, and I. G. Wright, paper 2.8 in *Proc. Twelfth Annual Conf. Fossil Energy Materials*, R. R. Judkins (comp.) U. S. Department of Energy, September 1998.

22. P. Kofstad, *High Temperature Corrosion*, Elsevier Applied Science, London, 1988.

23. P. F. Tortorelli, Oak Ridge National Laboratory, unpublished research, 1995.

THE MECHANICAL RELIABILITY OF PROTECTIVE ALUMINA SCALES

P. F. Tortorelli and B. A. Pint

Oak Ridge National Laboratory
Oak Ridge, Tennessee, U. S. A.

INTRODUCTION

The mechanical integrity of stable oxide scales ultimately determines whether they will protect materials from corrosion and other environmental effects at high temperatures. Accordingly, this effort is directed toward improving the high-temperature corrosion resistance of materials of importance for efficient energy production through study of the key factors controlling the combined chemical and mechanical failure of protective alumina scales.¹⁻³ Much of this work is accompanied by high-spatial-resolution electron microscopy techniques for microstructural and microchemical characterization of the alumina scale, oxide-metal interface, and substrate for Fe-Al, FeCrAl(Y), and NiCrAlY alloys. In addition, other techniques for probing the defect structures and stress states of protective oxide scales have been examined and assessed.

DISCUSSION OF CURRENT ACTIVITIES

CRITICAL FACTORS AFFECTING THE HIGH-TEMPERATURE CORROSION PERFORMANCE OF IRON ALUMINIDES

The corrosion performance of iron aluminides in various high-temperature environments was reviewed and it was shown that the ability to form and maintain a protective Al_2O_3 surface product is the common factor linking reports of the good corrosion resistance of iron aluminides in many elevated-temperature environments.⁴ Furthermore, while protective alumina is normally considered to be $\alpha\text{-Al}_2\text{O}_3$, which is typically not observed below 900°C, other forms of alumina that develop in the various mixed-gas environments at lower temperatures do provide corrosion protection.⁴

Based on the need to form protective alumina, analyses associated with this and other related projects at ORNL and elsewhere have led to the following conclusions.

- Consideration of a simple oxidation lifetime model based on the ability to maintain a protective alumina scale provides a way to relate Al levels and fundamental factors controlling

Al consumption to long-term corrosion performance. The high aluminum concentrations of the iron aluminides increase oxidation lifetime, but, overall, their performance in this regard is not better than FeCrAl alloys with < 20% Al, particularly at temperatures in excess of 1100°C.⁵ This is due to generally greater spallation susceptibilities of the iron aluminides. Therefore, improving alumina scale adherence is the key to extended lifetimes commensurate with the high aluminum levels in iron aluminides and progress in this area has recently been made.⁶

- Important factors controlling the development and adherence of protective Al₂O₃ on iron aluminides include (1) appropriate alloying elements and microstructures to promote alumina growth, (2) the level of sulfur in the alloy and its ability to segregate to the scale-alloy interface (as controlled by reactive elements), (3) the type and concentration of reactive element additions, (4) the nature of scale and interfacial defects (the concentrations of which tend to be higher for oxide grown on Fe₃Al alloys), and (5) alloy strength.⁴

STRESSES IN THERMALLY GROWN OXIDES

As a result of a workshop held in 1997 and some further evaluation, the state of knowledge about stresses in thermally grown oxides has been assessed. The key findings from this assessment were

- the magnitude of growth stresses can be a significant fraction of typical thermal stresses
- stress levels in oxide scales reach constant levels fairly early in the oxidation processes
- morphological instabilities and microstructure play an important role in stress evolution
- there is good agreement between stresses in alumina measured by photostimulated luminescence associated with Cr³⁺ fluorescence and by x-ray diffraction
- differences in stress levels within an oxide layer have been identified

Furthermore, important scientific and experimental needs related to stresses in oxide films/scales and associated failure mechanisms were identified. These include:

- modeling/data evaluation, particularly with respect to growth stresses, total energy considerations, and scale failure mechanisms
- better information regarding stress evolution and relaxation at relevant oxidation temperatures.
- relationship between stress and oxidation performance

THE USE OF POSITRONS TO PROBE THE DEFECT STRUCTURES OF PROTECTIVE ALUMINA FILMS

Defect structures of protective oxide scales control the diffusion processes involved in their growth and, as such, also influence the development of stresses and their mechanical integrity. Therefore, positron spectroscopy was explored as a potentially useful nondestructive characterization tool in examining the processes by which defects such as mono- and divacancies, vacancy clusters, and dislocations develop in an oxide film as a function of substrate variations and growth/oxidation conditions. This approach can be particularly valuable for oxide layers because stress or interstitial impurities do not contribute to the uncertainty in determining defect structures by positron spectroscopy. Despite the potential advantage of using positrons to probe the micro-defect structure of protective oxide films, little work in this area has been performed. This study was done in collaboration with B. Somieski, L. D. Hulett, and J. Xu of ORNL's Chemical and Analytical Sciences Division, who were separately funded under the auspices of DOE's Basic Energy Sciences Program and provided the expertise in positron spectroscopy.

Positron spectroscopy of thermally grown alumina on iron and nickel aluminides was used to determine the utility of techniques based on such to characterize the defect structures of protective oxide scales. Lifetimes of the positrons and Doppler broadening of the gamma photons generated by their annihilation were measured as the energy with which they were injected was varied. In this manner, densities and sizes of the micro-defects were determined as a function of depth from the outer surfaces of the surface oxides. Thermally grown alumina scales (1-2 μm thick) had high densities of open volume defects, mainly consisting of aggregated vacancies. The thermally grown alumina on iron aluminide had a uniform through-thickness defect distribution. This was not the case for the scale on the nickel aluminide: the average defect (vacancy cluster) size increased as a function of depth into the alumina film grown on this substrate. These observed differences in the defect structures of the films grown on the two aluminides may reflect variations in doping levels in the respective oxide layers as well as an effect of scale microstructure. Furthermore, positron spectroscopy showed that the defect structures of the substrates near the oxide-metal interfaces were significantly changed; high densities of vacancies were detected. Detailed defect analyses of these specimens can be found elsewhere.⁷

The results of this study indicated that positron spectroscopy can be an effective tool in [1] characterizing defect types and their distribution in alumina films and scales, [2] examining

the influence of dopants in the alumina scales on the defect structure, and [3] determining changes in substrate defect distributions due to diffusion processes associated with oxide growth. When combined with judicious choices of specimens and experiments, positron spectroscopy techniques can yield information about the relationships between substrate characteristics and the defect structures that are directly related to fundamental mass transport processes controlling high-temperature oxidation resistance based on protective surface oxides.

ACKNOWLEDGMENTS

This research was sponsored by the Fossil Energy Advanced Research and Technology Development (AR&TD) Materials Program and the Division of Materials Sciences, U.S. Department of Energy, under contract DE-AC05-96OR22464 with Lockheed Martin Energy Research Corporation.

REFERENCES

1. K. B. Alexander, K. Průbner, and P. F. Tortorelli, "The Mechanical Reliability of Alumina Scales and Coatings," pp. 419-27 in *Proc. Tenth Annual Conf. Fossil Energy Materials*, N. C. Cole and R. R. Judkins (comp.), U. S. Department of Energy, August 1996.
2. K. B. Alexander, K. Průbner, and P. F. Tortorelli, pp. 301-12 in *Proc. Eleventh Annual Conf. Fossil Energy Materials*, R. R. Judkins (comp.), U. S. Department of Energy, December, 1997.
3. K. B. Alexander, K. Průbner, B. A. Pint, and P. F. Tortorelli, "Role of Microstructure and Microchemistry on the High-Temperature Oxidation Resistance of Alumina-Forming Alloys," paper 4.6 in *Proc. Twelfth Annual Conf. Fossil Energy Materials*, R. R. Judkins (comp.) U. S. Department of Energy, September 1998.
4. P. F. Tortorelli and K. Natesan, "Critical Factors Affecting the High-Temperature Corrosion Performance of Iron Aluminides," *Mater. Sci. Eng. A* 258 (1998) 115-25.
5. B. A. Pint, P. F. Tortorelli, and I. G. Wright, "Long-Term Oxidation Performance of Ingot-Produced Fe₃Al Alloys," accepted for publication in *Mater. High Temp.*, 1998.
6. B. A. Pint, C. Leyens, J. R. Regina, P. F. Tortorelli, and I. G. Wright, "High-Temperature Corrosion Behavior of Iron-Aluminide Alloys and Coatings," this report.
7. B. Somieski, L. D. Hulett, J. Xu, B. A. Pint, P. F. Tortorelli, B. Nielsen, P. Asoka-Kumar, R. Suzuki, and T. Ohdaira, "Microstructure of Thermally Grown and Deposited Alumina Films Probed With Positrons," *Phys. Rev. B* 59 (1999) 6675-88.

EVALUATION OF IRON-ALUMINIDE HOT-GAS FILTERS

P. F. Tortorelli, C. G. McKamey, E. Lara-Curzio, B. A. Pint, I. G. Wright, and R. R. Judkins

Introduction

Hot-gas filtration is a key enabling technology for turbine-based power generation using coal-derived gases from integrated gasification combined cycles (IGCC) and pressurized fluidized bed combustors (PFBCs). Particle removal from hot gases produced by coal gasification or combustion is vital to achieving the efficiency and emission goals offered by such advanced systems as the gas turbine must be protected from degradation by erosion, corrosion, or deposition associated with the entrained species. Hot-gas filters offer a promising method of providing such protection if the reliability and durability of such devices can be assured.

Materials used in hot-gas filters are required to withstand prolonged exposure to corrosive, high-temperature gaseous environments as well as to condensable vapors and solid species, some of which may have the potential for localized interaction with the filter material after extended times. The gas streams may be oxidizing (PFBCs) or reducing, in which the sulfur species are largely in the form of H_2S (in the case of the product gas from IGCC processes or from carbonizers). Degradation of metallic filter elements has been observed under oxidizing, sulfidizing, and/or carburizing conditions and acts as a driving force for the development of ceramic hot-gas filters, particularly for the higher temperatures associated with advanced gasification and combustion designs. However, iron aluminides can also be considered for such applications because they offer the reliability advantages of metallic filters and typically have good to exceptional high-temperature corrosion resistance in a variety of sulfur-bearing environments relevant to coal-derived energy production systems.¹⁻⁴

Iron-Aluminide Filter Materials

The materials examined in this study were fabricated as sintered powder iron-aluminide filter products.⁵ Cylindrical, sintered metal filter elements of Fe-28 at.% Al-2% Cr with and without 0.1% Zr (FAS and FAS-Zr, respectively) were fabricated by Pall Corporation (Cortland, NY) from water-atomized alloy powder produced by Ametek, Inc. (Eighty-Four, PA). Prior work has shown that the as-fabricated materials contained numerous small oxides on pore surfaces and at the boundaries of agglomerated powder particles.^{5,6} These oxides appeared to be alumina and zirconia that formed during the water atomization process and then most likely coarsened during subsequent processing to form the filters. However, these oxide particles had little effect on the deformation behavior of the filter material. Fractography of ruptured o-rings cut from as-fabricated elements

showed transgranular failure through fully sintered material and that the fracture surfaces were free of oxide particles. As such, the fracture surfaces were typical of the ductile failures observed for fully dense iron aluminide and, when allowance is made for the reduced load-bearing area, the measured strengths appear to be consistent with those for similar dense alloys.^{5,6}

The particular composition of the Fe₃Al alloy used for these filter elements (see above) was chosen on the basis of several factors. First and foremost, prior studies showed that maximum sulfidation resistance in high p_{S₂}, low p_{O₂}, H₂S-containing environments was observed for Fe-Al alloys with > 20 at.% Al and ≤ 2 at.% Cr.^{1,4} An iron aluminide with 28 at.% Al therefore served as the base composition as most of the Fe₃Al development effort has been focused on alloys of this Al concentration and the chromium level was set at 2 at.% to minimize sulfidation and improve ductility.⁷ Other work showed that small concentrations of Zr improved the adherence of alumina scales grown on iron aluminides (albeit at 900°C and above).⁴ Indeed, a substantial research effort has now demonstrated that there are several reactive element (RE) additions, such as zirconium, that improve scale adherence of iron aluminides, but the effectiveness of these REs depends on an optimal concentration and its distribution in the alloy.⁸⁻¹⁰

Test-bed Exposures and Evaluation Procedures

Iron-aluminide filter elements (produced by Pall Corporation) that were exposed in either the Fluidized Bed Gasifier/Modular Gas Cleanup Rig¹¹ at the Federal Energy Technology Center (FETC), Morgantown, WV or in the Transport Reactor Demonstration Unit¹² at the University of North Dakota Energy and Environment Research Center (EERC) were evaluated. Exposure conditions are listed in Table 1 and a photo of one of the tubes exposed at EERC is shown in Fig. 1. Both test beds are mainly used for studies of process and operating conditions. Consequently, as indicated in Table 1, the environmental conditions were not constant during the course of the respective runs. In the case of the EERC exposure, gasification conditions in the transport reactor were preceded by a

Table 1. Exposure Conditions For Iron-Aluminide Filter Elements

Designation ^a	Temp. (°C)	Exposure Time (h) ^b	H ₂ S Concentration (vol. ppm)
FETC-3	570	100 (g)	1000 - 8000
FETC-2	570	300 (g)	1000 - 8000
EERC-1,2 ^c	540	300 (c) 280 (g)	500 -1200

^aFETC – exposures in the Fluidized Bed Gasifier/Modular Gas Cleanup Rig at the Federal Energy Technology Center, Morgantown, WV; EERC – exposures in the Transport Reactor Demonstration Unit in the Energy and Environment Research Center at the University of North Dakota, Grand Forks, ND.

^bg: gasification conditions, c: combustion conditions

^ctwo elements exposed under similar conditions



Fig. 1. Photograph of FAS filter element after exposure in EERC test bed. Diameter is approximately 60 mm.

combustion phase. Nevertheless, these types of test beds are valuable in providing some simulation of the types of complex environments in which filter materials will be exposed when used in operating plants.

O-ring specimens (nominal inner diameter of 56 mm and wall thickness of 2 mm) were cut from the exposed filters and also from unexposed, co-processed elements in order to evaluate changes in strength due to exposures in the respective test-bed environments. Evaluation procedures consisted of mechanical testing of o-rings by internal pressurization to determine tangential (hoop) stress-strain behavior and microstructural analysis by optical and scanning electron microscopy (SEM) and energy dispersive x-ray analysis (EDS).

The internal pressurization tests were conducted in ambient air at room temperature by using a positive radial-displacement wedge mechanism that is being developed for eventual use at high temperature. The o-ring specimens were 12.7 mm long. (The hoop strength of iron-aluminide filter material was independent of specimen length.) The machined edges of the specimens were dry-sanded to a smooth finish using 400 grit silicon carbide paper.

Results and Discussion

Exposures in the FETC test bed (Table 1) resulted in a 33% decrease in the tensile hoop strength of the filter elements for both 100- and 300-h exposures. These data are shown in Fig. 2, where the average peak loads are compared to that for the co-processed unexposed (control) element. The error bars in Fig. 2 represent the standard deviation from the average peak load based on evaluation of six specimens. In addition to the reduction in tensile strength, exposures in the FETC test bed resulted in a slight decrease in ductility compared to that of the co-processed unexposed element. However, exposed specimens still exhibited a well-defined yield point and non-linear stress-strain behavior. These results are consistent with fractographic observations that revealed that the specimens failed transgranularly through the connecting ligaments both in the unexposed and as-exposed conditions (see Fig. 3). Such ductile failure is characteristic of iron-aluminide alloys.⁷

Microstructural analysis revealed the presence of an Al-rich oxide scale along all exposed surfaces of the filter elements exposed in the FETC test bed for 100 and 300 h (see Fig. 4).

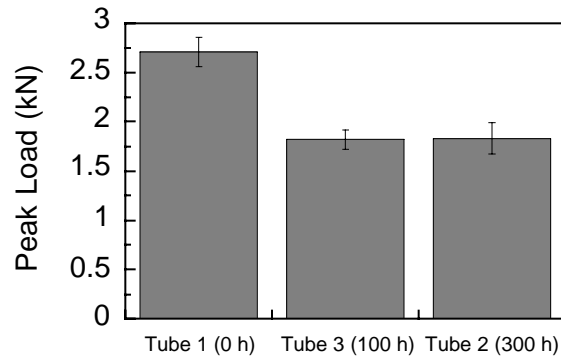


Fig. 2. Average tangential load of o-rings cut from filter elements, FETC exposures; Tube 1 was unexposed.

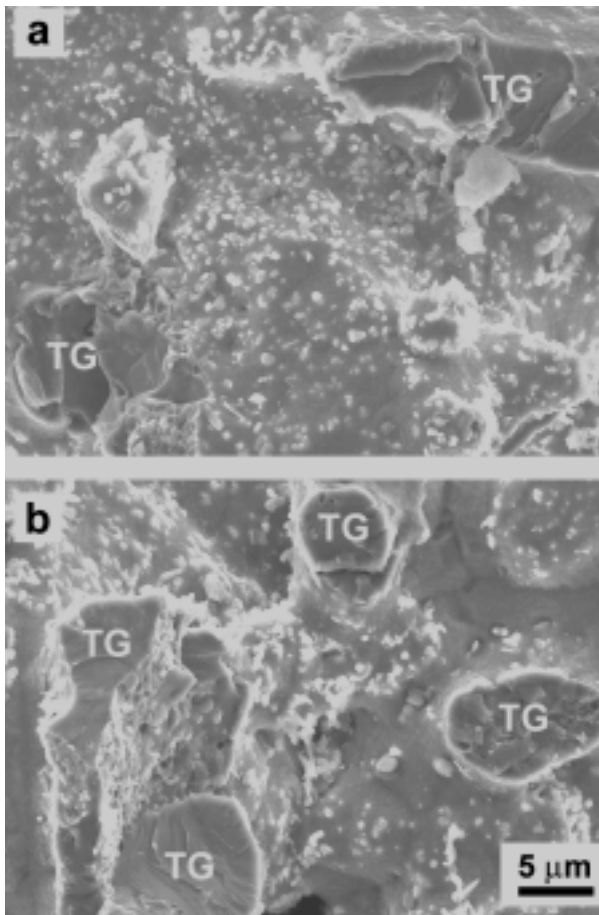


Fig. 3. Fracture surfaces of iron-aluminide filter material (a) as-processed, unexposed (b) after exposure for 300 h in FETC test bed. Similar transgranular (TG) fracture behavior was observed in both cases.

Compared to an unexposed filter specimen, which had an oxide layer of no more than 0.5 μm , these scales were $\sim 1 \mu\text{m}$ in thickness and appeared to have grown fairly uniformly; there was no indication of any localized corrosion. The scale thickness measured after 300 h was not much greater than what was observed after 100 h, thus indicating protective oxide behavior. A 1- μm scale is somewhat thicker than what would be expected based on extrapolation of laboratory data for FAS generated at higher exposure temperatures.^{1,6} This may reflect the influence of sulfur and, possibly other reactive species present in the test-bed environment, on the alumina scale growth rate.¹ Nevertheless, the amount of corrosion observed in the present case was quite limited compared to what would be observed for steels and nickel-based alloys exposed under somewhat similar conditions.¹³

In contrast to the results for the FETC exposures, the iron-aluminide elements from the EERC test bed (Table 1) showed very little

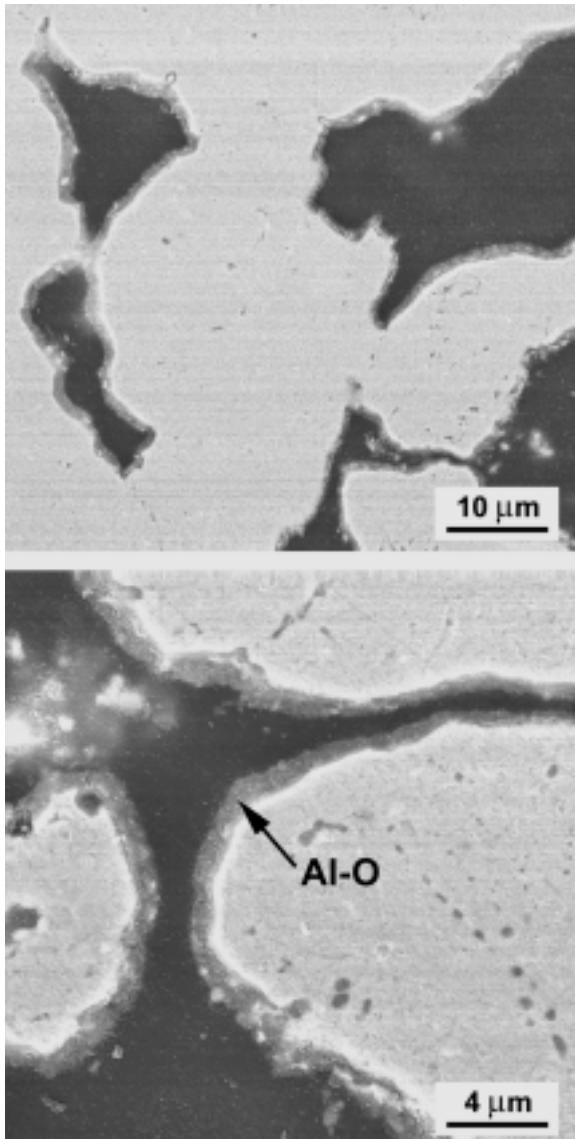


Fig. 4. Iron-aluminide filter material after exposure in FETC test bed for 100 h at 570°C.

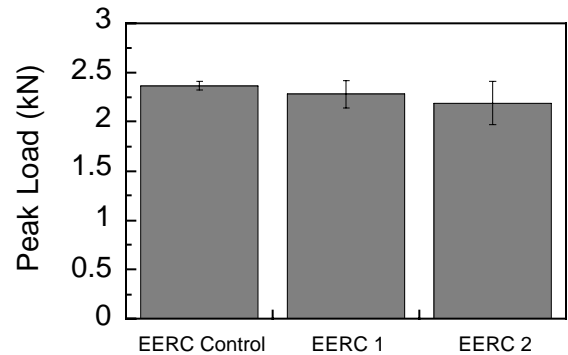


Fig. 5. Average tangential load of o-rings cut from filter elements, EERC exposures.

degradation of mechanical properties. There was only ~5 % reduction in tangential hoop strength relative to the starting (control) material (Fig. 5) and the fracture of the o-ring specimens was transgranular. The insignificant loss of strength observed for the EERC exposures is possibly related to the lower average H_2S concentration as well as the combustion phase of operation, which may have helped form a protective oxide layer before the onset of gasification. Preliminary SEM/EDS analyses have shown very limited corrosion of the filter materials from the EERC test bed. Observations of the fracture surfaces indicated the presence of a general growth of

the oxide coating similar in nature to that discussed above for the FETC filter specimens, but a more rigorous analysis, including determination of the scale thickness, is yet to be conducted.

Analyses to date have not indicated a direct cause of the strength loss for the FETC exposures. While it is reasonable to expect that the strength reduction must be related to the corrosion reactions, present and prior observations^{5,6} indicate that the depth of alloy affected by such is not great. Nevertheless, given that the filter materials of this study are composed of full-density ligaments of small diameter, relatively slight corrosion-induced modifications can result in a decrease in load bearing area and a concomitant reduction in strength. Also, localized corrosion reactions can facilitate fracture and lower strain to failure (and strength).⁶ However, in the present case, no such

products were observed. In addition, the thin alumina scale that forms on exposure can, in itself, serve to modify surface conditions such that cracks that lead to failure more readily form upon application of a load. This may be of particular relevance to iron aluminides as there have been some indications that the fracture behavior and strength of this type of alloy are sensitive to surface flaws.¹⁴

It is not unusual for metallic or ceramic hot-gas filter materials to lose strength due to exposure at elevated temperatures in application environments. Even so, in the present case, retained hoop strength and ductility appear more than adequate for the anticipated filter application. However, a key issue is whether strength will continue to decrease with increasing exposure time or, rather, reach a limiting value. While this time-dependence needs to be examined rigorously, the present data indicate that such a steady-state strength may be realized for the FETC exposures because the fraction of retained strength after 300 h of exposure was the same as after 100 h (Fig. 2). In both cases, the average as-exposed peak loads were similar as were the thickness of the respective scales that formed. These observations suggest that, as discussed above, strength loss could be associated with uniform scale growth and loss of load-bearing area. Alternatively, if strength loss was associated with creation of surface flaws by scaling, a steady-state retained strength could also be reached as the concentration of reaction products that initiate fracture saturate with time.

The issue of changes in retained strength with exposure time is being directly addressed by examining iron aluminide filter elements held in the same environment for a variety of exposure periods. This is done through laboratory exposures and also by evaluating filter elements that have seen service in operating advanced coal-fired plants. Analyses of elements from such plants will yield the most useful data regarding long-term corrosion effects on iron-aluminide hot-gas filters in appropriate environments.

Summary

Iron aluminides have shown good to excellent high-temperature corrosion resistance in sulfur-bearing environments and thus have potential for use as the material of construction for metallic filters used to clean fossil-fuel-derived gases prior to their introduction into gas turbines. Alloys based on Fe₃Al have sufficient ductility and strength for filter applications. Their corrosion resistance at elevated temperatures derives from the formation of a protective oxide layer even at low oxidizing potentials. Results of preliminary analyses of sintered-metal iron aluminides exposed at 540-570°C in test beds simulating environments experienced by filters exposed in gasifiers showed that a protective oxide layer still exists under these conditions and, accordingly, corrosion is limited. Insignificant (5%) to moderate (33%) strength reductions after 300 h of exposure to gasification-type conditions were measured. Strength loss did not monotonically decrease with time; similar filter elements exposed for 100 and 300 h showed the same retained strength consistent with the formation

of an ~1-um thick Al-rich oxide scale in both cases. Little environmental degradation of ductility was observed.

Acknowledgments

The authors thank M. June of Pall Corporation for filter materials and associated information regarding performance, control specimens, and certain exposure conditions and S. Richardson and T. McMahon at FETC and M. L. Swanson and J. P. Hurley at EERC for providing the exposed filter elements for evaluation. This research was sponsored by the U.S. Department of Energy, Office of Fossil Energy, through the Federal Energy Technology Center (Morgantown, WV) under contract DE-AC05-96OR22464 with Lockheed Martin Energy Research Corporation.

References

1. J.H. DeVan, pp. 107-15 in Oxidation of Intermetallics, T. Grobstein and J. Doychak, Editors, The Minerals, Metals, and Materials Society, Warrendale, PA, 1989.
2. F. Gesmundo, D. Poggi, O. Tassa, F. Viani, and A. DiGianfrancesco, pp. 1657-67 in Materials for Advanced Power Engineering, D. Cousouradis and et al., Editors, Kluwer Academic Publishers, 1994.
3. K. Natesan and P.F. Tortorelli, pp. 265-80 in Nickel and Iron Aluminides: Processing, Properties, and Applications, S.C. Deevi, et al., Editors, ASM International: Materials Park, OH, 1997.
4. P.F. Tortorelli and K. Natesan, *Mater. Sci. Eng. A.*, 258 (1998) 115-25.
5. M. June and J.W. Sawyer, paper PB16 in *Proc. Adv. Coal-Based Power and Environmental Systems '98*, U. S. Department of Energy, 1998.
6. P.F. Tortorelli, E. Lara-Curzio, C.G. McKamey, B.A. Pint, I.G. Wright, and R.R. Judkins, paper PB7 in *Proc. Adv. Coal-Based Power and Environmental Systems '98*, U. S. Department of Energy, 1998.
7. C.G. McKamey, J.H. DeVan, P.F. Tortorelli, and V.K. Sikka, *J. Mater. Res.*, 6 (1991) 1779-1805.
8. B.A. Pint, P.F. Tortorelli, and I.G. Wright, *Werskt. Korros.*, 47 (1996) 663-74.
9. B.A. Pint, *Mater. Sci. Forum*, 251-254 (1997) 397-404.
10. B. A. Pint, P.F. Tortorelli, and I.G. Wright, *Mater. High Temp.*, 1999. accepted for publication.
11. T.R. McLendon and S.W. Richardson, paper PB3 in *Proc. Adv. Coal-Based Power and Environmental Systems '97*, U. S. Department of Energy, 1997.
12. M.L. Swanson, M.D. Mann, and E.A. Sondreal, Energy and Environmental Research Center report 98-EERC-10-12, University of North Dakota, 1998.
13. M. Nieminen, K. Kangasmaa, E. Kurkela, and P. Ståhlberg, pp. 120-31 in High Temperature Gas Cleaning, E. Schmidt, P. Gäng, T. Pilz and A. Dittler, Editors, Institut für Mechanische Verfahrenstechnik und Mechanik, Universität Karlsruhe (TH), Karlsruhe, 1996.
14. C.G. McKamey, Oak Ridge National Laboratory, unpublished research, 1992.

ENVIRONMENTAL ANALYSIS SUPPORT

R. L. Miller

Activities in environmental analysis support included assistance to the Federal Energy Technology Center (FETC) at Morgantown and Pittsburgh in reviewing and preparing documents required by the National Environmental Policy Act (NEPA) for projects selected for the Clean Coal Technology (CCT) Program and for the Low Emission Boiler System (LEBS) Program. An important activity for the CCT Program was the preparation of an Environmental Impact Statement (EIS) for a new circulating fluidized bed (CFB) combustor fueled by coal and petroleum coke to repower an existing steam turbine at Jacksonville Electric Authority's (JEA's) Northside Generating Station in Jacksonville, Florida. An important activity for the LEBS Program was the preparation of an EIS for integrated coal-fired technologies for electric power generation at the proof-of-concept scale adjacent to the Turriss Coal Company's existing underground coal mine near Elkhart, Illinois.

ENVIRONMENTAL SUPPORT TO THE LOW EMISSION BOILER SYSTEM PROGRAM

R. L. Miller

Work during this period included the preparation for DOE's Federal Energy Technology Center (FETC) of an Environmental Impact Statement (EIS) to evaluate the potential environmental impacts associated with constructing and demonstrating a new coal-fired Low Emission Boiler System (LEBS) for electric power generation at the proof-of-concept scale. The EIS will be used by DOE in making a decision on whether or not to provide cost-shared funding to design, construct, and demonstrate the integrated technologies proposed by a team headed by DB Riley, a private sector participant in the LEBS program. The goal of the LEBS program is to provide the U.S. power industry with a reliable, economic, highly efficient, and environmentally preferred alternative to current coal utilization technologies.

The proposed project would demonstrate the technologies using a new 86-MW coal-fired power plant to be built adjacent to an existing underground coal mine owned and operated by Turriss Coal Company, a member of the project team. The site is situated in central Illinois, about 2 miles southeast of the town of Elkhart and about 17 miles northeast of Springfield. The project would incorporate the following technologies: (1) a slagging combustor, which is U-shaped to increase the combustion reaction time; (2) low oxides of nitrogen (low-NO_x) burners, staged combustion, and coal reburning (injecting about 10–15% of the coal higher in the combustor) for NO_x control during combustion, in combination with a selective catalytic reduction (SCR) post-combustion NO_x control system; (3) a wet limestone scrubbing system for sulfur dioxide (SO₂) capture; and (4) an electrostatic precipitator for particulate removal from the flue gas. The technologies are expected to capture at least 96% of SO₂ emissions, decrease NO_x emissions by 85%, and remove 99.8% of particulate matter.

Construction of the proposed facility would begin in October 1999 and continue until about October 2001. The demonstration would be conducted during a 6-month period in late 2001 and early 2002. If the demonstration is successful, commercial operation of the facility would follow immediately; the power plant would be designed for a lifetime of 30 years. The facility would be fueled with coal from the adjacent mine, and electricity generated by the facility would be provided to the mine and to the local power grid. The captured SO₂ would be converted to commercial-grade gypsum, which would be marketed as feedstock for wallboard production. Bottom ash from coal combustion would be marketed for commercial applications such as roadbed or construction material.

Potential impacts to environmental resources, including air quality, groundwater, and land availability, that could result from construction and operation of the proposed project were analyzed. Key findings include that emissions from the proposed facility would not exceed National Ambient Air Quality Standards (NAAQS) or Prevention of Significant Deterioration (PSD) increments. For the latter set of standards, the emissions would always be less than 20% of the allowable degradation. The contribution of emissions from the proposed facility to acidic deposition and to global climate change is expected to be negligible.

Initial results indicate that the aquifer may be capable of supporting the additional requirements of groundwater withdrawal during facility operation, but declines in groundwater levels may occur in nearby water supply wells, including the village of Elkhart municipal water well, located approximately 1 mile west of the proposed site. In addition, the relatively large additional consumption could degrade water quality in the aquifer, resulting in increased total dissolved solids, heavy metals, and dissolved minerals. However, the effects of drawdown and groundwater quality degradation can be mitigated somewhat by using multiple wells for groundwater withdrawal with sufficient separation from the village of Elkhart well. In addition, the use of field drainage runoff that passes through the Turriss property is being pursued as a mitigation measure that could supplement groundwater withdrawal.

With the construction of a new coal combustion waste disposal area at the adjacent mine, sufficient disposal capacity would be available to accommodate all solid wastes generated by the proposed facility during its 30-year commercial operation, even if no bottom ash or gypsum were sold or used. If the proposed waste disposal area is not constructed, the Turriss Coal Company would have other options to dispose of the material, including (1) reducing the current level of coal combustion ash received from offsite customers, and (2) transporting solid waste off the site to a permitted landfill.

Impacts to other resource areas would be minor. Flooding at the site is not anticipated, and floodplain encroachment would not occur. There are no significant wetland resources near the proposed site. No appreciable impacts on terrestrial or aquatic ecosystems are expected. There are no historic or archaeological resources known to occur on the project site. Construction and operation of the proposed facility are anticipated to have only minimal impacts on socioeconomic factors in the surrounding area, and no environmental justice impacts are expected. With respect to aesthetic resources, construction of the proposed project would produce slight short-term visual impacts, but visual characteristics would not differ appreciably over the long term from those at the site now. No appreciable impacts are expected with regard to noise, traffic, land use, and human health including worker safety.

ENVIRONMENTAL SUPPORT TO THE CLEAN COAL TECHNOLOGY PROGRAM

R. L. Miller

Work for FETC during this period included the preparation of an EIS to evaluate the potential environmental impacts associated with constructing and demonstrating a new circulating fluidized bed (CFB) combustor fueled by coal and petroleum coke to repower an existing steam turbine to generate nearly 300 MW of electricity. The EIS will be used by DOE in making a decision on whether or not to provide cost-shared funding to design, construct, and demonstrate the CFB technology under the Clean Coal Technology (CCT) Program. The proposed project would be located at Jacksonville Electric Authority's (JEA's) Northside Generating Station in Jacksonville, Florida, which currently consists of three heavy oil- and natural gas-fired steam generation units and four diesel oil-fired combustion turbine units. Construction would begin in October 1999 and continue until December 2001. Demonstration of the proposed project would be conducted during a 2-year period from March 2002 until March 2004. In addition, JEA plans to repower a second Northside steam turbine about 6 to 12 months after the proposed project without cost-shared funding from DOE.

The overall objective of the project is to demonstrate the feasibility of CFB technology at a size that will be attractive for large-scale utility operation. In a CFB combustor, coal and coal/fuel blends, air, and limestone are introduced into the lower portion of the combustor, where initial combustion occurs. As the fuel is reduced in size through combustion and breakage, it is transported higher in the combustor where additional air is introduced. Ash and unburned fuel and limestone pass out of the combustor, collect in a particle separator, and recirculate to the lower portion of the combustor. Sulfur reacts with limestone added in the furnace to form ash that can be marketed as a useful byproduct such as roadbed material. The project is expected to provide JEA with a low-cost, efficient, and environmentally-sound generating resource.

The EIS evaluates the principal environmental issues, including air quality, traffic, noise, and ecological resources, that could result from construction and operation of the proposed project. Key findings include that maximum modeled increases in ground-level concentrations of SO₂, nitrogen dioxide (NO₂), and particulate matter (for the proposed project alone or in conjunction with the second repowering) would always be less than 10% of their corresponding standards for increases in pollutants. For potential cumulative air quality impacts, results of modeling regional sources and the proposed project indicate that the maximum 24-hour average SO₂ concentration would be 97% of the corresponding Florida standard. After the second repowering, a decrease in ground-level concentrations of SO₂, NO₂, and particulate matter would be expected

most of the time at most locations in the surrounding area (the overall effect would be beneficial). Results indicate that the 24-hour average SO₂ concentration for regional sources and the proposed project in conjunction with the second repowering would be 91% of the standard. Concentrations for other averaging periods and pollutants would be lower percentages of their standards. Regarding other toxic air pollutants, findings indicate that the proposed project alone or in conjunction with the second repowering would not lead to any exceedances of, or close approaches to, guideline values except for cancer risk. The target value for cancer risk would be approximately equaled; however, given the upper-bound assumptions in the estimate, actual risk would be less.

With regard to threatened and endangered species, impacts to manatees, gopher tortoises, and other species would be minimal or non-existent. Construction-induced traffic could result in substantial congestion. In the unlikely event that all coal were transported by rail, additional trains per week would exacerbate impacts associated with noise, vibration, and blocked roads at on-grade crossings. Additional train traffic could be minimized by relying more heavily on barges and ships for coal transport, which is likely to be a more economic fuel delivery mode. During construction of the proposed project, noise levels would increase from the current operational levels. Except during steam blowouts, and possibly during operation of equipment used to construct a nearby segment of a conveyor, construction noise should not appreciably affect the background noise of nearby residences or exceed local noise limitations. The preferred alternative for management of the combustion ash would be to sell it as a by-product to offsite customers. If more than approximately 70% of the ash could be sold over the 30-year lifetime of Northside Generating Station, the 40-acre storage site would be sufficient for complete containment.

BIOPROCESSING RESEARCH

A. P. Borole

Work on the Fossil Energy Bioprocessing Research Program includes fundamental research for coal applications, with emphasis on advanced reactor design for conversion of coal synthesis gas to liquid fuels, biological upgrading of petroleum feedstocks and heavy oils via microbial and enzyme biocatalysis, and integration of combustion power systems with CO₂ sequestration. In addition, the program includes studies of the biological quality of soils containing hydrocarbons and bioremediation alternatives to reduce ecological risk.

BIOLOGICAL UPGRADING OF PETROLEUM FEEDSTOCKS AND HEAVY OILS VIA MICROBIAL AND ENZYME BIOCATALYSIS

Borole A. P. and E. N. Kaufman

INTRODUCTION

Biological removal of organic sulfur from crude oil offers an attractive alternative to conventional thermochemical treatment due to the mild operating conditions afforded by the biocatalyst. In order for biodesulfurization to realize commercial success, reactors must be designed which allow for sufficient liquid / liquid and gas / liquid mass transfer while simultaneously reducing operating costs. To this end, we have developed an electro-spray reactor for the desulfurization of the model compound dibenzothiophene (DBT) as well as actual crude oil. The electro-spray reactor (ESR) creates an emulsion of aqueous biocatalyst (5 - 20 μm diameter droplets) in the organic phase by concentrating forces at the liquid /liquid interface rather than imparting energy to the bulk solution as is done in impeller mixed reactors. This reactor was further developed to demonstrate its applicability to heavy oil processing. This work was conducted as part of a cooperative research and development project involving Oak Ridge National Laboratory (ORNL) and the following companies: Baker Petrolite, Chevron, Energy BioSystems Corporation (EBC), Exxon and Texaco. These industrial partners contributed crude oil, biocatalyst and conducted chemical analysis of the crude oil samples. This project was completed in October 1998 and a final report issued to DOE.

In our continued efforts towards development of alternate technologies for heavy oil upgrading, our proposal to investigate enzymatic methods to effect changes in heavy oil via partial oxidation and bioconversion was accepted and the work was initiated in April 1999. Several oil companies have indicated their interest in working with us to develop this technology and we are in the process of forming a cooperative research and development agreement with these companies.

A third project to study biodesulfurization of diesel was initiated in November 1998. This work is being conducted in collaboration with Petro Star, Inc, a refinery located in Anchorage, Alaska. The researchers at Petro Star have developed a process to selectively oxidize organosulfur compounds present in diesel followed by extraction of the oxidized sulfur compounds with an organic solvent, resulting in a high sulfur diesel extract. ORNL is working with Petro Star and Dr. Eduardo Diaz from Consejo Superior de Investigaciones Cientificas (CSIC), Madrid, Spain to develop a biological desulfurization process to remove sulfur from the high sulfur diesel extract.

DISCUSSION OF CURRENT ACTIVITIES

Reactor Development for Heavy Oil Processing

Biodesulfurization experiments were conducted in the electro-spray reactor to demonstrate removal of sulfur from the model system dibenzothiophene dissolved in hexadecane. Further development of the reactor was conducted to determine its applicability to process heavy oils. Previous demonstrations of formation of a fine emulsion in the reactor with model organic liquids was done visually using fiber optic probes and high speed video microscopy. However this was not possible in crude oil system due to its opaqueness. Therefore experiments were conducted using transparent model organic liquids with high viscosity such as mineral oils. The parameters obtained from these systems were used to develop a model between nondimensional groups, Reynolds number and electrical Bond number. This model was used to predict spraying parameters (applied voltage and frequency) for heavy oils and the results confirmed by microscopic observations of reactor samples. Figure 1 shows the crude oil/aqueous emulsions formed at different voltages. Crude oils with API gravity varying from 23° to 16° were studied and the spraying parameters determined.

In addition to the microscopic observations, moisture content was determined using Karl-Fisher titration. Pure Sand Flat oil used in the above experiment contained about 0.7% water. The sample collected from the spraying zone contained about 10.9% water. These results demonstrate feasibility of spraying an aqueous phase into heavy oils in the electro-spray reactor.

Sulfur Removal from Crude Oils

The biocatalyst provided by Energy BioSystems (a *Rhodococcus* species, see Figure 2) was used to study desulfurization of heavy crudes. In order to determine the effect of API gravity (and viscosity) on biodesulfurization, experiments were conducted with crude oils by varying the API gravities from 23 to 16.4° in the batch stirred reactor and electro-spray reactor. These crude oils were obtained by blending Sand Flat (API gravity 23°) and Kern River (API gravity 14.0°) crude oils. The oil blends were provided by Dr. Robert Shong at Texaco. The oils were also spiked with dibenzothiophene (DBT) to bring the level of the sulfur substrates (DBT and branched DBTs) to a high enough level to allow desulfurization studies. The samples collected from the batch stirred reactor were analyzed by GC-SCD. The results are shown in Figure 3. The results indicate a substantial decrease in DBT and sulfur concentration. The rate of DBT removal was different for each oil; however, no specific trend was observed in relation to the API gravity.

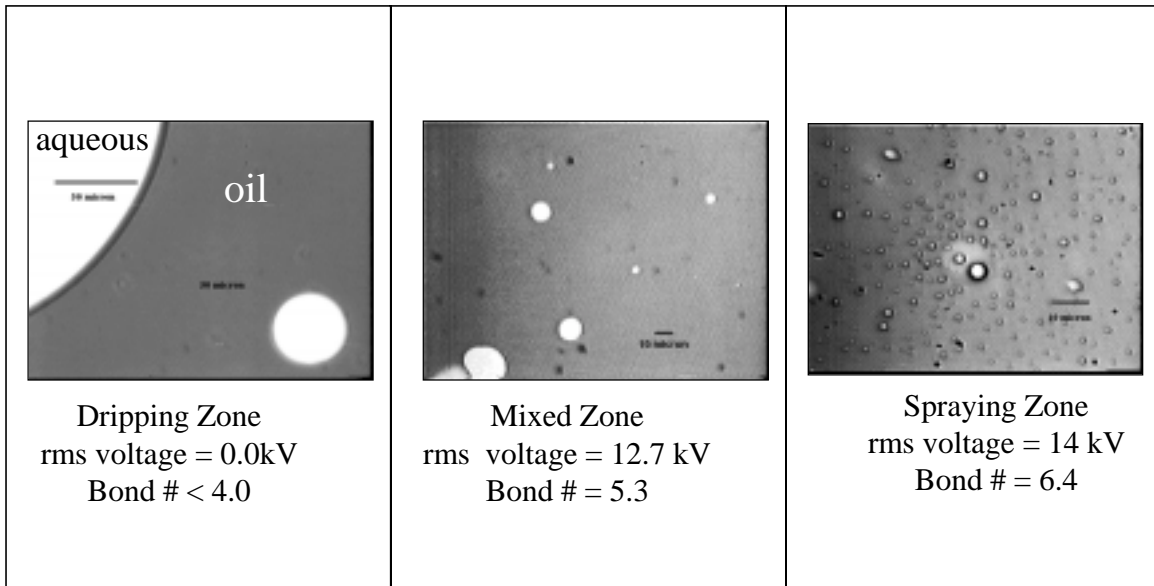


Figure 1. Microscopic observations of aqueous/oil (Sand Flat crude oil) emulsion samples collected from the EPC under varying electrical field strength conditions.

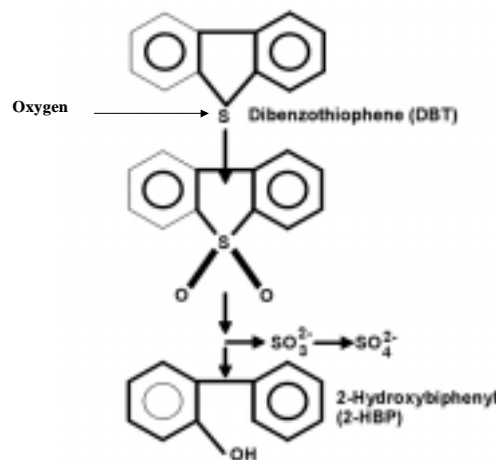


Figure 2. Biochemical mechanism of desulfurization by *Rhodococcus* sp.

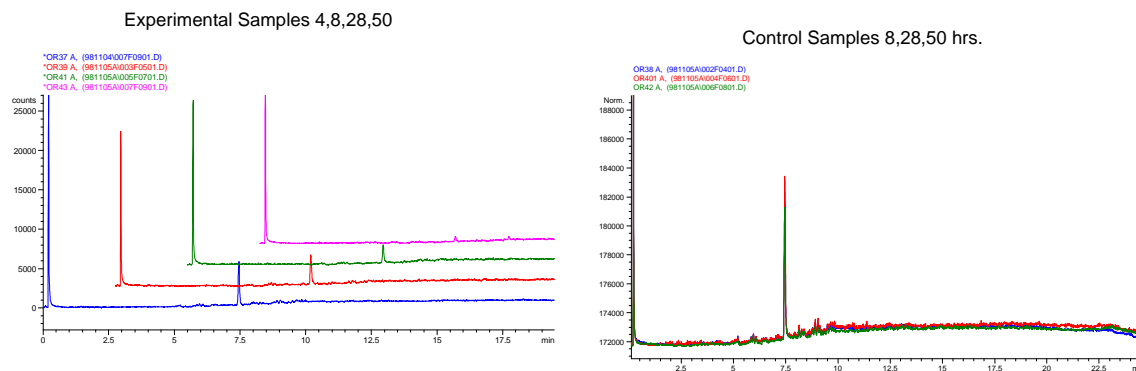


Figure 3. GC-SCD analysis of 16.4° API oil blend showing removal of DBT with time in the presence of a biocatalyst. No removal was observed in the control reactor.

Biological Desulfurization of Diesel Extract

The diesel extract produced from Petro Star's chemical oxidation and extraction process consists of aromatic sulfones as the major species. In order to remove sulfur from these organosulfur compounds ORNL is investigating aerobic as well as anaerobic pathways. CSIC has supplied ORNL with engineered strains which are being tested against model sulfone compounds and the diesel extract to develop a biodesulfurization process.

ACKNOWLEDGMENTS

The multi-oil company CRADA project was supported by the Office of Oil & Gas Processing, U.S. Department of Energy under contract DE-AC05-96OR22464 with Lockheed Martin Energy Research Corp. The desulfurization of diesel project is being supported by Petro Star, Inc.

REFERENCES

Borole, A. P. and Kaufman E. N.; "Process considerations in crude oil biodesulfurization," a paper was presented at the *American Chemical Society Annual Meeting*, at Annahiem, CA in March 1999.

Borole, A. P. and Kaufman E. N.; "Bioprocessing of heavy oils and desulfurization using electro-spray reactors," a paper was presented at the *American Chemical Society Annual Meeting*, at Boston, MA in August 1998.

Tsouris, C.; Borole, A. P; DePaoli, D.; and Kaufman, E. N.; "Hydrodynamic behavior of an electrically driven bioreactor for oil desulfurization," accepted for publication in *Ind. & Eng. Chem. Res.*, 1999.

Kaufman, E. N.; Harkins, J. B. and Borole A. P.; 'Comparison of electro-spray and batch stirred reactors for biodesulfurization of dibenzothiophene in crude oil and petroleum feedstocks,' p. 127-140, **73**, *Appl. Biochem. Biotech.*

FUNDAMENTAL BIOPROCESSING RESEARCH FOR COAL APPLICATIONS

Thomas Klasson and Brian Davison

The purpose of this program is to gain a fundamental understanding and sound scientific and technical basis for evaluating the potential roles of innovative bioprocessing concepts for the utilization and conversion of coal and the mitigation of carbon dioxide. This will be done in the context of the ongoing bioprocessing R&D effort supported in the Office of Fossil Energy AR&TD program area. Experimental studies are exploring the three areas of biological processes. The funding for this project began March 1999.

- 1. Biofiltration of NO_x Compounds:** Oxygen Effects on Microorganisms, Oxygen Removal, and Mathematical Modeling. This is a collaborative research effort by ORNL and Idaho National Engineering and Environmental Laboratory (INEEL). The work will build on previous research at INEEL in the area of NO_x biofiltration of coal combustion gas and the recent work conducted at ORNL in mathematical modeling and prediction of trickling biofilter performance.

Accomplishments: Based on discussions with INEEL researchers, a blend of nitrogen (N₂) and nitrous oxide (NO) was purchased for use in trickling biofilters at ORNL. Enzymes immobilized in a gel matrix have been developed in collaboration with a local company for evaluation of oxygen removal from NO/N₂ mixtures.
- 2. Biological Conversion of Poorly Water-soluble Gases:** This task based on previous work conducted at ORNL under this program in FYs 1997–98. During these studies it was found that alteration of water solubility of poorly water-soluble gases could significantly increase the biological growth and conversion of gas phase reactants. The work will focus on the enhancement of water solubilities by using a variety of co-solvents and will benefit the conversion of NO_x and other such gases.

Accomplishment: An aerobic system was studied in March for the enhancement of conversion of gases. As a model system the conversion of toluene by *Pseudomonas putida* F-1 was studied in stirred tank reactors. The work showed a increase in conversion of the gas when silicone oil was added to one reactor. A bioreactor containing the same amount of cell mass served as control. The experimental result is shown in Figure 1.

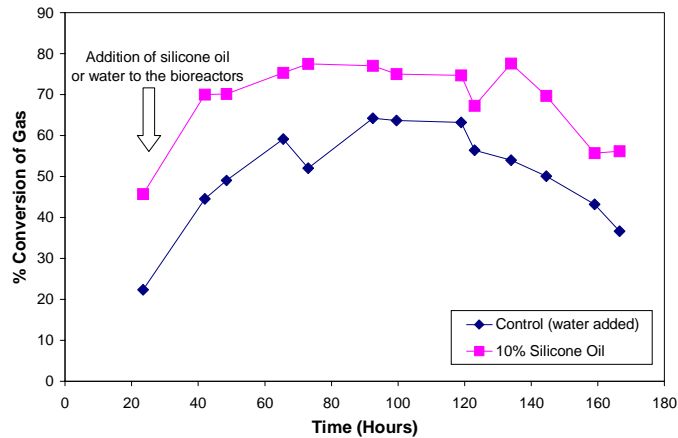


Figure 1. Silicone oil used as a solvent system to enhance the mass transfer rate. The total volume in each reactor was 1 liter. Cells were grown in each reactor in sterile basal salts medium. After 26 h, the contents from each reactor were mixed in a sterile 2-liter bottle. Then, 900 mL of this mixed culture was added to each reactor. Finally, 100 mL of sterile water was added to one reactor and 100 mL of silicone oil was added to the other.

3. Whittings as a Potential Mechanism for Controlling Atmospheric Carbon Dioxide

Concentrations: This is a joint task between ORNL and INEEL to develop a program targeting the understanding and influence of natural processes such as whittings and algal blooms for the purpose of CO₂ sequestration. This work will began in FY 1999 and continue in the out-years as a major effort. ORNL and INEEL are submitting complementary proposals.

Accomplishments: Several algal strains have been secured for studies of algal-mediated precipitation of carbonated and formation of extracellular skeletons.

BIOLOGICAL QUALITY OF SOILS CONTAINING HYDROCARBONS AND EFFICACY OF ECOLOGICAL RISK REDUCTION BY BIOREMEDIATION ALTERNATIVES

A. J. Stewart, B. E. Sample, and R. A. Efroymsen

INTRODUCTION

This project provides data and technical guidance to the Petroleum Environmental Research Forum (PERF; see <http://www.perf.org>), a consortium of petroleum-producing companies, about environmentally acceptable endpoints in relation to ecological risk of petroleum hydrocarbon residuals in soils. Technical aspects of this project focus on the relationship between χ chemically available= and χ biologically available= measurements of petroleum hydrocarbon compounds in soils, from a risk-based perspective. In many cases, clean-up standards for soils contaminated with petroleum hydrocarbons compounds are based either on concentrations of total petroleum hydrocarbons (TPH), or on concentrations of particular chemicals of concern (e.g., benzene, benzo[a]pyrene, etc.), measured in solvent extracts of soil samples. However, various chemicals present in TPH can permeate into soil particles. If this occurs, the particle-embedded hydrocarbons may be extractable by use of organic solvents, yet be essentially unavailable biologically. This situation clearly would reduce risk to biological receptors, and should be taken into account in (1) setting risk-based clean-up standards, and (2) developing and verifying efficacy of bioremediation clean-up techniques. The ideas summarized above guide the activities in our project.

DISCUSSION OF CURRENT ACTIVITIES

As in previous years, project activities in FY 1998 involve close collaboration with industry partners. We participated in two industry-hosted PERF meetings and gave invited presentations at a DOE National Petroleum Technology Office (NPTO) - PERF workshop on ecological risk assessment activities at petroleum exploration and production (E&P) sites (Table 1). We also attended annual meetings of the Society for Environmental Toxicology and Chemistry (SETAC) to present the results of tests conducted to estimate the toxicity of PERF soils to earthworms. At each of these meetings, we provided information on project status and shared technical information with petroleum industry partners and Department of Energy representatives. Each of these meetings also was formative, in that we received constructive, detailed feedback about industry needs in relation to ongoing or proposed project activities. As a result of this dialog, we elevated or lowered the priority of specific ongoing

or pending activities, in accordance with industry needs and recommendations. Noteworthy meetings and workshops attended which fostered project objectives are summarized below.

Table 1. PERF project-related travel

Meeting location	Meeting date	Meeting purpose
Bartlesville, OK	June 10-11, 1998	DOE-NPTO/ PERF workshop on assessing ecological impacts at upstream petroleum sites.
San Francisco, CA	September 1-4, 1998	PERF, 94-06 working group
Charlotte, NC	November 16-19, 1998	Present results of research with PERF soils at SETAC ¹ meetings
Houston, TX	January 25-28, 1999	PERF, 94-06 working group

¹Annual meeting of the Society for Environmental Toxicology and Chemistry; presentations given by Stewart et al. (1998), Sample et al. (1998), and Sample and Arenal (1998).

Development of ecological risk assessment tools

The biological-survey approach for acquiring data that could be used to support an ecological risk assessment was explored in FY 97 by field-testing selected methods at a Chevron site, and was well received by industry representatives. As a result, we elaborated on this approach in invited presentations at the NTPO-PERF workshop in Bartlesville (Table 1). There, Dr. Brad Sample (ORNL) spoke about developing an effective framework for assessing ecological risks of petroleum-derived materials in soil, and Art Stewart discussed the weight of evidence approach for use in ecological risk assessments of contaminated soils. Cost-effective methods suitable for documenting biological conditions at petroleum industry sites are presently being compiled as a project task.

Another activity during FY 98 was that of developing toxicological benchmarks for evaluation of exposures to petroleum materials. This task involved the preparation of a report, wherein we developed screening benchmarks (conservative estimates of thresholds for toxicity) for petroleum constituents (Sample et al. 1998). The primary focus of this report was on terrestrial organisms, but we also identified toxicity benchmarks for several aquatic and sediment-associated organisms. Toxicity benchmarks are used to focus an ecological risk assessment on particular chemicals of concern, and to eliminate from further consideration

chemicals that are clearly not of concern (see <http://www.hsrp.ornl.gov/ecorisk/ecorisk.html>). We found that benchmark development for petroleum mixtures and their constituents may not be definitive at this time, because the toxicity of many petroleum compounds varies among soils and in response to factors such as how long the chemicals have been in the soil, the environmental conditions under which the compounds Age@, etc. The exercise of compiling the literature and existing benchmarks for petroleum hydrocarbons is expected to be useful for assessments that follow the Risk-Based Corrective Action Framework or the ecological risk assessment framework for petroleum hydrocarbons that was developed previously by this project (cf. Suter 1997). The Benchmark report@ was reviewed by petroleum industry representatives in October, 1998; it will be revised and converted to a peer-reviewed manuscript in autumn, 1999. When the document is being revised, we will incorporate new data and identify trends in toxicity of different mixtures and soils.

Field demonstration of risk assessment framework

Our project's most ambitious, large-scale, long-term goal has been that of conducting a demonstration field-scale ecological risk assessment for one or more oil-contaminated sites, transparent to regulatory officials and in collaboration with industry representatives. In conceptualizing this task, we expected to determine the feasibility of this type of activity; identify the appropriate field and laboratory methods; identify field sites that could be used to support the study; and identify appropriate collaborators among other PERF participants. Several companies expressed interest in this task, because the key objective was that of progressing towards a high-level programmatic risk assessment for upstream sites, with a focus on screening out large numbers of sites that either have low ecological risk, and/or which would be expected to recover on their own by natural attenuation. The approach we outlined also seemed appropriate because the Gas Research Institute (GRI) and American Petroleum Institute (API) are now involved with upstream risk-based corrective action (RBCA) studies, some of which include elements developed from an ecological risk-assessment perspective. The plan we outlined to industry representatives at the PERF meetings in San Francisco and Houston (Table 1) was also submitted as a proposal to DOE-NPTO. But the general consensus of industry representatives was that the proposed activity was too costly and too long-term to be worth pursuing at this time.

Testing of biotreated TPH-contaminated soils for toxicity to earthworms

One task involved performing tests with earthworms to determine changes in soil biological quality resulting from a biotreatment method designed to lower the concentrations of TPH in soil. Two PERF Areference@ soils (which lacked significant TPH contamination) and two PERF Atest@ soils (contaminated with TPH) were used

in this task. These soils had been prepared previously in bulk quantities for PERF project 94-06 investigations (Linz and Nakles 1997). The four soils were biotreated in pan-test batches by Chevron investigators before being sent to ORNL for evaluation. We prepared dilutions of each test soil, the day before testing began, by mixing appropriate quantities of a test soil and that soil's corresponding reference soil, in amounts sufficient to make 1.50 kg of material. For example, test soil B was evaluated at three concentrations -- 25%, 40% and 60% of full-strength (Table 2), with dilutions being prepared by mixing B test soil and B reference soil in appropriate proportions. After the soil mixtures had been prepared, they were tested using procedures developed previously (Gibbs et al. 1996). Earthworm (*Eisenia foetida*) survival data from these tests showed that the biotreatment procedure seemed to improve the biological quality of each of the four soils (Table 2).

Table 2. *Eisenia foetida* survival in various concentrations of Petroleum Environmental Research Forum (PERF) test soils A, B, E and I, before and after the soils were aggressively biotreated in Chevron pan-tests.

Soil	Concentration Tested (% contaminated soil)	Earthworm Survival (%)		Improved? ¹
		Before Biotreatment	After Biotreatment	
A	10	90	85	---
A	30	90	85	---
A	100	45	75	Yes
B	25	95	95	---
B	40	85	80	---
B	60	75	90	Yes
E	75	80	100	Yes
E	100	95	100	---
I	75	100	100	---
I	100	40	95	Yes

¹Biotreatment-related changes in earthworm survival were scored as improved (yes) if survival percentage increased by 15 or more percentage points, and as worse (no) if earthworm survival percentage decreased by 15 or more percentage points, compared to survival in the soil before it was biotreated.

Miscellaneous progress

Publications in peer-reviewed technical journals

Napolitano, G. E., J. E. Richmond and A. J. Stewart. 1998. Characterization of petroleum-contaminated soils by thin-layer chromatography with flame ionization detection. *J. Soil Contam.* 7:709-724.

Technical presentations at national meetings

Sample, B. E. and C. A. Arenal. 1998. Allometric models for inter-species extrapolation of wildlife toxicity data: expanding the database. Poster presentation, Society of Environmental Toxicology and Chemistry 19th annual meeting, 15-19 November, 1998, Charlotte, NC.

Sample, B. E., Rose, K. A. Rose, Suter, G. W. II, and C. A. Arenal. 1998. Wildlife toxicity data and ecological risk assessment: problems and solutions. Platform presentation, Society of Environmental Toxicology and Chemistry 19th annual meeting, 15-19 November, 1998, Charlotte, NC.

Stewart, A. J., Wicker, L. F., Nazerias, M.S., Merchant, S. D., and D. K. Short. 1998. Testing an earthworm test for assessing the biological quality of soils: what works, and why? Platform presentation, Society of Environmental Toxicology and Chemistry 19th annual meeting, 15-19 November, 1998, Charlotte, NC.

Administrative accomplishments

An executed proprietary information agreement between Lockheed Martin Energy Research Corporation and Chevron Research and Technology Company was achieved on April 22, 1998, for PERF project No. 98-08.

REFERENCES

Gibbs, M. H., L. F. Wicker and A. J. Stewart. 1996. A method for assessing sublethal effects of contaminants in soils to the earthworm, *Eisenia foetida*. *Environ. Tox. Chem.* **15**:360-368.

Linz, D. G. and D. V. Nakles (eds.). 1997. *Environmentally Acceptable Endpoints in Soil: Risk-Based Approach to Contaminated Site Management Based on Availability of Chemicals in Soil*. American Academy of Environmental Engineers. 630 pp.

Sample, B. E., R. A. Efrogmson, D. S. Jones, and G. W. Suter, III. 1998. *Ecotoxicological Benchmarks for Evaluation of Exposures to Petroleum Materials*, ORNL/TM-13691, Oak Ridge National Laboratory, Oak Ridge, TN.

Suter, G. W., II. 1997. *A Framework for Assessing Ecological Risks of Petroleum-Derived Materials in Soils*, ORNL/TM-13408, Oak Ridge National Laboratory, Oak Ridge, TN.

FOSSIL FUELS SUPPLIES MODELING AND RESEARCH

P. N. Leiby

The fossil fuel supplies modeling and research effort focused on U.S. Strategic Petroleum Reserve (SPR) planning and management. Topics covered included planning for an Asian Pacific emergency oil stockpile, reassessing the benefits of expanding the size of the U.S. SPR, updating models for SPR risk analysis, and fill-draw planning.

STRATEGIC PETROLEUM RESERVE PLANNING AND MODELING

P. N. Leiby

INTRODUCTION

The Strategic Petroleum Reserve (SPR) is a government-owned stockpile of crude oil intended to serve as a buffer against possible oil market disruptions. The overall purpose of this project is to assist with SPR planning and management, through the development and application of improved models and tools. Current project efforts emphasize developing new modeling tools to explicitly and flexibly portray oil market uncertainty and SPR planning risk.

DISCUSSION OF CURRENT ACTIVITIES

Oak Ridge National Laboratory (ORNL) conducts model development and planning analyses for Strategic Petroleum Reserve (SPR) drawdown, distribution and other management activities, in support of the Office of Management Operations, Petroleum Reserves. The roles and objectives are:

1. to evaluate SPR planning alternatives and roles of SPR;
2. to support development of SPR oil valuation and bid analysis tools;
3. to evaluate potential applications of DIS-Risk model approach to related energy policy issues;
4. to study role and value of risk information in SPR planning;
5. to utilize, maintain, modify, and report on SPR analysis models;
6. to provide analytical support for the SPR office.

Activities This Year

- Completed an initial study of the merits of an Asian Pacific emergency oil stockpile.

In spite of ample oil supply and historic low world oil prices, security of oil supply is of concern to many APEC economies.¹ Oil has been a critical fuel for the decades of rapid economic growth in the Asia Pacific

¹The APEC (Asia Pacific Economic Cooperation) economies included in this study are: Australia; Brunei; Canada; Chile; China; Hong Kong, China; Indonesia; Japan; Malaysia; Mexico; New Zealand; Papua New Guinea; Philippines; Republic of Korea; Singapore; Thailand; and Chinese Taipei. The focus was on APEC economies other than the United States, that is, the U.S. was excluded from the benefit calculations.

region. According to many studies, oil will remain a dominant fuel for the APEC region, comprising 40% of total primary energy consumption, at least until 2010. Further, a number of oil producing economies in the region either have recently become oil importers or will be importing oil from outside the region in the near future. As a result, by 2010, APEC will be importing 60% of oil supply from outside sources.

The world oil market has endured at least 18 significant oil supply shocks since 1951. The most memorable of these, the 4 largest world oil shocks between 1973 and 1991, are now recognized to have cost the Asian Pacific Economic Cooperation (APEC) economies hundreds of billions of dollars. These costs occurred as lost GDP and higher payments for oil imports. Emergency oil stocks, by buffering supply losses and mitigating sudden major price shocks, are a direct and effective means for dealing with the risk to economies of persistent supply and price volatility.

An assessment of alternative APEC reserve sizes was done with a numerical simulation model, and probabilistic cost-benefit analysis. The analysis presented here strongly supports the conclusion that expanding the APEC reserves by 200-500 Million barrels is justified on the basis of its expected net benefits to APEC economies (see Figure 6-1). Our evaluation considered the combined net benefit of expanded reserve sizes to all APEC economies other than the U.S.. It included the reserve's ability to reduce GDP losses and oil import costs during oil shocks, and subtracted the costs of building, filling, and operating the reserve. The conclusion that a substantial reserve expansion is justified holds true over a range of conditions, including more optimistic oil market assumptions that entail lower disruption risk over the next few decades. It also holds true for a range of variation in other key parameters such as the GDP elasticity with respect to oil price shocks, and for substantially higher storage costs than those of the least expensive alternative, underground salt caverns.

Publications:

“The Value of Expanding Asian Pacific Emergency Oil Stocks,” Paul N. Leiby and David Bowman, Oak Ridge National Laboratory, ORNL-1999/39, February 16, 1999

“Strategic Oil Stocks in the APEC Region,” Inja Paik, Paul Leiby, Donald Jones, Keiichi Yokobori, David Bowman April 6, 1999. Proceedings of the 22nd IAEE Annual International Conference, International Association for Energy Economists, Rome, Italy, 9-12 June, 1999

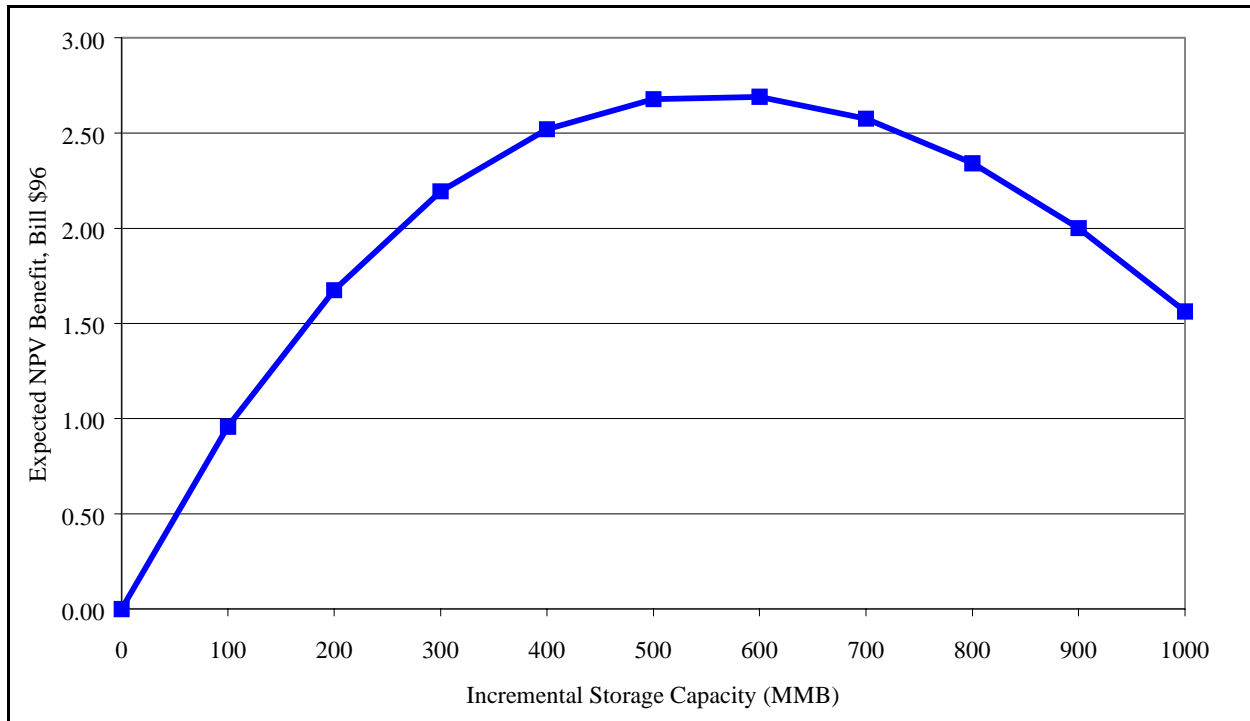


Figure 6-1: Base Case Results for the Benefits to APEC of Incremental Storage Capacity. (Mid Case inputs. For details, see Leiby and Bowman 1999.)

- Began an analysis of the economic consequences of expanding the U.S. Strategic Petroleum Reserve. This study is considering a range of alternative expansions of the U.S. oil reserve, and their net economic benefit, compared to the current size of 560 million barrels. The SPR size expansion benefits will be estimated for some key sensitivities, notably GDP elasticity, the availability of slack (excess) supply capacity, and disruption length. This study should be completed in draft form by July, 1999.

OIL AND GAS PRODUCTION

T. W. Schmidt

Research in oil and gas production at Oak Ridge National Laboratory is represented by activities in three research divisions, Chemical Technology, Computer Science and Mathematics, and Environmental Sciences. The areas of study involve: measurements of wax points in crude oils and petroleum fluids, an evaluation of the hydrocarbon potential of part of the Appalachian basin, the application of nuclear fuel reprocessing technology to the separation of petroleum and water downhole in an oil well, characterization and treatment of soluble organics in produced water, the application of global optimization methods to residual statics in seismic imaging, the use of neural networks in oilfield parameter estimation, and providing environmental compliance information for the National Petroleum Technology Office's Web site.

NATURAL GAS AND OIL TECHNOLOGY PARTNERSHIP SUPPORT

T. W. Schmidt

INTRODUCTION

The Natural Gas and Oil Technology Partnership expedites development and transfer of advanced technologies through technical interactions and collaborations between nine national laboratories and the petroleum industry - majors, independents, service companies, and universities.

The Partnership combines the expertise, equipment, facilities, and technologies of the Department of Energy's national laboratories with those of the US petroleum industry. The laboratories utilize unique capabilities developed through energy and defense R&D including electronics, instrumentation, materials, computer hardware and software, engineering, systems analysis, physics, and expert systems. Industry contributes specialized knowledge and resources and prioritizes Partnership activities.

The areas of technology are:

Diagnostics and Imaging Technology addresses cutting-edge geophysical methods for improved reservoir characterization with a focus on improved borehole hardware and computational efforts for seismic processing and other exploration issues. The Partnership catalyzed formation of a 25-company collaboration which has become the industry focal point for this technology.

Oil and Gas Recovery Technology addresses a broad range of technologies aimed at improving production from existing fields and with specific emphasis on assisting independent producers. The industry interface is an Industry Review Panel consisting of more than 20 individuals representing independents, majors, and the service companies.

Drilling, Completion, and Stimulation Technology aims at better access to the reservoir through improved drilling and completion technologies. Currently, the laboratories participate in several joint industry projects fostered by two industry organizations: the Drilling Engineering Association (DEA) and the Completion engineering Association (CEA).

Environmental Technology addresses new technologies that are needed to produce more oil and gas from mature domestic sources while safeguarding the environment. Key issues to be addressed include: 1. Produced Water, 2. Stationary Source Emissions, 3. Risk Assessment, 4. Tank Bottoms and Sludge, 5. NORM, 6. Soil Remediation, 7. Vapor Recovery, 8. Offshore Structure D&D, and 9. Drilling Wastes.

Downstream Technology is a new area of technology that is being coordinated under the Natural Gas and Oil Technology Partnership for the first time in Fiscal Year 1999. Downstream projects, largely in the area of heavy oil processing, are focused primarily in the areas of PM_{2.5} and bioprocessing. T. W. Schmidt of ORNL is the coordinator for the Partnership's Bioprocessing Program.

DISCUSSIONS OF CURRENT ACTIVITIES

T. W. Schmidt participated in the development of the recommendations for funding of the Partnership Programs on behalf of Oak Ridge National Laboratory. In addition to existing projects in Oil and Gas Recovery Technology, Diagnostics and Imaging Technology, and Environmental Technology areas, T. W. Schmidt has assisted in the development of three new projects in the Environmental Technology and Downstream Technology areas and a CRADA with Phillips Petroleum Company on wax point determination. Other activities include program planning with the Partnership, selection of a Partnership Steering Committee, and coordinating all of the national laboratory participation in the Downstream Technology Area.

ADVANCED COMPUTATIONAL TOOLS FOR 3-D SEISMIC DATA FUSION

D. B. Reister, E. M. Oblow, J. Barhen, and J. B. DuBose, Jr.*

The long-term objective of the project has been to develop and test advanced computational tools for *data fusion* in 3-D seismic analysis. During the period covered by this report, the primary activity was the development of a novel global optimization method for focusing seismic images. A paper "Application of global optimization to the estimation of surface-consistent residual statics" has been written. This report will summarize the paper.

Since the objective function that is used to estimate surface-consistent residual statics can have many local maxima, a global optimization method is required to find the optimum values for the residual statics. As reported in several recent papers, we had developed a new method (TRUST) for solving global optimization problems and had demonstrated it was superior to all competing methods for a standard set of nonconvex benchmark problems. The residual statics problem can be very large with hundreds or thousands of parameters and large global optimization problems are much harder to solve than small problems. To solve the very challenging residual statics problem, we have made major improvements to TRUST (Stochastic Pijavskij Tunneling) and we have made several significant advances in the mathematical description of the residual statics problem (derivation of two novel stack power bounds and disaggregation of the original problem into a large number of small problems). Using the enhanced version of TRUST, we have performed extensive simulations on a realistic sample problem that had been artificially created by large static disruptions. Our simulations have demonstrated that TRUST can reach many plausible distinct "solutions" that could not be discovered by more conventional approaches. An unexpected result was that high values of the stack power may not eliminate cycle skips.

1. INTRODUCTION

Since the earliest days of seismic exploration, geophysicists have recognized the need to correct for the low velocity in the weathered and unconsolidated sediments near the earth's surface. The data processing procedure has been described by (Yilmaz [1987], Marsden [1993], and Sheriff and Geldart [1995]). The first corrections for elevation and low velocity are field statics. A reference level is determined that is below the low velocity layer (LVL) and field statics move the sources and receivers to the reference level. Common midpoint (CMP) gathers are used to generate a set of preliminary velocity picks that are used to calculate normal moveout (NMO) corrections. Residual statics corrections are calculated using the corrected data. The process is repeated (velocity picks, NMO corrections, and residual statics) until the results converge.

The conventional method for calculating residual statics corrections was developed in the seminal paper of Taner et al. [1974]. The time delays caused by the passage of seismic signals through the LVL should depend on path. After the NMO corrections, we assume that all of the paths are vertical and estimate a single time delay that is "surface consistent" (each source and receiver location has a time delay that does not depend on the wave path). The time delay (T_{srk}) for a trace that follows a

* Paradigm Geophysical Ltd., Houston, TX.

path from a source (s) to a receiver (r) via a common midpoint (k) is determined by maximizing the crosscorrelation between the trace and the CMP gather. The total time delay has four components: the source static (S_s), the receiver static (R_r), the two way travel time from the reference level to a reference subsurface reflector (Γ_k), and a residual NMO correction [$M_k (X_{sr})^2$] where X_{sr} is the distance from the source to the receiver [see Eq. (1)].

$$T_{srk} = S_s + R_r + \Gamma_k + M_k X_{sr}^2 \quad (1)$$

Although the total time delay (T_{srk}) is an independent value for each trace, the parameters on the right side of Eq. (1) each occur in many traces. Thus, the parameters are overdetermined (we have many more equations than parameters). We will consider a problem with 4776 traces, 100 shots, 216 receivers, and 423 common midpoints. For our problem we have 4776 equations and 1162 parameters. Since the equations are overdetermined, they can only be solved by minimizing the errors (by using the method of least squares).

One of the conventional methods for calculating residual statics corrections has two steps: use crosscorrelation to estimate the total time delay (T_{srk}) for each trace and use least squares to find the parameters in Eq. (1). In 1985, Ronen and Claerbout proposed a one step alternative approach: stack power maximization. They defined an objective function that measures the correlation between all of the traces in each CMP gather. Changes in the parameters in Eq. (1) cause a time shift for each trace and change the correlation between traces. They search for parameter values that maximize the stack power.

In 1985, Rothman recognized that the residual statics problem was a global optimization problem and proposed to solve the problem using the simulated annealing method. He defined the stack power optimization using two of the four types of parameters on the right side of Eq. (1); his parameters are the static corrections for the sources and receivers. Since the total stack power is a sum of the stack power for each CMP, the CMP term (Γ_k) shifts all of the traces in the stack and does not change the stack power. He argued that the residual NMO correction [$M_k (X_{sr})^2$] was cumbersome to estimate and had a small impact on the stack power.

Recently, an improved algorithm for solving global optimization problems was developed at the Center for Engineering Science Advanced Research (CESAR) at the Oak Ridge National Laboratory (ORNL) [see Barhen, Protopopescu, and Reister (1997)]. The algorithm is called TRUST (terminal repeller unconstrained subenergy tunneling). In 1996, we began a collaborative project to apply TRUST to the residual statics problem using an objective function defined by DuBose [the function is not identical to the function used in DuBose (1993)]. The results reported in Barhen (1997) are for statics problem with fewer parameters and fewer traces than the problem considered here. In applying TRUST to the statics problem, we have made significant improvements in TRUST. Details of the most recent improvements are in Oblow (1999) and will be summarized here.

The next section will define the stack power, discuss an upper bound for the stack power, and define a decoupled stack power. The solution of the decoupled problem both provides an initial estimate of the parameters for the coupled problem and provides a closer upper bound for the stack power of the coupled problem. The third section will discuss both TRUST and the recent improvements in TRUST. The fourth section will discuss our results for a test problem based on field data. The fifth section will present our conclusions.

2. THE RESIDUAL STATICS OPTIMIZATION PROBLEM

2.1. Stack Power.

Seismic energy is detected by receivers that are located along a line. The source of seismic energy is moved along the line to produce a each shot. Time series data is collected from the receivers for each shot and the source of seismic energy is moved to the next source location for the next shot. The time series data is stored as Fourier coefficients. Common midpoint (CMP) stacking is used to increase the signal-to-noise ratio. The fold of the data is the number of data sets with the same CMP. Between 1960 and 1980, improvements in data acquisition systems allowed typical values for the fold to increase from one to twelve. Today, thirty is a typical value.

Data are provided by trace $[t = 1, N_t]$. For each trace, the data consist of the Fourier components $[f = 1, N_f]$ of the measured signal. The Fourier components $[D_{f t}]$ are complex numbers. The seismic energy travels from a source $[s_t]$ to a receiver $[r_t]$ via a midpoint $[k_t]$. For each midpoint (k), the data are stacked:

$$H_{kf} = \sum_t \exp[2\pi i f (S_s + R_r)] D_{ft} \quad (2)$$

The statics corrections (S_s and R_r) are determined to maximize the total power (E) in the stacked data:

$$E = \sum_k E_k \quad \text{where} \quad E_k = \sum_f |H_{kf}|^2 \quad (3)$$

2.2. Coherence Factor.

We have derived an upper bound (G_k) for each of the E_k :

$$G_k = \sum_f \sum_t \sum_\tau \alpha_{ft} \alpha_{f\tau} = \sum_f \left(\sum_t \alpha_{ft} \right)^2 \quad (4)$$

The coherence factor (Q_k) is the ratio of E_k and G_k :

$$Q_k = E_k/G_k \quad (5)$$

Since the E_k are positive, each of the coherence factors will be in the range $[0,1]$.

2.3. Decouple the Components of the Stack Power.

We have defined the power (E_k) and a coherence factor (Q_k) for each CMP. However, each of the statics can influence many of the CMP gathers. In this subsection, we introduce new variables that decouple the CMP gathers. The advantage of this approach is that we can solve a large number of small problems rather than one large problem and derive a closer upper bound for the stack power of the coupled problem. The solutions of the decoupled problems provide an excellent initial estimate for the parameters for the coupled problem.

For each trace (t), we define v_t by:

$$v_t = S_s t + R_r t \quad (6)$$

Using matrix notation, Eq. (6) may be written:

$$\mathbf{v} = \mathbf{A}\mathbf{x} \quad (7)$$

where \mathbf{x} is the parameter vector that combines the vector of source statics corrections (\mathbf{S}) and the vector of receiver statics corrections (\mathbf{R}).

Using the new variables, Eq. (2) becomes:

$$H_{kf} = \sum_t \exp[2\pi i f v_t] D_{ft} \quad (8)$$

Thus, each of the H_{kf} depends on a unique subset of the v_t [\mathbf{v}] and the problem is decoupled. Each of the K decoupled global optimization problems can be solved independently using TRUST to find the components of the vector \mathbf{v} [v_t]. Using singular value decomposition, the optimal coordinates [\mathbf{v}] can be mapped back to the original coordinates:

$$\mathbf{x} = \mathbf{B}\mathbf{v} \quad (9)$$

3. GLOBAL OPTIMIZATION ALGORITHM

ORNL has developed a state-of-the-art algorithm for global optimization: TRUST (Terminal Repeller Unconstrained Subenergy Tunneling). TRUST solves the following optimization problem: given an objective function [$f(\mathbf{x})$ where \mathbf{x} is an N dimensional vector that is constrained to lie in a domain (P)], find the global minimum (\mathbf{x}_g). That is, find a point \mathbf{x}_g in P such that $f(\mathbf{x}_g) \leq f(\mathbf{x})$ for all \mathbf{x} in P . Since the goal in the statics problem is to maximize the total stack power (E), the objective function for TRUST is: $f(\mathbf{x}) = -E$. Several papers have been published that describe the deterministic version of TRUST [see Cetin, Barhen, and Burdick (1993); Barhen and Protopopescu (1996); and Barhen, Protopopescu, and Reister (1997)]. Recently, substantial enhancements have been incorporated into the TRUST algorithm. Here, we will only highlight some of these innovations. A more detailed discussion of the most recent improvements can be found in Oblow (1999).

In our initial approach to the statics problem, we were using a deterministic version of TRUST that found the global minimum by executing a series of cycles of tunneling and descent. As discussed in Barhen (1997), TRUST begins at one corner of the hyperparallelepiped P . From the initial point, TRUST takes a small step into the interior of P in the \mathbf{p} direction. If $f(\mathbf{x})$ is lower at the second point than at the first point, TRUST will descend to a local minimum. Otherwise, TRUST will tunnel following a curved path until it reaches a new basin of attraction (where $f(\mathbf{x})$ is lower than the current candidate for global minimum) or \mathbf{x} leaves the region P . From each local minimum, TRUST takes a small step in the \mathbf{p} direction and begins to tunnel. The TRUST algorithm terminates when \mathbf{x} leaves the region P .

Two enhancements to TRUST are described in Barhen (1997): reflection of the path at the boundary of P and one dimensional tunneling paths. Later in this section, we will discuss the one dimensional tunneling paths.

A rigorous proof had shown that the deterministic version of TRUST would find the global minimum for the one dimensional case (where \mathbf{x} is a scalar). If we approximate an N dimensional problem by a 1D curve that covers the N-dimensional (ND) region P (or by a regular grid), we can formally solve all global optimization problems. However, this method is not practical for large problems because the number of function evaluations increases exponentially with the number of dimensions (the number of evaluations is M^N , where M is the number of function evaluations in each dimension).

While the deterministic version of TRUST has been very successful in solving standard non-convex benchmark problems that have up to 20 parameters, it does not always find the globally optimum values for large residual statics problems with 100 or more parameters. The basic reason that TRUST may be less successful with large problems is that the size of the problem increases exponentially with the number of parameters. We will use two examples to illustrate this point. The first example was discussed in the last paragraph, we found that a comprehensive search of a regular grid in an ND space requires M^N function evaluations. For the second example, we recall that TRUST begins at one corner of the hyperparallelepiped P. For an ND problem, there are 2^N corners where TRUST could start. In general, TRUST would explore a different path from each of the corners.

Since the deterministic version of TRUST does not always find globally optimum values for large residual statics problems, we enhanced TRUST by using one dimensional tunneling paths [see Barhen (1997)]. From a local minimum, we use the 1D version of TRUST to explore each of the N dimensions of the problem one at a time. When we find a point where the objective function has a lower value than the previous local minimum, we descend to the next local minimum. If we have explored all of the N directions and have not found a lower value, we stop the algorithm. For the 1D searches, we can use a uniform grid or the nonuniform grid that results from the terminal repeller and the subenergy tunneling transformation. The choice of the dimension to search next can be numerical order or random.

Using the 1D tunneling paths allowed us to find much better values for the stack power. Subsequently, Obloj developed SPT (Stochastic Pijavskij Tunneling) that greatly speeds up the 1D tunneling phase and has found many large values for the stack power.

4. RESULTS

Our objective was to use TRUST to estimate surface-consistent residual statics. We have applied TRUST to several synthetic data sets. In all cases, TRUST attempted to solve the global optimization problem without using the values of the synthetic disrupting statics. The first (small) data set contained 24 shots and 50 receivers, for a total of 74 parameters. Although TRUST quickly solved the problems for the small data set, the values of the statics corrections were small and the solutions were found by descent from the initial point ($\mathbf{x} = \mathbf{0}$). The second (medium) data set was designed to be more of a challenge for TRUST with large statics corrections that can not be found by a descent from the initial point. The medium data set contained 77 shots and 77 receivers, for a total of 154 parameters. Several major changes in TRUST (that were discussed in Sections 2 and 3) were required to solve the problems with the medium data set. For the both the small and medium data sets, the coherence factors were large (near 1.0) and the increase in stack power was very large.

The third (large) data set was created by adding disrupting statics to measured seismic data. The large data set has 100 shots and 216 receivers, for a total of 316 parameters. The number of CMPs is 423. The number of traces is 4776 and the number of frequencies is 118. Time required to calculate the stack power and the gradient of the stack power is 100 times longer than for the medium data set. The stack power at the initial point ($\mathbf{x} = \mathbf{0}$) was 882. The upper bound on the stack power [G see Eq. (4)] is :

$$G = \sum_k G_k = 6589.$$

We applied TRUST to the 423 decoupled problems. Most of the best values for the coherence factor were much less than 1.0. The total energy for the 423 decoupled problems (${}^D G$) is 2706. Using Eq. (9), the 4776 v coordinates were mapped back to the 316 x coordinates to determine an initial point (\mathbf{x}_d) for the 316 parameter global optimization problem. The initial value for the energy was 1035. The first local maximum was 2183. After 98 iterations, an interim version of TRUST found the maximum value at 2366.

After the development of the SPT version of TRUST, we have found many points with high values of the stack power (In our paper, we discuss 22 points with stack power greater than 2365). We begin with two seismic images: before correction and after correction. The disrupted seismic image is plotted in Fig. 1 while the image after the static corrections is shown in Fig. 2. The seismic reflections are well defined in Fig. 2 and not defined in Fig. 1.

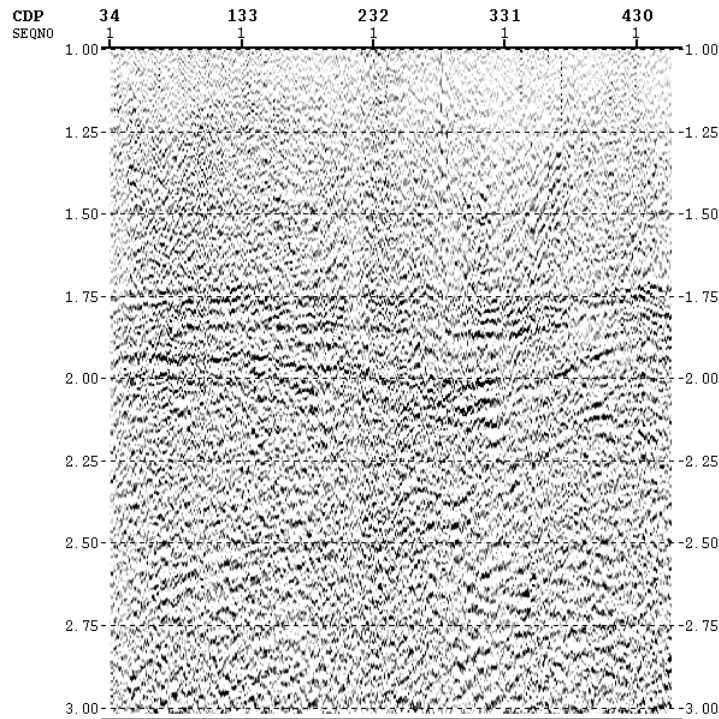


Fig. 1. The disrupted seismic image before the application of residual statics corrections.

In Section 2.3, we introduced new variables (\mathbf{v}) that decouple the CMP gathers. Each of the decoupled global optimization problems can be solved independently using TRUST to find the stack power for the decoupled problem: G_k . Using the G_k , we can define a best (close upper bound for the) coherence factor (see Fig. 3). Most of the values for the best coherence factor range from 30% to 50%.

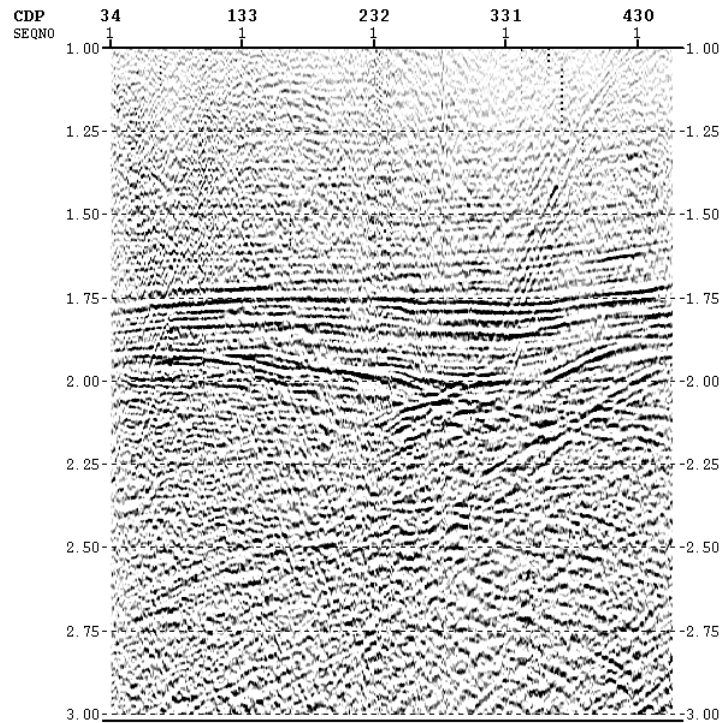


Fig. 2. The seismic image after the application of residual statics corrections.

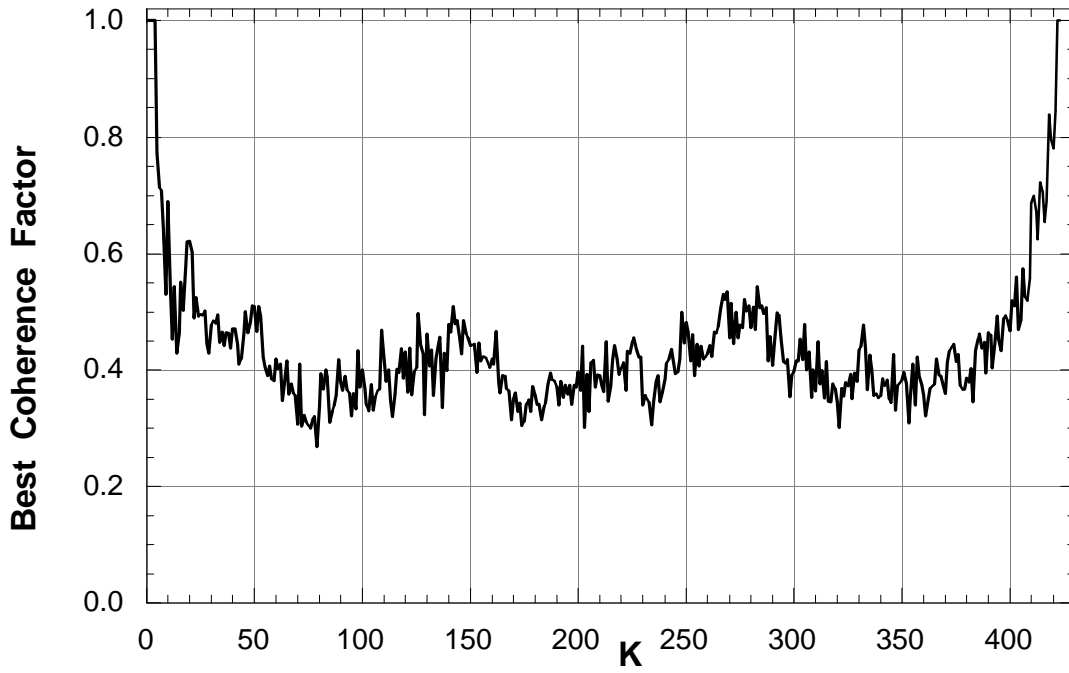


Fig. 3. The best coherence factor.

To measure our progress as we search for the maximum stack power, we normalize the values of the coherence factor by dividing by the best values for the coherence factor (see Fig. 4). In Fig. 4, most of the values for the normalized coherence factor are above 80% when the power is large (2441).

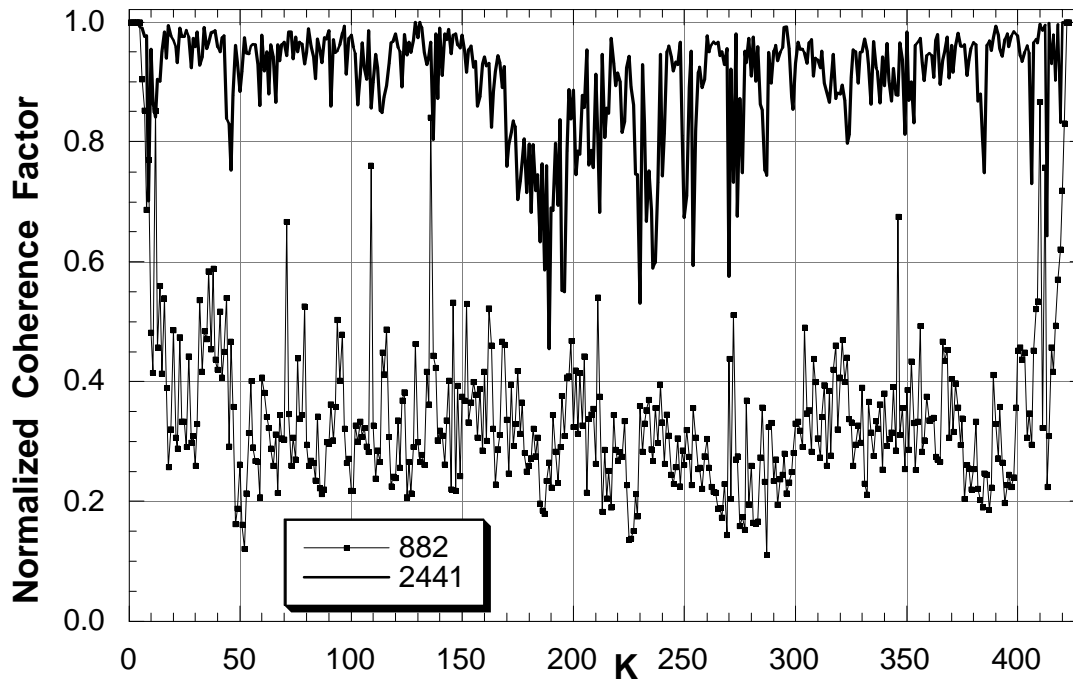


Fig. 4. The normalized coherence factor for two cases: 882 and 2441.

5. CONCLUSIONS

Working in the frequency domain, we have used stack power maximization to estimate surface-consistent residual statics. Since the stack power objective function can have many local maxima, a global optimization method is required to find the optimum values for the residual statics. We had developed a new method (TRUST) for solving global optimization problems and had demonstrated it was superior to all competing methods for conventional benchmark problems. The residual statics problem can be very large with hundreds or thousands of parameters. In this paper, we have applied TRUST to the residual statics problem.

To solve this very challenging problem, we have made major improvements to TRUST and we have made several significant advances in the mathematical description of the residual statics problem. In our initial approach to the statics problem, we were using a deterministic version of TRUST that found the global minimum by executing a series of cycles of tunneling and descent. While the deterministic version of TRUST has been very successful in solving standard non-convex benchmark problems that have up to 20 parameters, it does not always find optimum values for large residual statics problems with 100 or more parameters. The basic reason that TRUST may be less successful with large problems is that the problem size increases exponentially with the number of parameters.

In general, we cannot "solve" a global optimization problem. We must apply resource allocation: Apply finite resources (function evaluations) in an optimal way to find the best estimate of the global optimum. Since the deterministic version of TRUST does not always find optimum values for large residual statics problems, we enhanced TRUST by using one dimensional tunneling paths. From a local minimum, we use

the 1D version of TRUST to explore each of the N dimensions of the problem one at a time. When we find a point where the objective function has a lower value than the previous local minimum, we descend to the next local minimum. Using the 1D tunneling paths allowed us to find much better values for the stack power. Subsequently, Oblov developed SPT (Stochastic Pijavskij Tunneling) that greatly speeds up the 1D tunneling phase and has found many large values for the stack power.

The key parameter in SPT is the pseudo-Lipschitz constant which determines the slope of the two sides of the Pijavskij cone. The Pijavskij cones exclude regions of the search space. The SPT method has two other parameters (an estimate of the global minimum and the resolution) that can be used to estimate the pseudo-Lipschitz constant. We find that the Pijavskij cones quickly eliminate the search space and we usually evaluate the function about ten times to achieve a resolution of 100,000 points in the parameter range.

We have made several significant advances in the mathematical description of the residual statics problem. We have derived an upper bound for the stack power and defined a decoupled stack power. The solution of the decoupled problem both provides an initial estimate of the parameters for the coupled problem and provides a closer upper bound for the stack power of the coupled problem.

Residual statics are phase adjustments that are used to get all of the components of a CMP gather in phase and increase the stack power for the CMP. We have derived an upper bound for the stack power for each of the CMP. The coherence factor is the ratio of stack power and the upper bound for each of the CMP.

Each of the statics can influence many of the CMP gathers. We have introduced new variables that decouple the CMP gathers. The advantage of this approach is that we can solve a large number of small problems rather than one large problem and derive a closer upper bound for the stack power of the coupled problem. The solutions of the decoupled problems provide an excellent initial estimate for the parameters for the coupled problem.

We have found many parameter vectors that give high values for the stack power. We have developed two methods for measuring the difference between two vectors: the Euclidean norm and the power norm. We remove the null space components before we calculate the Euclidean norm. We expect tradeoffs; as a parameter changes, the power will increase for some CMP and will decrease for others. The power norm is the sum of the absolute value of the differences in stack power for each CMP. The power norm is the best method for measuring the difference between two parameter vectors.

We have found many distinct parameter vectors that give high values for the stack power for a realistic sample problem that had been artificially created by large static disruptions. Since we knew the disrupting statics, we thought we knew the "true solution" for the sample problem. However, since the "true solution" does not maximize the stack power, we do not know the true solution for the stack power maximization problem for this data set. In this paper, we have argued that the exponential growth in difficulty prevents us from ever knowing "the solution" for a large global optimization problem. For this problem, the disaggregated problems provide a close upper bound for stack power. Since our best estimate (2441) is near the upper bound (2706), we know we have found a very good estimate for the global maximum.

6. REFERENCES

- Barhen, J. and Protopopescu V., 1996, Generalized TRUST algorithms for global optimization, in State of the Art in Global Optimization: Computational Methods and Applications, Floudas, C. A. and Pardolas, P. M., Eds., Kluwer Academic Press, Dordrecht, Netherlands, 163-180.
- Barhen, J., Protopopescu V., and Reister, D. B., 1997, TRUST: A deterministic algorithm for global optimization, *Science*, **276**, 1094-1097.
- Cetin, B. C., Barhen, J., and Burdick, J. W., 1993, Terminal repeller unconstrained subenergy tunneling (TRUST) for fast global optimization, *Journal of Optimization Theory and Applications*, **77**, 97-126.
- DuBose, J. B., Jr., 1993, Practical steps toward realizing the potential of Monte Carlo automatic statics: *Geophysics*, **58**, 399-407.
- Marsden, D., 1993, Static corrections - a review, *The Leading Edge*, 12, Part 1, 43-49, Part 2, 115-120, Part 3, 210-216.
- Obloj, E. M., 1999, SPT: A Stochastic tunneling algorithm for global optimization, ORNL/TM-1339, Oak Ridge National Laboratory, Oak Ridge, TN.
- Ronen, J. and Claerbout, J. F., 1985, Surface-consistent residual statics estimation by stack-power maximization: *Geophysics*, **50**, 2759-2767.
- Rothman, D. H., 1985, Nonlinear inversion, statistical mechanics, and residual statics corrections: *Geophysics*, **50**, 2784-2796.
- Sheriff, R. E. and L. P. Geldart, 1995, *Exploration Seismology*, Second Edition, Cambridge University Press, Cambridge, England.
- Taner, M. T., Koehler, F., and Alhilali, K. A., 1974, Estimation and correction of near-surface time anomalies: *Geophysics*, **39**, 441-463.
- Yilmaz, O., 1987, *Seismic Data Processing*, Society of Exploration Geophysics, Tulsa, Oklahoma.

ENVIRONMENTAL COMPLIANCE ASSISTANCE SYSTEM

S. M. DePaoli



The Environmental Compliance Assistance System (ECAS) is a web site provided through the National Petroleum Technology Office (NPTO). This web site is targeted at the independently owned and operated oil and gas exploration and production (E&P) industry. In general, these E&P facilities are small, family-owned operations, and therefore do not have the capital to support the personnel needed to research and maintain information regarding environmental compliance issues concerned with their industry. This web site has been provided to aid these and other interested parties with regulatory information on the E&P industry; local, state, and federal contacts; waste handling/treatment/disposal options; and to direct them to other related web sites. A link to the ECAS can be found on the NPTO homepage, (<http://www.bpo.gov/>).

This NPTO funded project is tasked with updating the ECAS system that is currently on the web. A meeting was held in early December to outline the steps necessary to complete this project. Present at the meeting were: Nancy Holt (NPTO-Project Manager), F. Michael King (NPTO-Management Analyst), Beverly Fox (NPTO-Webmaster), Sharon Robinson (Oak Ridge National Laboratory (ORNL)-Program Manager), and Susan DePaoli (ORNL-Principle Investigator). Several decisions/goals were made at this meeting. Foremost was the need to produce a logo for the site. A logo was designed by Karen Billingsley of Advanced Integrated Management Services (AIMS) in Oak Ridge under a subcontract on this project, and is shown above. Some changes are being worked regarding the background color of the logo. The basic logo has been approved by the NPTO. Other goals regarding advertising of the site were discussed such as producing a trifold, and/or postcard about the site. These supporting efforts will not be completed until the web site is fully updated.

Work on updating the web site began in January 1999. A fully updated and approved web site format has been completed. The new site will include the old information (which has been updated as of 4/1999). In addition, information is to be added regarding links to other pertinent sites; federal regulatory contacts; regulatory/legislative changes that are pending; and other links to sites within the NPTO. A conference call was held in late March 1999 to update Nancy Holt

on the status of the ECAS web site. Discussions were held and decisions issued on the logo and the web site format. Final clearance on the new format was received.

As mentioned, the update of the information that currently resides on the web has been completed; however, the text has not yet been transferred to the NPTO server. This may take place as one major step, with the updating and “test” site all residing in Oak Ridge at the AIMS server until completed, and access limited to the NPTO, ORNL, and AIMS personnel involved on the project.

**GEOLOGIC CONTROLS OF HYDROCARBON OCCURRENCE IN PART OF THE
APPALACHIAN BASIN IN TENNESSEE, SW VIRGINIA, SOUTHERN WEST VIRGINIA, AND
EASTERNMOST KENTUCKY**

Robert D. Hatcher, Jr.

Environmental Sciences Division, ORNL

and

Department of Geological Sciences, University of Tennessee-Knoxville

This project has as its main goal the better understanding of the occurrence of hydrocarbons in the southern part of the Appalachian basin in Tennessee, southwestern Virginia, and parts of Kentucky and West Virginia. Despite the fact that this is historically part of the oldest hydrocarbon province in the U.S., the application of a combination of new technologies and concepts to the southern part of the Appalachian basin may yield additional production, as well as insight that can be applied to exploration in other basins. We intend to quantitatively characterize the 3-D geometry and reservoir architecture within the basin, the thermal history of the basin, and better ascertain the parameters that are responsible for hydrocarbon generation and migration, e.g., the timing of migration relative to the timing of deformation and formation of the primary reservoir architecture of this region. This is a collaborative project between the Oak Ridge National Laboratory (and University of Tennessee-Knoxville), the U.S. Geological Survey (USGS), and several industry partners.

The approach being employed is to collect critical data in several different subdisciplines ranging from structural geology and field relationships (ORNL and USGS) to paleontological (yielding thermal maturation data) and stratigraphic data (USGS) to organic geochemical data on hydrocarbons (USGS) in order to better understand the distribution, controls, and nature of the source and host materials in which known hydrocarbons occur. There are a number of existing oil and gas fields in the Cumberland Plateau in Kentucky and Tennessee where the controls of hydrocarbon occurrence are well established. The conditions of formation of hydrocarbon accumulations in the relatively few fields in the Valley and Ridge, e.g., the Rose Hill field in southwestern Virginia, remain poorly known despite several decades of production. The newly opened Swan Island field in Hancock County, Tennessee, provides fresh insights into the reasons for hydrocarbons to occur in a setting beneath a large thrust fault and opens the possibility for additional fields in similar settings throughout this region. It is likely that the same unit (Knox Group) that serves as the reservoir for large reserves of natural gas in the Swan Island field is the source for the hydrocarbons as well.

We have also compiled maps showing the available thermal maturation data and its relationships to the structural patterns in the region. We will be obtaining additional thermal maturation data in the form of conodont alteration index values determined from conodonts separated from samples collected from both surface rocks and from core, some from ORNL. Separations and analyses will be conducted at the USGS laboratories in Reston, VA.

An additional area of study has been the southern Appalachian triangle zone, a potentially productive structure that is an unexplored hydrocarbon play in this part of the Appalachians. Triangle zones consist of anticlinal folds in which faulting has occurred in the core of the anticline to help compensate for space changes that occur as the anticline is tightened. These structures have been very productive in the Canadian Rockies and other parts of the world. The southern Appalachian triangle zone marks the boundary between the Valley and Ridge and Cumberland Plateau in Tennessee, and extends from Lake City to Chattanooga. The complexly deformed organic-rich rocks in the Knox Group and also the overlying Mississippian carbonates beneath the foreland-most Valley and Ridge thrust fault may be potential hydrocarbon plays. The goal of our work on this particular structure has been to carefully map the structure of the triangle zone and then conduct fracture analysis to better understand the plumbing of this and similar systems. Structural data from an excellent exposure of complexly deformed Pennsylvanian rocks in the core of the Tennessee portion of the southern Appalachian triangle zone have been collected and analyzed to help understand the evolution of this structure. In order to evaluate possible lithologic and structural variations along the length of the triangle zone, a search for other well-exposed portions of the structure is being conducted.

We have also taken a more general look at the hydrocarbon potential of the southern portion of the Wartburg basin in Tennessee. Project tasks included bringing well data from the Tennessee Division of Geology oil and gas well database into Geosec 3D, permitting 3D visualization of producing zone geometry; analyzing the Tennessee Division database and paper records, historical data, and other well records to better locate producing zones; analyzing well cuttings from two basement wells to identify potential producing zones in units deeper than those traditionally explored in this part of Tennessee; creating structure contour maps of important units (top of the source unit, Mississippian-Devonian Chattanooga Shale, and top of the productive Mississippian section) from a combination of well logs included in the database, historical records, geophysical logs, and calculations based on surface geology and stratigraphy. From these activities, we were able to identify several gentle structures in the southern portion of the Wartburg basin that may have hydrocarbon potential, several of which have not yet been explored, and also identify additional deeper units that may produce economical quantities of

hydrocarbons. The results are now being converted to a GIS. Integrating all the data into ArcView will permit interested parties to more easily and quickly visualize and retrieve the information they need.

Another subproject within the main project is a better understanding of the relationships between fracture development and faulting in a well-exposed medium-size duplex structure in Tuckaleechee Cove in southeastern Tennessee. This effort is just getting underway and it promises to shed light on the plumbing system in another setting where fractures play an important role in reservoir development that will permit comparisons to the fracture development in triangle zones.

The primary goal of this research will remain as stated above but greater emphasis will be placed more on reconstruction of the basic structural geometry and reservoir architecture of the southern Appalachian Valley and Ridge within the study area, as well as to continue to provide samples of hydrocarbons for analysis and collaboratively obtain samples for other types of analyses to be carried out by USGS as part of this investigation. Our goal here is to begin 3-D reconstruction of this part of the Valley and Ridge using a combination of surface geologic data and available seismic reflection and other geophysical data. This will permit a better regional assessment of trends in hydrocarbon occurrences as well as to refine the principles being developed related to the new hydrocarbon development(s) in the study area. We also will be attempting to determine the relationships between hydrocarbon generation and migration and the deformation (faulting, folding, fracturing) that affected the rocks of this region.

Our results to date have been presented at meetings of the American Association of Petroleum Geologists and the Geological Society of America. In addition, we made efforts to keep the state geological surveys and state oil and gas associations informed of the progress of this research.

Determining the geologic controls of hydrocarbon occurrence presently requires an understanding of their complete “life cycle:” What is their source? When did they migrate, and what paths did they follow? When did traps and reservoirs develop? Toward this end, successful completion of this research requires a sophisticated 3-D approach to resolving the structural, thermal, and stratigraphic framework of the southern Appalachian hydrocarbon province.

OZONE TREATMENT OF SOLUBLE ORGANICS IN PRODUCED WATER

Thomas Klasson and David DePaoli

Oil production is shifting from “shallow” wells (0-650 ft water depth) to off-shore deep-water operations (>2,600 ft.). Production from these operations is now less than 20%. By 2007, it is projected that as much as 70% of the U.S. oil production will be from deep-water operations. The crude oil from these deep wells is more polar, increasing the amount of dissolved hydrocarbons in the produced water. Early data from Gulf of Mexico (GOM) wells indicate that the problem will increase significantly as deep-water production increases. Existing physical/chemical treatment technologies used to remove dispersed oil from produced water will not remove soluble organics. GOM operations are rapidly moving toward design of large, expensive, high-capacity platforms that will require compact, low-cost, efficient treatment processes to comply with current and future water quality regulations.

This project is an extension previous research to improve the applicability of ozonation for treating organics and will address the petroleum industry-wide problem of handling soluble organics from deep-water operations. The goal of this project is to maximize oxidation of water-soluble organics during a single-pass operation. The project investigates:

1. ozone and hydrogen peroxide production by electrochemical methods,
2. increasing the mass transfer rate in the reactor by forming micro bubbles during ozone injection into the produced water, and
3. using ultraviolet irradiation to enhance the reaction if needed.

Accomplishments: The Experimental Plan was completed in October 1998, outlining experiments for the initial phase of this project, and several surrogate formulations of produced water were received from PERF partners. Complete destruction of the water-soluble organics benzene, toluene, ethylbenzene, xylenes, and aliphatic acids have been obtained in experiments conducted with ozone and UV induction in artificial seawater. Near complete destruction of aromatics has been obtained with a sonochemical system that in situ generates hydrogen peroxide in the produced water. Studies have shown that sharp improvement in ozone system is closely linked to the generation of small bubbles. Several sparging mechanisms have been tested to date.

Future experiments will focus on the destruction of the water-soluble organics in continuous flow mode.

DETERMINATION OF ESSENTIAL THERMOPHYSICAL PROPERTIES FOR SUSTAINABLE ENERGY

W. V. Steele

INTRODUCTION

This activity is focused on the determination of thermophysical and thermochemical property measurements on hydrocarbon systems. This will include pure components as well as mixtures and spans the range of hydrocarbon mixtures from natural gases to crude oils. One of the major initial focus areas will be wax point determination. To aid in that accomplishment, DOE Fossil Energy has agreed to partially fund the acquisition of an Acoustic Cavity Resonance Spectrometer (ACRS) for experimental measurement of thermophysical properties. The ACRS has the capability to, accurately and cost-effectively, obtain a wide variety of essential thermophysical properties for physical properties databases, computational molecular science modeling, and ultimately commercialization of industrial processes. Planning the moving and re-establishment of DOE-owned thermophysical and thermochemical equipment from Oklahoma to ORNL is included within the scope of work for this project.

The scope of the FY 1999 work includes; (a) acquisition and modification of the ACRS, (b) establishment of a suite of laboratories for the measurement of thermophysical properties of heavy oil components, and (c) using the ACRS for the measurement of thermophysical properties for wax point determinations in systems typical of underground petroleum reservoirs. Advanced computational techniques will be used to predict the thermophysical properties measured by the ACRS. This will serve as a mechanism to improve and validate the models of intermolecular potential energy used in molecular simulations that are otherwise exact. The ultimate goal is to be able to rely substantially or entirely on computational results when necessary.

DISCUSSION OF CURRENT ACTIVITIES

Background:

Worldwide demand for petroleum products continues to expand as the nations develop. However, if the demand is analyzed in terms of the three major classes of petroleum cuts: light products such as gasolines; petrochemical feedstocks, middle distillates such as jet fuels and diesels; and heavy products such as fuel-oils and lubricants; then there has been a drastic shift in emphasis toward the light end. Whereas in 1972 both the light products and the middle distillates accounted for approximately 30% by mass of the market, by 1990 they had each risen to approximately 36% of the market. Analysts believe that by the turn of the century the light products will have 38%, the middle distillates 40%, leaving only 22% for the 1973 major component the heavy-ends.

The development of methods for refining light crudes required property data on a relatively narrow set of compound classes for which data up through a carbon number of about C₁₀ were carefully evaluated and correlated. The data evaluation was undertaken in the American Petroleum Institute (API) Project 44. Those data have been incorporated in a number of correlations devised and used by chemical engineers in process development in the petroleum industry in the manufacture of our present fuel slate. Those data also have been used as the basis of numerous computational derived to estimate the properties of related compounds for which data have not been measured. The fruits of Project 44 have ensured a petroleum industry operating at 95 per cent thermal efficiency with light crudes.

Whether it is an East Coast refinery importing crude oil from Nigeria, or a U.S. Gulf Coast refinery importing crude oil from Saudi Arabia, or even a U.S. West Coast refinery operating on Alaskan North Slope crude, over the last decade or more for which records are available (1986-96), the quality of the crude oil processed by refineries has declined. If the decline in the quality of crude processed in U.S. refineries is denoted in terms of the API gravity, the gravity has decreased by an average of 0.15° per year in the decade 1986-95 (Swain, E. J., *Oil & Gas Journal*, November 10, 1997: pp. 79-82). Furthermore, the decline appears to have accelerated back to the rate applicable in the early 1990's. Measured as a five-year average (1989-93), the API gravity had declined by 0.22° per year. After leveling at 31.3° for the next four years, in 1996 it was back on the line pointing to a value of 30.5° for the API gravity in the year 2000. As the API gravity of crude oil falls, the aromatic content (carbon content) increases and the correlations derived for the light crudes begin to breakdown. The failure of the correlations is well documented in the literature. New or

revised correlations are necessary for continued high thermal efficiency in the refining of present and future crudes.

The heavier crudes contain more carbon, oxygen, sulfur, and nitrogen (polycyclic aromatics and heteroatom-containing compounds) than the benchmark West Texas Intermediate. These heteroatom-containing compounds are difficult to remove. Processing crudes containing increasing levels of oxygen, sulfur, and nitrogen using present-day technology has produced fuels with high heteroatom contents and a tendency toward instability. The refractory nature of the heteroatom-containing compounds is the main reason for the increase in coke production. Using heavy oil to make quality transportation fuels requires an understanding of the chemistry and the thermodynamics of adding hydrogen to the feedstocks. The major goal of this research project was to aid in that understanding.

Wax Point Determinations: Wax formation and deposition in pipelines and process equipment results in significant operational difficulties for the petroleum industry. The understanding of the crystallization of paraffin deposits from selected crude oils and the relationship of paraffin inhibitor structure to performance are essential to develop improved classes of inhibitors to reduce the production costs in the early stages of the petroleum production from some deep and ultra deep water wells. Although it is known that the paraffin deposits are formed from long straight-chain alkanes which can crystallize from the crude under some conditions of temperature, pressure, composition, and shear rate, conventional molecular simulations have failed to give significant insight into this behavior mainly because of the prohibitive computational costs for the systems which are required for realistic modeling. However, with recent advances in computer hardware and computational techniques to study such systems, it is now possible to tackle these large problems in a reasonable time period.

ACRS Devise: The ACRS is a novel instrument which appears to have broad application and provide higher degrees of accuracy over wide ranges of pressure and temperature than conventional methods of determining physical properties. The literature on the ACRS promotes that it can precisely measure many thermophysical properties of materials that are required in recovery, separation, and processing: i.e., heat capacities, dew points, bubble points, virial coefficients, vapor pressures, critical points, solubilities, diffusion coefficients, etc. it can maintain temperature to within 0.001 K, pressures to within 0.005 psia of the setpoint, and system volumes to within 1 microliter., while operating over broad range of temperatures and pressures (typically 100 – 700 K and 0 – 25000 psia). In addition it is much faster and easier to use than more traditional instruments.

Progress:

During the period April 1998 to March 1999 the activities within this project have shifted from acquisition of the ACRS, preparing laboratory facilities to house the thermophysical property measurement equipment from the previously DOE-owned Oklahoma site, obtaining key staff, moving and setting up the equipment, through to bringing the equipment on-line ready for calibration and then experimental measurements.

In the first quarter of the reporting period arrangements were completed to acquire from Phillips Petroleum Company, Bartlesville, Oklahoma the Acoustic Cavity Resonance Spectrometer (ACRS). The ACRS was collected from Phillips at the end of December 1998, and shipped to Florida University (Professor Colgate) for refurbishment. Modifications will be completed by June 1999.

To accommodate the equipment from the previous DOE Oklahoma site, and the ACRS, four (4) rooms within Building 4501 at ORNL were refurbished during the first half of the reporting period. Refurbishment included decommissioning two of the rooms previously under radiation restrictions. Three (3) of the rooms required removal of benches, hoods, and sinks to accommodate the specialized equipment. The fourth room required installation of a new HVAC, floor, ceiling, lights, and sprinkler system. ORNL program development funds were secured for the refurbishment. Work in the area was completed by the end of the calendar year.

During the first half of the reporting period the equipment from the Thermodynamics Section of what was the National Institute for Petroleum and Energy Research (NIPER) in Oklahoma was dismantled, packaged, and shipped in two tractor-trailers to ORNL. On arrival the equipment was allocated to the laboratory space and the required facilities (water, vacuum, blanket gas, and electric power requirements) were made available for each piece of equipment.

To aid in the installation of the "one-of-a-kind" equipment and instrumentation, Stephen E. Knipmeyer was contacted and agreed to spent some time at ORNL in early 1999. Steve was a Senior Experimentalist for over 20 years responsible to construction and maintenance of the majority of the equipment when it was in operation in Oklahoma. During a 10 day period in February 1999 the most the "skeletons" of the equipment was assembled within the laboratory complex. As of the end of the reporting period all the equipment has been reassembled and work on assuring that it meets ORNL Safety Codes is in progress.

Initial efforts at equipment calibration have focused on Laboratory 110 where refurbishment was completed first. The Differential Scanning Calorimeter (DSC) has been recalibrated. Physical property measurements for a DOE non-Fossil Energy project using the DSC are about to commence. Also in Laboratory 110, the rotating-bomb combustion calorimeter

has been refurbished and passed ORNL Electrical Safety Codes. Initial tests on the constant temperature bath control system associated with the apparatus gave excellent results. Control within +/- 0.001 K over a period of 24 hours was obtained rivaling the best previous operation of the equipment. Calibration of the bomb with benzoic acid is slated for early in the coming quarter. Work bringing the remainder of the equipment "on-line" remains on schedule.

Future Progress:

The FY 1999 milestones include the initial measurements to establish the ACRS's capabilities in wax point determinations, and testing to ascertain its range of measurement, accuracy and precision. The wax point determination effort will be directed at establishing the foundations for understanding the interaction of specific wax formation inhibitor - crude oil combinations. This will form a foundation for the subsequent modeling effort. In FY 2000 advanced computational techniques will be used to predict the thermophysical properties measured by the ACRS. This will serve as a mechanism to improve and validate the models of intermolecular potential energy used in molecular simulations that are otherwise exact. The ultimate goal is to be able to rely substantially or entirely on computational results when necessary. Results obtained in this project will be of use to the petroleum production and refining industries in the development of new processes whilst invoking stringent pollution control, waste minimization, and environmental regulations.

FUNDAMENTAL CHEMISTRY OF HEAVY OIL

W. V. Steele

INTRODUCTION

Catalytic hydroprocessing continues to be the core method for upgrading of feedstocks with high aromatic content. European environmental organizations have already established standards in this area and the US is expected to follow in the near future. The reduction of aromatics in heavy petroleum upgrading will require careful management of hydrogen during hydroprocessing. Effective hydrogen management requires an understanding of the relationship between the distribution of the hydrogenated products in the process streams and the conditions of their formation, i.e. temperature and pressure.

To counteract the adverse effects of carbon rejection methods, refiners have the option of hydrogen-addition (hydroprocessing) methods. However, hydroprocessing consumes large quantities of hydrogen. As refineries reconfigure to produce the new “clean fuels” (“reformulated fuels,” i.e., those with oxygenates present), hydrogen shortages are occurring, and new sources of supply are required. The addition of oxygenates to gasoline means that less octane is required from the reformer, lowering the severity of the operation and the amount of hydrogen formed. Also, the mandated reduction of aromatics content by the U.S. government in the 1990 Clean Air Act Amendments has resulted in a further reduction of reformer operating severity, hence, severely reducing hydrogen production. Other contributions to the problem in managing hydrogen result from mandated lower gasoline temperature endpoints and reduced sulfur levels. Hence, the use of hydrogen exactly where it will “do the most good” is paramount. Overhydrogenation will have to be minimized.

DISCUSSION OF CURRENT ACTIVITIES

Background:

Worldwide demand for petroleum products continues to expand as the nations develop. However, if the demand is analyzed in terms of the three major classes of petroleum cuts: light products such as gasolines; petrochemical feedstocks, middle distillates such as jet fuels and diesels; and heavy products such as fuel-oils and lubricants; then there has been a drastic shift in emphasis toward the light end. Whereas in 1972 both the light products and the middle distillates accounted for approximately 30% by mass of the market, by 1990 they had each risen to approximately 36% of the market. Analysts believe that by the turn of the century the light products will have 38%, the middle distillates 40%, leaving only 22% for the 1973 major component the heavy-ends.

Within the petroleum industry, catalytic hydroprocessing continues to be the core method for upgrading of feedstocks with high aromatic content, as well as for heteroatom removal through HDS and HDN. The 3-day symposium "Recent Advances in Heteroatom Removal" presented at the Division of Petroleum Chemistry meeting as part of the ACS biannual meeting held in Dallas March 1998 demonstrated extensive interest by the petroleum and catalysis industries in this area. In a review of fuel-quality specification for transportation fuels, Touvelle et al. of Exxon Research and Engineering discussed trends in the regulation of aromatics in fuels. Although benzene content is carefully scrutinized, the total aromatics content is not regulated specifically in the US. In contrast, European environmental organizations have already established standards in this area and the US is expected to follow in the near future.

The reduction of aromatics in petroleum and particularly in heavy petroleum will require careful management of hydrogen during hydroprocessing. Effective hydrogen management requires an understanding of the relationship between the distribution of the hydrogenated products in the process streams and the conditions of their formation, i.e. temperature and pressure. To meet this need a dual-track approach involving both state-of-the-art property measurement and advanced Ab Initio computations is proposed.

The property measurement program previously funded by DOE Fossil Energy in Oklahoma has accumulated extensive results for partially hydrogenated two, three and four-ring aromatics. The majority of these results have not been published; particularly those which allow calculation of hydroaromatic distributions under processing conditions. Ab Initio computational coding is in its infancy in this area. Accurate atomistic modeling of hydroaromatic systems will use the codes and techniques we have developed for parallel molecular simulations on the ORNL

Paragons and other parallel supercomputers. Using our simulation capabilities, we believe we can substantially surpass the best prior efforts in realism and quantitative, predictive accuracy. These simulations will build on existing ORNL world-class efforts on simulating high temperature liquid and supercritical aqueous systems.

The experimental database and the fundamental understanding from the simulations will be brought together to develop useful models for correlating data and predicting stability under hydroprocessing conditions. The two fundamental questions to be address in this research are: i) What are the “ideal conditions” for meeting low aromatics levels and still meet sulfur levels, smoke point etc., ii) How does the model react to changes in the complex heterogeneous and multi-component systems (i.e., addition of a new crude oil from say Nigeria to the refinery)?

Results from this research will allow the industrial participants to lead the field in catalyst development and process condition controls in processing particularly middle distillates. It can be anticipated that severe operating conditions such as high temperatures, low space velocities, and high pressures can be mediated as the result of insights developed within the program. For example at low temperatures and high space velocities the amount of monoaromatics in the product can be higher than in the original feed. This is not unexpected since every mole of triaromatic compound that is saturated would add a mole to the diaromatics, each diaromatic compound hydrogenated would add a mole to the monoaromatic category, and as the number of rings decrease the rate of saturation should also decrease. Interaction between the various options can be simulated in the model and options such as increased catalytic activity balanced again two- or even three-stage process designs.

Progress:

As of the information cut-off date for this report, funding had not been received in the ORNL Financial Plan for this new task for FY 1999. Hence this section will address the planned research program.

In Phase 1 (FY99) the thermophysical property equipment will be tested and calibrated ready for any thermophysical property measurements required in the furtherance of the goals of this project. Also in Phase 1 an initial literature search will be performed to ascertain the relative importance of the various aromatic compounds in the range of heavy petroleums being imported to refineries in the U.S.

In Phase 2 of the project the thermochemical and thermophysical properties of the major aromatics and their partially/fully hydrogenated products will be collected. The majority of these results have not been published; particularly those which allow calculation of hydroaromatic distributions under processing conditions. The thermophysical properties will be gathered in a DOE Fossil Energy Report and submitted for publication in the refereed scientific literature. Hydroaromatic distributions will be derived where possible and a list of gaps in the database highlighted.

In Phase 3 of the project the gaps in the database will be the subject of thermochemical and thermophysical property measurement or calculation using Ab Initio computational . Accurate atomistic modeling of hydroaromatic systems will use the codes and techniques we have developed for parallel molecular simulations on the ORNL Paragons and other parallel supercomputers. Using our simulation capabilities, we believe we can substantially surpass the best prior efforts in realism and quantitative, predictive accuracy. These simulations will build on existing ORNL efforts on simulating high temperature liquid and supercritical aqueous systems.

DEVELOPMENT OF A CENTRIFUGAL DOWNHOLE SEPARATOR

J. F. Walker, Jr., and R. L. Cummins

INTRODUCTION

Produced water is the largest generated waste stream by volume in the Gulf Coast region and is typically a mixture of formation and injection process water that contains oil, salts, chemicals, solids, and trace metals. In 1991, Louisiana generated over 1 billion barrels and Texas generated 7.5 billion barrels of produced water as a result of oil and gas operations. More than 250 million barrels of produced water are discharged each year to surface waters in both Texas and Louisiana.

Two primary alternatives exist for disposal of produced water in the future: (1) improve the treatment of produced water prior to surface or subsurface disposal and (2) reduce the volumes of produced water by using downhole, or in-well, separations or reinjection. Newer technologies being considered by the industry for contaminant removal include hydrocyclones, reverse osmosis, membrane filtration, gas flotation, carbon adsorption, bioreactors, chemical oxidation, stripping/extraction, and UV oxidation. These processes are complicated and expensive, and several of these unit operations will be required to reduce the conventional, unconventional, and toxic pollutant concentrations to new discharge limits.

Therefore, emphasis should be placed on reinjection or in-well separations/recycle of produced water. Successful use of reinjection has increased in the last several years, but enhanced treatment is often required to remove oil and particulate matter to avoid damaging or plugging the rock formations. The suitability of produced water for reinjection is determined by the enhanced recovery process, the water quality, and the rock formation properties. Options for in-well separations have been evaluated, but no technology has reached maturity.

This project will extend the application of remotely operated separations equipment developed for the nuclear industry to in-well recovery of oil generated by enhanced oil recovery techniques. A conceptual drawing for the process, which combines a centrifugal separator with two downhole pumps, is presented in Fig. 1. Centrifugal solvent extraction contactors, originally developed by the Department of Energy for nuclear fuel reprocessing, have been successfully used for surface treatment of produced water and wastewater generated during environmental clean-up operations. Centrifugal contactor units with rotor diameters of 5.5 and 8.4 cm have been previously tested at Oak Ridge National Laboratory (ORNL), and a larger unit has been designed for Costner Industries Nevada, Inc., for these applications.

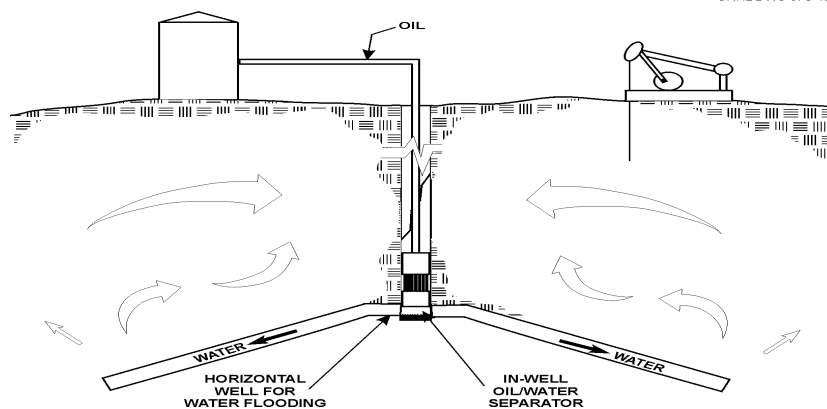


Fig. 1. A conceptual drawing for the installation of a centrifugal separator in an oil recovery shaft, with the separated oil being pumped to the surface for recovery and the produced water being recycled through horizontal wells.

Performance data has shown that centrifugal contactors are capable of separating stable emulsions into “single-phase” streams with generally less than 1% cross-phase contamination. Centrifugal contactors, therefore, have the potential to achieve higher capacity and separations efficiencies that traditional oil/water separator equipment.

The goals of this project are to (a) modify the centrifugal contactor design for use in downhole separation of oil and produced water, (b) evaluate the applicability of the modified centrifugal downhole separator (CDHS) for in-well operations, and (c) evaluate the potential for coupling the CDHS with recently developed horizontal drilling technology to implement in situ recycle of produced water for enhanced oil recovery applications. The development strategy for accomplishing these goals includes (a) conducting bench-scale mixer/settler tests to provide the design parameter for the separator, (b) conducting bench tests with a lab-scale centrifugal unit to determine separation efficiencies with crude oils, (c) designing and operating a larger-scale prototype in the lab to examine scale-up and to identify operational problems (i.e., buildup of solids in the rotor), and (d) conducting a full-scale field demonstration of the CDHS system.

Centrifugal Separator Background

Centrifugal contactors of various sizes (from 2- to 25-cm rotor diameter) have been built and operated over the past three decades at the Savannah River Plant, Argonne National Laboratory (ANL), and ORNL for use in solvent extraction processing of production reactor fuel. During this period, modifications were made to increase the overall reliability of the contactor system with operation shifting from paddle-mixed contactors to annular-mixed contactors. A schematic diagram of the annular-mixed contactor is presented in Fig. 2.

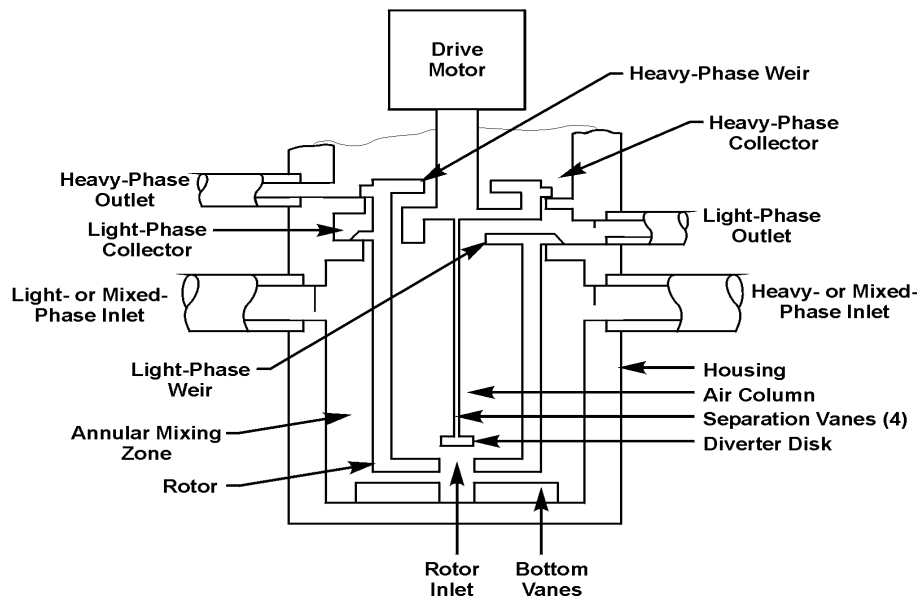


Fig. 2. A schematic drawing of the annular-mixed contactor.

These units have several characteristics that make them attractive for consideration in downhole separation of oil and produced water. These include (a) excellent phase separation characteristics and the ability to break stable emulsions; (b) reliability in remote applications with >20,000 hours of operation prior to maintenance; and (c) the ability to handle high volumetric throughput with a very low residence time. However, several modifications must be made to the unit prior to successful use as a CDHS. These include (a) lengthening the rotor to increase the throughput, (b) introducing the oil/water mixture directly into the bottom of the rotor to limit mixing, (c) overcoming problems associated with the accumulation of solids in the rotor, and (d) connecting the separator to downhole pumps for pumping the oil to the surface and for reinjecting the produced water. Discussions with representatives from Chevron, Phillips Petroleum, Texaco, Unocal, and the Department of Energy have resulted in the formulation of a set of functional criteria for use in the development of the CDHS. These functional criteria are presented in Table 1.

Table 1. Functional Criteria to Be Used in the Development of the CDHS

Flow rate	2000 to 10,000 barrels per day (~60–300 gal/min)
Diameter	Concentrate on side casing diameter of 6 3/4 in. Allow 3/4 in. of clearance for tube, cables, etc. Larger-diameter casing can be considered.
Temperature	Use ambient temperature in initial bench tests. Nominal field temperatures from 100 to 180°F. Maximum temperature of 250°F should be considered
Oil/water ratio	Range from 1:10 to 10:1
Solids	Range from 0 to 3% and from sand to clay
Product quality	Maximum 2000 mg/L oil in water
Reliability	Same as elective submersible pump (8 months mean time between failure)

Bench-scale Testing And Results

A schematic diagram of the system used in the bench-scale tests is provided in Fig. 3. The crude oil and synthetic seawater are pumped from separate 227-L (60-gallon) tanks at set flow rates into a 4-L container equipped with a homogenizer. The homogenizer, which operates at speeds of up to 24,000 rpm, emulsifies the two phases. The emulsion is then pumped into the centrifugal separator. The organic effluent from the separator drains back to the crude oil tank, and the aqueous effluent drains to the seawater tank. The separator used in these tests was provided by CINC, Inc. The separator is a model V-2 unit equipped with a 1/6 HP motor. It has a rotor diameter of 5 cm (2 in.) and is rated for flows up to 2 L/min.

The separator was initially tested using an organic mixture of tributyl phosphate (TBP) and dodecane and an aqueous solution of dilute nitric acid to verify the performance of the unit. These liquids were utilized because previous models developed at ANL and modified at ORNL had been developed for TBP/dodecane systems. This model has been shown to accurately predict the throughput for TBP/dodecane systems, with cross-phase contamination of less than 1% in either the aqueous or the organic effluent in units with rotor diameters varying from 2 to 25 cm and rotor speeds varying from 600 to 6000 rpm. A comparison of the typical operating data and the model prediction for this organic/aqueous solution is presented in Fig. 4. As can be seen, the model accurately predicts the throughput for the TBP/dodecane and nitric acid solutions at rotor speeds ranging from 1500 to

3500 rpm. The unit was not operated outside of these limits. The agreement between the model and the operational data indicates that the unit was functioning properly.

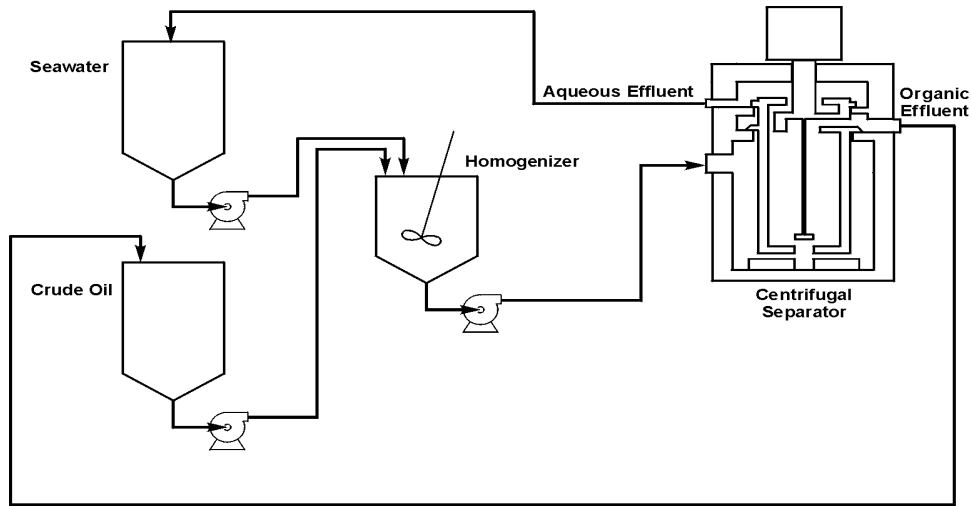


Fig. 3. Aschematic diagram of the system used for bench-scale testing.

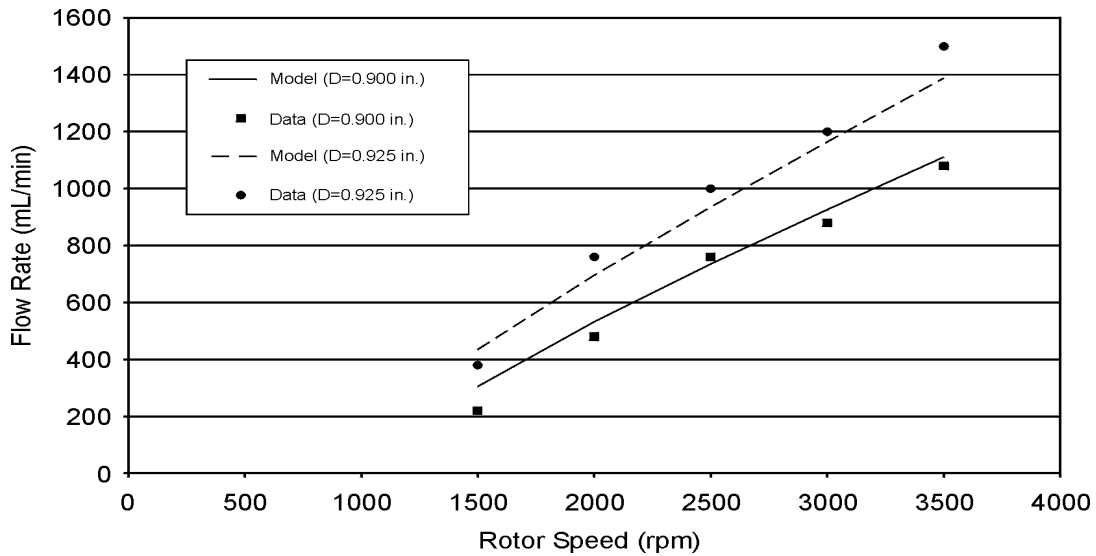


Fig. 4. Comparison of operating data and model prediction for a TBP/dodecane and dilute nitric acid feed.

A crude oil, designated as Ladybug Crude, has been provided by Texaco for bench-scale testing with the centrifugal separator. Ladybug Crude is a Gulf of Mexico crude with an API gravity of 34.06°,

a specific gravity at 60°F of 0.8547, a viscosity at 70°F of ~1030 cP, and a viscosity at 80°F of ~217 cP. The ASTM Standard Specification for Substitute Ocean Water (ASTM: D1141-90) is being used for the aqueous phase in the bench-scale tests with these crude oils. All tests results reported in this paper for Ladybug Crude used a 1:1 ratio of crude to synthetic ocean water for feeding the separator and were conducted at ambient conditions (70–80°F).

A comparison of the predicted flow rate and the actual flow rate as a function of rotor speed and aqueous weir diameter is presented in Fig. 5. The solid lines represent the predicted throughput with <1% phase crossover in either the aqueous or crude oil effluent from the separator. The data points represent the actual measured flow rate through the unit. As can be seen for the 0.900-in.-diameter aqueous weir, the model predicts a throughput of ~900 mL/min at 2000 rpm and ~1900 mL/min at 3500 rpm. The measured flows, with <1% cross-phase contamination, were 40 and 100 mL/min at 2000 and 3500 rpm, respectively, which is much less than predicted by the model. The actual throughput for the separator, with >1% cross-phase contamination, is also presented in Fig. 5 for both the 0.900- and 0.925-in.-diameter aqueous weirs. The operational data for those runs with carryover >10% represent the maximum throughput obtained prior to the crude oil carrying over the aqueous weir (i.e., the crude oil in the aqueous effluent from the separator exceeding >1% by volume). During these runs, the quantity of seawater carried over in the crude effluent increased with throughput. A comparison of the average percentage of water in the crude (averaged for constant rpm) versus flow rate with error bars of 1 standard deviation is presented in Fig. 6. As can be seen, the percentage of water in the crude is essentially linear with respect to the flow rate for both weirs up to flow rates of 1200 mL/min. Above 1200 mL/min, the percentage of water in the oil tends to level out in the 20–22% range.

The concentration of silica-gel-treated hexane extractable material (SGT-HEM), which is a measure of the insoluble organics remaining in the water, is presented in Fig. 7 as a function of flow and rotor speed. The concentration of SGT-HEM increases with the flow rate and tends to level out at a maximum of ~400 mg/L. When comparing the concentration with the functional criteria listed in Table 1, it can be seen that the residual oil is less than the 2000-mg/L requirement and is generally in the range of 200–400 mg/L. Therefore, the quality of water from these tests appears to be suitable for reinjection.

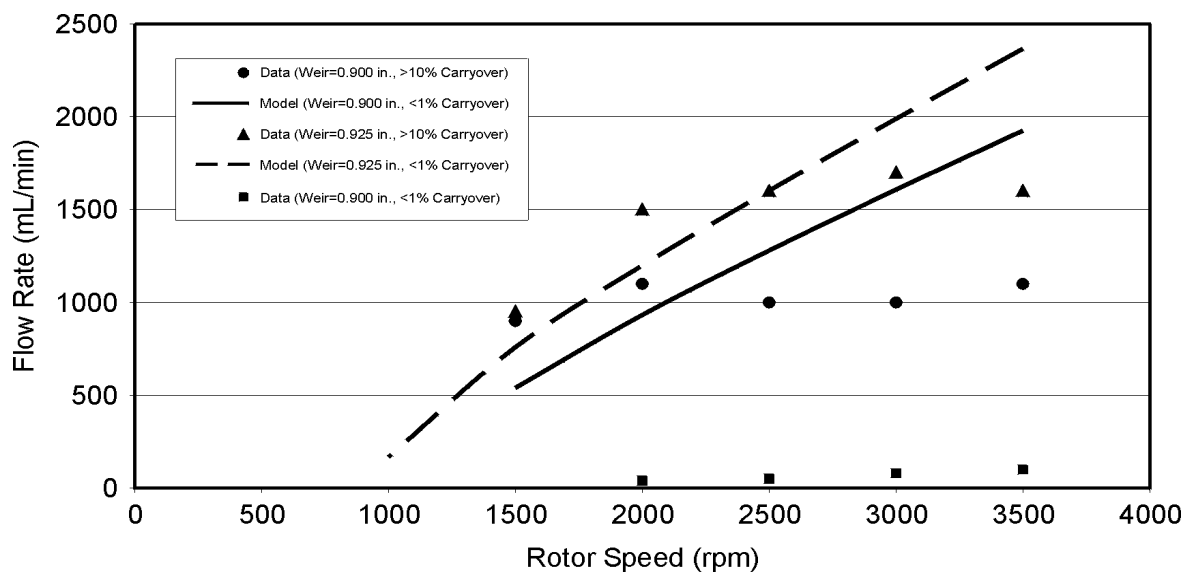


Fig. 5. A comparison of the predicted flow rate and the actual flow rate as a function of rotor speed and aqueous weir diameter.

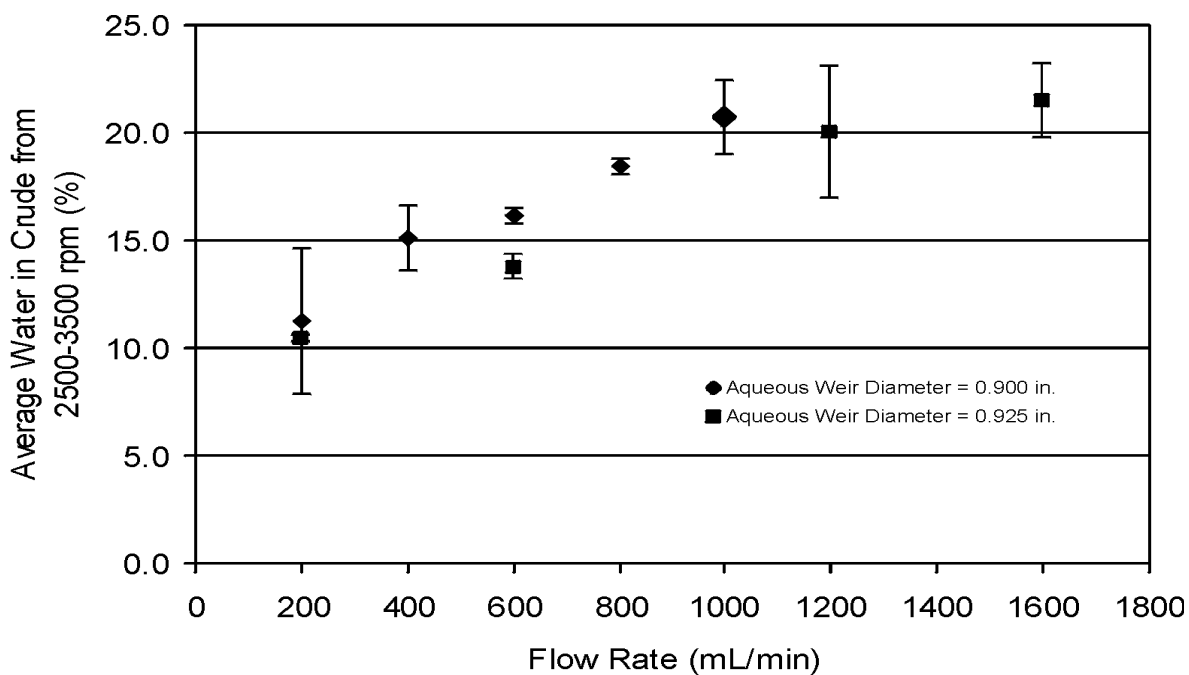


Fig. 6. A comparison of the average percentage of water in the crude (averaged for constant rpm) versus flow rate with error bars of 1 standard deviation.

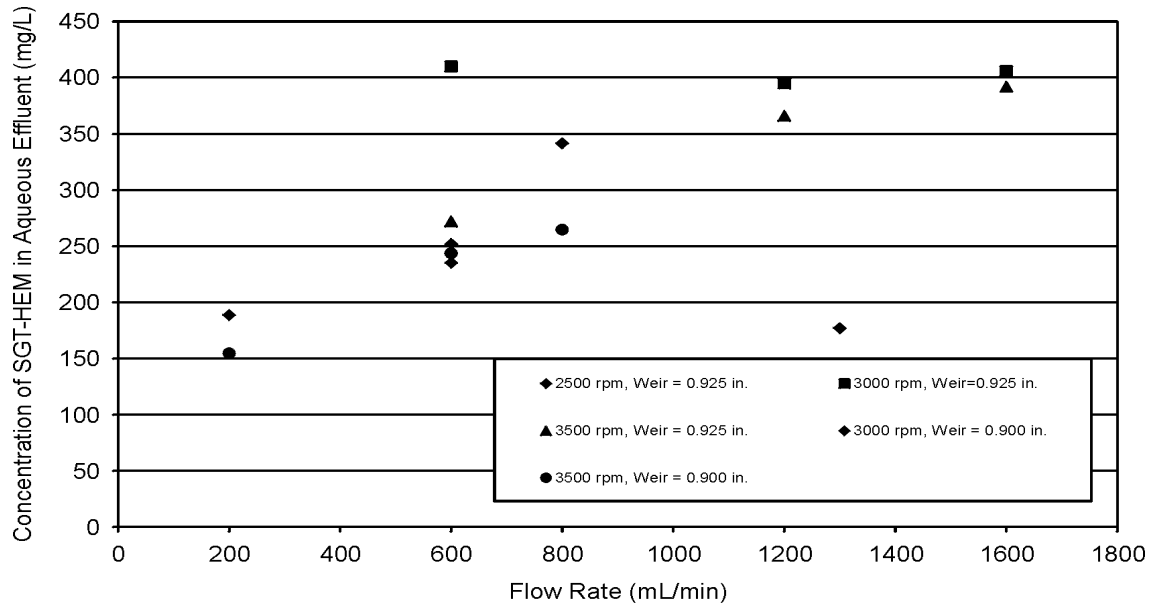


Fig. 7. The concentration of silica-gel-treated hexane extractable material (SGT-HEM), which is a measure of insoluble organics remaining in the water as a function of flow and rotor speed.

From Figs. 5-7 above, it can be noted that while processing the Ladybug Crude, the throughput for the separator was substantially less than predicted by the model and the aqueous effluent from the separator meets the functional criteria for reinjection. The primary reason that the model did not predict the throughput was that even at very low flows there was >1% water present in the crude effluent from the separator. This was most likely due to the formation of a stable oil/water emulsion that did not completely break under the gravitational force (up to ~350 g) exerted by the centrifugal separator. As the separator is scaled up to a larger diameter and longer length, it will exert a greater centrifugal force for an extended length of time on the oil/water emulsion. This may be enough to break the emulsion. It should be noted that even at the existing conditions, with 10–20% water in the crude and the water meeting reinjection limits set by the functional criteria, pumping costs are reduced by 40 to 45% and water disposal costs are reduced by 80 to 90%.

It should also be noted that from observations while operating with Ladybug Crude, the separator appeared to be limited by the size of the heavy-phase and light-phase collectors. At higher flow rates the aqueous effluent from the rotor would overflow the heavy-phase collector and the crude would overflow the light-phase collector. This resulted in (1) contamination of the crude effluent by the water, which could have also have attributed to the quantity of water seen the in crude effluent, and (2) recycle of both the crude and water back to the rotor inlet which would reduce the throughput of the separator. A new housing, which increased the volume of the collector rings by a factor of ~4, was designed and fabricated

to solve this problem. Tests with the new housing fed with TBP/dodecane and a dilute nitric acid solution indicated that the throughput of the separator was approximately doubled, while still being able to maintain <1% cross phase contamination both the aqueous and organic effluents from the separator. Tests with Ladybug crude and the new housing have not yet been conducted.

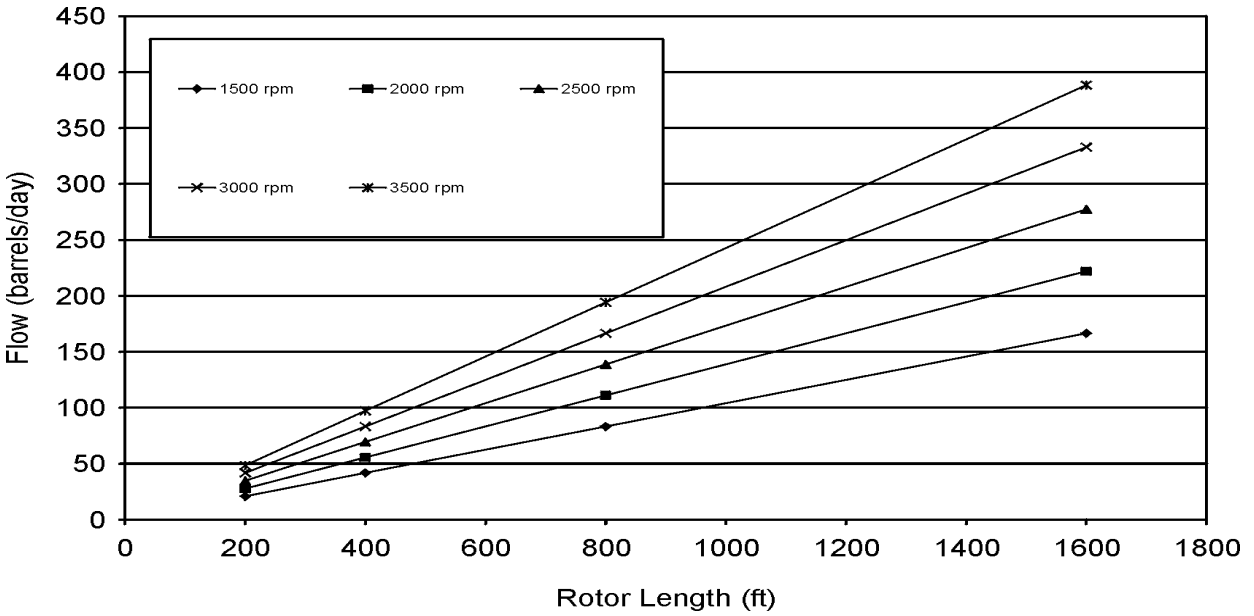
The functional criteria developed by the oil producers participating in the development of the CDHS suggested the use of a separator which would fit into a 6-3/4-in. inside diameter casing. Therefore, the model was run to predict the maximum throughput which could be expected with a 15-cm (6-in.)-diameter rotor as a function of rotor length and speed. The results are presented in Fig. 8. By comparing this figure with the functional criteria in Table 1, it appears that the functional criterion for a throughput of 2000 to 10,000 barrels per day is achievable with a rotor length of less than 3.7 m (12 feet). However, the data indicates that there may be substantially more water in the crude effluent from the separator than the <1% predicted by the model. Additional work is needed to resolve the discrepancies between the model and the actual operational data from the Ladybug Crude.

SUMMARY

A CDHS is currently being developed at ORNL that will extend the application of remotely operated separations equipment developed for the nuclear industry to in-well recovery of oil with in situ recycle of the produced water. The development strategy used will include (a) bench-scale testing with crude oils to determine preliminary separation efficiencies and flow, (b) design and laboratory testing of a larger prototype separator that will be utilized to verify scaleup and to identify and overcome operational problems (e.g., buildup of solids in the rotor), and (c) a full-scale field demonstration of the developed CDHS system. This paper reports on the current status of the development, which is in the bench-scale testing phase.

Bench-scale testing is currently being conducted with a crude oil provided by Texaco and designated as Ladybug Crude. This is a Gulf of Mexico crude with an API gravity of 34.06°, a specific gravity at 60°F of 0.8547, a viscosity at 70°F of ~1030 cP, and a viscosity at 80°F of ~217 cP. Model predictions for the Ladybug Crude indicate that a separator with a rotor diameter of 15 cm (6 in.) and a length 4 ft could produce ~2000 barrels per day at rotor speeds of ~1500 to 3500 rpm. For a throughput of 10,000 barrels per day and a 15-cm-diameter rotor, a rotor length of 3.7 m (12 ft) would be required.

Fig. 8. The maximum throughput that could be expected with a 15-cm (6-in.)-diameter rotor as a function of rotor length and speed from model predictions.



The percentage of water remaining in the organic effluent varies with the throughput of the separator. At low flows (~200 mL/min for the bench-scale unit), the crude oil contains ~10% water, and near the maximum flow (~1600 mL/min), the crude contains ~20% water. This could possibly be attributed to (1) the formation of a stable oil/water emulsion that was not completely broken by the centrifugal force of the separator in these studies or (2) overflow of water from the heavy-phase collector into the light-phase collector. The unit has been redesigned to eliminate the overflow of water from the heavy-phase collector into the light-phase collector; however, the new design has not yet been tested with crude oil.

The residual oil in the aqueous effluent stream also tended to increase with flow. At low flows, the aqueous stream contained ~150–250 mg/L SGT-HEM, and at the maximum flows, the aqueous effluent contained ~400 mg/L SGT-HEM. Therefore, the quality of the aqueous effluent from the separator appears to be suitable for reinjection.